Methane Hydrate Production from Alaskan Permafrost

Core and Fluid Analysis

Topical Report

October 1, 2001 to January 31, 2005

by

Richard Sigal (Anadarko Petroleum Corp.)

Kent Newsham (Anadarko Petroleum Corp.)

Thomas Williams (Maurer Technology Inc.)

Barry Freifeld (Lawrence Berkeley National Laboratory)

Timothy Kneafsey (Lawrence Berkeley National Laboratory)

Carl Sondergeld (University of Oklahoma)

Shandra Rai (University of Oklahoma)

Jonathan Kwan (Anadarko Petroleum Corp.)

Stephen Kirby (U.S. Geological Survey)

Robert Kleinberg (Schlumberger-Doll Research)

Doug Griffin (Schlumberger-Doll Research)

February 2005

DE-FC26-01NT41331 (Task 11)

Maurer Technology Inc.
13135 South Dairy Ashford
Sugar Land, TX 77478

University of Oklahoma
1000 Asp Avenue
Norman, OK 73019

Anadarko Petroleum Corp.
1201 Lake Robbins Drive
The Woodlands, TX 77380

U.S. Geological Survey
345 Middlefield Road
Menlo Park, CA 94025

Lawrence Berkeley National Laboratory
1 Cyclotron Road
Berkeley, CA 94720

Schlumberger-Doll Research
Old Quarry Road
Ridgefield, Connecticut 06877

Disclaimer

This report was prepared as an account of work sponsored by an agency of the United States Government. Neither the United States Government nor any agency thereof, nor any of their employees, makes any warranty, express or implied, or assumes any legal liability or responsibility for the accuracy, completeness, or usefulness of any information, apparatus, product, or process disclosed, or represents that its use would not infringe privately owned rights. Reference herein to any specific commercial product, process, or service by trade name, trademark, manufacturer, or otherwise does not necessarily constitute or imply its endorsement, recommendation, or favoring by the United States Government or any agency thereof. The views and opinions of authors expressed herein do not necessarily state or reflect those of the United States Government or any agency thereof.

Abstract

Natural-gas hydrates have been encountered beneath the permafrost and considered a nuisance by the oil and gas industry for years. Engineers working in Russia, Canada and the USA have documented numerous drilling problems, including kicks and uncontrolled gas releases, in arctic regions. Information has been generated in laboratory studies pertaining to the extent, volume, chemistry and phase behavior of gas hydrates. Scientists studying hydrate potential agree that the potential is great – on the North Slope of Alaska alone, it has been estimated at 590 TCF. However, little information has been obtained on physical samples taken from actual rock containing hydrates.

The work scope drilled and cored a well The Hot Ice No. 1 on Anadarko leases beginning in FY 2003 and completed in 2004. An on-site core analysis laboratory was built and utilized for determining the physical characteristics of the hydrates and surrounding rock. The well was drilled from a new Anadarko Arctic Platform that has a minimal footprint and environmental impact. The final efforts of the project are to correlate geology, geophysics, logs, and drilling and production data and provide this information to scientists developing reservoir models. No gas hydrates were encountered in this well; however, a wealth of information was generated and is contained in this report.

The Hot Ice No. 1 well was drilled from the surface to a measured depth of 2300 ft. There was almost 100% core recovery from the bottom of surface casing at 107 ft to total depth. Based on the best estimate of the bottom of the methane hydrate stability zone (which used new data obtained from Hot Ice No. 1 and new analysis of data from adjacent wells), core was recovered over its complete range. Approximately 580 ft of porous, mostly frozen, sandstone and 155 of conglomerate were recovered in the Ugnu Formation and approximately 215 ft of porous sandstone were recovered in the West Sak Formation. There were gas shows in the bottom part of the Ugnu and throughout the West Sak. No hydrate-bearing zones were identified either in recovered core or on well logs. The base of the permafrost was found at about 1260 ft.

With the exception of the deepest sands in the West Sak and some anomalous thin, tight zones, all sands recovered (after thawing) are unconsolidated with high porosity and high permeability. At 800 psi, Ugnu sands have an average porosity of 39.3% and geometrical mean permeability of 3.7 Darcys. Average grain density is 2.64 g/cc. West Sak sands have an average porosity of 35.5%, geometrical mean permeability of 0.3 Darcys, and average grain density of 2.70 g/cc. There were several 1-2 ft intervals of carbonate-cemented sandstone recovered from the West Sak. These intervals have porosities of only a few percent and very low permeability. On a well log they appear as resistive with a high sonic velocity. In shallow sections of other wells these usually are the only logs available. Given the presence of gas in Hot Ice No. 1, if only resistivity and sonic logs and a mud log had been available, tight sand zones may have been interpreted as containing hydrates. Although this finding does not imply that all previously mapped hydrate zones are merely tight sands, it does add a note of caution to the practice of interpreting the presence of hydrates from old well information.

The methane hydrate stability zone below the Hot Ice No. 1 location includes thick sections of sandstone and conglomerate which would make excellent reservoir rocks for hydrates and below the permafrost zone shallow gas. The Ugnu formation comprises a more sand-rich section than does the West Sak formation, and the Ugnu sands when cleaned and dried are slightly more porous and significantly more permeable than the West Sak.

Table of Contents

1. Introduction

During the winter operations seasons of 2003 and 2004, Anadarko Petroleum Corporation, in cooperation with Maurer Technology and the Department of Energy, drilled and cored a shallow well (Hot Ice No. 1) located in Sec.30-T9N-R8E, Umiat Meridian, on the North Slope of Alaska. The well location is on an Anadarko lease that is located down-dip and about five miles east of established hydrate occurrences in the ARCO Cirque well and in wells in the Tarn Field.

Primary objectives of this project were to:

1. Analyze existing geological and geophysical data and obtain new field data required to choose a drilling location
2. Test the best methods and tools for drilling and recovering hydrates
3. Plan, design, and implement a program to safely and economically drill and produce gas from hydrates in Alaska

An important goal was to recover and characterize hydrate-bearing core and potential hydrate and shallow gas reservoir rocks. To provide core material for this characterization, a continuous coring system was used to drill the well. Additionally, Anadarko, in cooperation with Rock Properties Resources (who was responsible for construction), designed a mobile core characterization laboratory operated on the site. (The mobile laboratory is described in Section 2.) This report focuses on information obtained from recovered core and measurements made in the mobile laboratory.

The mobile core laboratory includes capability for both standard core characterization and equipment specially designed to measure properties of sediments containing gas hydrate. The laboratory has the capacity to make measurements on plugs at temperatures below freezing, while under specified confining and pore pressures. This laboratory was operated on the drill site by a team from Corpro and PTS Labs. (During 2003 field operations, technologists on site were Graham McLeod (operations manager), Jeff van Eerder, Nathan Emery, and Guy McCardle. In 2004 the staff was Jeff van Eerder (operations manager), Nathan Emery, Guy McCardle, and Richard Schweizer.) All measurements discussed in this report were made in the mobile core laboratory, either on the drilling platform or in Deadhorse, Alaska.

2. Experimental

2.1 Background

During both the 2003 and 2004 coring seasons, a special mobile core laboratory (**Figure 1**) was employed to immediately perform measurements on both whole core and 1-inch plugs taken from the whole core, while maintaining temperature. Whole core measurements included: core gamma log, infrared temperature, velocity measurement, geologic description and white light photographs, high-resolution CT scan (equipment from LBNL), and a nuclear magnetic resonance measurement (with CMR tool from Schlumberger) on a portion of each section of core. Plug measurements included: bulk volume, grain density, helium porosity and permeability at confining stress, P and S wave velocity, resistivity, and thermal conductivity. For hydrate samples, the NMR system (Schlumberger CMR Tool) would be used to determine fluid volume in the sample at various steps in the dissociation process, while released gas volumes and composition were also recorded.

Figure 1. Mobile Core Laboratory being Shipped (top) and at Hot Ice No. 1 Site (bottom)

2.2 Task Statement

Task 11.0 – On-Site Core and Fluids Analysis

The team will analyze core and fluids using a specially constructed mobile core laboratory, staffed by trained laboratory technicians. Core will be received in the cold module, where it will be photographed and assessed for the presence of hydrate. One-inch plugs will be removed from the core, and these plugs will be measured for porosity, permeability, compressional and shear wave velocity, resistivity, thermal conductivity, and NMR with specialized equipment specifically designed for making these hydrate core measurements, including a Schlumberger CMR tool. All of these measurements will be made under controlled pressure and temperature. Hydrate dissociation will be monitored. Laboratory technicians will assist in preparing core for additional testing at other locations. Results of core and fluids handling procedures will be provided to Westport for incorporating into the DOE-funded Westport Hydrate Core Handling Manual. The results of the analysis will be incorporated in Tasks 17, 18, 19 and 20.

2.3 Mobile Core Laboratory

To allow on-site analysis of core, a special mobile core laboratory was designed and constructed (**Figure 2** (see next page)). Anadarko, in cooperation with Rock Properties Resources, designed the mobile core laboratory which was operated on the drilling site. Rock Properties Resources constructed the laboratory as well as provided critical support throughout the project. Resulting from the effort was a state-of-the-art, winterized, mobile core characterization laboratory capable of measuring large volume of core in a cost-effective manner in arctic conditions. This effort represents the first comprehensive on-site gas hydrate analytical laboratory of its kind to be deployed in the Arctic.

On-site analysis of cores was considered a critical capability due to the following:

- Cores are unstable, i.e., they decompose into methane, water and sand.
- Core must be maintained at subzero °C during handling and measurement.
- Cores must simultaneously be pressurized and cooled to *in-situ* conditions for measurement and preservation.

At the Hot Ice No. 1 site, core was received in the cold core module, where it was photographed and assessed for presence of hydrate. One-inch plugs were removed from the core, and these plugs measured for porosity; permeability; compressional and shear wave velocity; resistivity; thermal conductivity; and NMR with specialized equipment specifically designed for making these hydrate core measurements, including a Schlumberger CMR tool. All of these measurements were completed under controlled pressure and temperature. Dissociation of hydrates (when encountered) was also to be monitored.

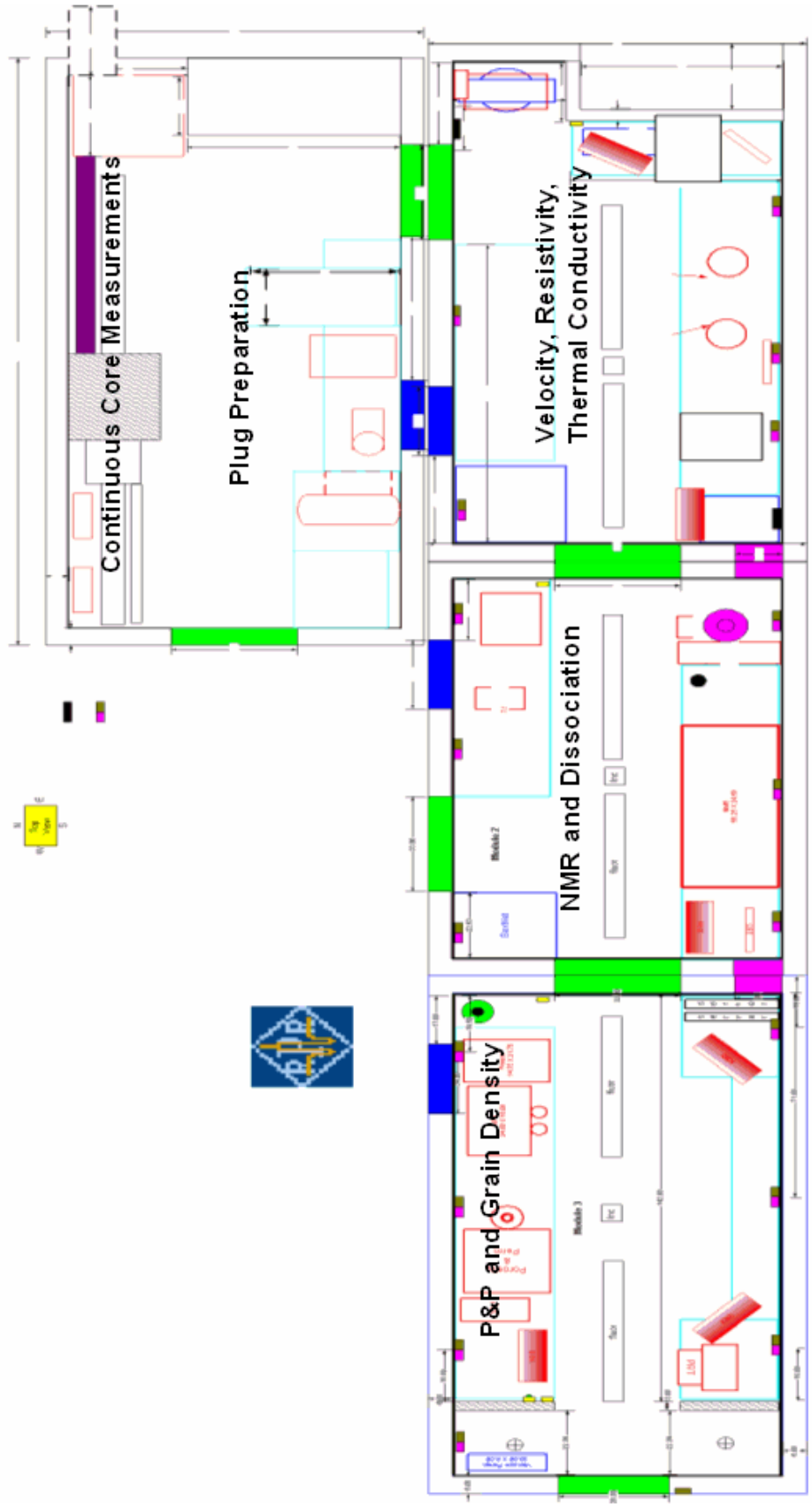

Figure 2. Schematic of Mobile Core Laboratory

The mobile core laboratory was designed with the following features: 1) self-contained units (modules); 2) requires only power connection; 3) climate-controlled to operate between -40°C to 45°C; and 4) truck or helicopter transportable. Services in each of the four interconnected modules are listed in **Table 1**.

Table 1. Mobile Core Laboratory Modules

	Services/Equipment
Module 1	> Velocity > Resistivity > Thermal Conductivity
Module 2	> NMR > Hydrate Dissociation > Dimensions > Core Cleaning and Drying
Module 3	> Porosity > Permeability > Grain Density > Saturation System > Computer Systems
Module 4	> Whole-Core Measurements > Core Handling

Photos from each of the four modules comprising the mobile core laboratory are presented in **Figures 3-6**.

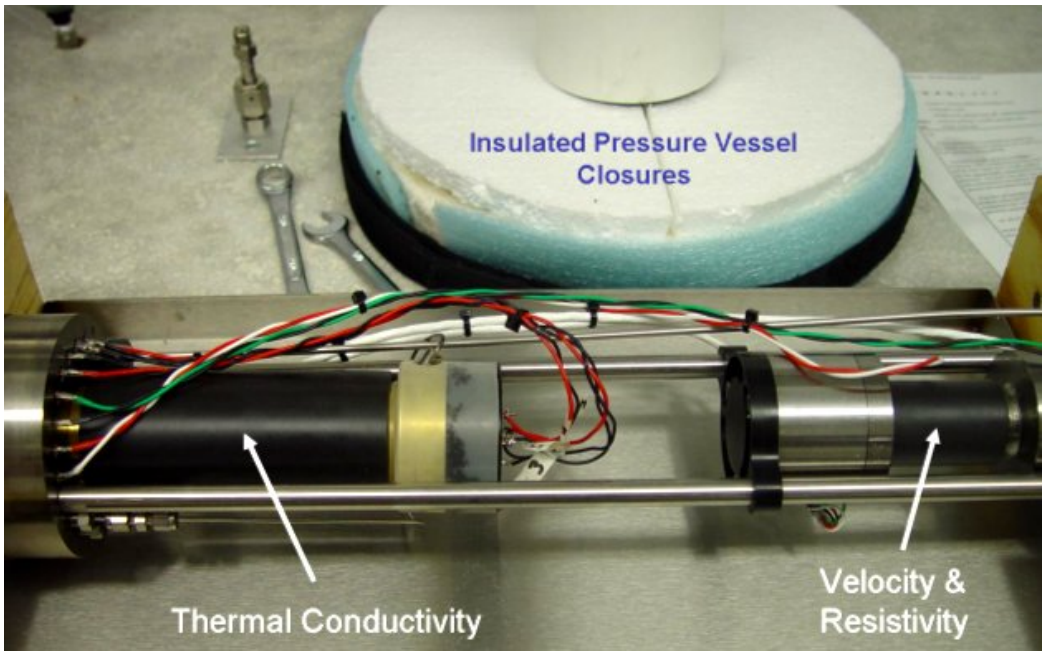

Figure 3. Equipment in Module 1 of Mobile Core Laboratory

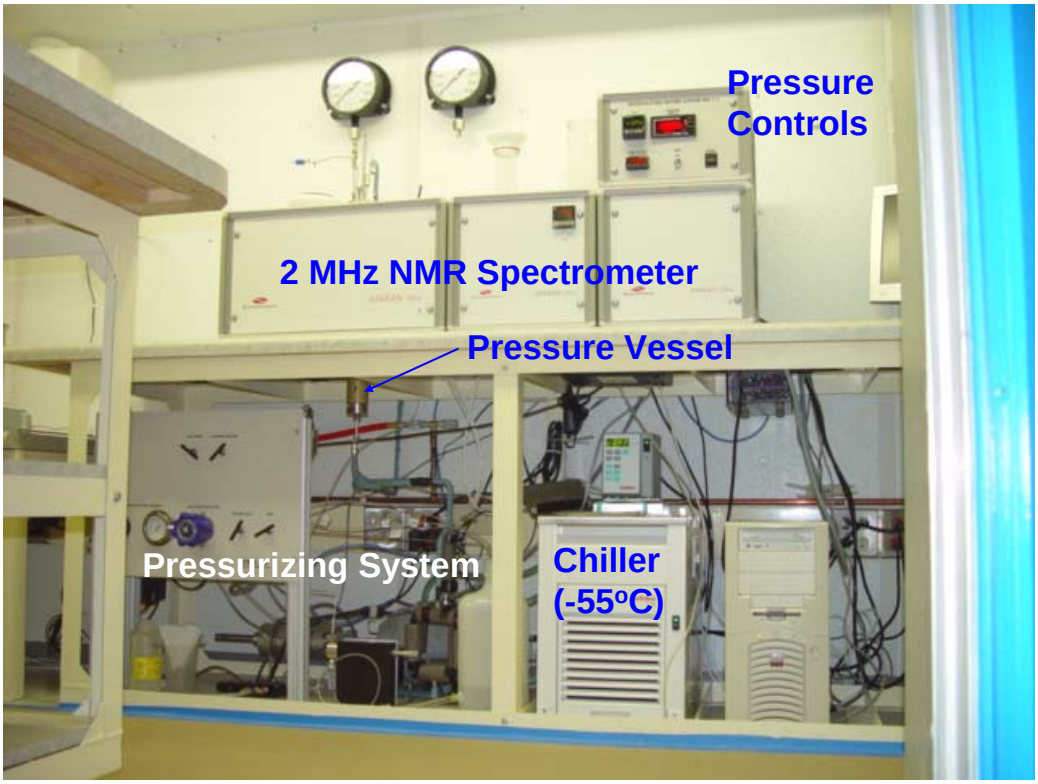

Figure 4. Equipment in Module 2 of Mobile Core Laboratory

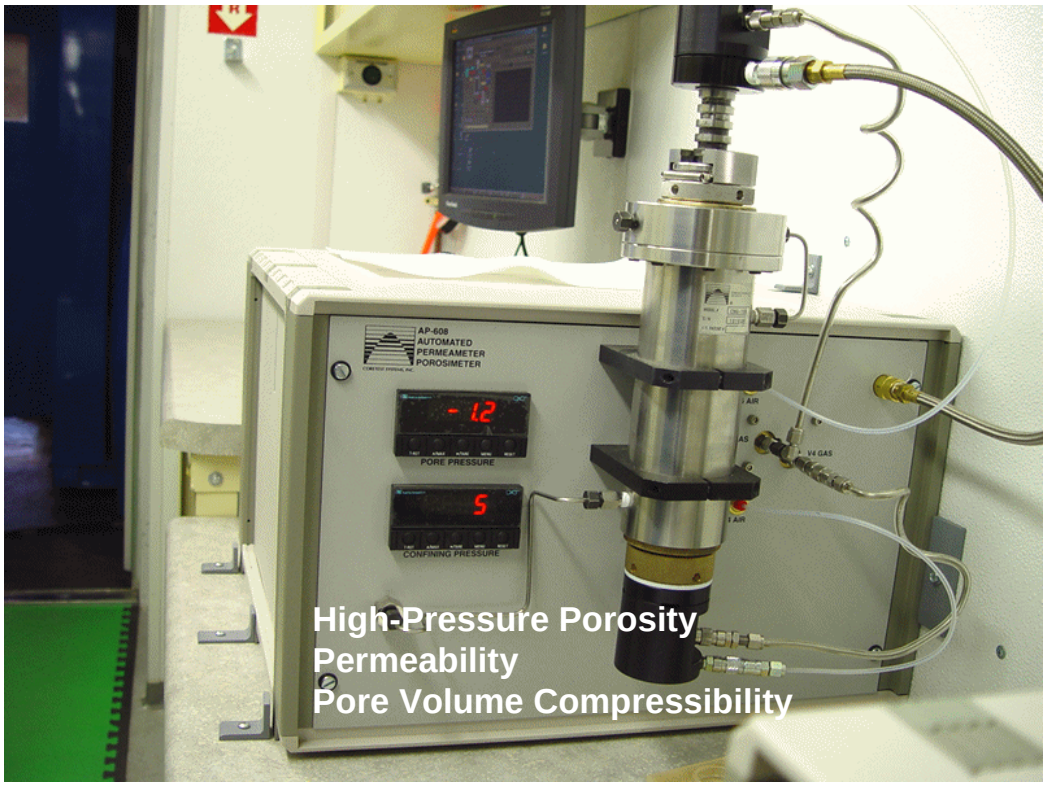

Figure 5. Equipment in Module 3 of Mobile Core Laboratory

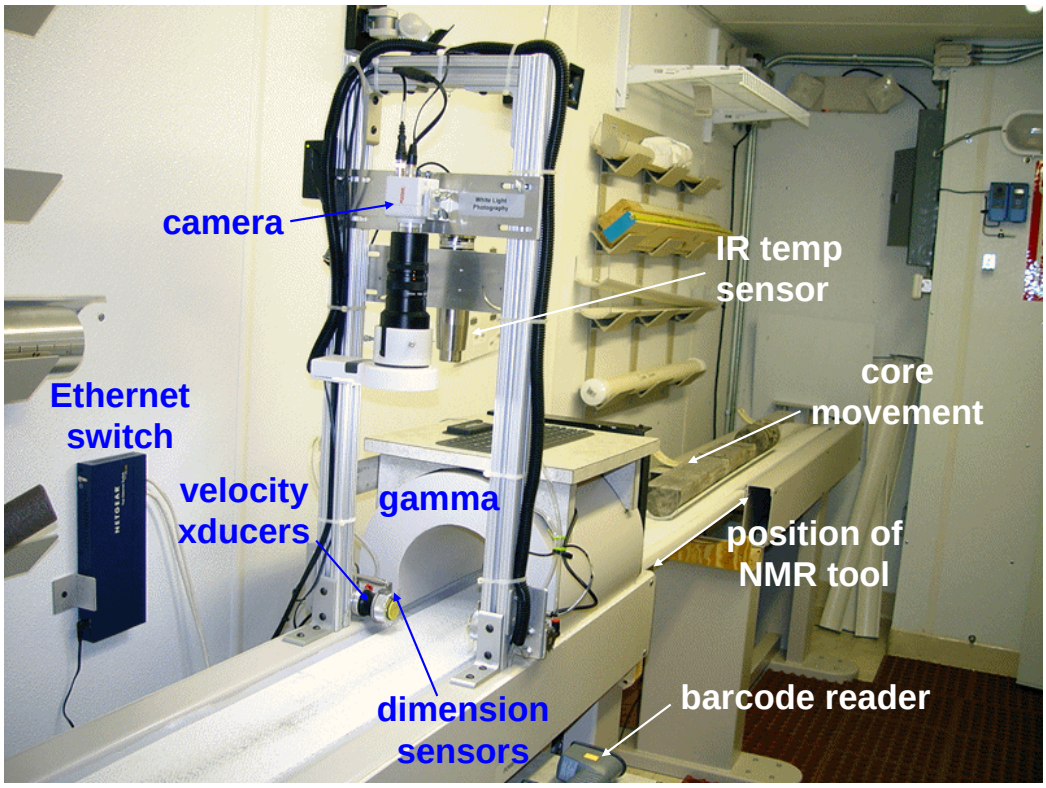

Figure 6. Equipment in Module 4 of Mobile Core Laboratory

2.4 Porosity and Permeability Measurements

During the 2003 winter operations season, the Hot Ice No. 1 well was cored continuously from 107 ft below kelly bushing (BKB) to 1400 ft BKB. In 2004 (during the next arctic drilling season) the well was deepened to 2300 ft and core was continuously recovered from the deeper section. Core recovery was close to 100%, and about 2200 ft of core were available for study. KB was at 214 ft above mean sea level (MSL), and ground level was at 188 ft MSL. Operations recovered core from the Ugnu formation in 2003 and from the West Sak formation in 2004. Following the conclusion of the project, core was provided to the University of Alaska for future analysis.

Core was described on site by geologists, Bill Zogg and Jim Ebanks (see **Section 4**). The bottom of permafrost was identified in a thick sand zone at about 1260 ft. Identification was made independently on both the core and log measurements.

Zogg and Ebanks identified locations to plug for core analysis in the sandstone sections. Extraction of plugs was essentially restricted to sandstone sections as these are the most interesting from a reservoir prospective. Additionally, it is very difficult to plug and make meaningful measurements on shale and conglomerate sections. Locations were chosen to provide as unbiased a sampling as possible of the geology of the sandstone sections. At most locations at least two horizontal companion plugs were taken to provide materials for a variety of measurements. Measurements on companion plugs were necessitated as Ugnu core was frozen and when thawed was unconsolidated. The West Sak sands (except in the deepest zones) were also completely unconsolidated.

Porosity, permeability, and grain density were measured on cleaned and dried plugs. Plugs were dried in a vacuum oven at 150°F. The plugs were wrapped and screened while frozen. Porosity and permeability were measured in a CoreTest unsteady-state permeameter. Grain density was measured in a high-pressure picnometer built by Rock Properties Resources. Both porosity and permeability were measured at three confining pressures nominally set at 800 psi, 1200 psi and 1800 psi.

Plug measurements of porosity and permeability are described in **Section 5**.

2.5 Compressional and Shear-Wave Velocity Measurements

The mobile core laboratory contains two separate computer-controlled systems for measuring acoustic velocities on 1-inch plugs. These systems were manufactured by New England Research. Each has computer servo-controlled pore and confining pressure capabilities. They are externally cooled via a programmable chiller capable of temperature control from -8°C to +40°C. Velocity measurements are made at a nominal frequency of 1 MHz. A compressional velocity, Vp, and two polarized shear velocities, Vs1 and Vs2, are recorded on each sample at each pressure or temperature.

Measurements are automatic at programmed confining stresses and temperatures. Pore pressure in the sample is independently controlled. If hydrates had been found at Hot Ice No. 1, CH_4 would have been used as the pore pressure fluid. Since no hydrates were found, no pore pressure was maintained. This same system is also used to make a simultaneous resistivity measurement on the same 1-inch sample. Thermal conductivity can also be measured on a

separate 0.5-inch sample colocated in the same pressure cell above the velocity/resistivity sample.

Results of velocity measurements are discussed in detail in **Section 6**.

2.6 Resistivity Measurements

Resistivity was measured in a two-electrode system on plugs that were nominally 1 inch diameter and 1 inch long. The system was manufactured by New England Research. It is designed to perform an automated sequence of measurements that measure resistivity, compressional velocity, and two components of shear velocity at a series of confining stresses. Pore pressure and pore pressure fluid are separately controlled. Temperature at which the measurement is made can vary from below freezing to above room temperature.

Currently there is no direct measurement of the sample dimensions after confining stress is applied. This introduces a small error in calculated resistivity for unconsolidated unfrozen samples. The unfrozen unconsolidated samples were all wrapped in Teflon tape during measurement. Some were measured with steel screens on and some had the steel screens removed. The mobile laboratory system has two pressure cells (NER1 and NER2) in which measurements were made. No systematic differences in resistivity measurements were observed between the two systems or between screened and unscreened samples.

Results of resistivity measurements are discussed in detail in **Section 7**.

2.7 NMR Measurements

NMR measurements were made on 49 Ugnu and 46 West Sak plugs recovered from zones identified as sands by well site geologists. These sands are the potential reservoir rocks in the cored section. Measurements were made in a Marian Ultra 2 MHz bench-top system. The system was augmented with a pressure cell in which confining and pore pressure along with temperature could be controlled. If hydrates had been found, pore pressure gas would have been CH_4.

On samples taken from permafrost zones in the Ugnu formation, measurements were made on recovered state samples both in a frozen state and after they had been allowed to thaw. Measurements were also made on cleaned, dried and resaturated samples. For samples from the West Sak formation, only resaturated samples were measured. For the Ugnu samples four samples were measured in a frozen state at a temperature of approximately -5°C. All four of these samples were also measured at room temperature after thawing. Three of the four were also remeasured after resaturation. A total of 45 recovered state plugs were measured after thawing. Of these, 17 were also measured after resaturation. Four Ugnu samples were only measured after resaturation.

Results of NMR measurements are discussed in detail in **Section 8**.

3. Results and Discussion

3.1 Summary Results for Task 11.0

Task 11.0 – On-Site Core and Fluids Analysis

The project team analyzed core and fluids using a specially constructed mobile core laboratory, staffed by trained laboratory technicians. Core was received in the cold module, where it was photographed and assessed for the presence of hydrate. One-inch plugs were removed from the core, and these plugs were measured for porosity, permeability (see **Section 5**), compressional and shear wave velocity (see **Section 6**), resistivity (see **Section 7**), thermal conductivity, and NMR with specialized equipment specifically designed for making these hydrate core measurements (see **Section 8**), including a Schlumberger CMR tool. All of these measurements were made under controlled pressure and temperature.

A summary of the geology description of the core is presented in **Section 4**.

A discussion of factors and assumptions applied to estimate the depth of the base of the hydrate stability zone is presented in **Section 9**.

Because no hydrates were encountered, hydrate dissociation testing was not conducted, although procedures and equipment are described here and in the final report. Laboratory technicians assisted in preparing core for additional testing at other locations. Results of core and fluids handling procedures were provided for the DOE-funded Westport Hydrate Core Handling Manual. Results of core analyses were incorporated into Tasks 17, 18, 19 and 20.

3.2 Summary Results for Subtask 11.1

Subtask 11.1 – Mobile Laboratory Repair and Upgrade

The project team repaired and upgraded the mobile core laboratory in Tulsa during the summer and fall of 2003 (after the first drilling season) specifically to: 1) redesign the pressure and cooling system for the NMR spectrometer to achieve significantly lower temperature capability required for analysis of hydrate samples; 2) improve insulation for the velocity/thermal conductivity/resistivity measurement system; 3) configure the NMR and VCR systems with capability to allow positive pore pressures of methane for hydrate stability; and 4) develop a central database for managing and storing all data measured in the mobile core laboratory.

Regarding the use of the LBNL CT scanner on site:

1. One end of a 20-ft Conex was partitioned with a separate door to the outside for the X-ray room.
2. There was a heater located in the room.
3. The x-ray room is adjacent to the station where core was cut to 3-ft lengths.
4. Core sections were taken outside and then into the x-ray room.

5. The x-ray machine can be started in a temperature-controlled environment.
6. During shipment, the machine will be capable of being subjected to ambient temperatures as low as -40°F (unless special measures are taken).

The x-ray scanner is certified to be "cabinet safe." This means that personnel can be near it for normal operation, and the user does not need to be fitted with a dosimeter. Only a certified "system maintainer" can use tools to perform maintenance and has the ability to modify or override interlock safety features. This authority is granted from our EH&S department.

With respect to operation, the machine needs to be "tuned" to the samples that are collected. This means that adjustments must be made to both x-ray voltage and current depending on the density and composition of the samples. There could also be adjustments to the camera behind the image intensifier. It is hard to predict how often and when this task will need to be performed. Since we will be performing dual-energy scanning, both our hard and soft x-ray energies will need to be periodically readjusted depending on the collected core density and composition.

LBNL modified the machine so that it will hold a 3-ft piece of core. Four-ft long core holders were constructed since the extra space at the top of the core holder will be empty, preventing concern about core length. The quick scan will be performed in about 2-3 minutes from the time the sample in the sample holder is placed in the x-ray unit, to when it can be removed from the x-ray unit. A more detailed full 3-D CT characterization will take about 12 minutes for the entire 3-ft length. A shorter interval (i.e., 4 inches) can be scanned in full 3-D mode in about 2 minutes. We will have three to five core holders so that one can be loaded, while another one is being cleaned or prepped and a third can be in the scanner.

Use of the x-ray CT scanner is described in **Appendix A**.

4. Geological Description

4.1 Geological Description from Core Analysis

The project team analyzed core and fluids using a specially constructed mobile core laboratory (see Section 2), staffed by trained laboratory technicians. Core was received in the cold module, where it was photographed and assessed for the presence of hydrate. One-inch plugs were removed from the core, and these plugs measured for porosity, permeability, compressional and shear wave velocity, resistivity, thermal conductivity, and NMR with specialized equipment specifically designed for making these hydrate core measurements, including a Schlumberger CMR tool. All measurements were made under controlled pressure and temperature.

4.1.1 Phase I Coring (107 – 1400 ft)

A thick section of sandstones, mudstones, coals and conglomerates was cored continuously in the Anadarko Hot Ice No. 1 well during Phase I (the 2003 drilling program) from 107 ft to total depth of 1400 ft (**Figure 7**). At this depth the well was temporarily suspended because of early thaw beginning on the North Slope. Surface protective casing was set at this point, just below the base of the ice-bearing permafrost. No gas-hydrate-bearing sediment had been encountered as of the suspension of coring.

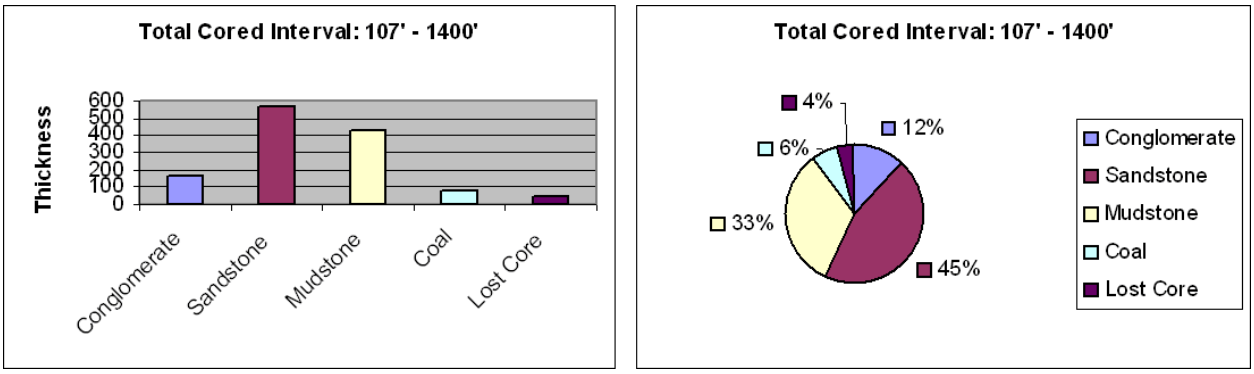

Figure 7. Geologic Description of Phase I Cores

Correlations with wireline logs and descriptions of cuttings taken in nearby wells support the idea that frozen sediments cored in this well are part of the Sagavanirktok Formation. The cored sediments are part of a thick sequence of rocks that are probably of late Cretaceous to early Tertiary age. Paleontologic evidence of this age is lacking, but stratigraphic position of these units and absence of tectonic complications in this area of the North Slope support this age assignment. Like similar sequences studied in nearby outcrops of the North Slope, they have characteristics of marginal marine or deltaic deposits. If correlations are correct, then the bottom of the cored interval at 1400 ft was in the mudstone that separates the Ugnu sands from the underlying West Sak sands, informal members of the Sagavanirktok Formation.

The thick mudstone at the base of the cored interval, 1358-1400 ft, may be a marine tongue of fine-grained sediment representing a brief transgression of the late Cretaceous sea over the

mostly terrestrial environments of this area. Sandy sediments above this mudstone are thin sequences that form alternations of fining-upward and coarsening-upward units. They become very carbonaceous upward and are capped by a thick coal and mudstone interval. This overall interval includes a prominent, very sandy and carbonaceous, mudstone unit more than a hundred feet thick. These sequences, from 951 ft to 1358 ft, probably represent the attempted, repeated progradation of several wedges of sandy sediment from the southwest into a more marine environment to the northeast. These progradations culminated in the persistent presence of coal-forming environments in this area, such as coastal marshes and delta-top swamps, which resulted in the thick coals at the top of the sequence.

Following this time of coal formation, sand and mud sedimentation resumed, and the first 50 ft of deposits above the coal was a coarsening-upward sequence of sandy mudstone and sandstone. Following deposition of these units, however, the alternations of finer grained and coarser grained sediments mostly followed the pattern of fining-upward. These patterns suggest deposition of distributary mouth bars and crevasse splay sediments, which prograded over a subsided area of coastal swamp environments. These deposits were then buried by deltaic distributary and overbank sediments as shallow water deltas worked over the prograding coastal plain. Another coal, 6 ft thick, was deposited at the top of these sediments, attesting to the natural variability inherent in coastal plain deposits. This sequence of events is represented by the sediments cored from 649 ft to 951 ft.

After this period of sedimentation when alternations of coarser and finer grained sediments were so common, a thick sequence of mixed-clast conglomerates was deposited in this area, seen in the sediments from cores of the interval 446 ft to 649 ft. This would seem to represent a time of maximum progradation of the onshore, terrestrial environments of deposition, such as when short-headed, high energy streams could have crossed a very narrow deltaic shelf and/or when there was increased tectonic activity in the source area to the south and southwest, as suggested by Molenaar (1983). This would have resulted in very coarse sediment being delivered to this area of deposition.

The next phase of sedimentation in this area resulted from return of more typical upper deltaic environments, with fluvial sequences being dominant over the area, represented by cores from 143 ft to 446 ft. The earlier of these sediments may have been deposited by braided streams, as they contain basal units of pebbly, coarse sand, grading upward into finer grained sediment. Higher in the section, sandstones are fine-to-medium grained, also grading upward into sandy mudstones. Two prominent coals occur within and at the top of this interval of fluvial sediments, again suggesting the shifting nature of environments of deposition and re-establishment of peat swamps and lakes or other very low energy environments in this area.

Finally, just above the uppermost coal, is a thick mudstone, from 114-143 ft, which may represent another incursion of marginal marine conditions over the low-relief, coastal or freshwater swamp environments represented by the underlying coal. Above this mudstone are a few feet of conglomerate, stained dark by carbonaceous material from above, that probably represents the near surface gravel of the Gubik Formation, of Tertiary age.

A summary geologic description of the complete core from Phase I was prepared by Jim Ebanks of PTS Labs and Bill Zogg of CORPRO and is presented in **Appendix B**.

4.1.2 Phase II Coring (1403 – 2300 ft)

A thick section of mudstones and sandstones, with occasional siltstones, was cored continuously in the Anadarko Hot Ice No. 1 well during Phase II of the drilling program (**Figure 8**). Phase II of the operation began at 1403 ft. Total depth of the well was 2300 ft. Despite minor indications of gas being present in some low-permeability units, no gas hydrates were found.

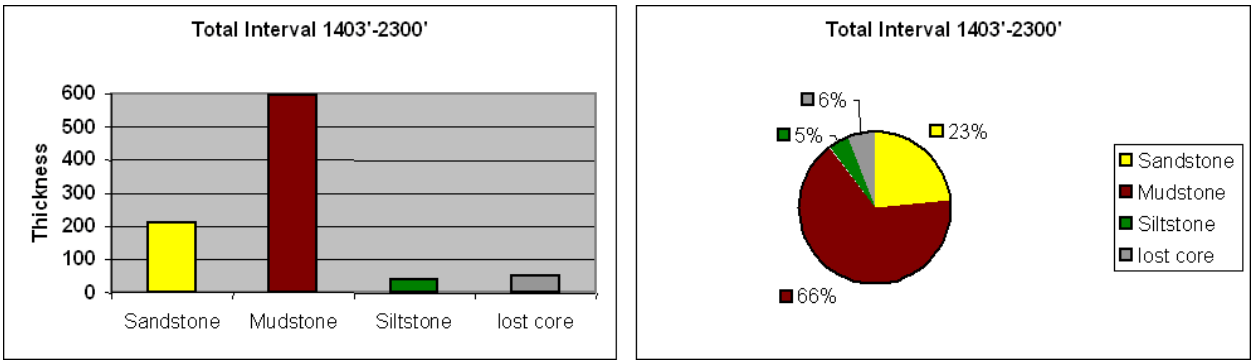

Figure 8. Geologic Description of Phase II Cores

Sediments cored from 1462-2300 ft are a series of coarsening-upward mudstone-sandstone intervals. They may be grouped for descriptive purposes into four major intervals: 2300-2201 ft, 2201-1908 ft, 1908-1727 ft, and 1727-1462 ft. Each of these major subdivisions of the cored interval begins with a thick, somewhat silty, fossiliferous mudstone and is capped by a very fine- to medium-grained, upward-coarsening, fossiliferous, silty sandstone. Each major, capping sandstone, in succession upward, is thicker than the next one below it.

Within each of these major sequences are numerous smaller subdivisions, each with a prominent sandstone that lies above a silty mudstone and each of which exhibits greater or lesser degrees of interbedding of finer and coarser sediments within its interval. The mudstones and sandstones commonly have gradational contacts and there is frequent occurrence of fossil mollusk shells and thin beds of shell debris in both kinds of sediment.

These characteristics support the interpretation that sediments of the entire Phase II cored interval were deposited in a shallow marine shelf environment. They probably owe their cyclic variability to differences through time in activity and location of deltaic complexes in the south and southwest, which were active at the same time (Molenaar, 1983). As coarser-grained sediment was delivered to the marine environment, it was reworked and re-distributed by marine waves and currents into offshore bars and sheets of sand, some of which may be continuous laterally with their shoreline or river mouth equivalents. Between episodes of coarser-grained sedimentation, longer periods of deposition of finer-grained sediment allowed accumulation of silt and clay burying and enclosing the sandier deposits from the last progradation of the coastal environments.

A summary geologic description of the complete core from Phase II was prepared by Jim Ebanks of PTS Labs and Bill Zogg of CORPRO and is presented in **Appendix B**.

4.2 Daily Geological Reports

The project team analyzed core and fluids using a specially constructed mobile core laboratory, staffed by trained laboratory technicians. Core was received in the cold module, where it was photographed and assessed for the presence of hydrate.

Below are summaries of general observations from geologists at the well site regarding core operations during the 2004 drilling/coring season. (General observations were not available for the 2003 drilling/coring season.)

31 January 2004 – 6 PM

Cored from 1422.9 ft to 1470.3 ft, recovered 43.1 ft (91% recovery).

Upper part of formation is mostly silty mudstone, except for one interval of very clay- and silt-rich very fine sandstone, 1436.5-1443.8 ft. Below this, sandy intervals are much more common, and a slightly gas-bearing sand was encountered near the bottom, at 1469 ft. These sands are relatively soft, and do not contain hydrate, but they indicate proximity to the most prospective section of sands and the presence of gas in the section.

1 February 2004 – 6 AM

Cored interval from 1470.3 ft to 1551.0 ft (80.7 ft.); recovered 77.0 ft (95% recovery).

The formations are firming as we progress and thus recoveries are improving. The drilled formation is predominantly sandstone with minor amounts of mudstone and siltstone in the upper part. Most of the upper section drilled shows evidence of gas-bearing zones with the finer grained ones more evident as they retain the gas and bubble after the core is removed from the core tube. The lower part of the section is definitely finer grained with a marked increase in siltstone and mudstone from 1510 ft to 1551 ft.

1 February 2004 – 6 PM

Drilled 1551.3 ft to 1645.4 ft (94.1 ft), and recovered 89.4 ft (95% recovery).

The sediments drilled are a continuation downward of the silty, calcareous mudstones drilled at the end of the previous tour. The favorable sandstones seen early yesterday are not present below 1540 ft; only fossil-bearing, marine mudstones and siltstones are present in the section drilled during the daylight tour today.

2 February 2004 – 6 AM

Cored interval from 1470.3 ft to 1551.0 ft (80.7 ft.); recovered 77.0 ft (95% recovery).

Formations are firming as we progress and thus recoveries are improving. The drilled formation is predominantly sandstone with minor amounts of mudstone and siltstone in the upper part. Most of upper section drilled shows evidence of gas-bearing zones with finer grained ones more evident as they retain gas and bubble after core is removed from the core tube. The lower part

of the section is definitely finer grained with a marked increase in siltstone and mudstone from 1510 to 1551 ft.

2 February 2004 – 6 PM

Cored the interval 1726.1 ft – 1816.1 ft (90 ft); recovered 90 ft (100%).

The uppermost core is 9 ft of sandstone, which is fine-grained, very even textured, and unconsolidated, with excellent permeability; no gas or hydrate occurred in this unit. Below this sand is about 40 ft of interbedded sands and mudstones, which are fossiliferous, with many thin layers of shell fragments. Within this interval are three layers of thin, very hard sandstones, cemented by calcite. Below this section of interbedded lithologies is about 40 ft of mostly mudstone, which includes only a few beds of silty, very fine sand and shell fragments.

3 February 2004 – 6 AM

Cored the interval 1816.1 ft to 1865.9 ft (49.8 ft), recovered 41.1 ft (82%).

Most of the cored interval is mudstone with thin sandy and silty intervals and scattered shell fragments as seen previously. One very good sandstone interval occurs from 1825 ft to 1835 ft; the top 1.5 ft of this sandstone is strongly cemented by calcareous cement, as has also been seen previously. This sandstone is fine grained, quartz-lithic, well-sorted, fossiliferous and probably has excellent permeability where it is not cemented, but no gas was seen here.

3 February 2004 – 6 PM

Cored the interval 1865.9 ft – 1953.0 ft (95.2 ft), recovered 91.2 ft (95.8%).

The upper half of the cored interval consists of a 10 ft thick sandstone overlying a 30 ft thick mudstone. This fossiliferous sand coarsens upward from VF to Medium grainsize. It includes numerous thin claystone and siltstone layers that reduce vertical permeability. The mudstone includes numerous thin silty laminae. Below this, at about 1910 ft begins a section about 40 ft thick of mostly VF-Fine grained sandstone that is very soft and friable. There are many thin, silty or clayey laminae and thin beds with fossil fragments, a cemented layer, and two thin mudstones, which all impair vertical permeability. Even in better quality sands, no hydrate or bleeding gas was seen. This sandy interval overlies another mudstone and the bottom of the cores ends in a sandstone.

4 February 2004 – 6 AM

Cored the interval 1953.0 ft to 2033.0 ft (80.0 ft), recovered 77.2 ft (96%).

The entire upper part of this interval is mudstone except for a fine-grained, dark gray, slightly silty, well sorted sandstone from 1955.5 ft to 1960.3 ft. It contained no hydrate and no bleeding gas was observed. Below this lies a thick mudstone interval until another sandstone is encountered at about 1998 ft. The upper part of this sandstone zone (approximately 3 ft) is fine grained, well sorted sandstone. Below, this the sand becomes increasingly silty and argillaceous before an 8 ft thick siltstone interval is encountered at about 2006 ft. Below this siltstone is an alternating sequence of silty, sandy mudstones, sandy argillaceous siltstones and

silty, argillaceous, fine grained sandstone stringers. No gaseous zones were encountered during this tour and the background mud gas measured by the Pason instruments is about 20% of the levels measured in the Upper West Sak sands.

4 February 2004 – 6 PM

Cored the interval 2033.0 ft – 2064.7 ft (31.7 ft), recovered 24.4 ft (77%).

The tour began with a broken retrieval wireline and having to pull the drill string to recover it, which reduced effective coring time. Coring did not resume until 1 PM. A malfunctioning gamma ray logger is being investigated and may require re-running some of the core. Plugs are being taken from previous cores at depths where R. Sigal specified.

The cored interval consists of mostly mudstone, with scattered silty laminae and shell frags. Only one very fine, silty sand was encountered, from 2042-2046 ft, and no shows of hydrate were found.

5 February 2004 – 6 AM

Cored the interval 2064.7 ft to 2129.4 ft (64.7 ft), recovered 64.1 ft (99%).

Entire upper part of the interval encountered during this tour from 2064.7 ft to 2115.7 ft (51 ft) consists of silty mudstone with rare, thin interbeds of fine grained silty sandstone; sandstone makes up less than 5% of this interval. At 2115.7 ft a fine to medium grained, brown, oil stained sandstone was encountered. The sandstone was interbedded with light to medium gray mudstone and contained fine laminations of siltstone and mudstone. Good oil odor was noted throughout the interval and a gas increase to 20 units (~5X background) was detected by the Pason mud gas detector. Total sandstone in this interval was 3.15 ft. Mudstone, with several very thin (<0.1 ft), oil stained sandstone lenses was encountered below the oil bearing sandstone and this mudstone continued to the final depth at 2129.4 ft.

5 February 2004 – 6 PM

Cored the interval 2128.8 ft – 2195.5 ft (66.7 ft), recovered 63.7 ft (95%).

Following the more sandy intervals encountered in previous drilling, and after discovery of the thin, oil-bearing sandstone last tour (depth 2115.7 ft), the section cored this tour has been completely mudstone. There has been slight variation in the amount of silt and the carbonaceous partings in the mudstone. Hardness varies slightly also, causing some problems with the core bit “balling-up” and slowing drilling progress. We are now about 760 ft below “Top of West Sak Formation”.

6 February 2004 – 6 AM

Cored the interval 2195.5 ft to 2246.8 ft (51.3 ft), recovered 44.3 ft (86%).

Mudstone encountered during previous tour continued until 2210 ft where a relatively clean sandstone interval was entered. The interval is a multi-storied sandstone approximately 18 ft thick and comprises at least 8 sand packages, fine to medium grained at the top, coarsening

upward and having a silty sand base. These sand packages are 1.5 to 3 ft in thickness and are occasionally separated by thin mudstone layers (0.2 ft thick). The lower part of the sand interval becomes increasingly silty and carbonaceous. No oil stain or odor was detected in this interval. Below the sandstone is approximately 17 ft of sandy, argillaceous siltstone and silty mudstone. Then a 1.5-foot thick oil stained sandstone was encountered. This sandstone is fine grained and very silty at the top; it has a sharp basal contact with the underlying mudstone. The sand shows good brown oil stain and had some oil odor. Below this sandstone approximately 3 ft of mudstone were recovered before a broken wireline cable halted coring operations. Seven feet of core have been cut and remained to be recovered.

6 February 2004 – 6 PM

Core referred to in the previous tour's report was recovered when pipe was pulled, and consists of mostly mudstone with a thin, 2243.5 ft-2245.3 ft, weakly oil stained sand. Coring did not resume during this tour.

7 February 2004 – 6 AM

Cored the interval 2246.8 ft to 2261.2 ft (14.4 ft), recovered 14.4 ft (100%).

The only lithology encountered during this tour was mudstone. BOP testing was completed during the first part of the tour, then the wireline was replaced and pipe was run back in the hole. Coring did not begin until the early morning hours.

7 February 2004 – 6 PM

Cored the interval 2261.2 ft to 2300 ft (38.8 ft), recovered 38 ft (98%).

Cores recovered this tour were almost all mudstone, except for a thin, very fine grained sand that occurs at 2273.5-2274.9 ft, but which contains no shows. About 17 ft of the mudstone appears dark brown in color, possibly signifying unusually high content of organic matter (macerated plant debris). Total depth of 2300 ft was reached at about noon. The last 1 ft of core was hard mudstone.

5. Porosity and Permeability Measurements

5.1 Ugnu Formation

5.1.1 Porosity

With the exception of the very bottom part of the section, all core arrived at the onsite core laboratory frozen. Core was examined and plugged in a laboratory module kept at about -5°C. All Ugnu core recovered was unconsolidated after it thawed. Following standard procedures for unconsolidated samples, these were wrapped and screened as the first step in the analysis process while they were frozen.

Measured porosities are consistent with rocks at the upper limit of a grain-supported system. Unconsolidated rocks normally show significant porosity and permeability loss under increased net confining pressure. To quantify this behavior, porosity was measured at three net confining pressures – 800 psi, 1200 psi, and 1800 psi. **Table 2** shows average and median porosity values at each confining stress. Porosity was computed from pore volume measured at each confining stress and measured grain volume which for these low stresses can be assumed to be stress independent. There is about a two-porosity-unit decrease in porosity when net confining stress is increased from 800 psi to 1800 psi.

Table 2. Porosity of Ugnu Sands

Porosity	800 psi	1200 psi	1800 psi
Average	39.3 %	38.4 %	37.3 %
Median	39.6 %	38.7 %	37.7 %

Figure 9 shows porosity as a function of depth for the three confining pressures. There is no obvious trend between 200 and 1250 ft depths. However, the bottom section appears to be slightly more consolidated. In the section above 1250 ft the median value for porosity is 39.7%, while below 1250 ft it is 37.5%.

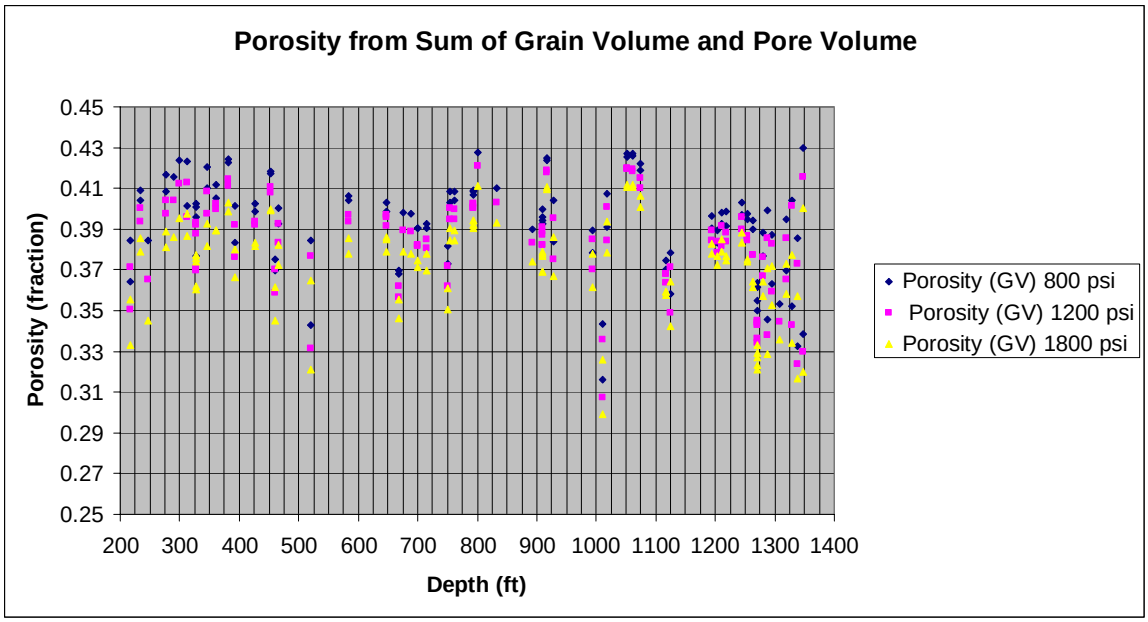

Figure 9. Porosity distribution of Ugnu sands

5.1.2 Grain Density

Grain density was computed from measured grain volume and sample weight. **Figure 10** shows calculated grain density as a function of depth. Both average and median grain densities are 2.64 g/cc. There is perhaps a small increase in grain density visible at 1200 ft. The average above 1200 ft is 2.64 g/cc, while below it is 2.66 g/cc.

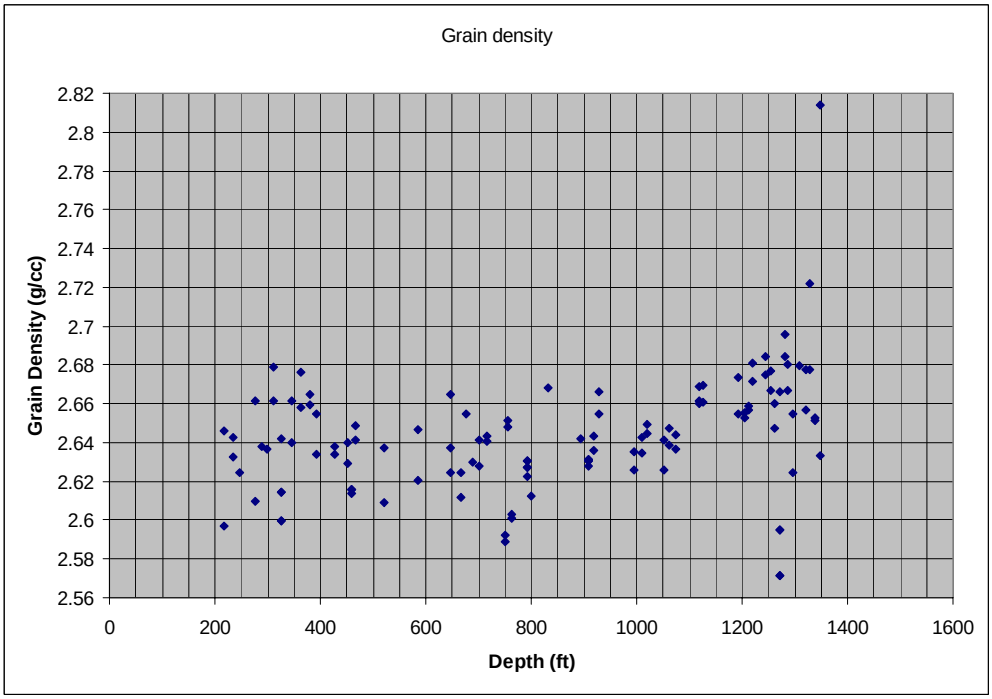

Figure 10. Grain density distribution of Ugnu sands

5.1.3 Permeability

Permeability of the samples is very high, but not inconsistent with other young unconsolidated sandstones. Horizontal permeability was measured at three net confining stresses – 800 psi, 1200 psi, and 1800 psi. As with porosity, there is significant loss of permeability with increase in confining stress. **Table 3** shows geometrical mean and median horizontal Klinkenberg-corrected permeability for each stress. The geometrical mean permeability was computed by averaging the logarithm base 10 of permeability, and then computing the antilog. There is roughly a 20% reduction in permeability with increase of net confining stress from 800 psi to 1800 psi.

Table 3. Permeability of Ugnu Sands

Permeability	800 psi	1200 psi	1800 psi
Geometrical Mean	3718 md	3581 md	3149 md
Median	5096 md	4579 md	4041 md

Figure 11 shows permeability as a function of depth for the three confining stresses. There is perhaps a slight decrease in permeability visible below 1200 ft, but there is no strong trend. **Figure 12** is a cross plot of the log of permeability against porosity. It is clear that there is no reasonable correlation.

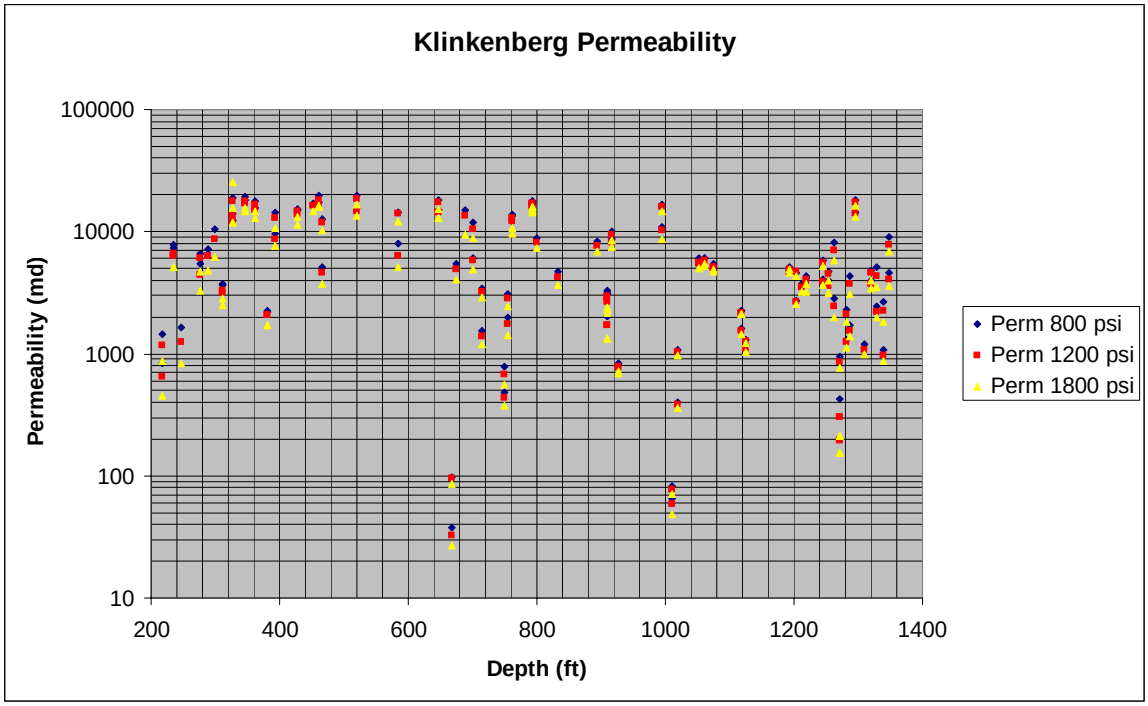

Figure 11. Permeability distribution for Ugnu sands

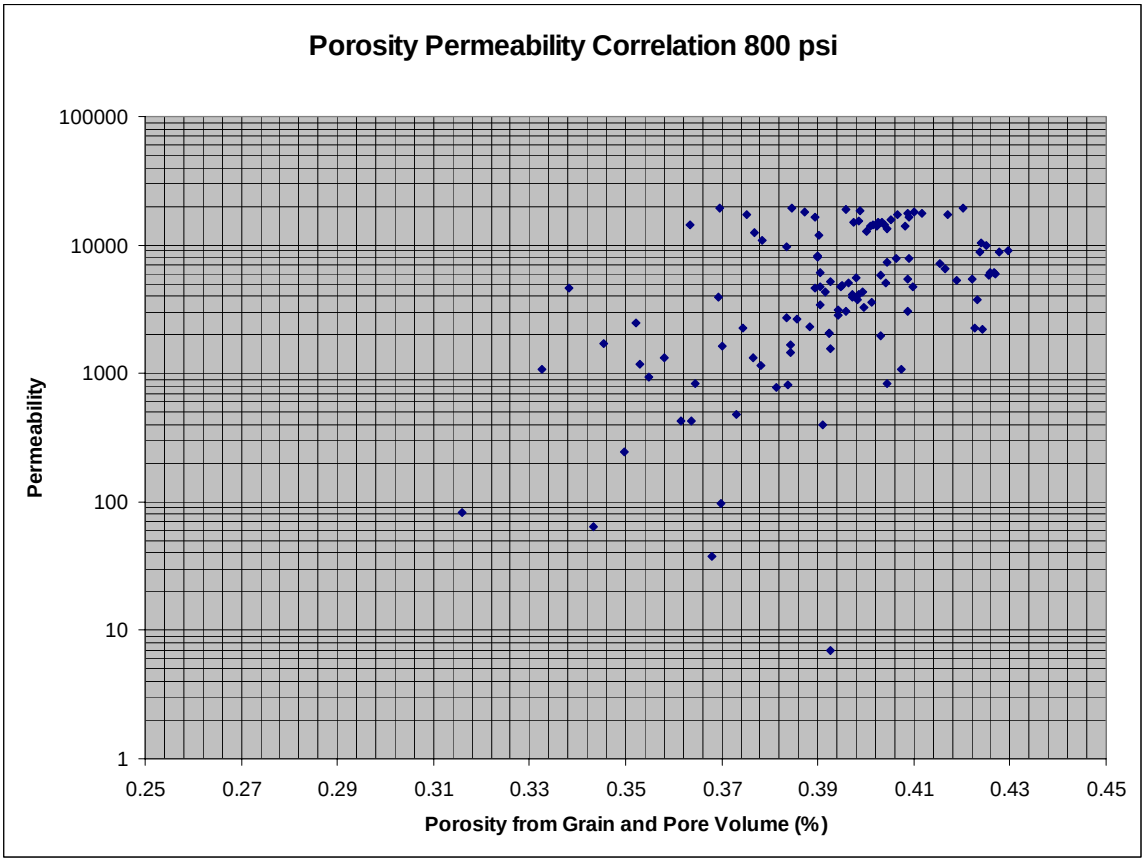

Figure 12. Lack of correlation between porosity and permeability in Ugnu sands

5.1.4 Bulk Modulus

Effective dry bulk modulus K_{eff} of a sample can be estimated from the change in porosity ϕ with stress P using (Sigal , 2001)

$$K_{eff} = \frac{p_2 - p_1}{\ln\left(\frac{\phi_2 - 1}{\phi_1 - 1}\right)}$$

Subscripts 1 and 2 refer to initial and final pressures. It is necessary here to assume grain volume does not change when net confining stress is increased. This approximation is very good for high porosity samples such as these that have a bulk modulus about two orders of magnitude less than the bulk modulus of the grains. The modulus is referred to as effective since weak samples such as these are not truly a linear elastic media. For each sample effective bulk modulus K_{eff} was computed from the porosities measured at 800 psi and 1800 psi. **Figure 13A** shows K_{eff} as a function of depth. Effective bulk modulus shows a weakly increasing trend with depth starting at 25,000 psi and ending at 40,000 psi. Again samples from deeper than 1250 ft may be on a different trend. **Figure 13B** shows the same plot with deep data removed.

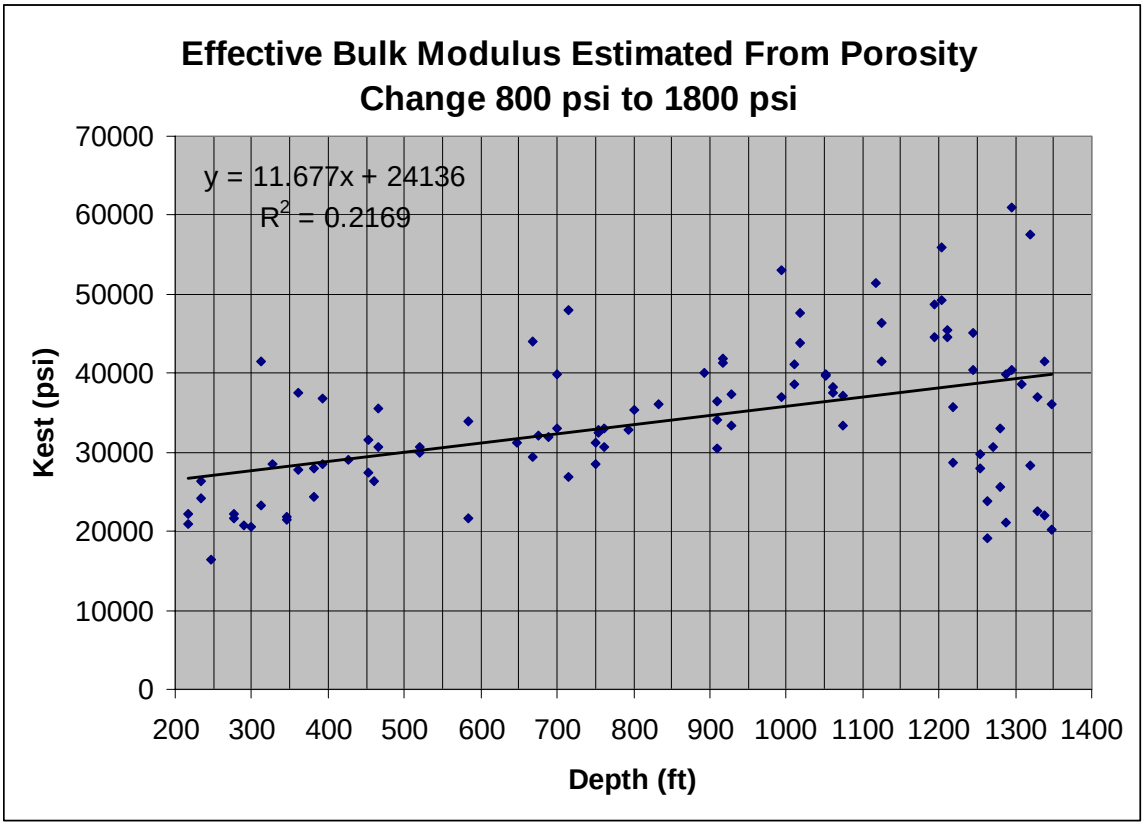

Figure 13A. Bulk modulus distribution for Ugnu sands

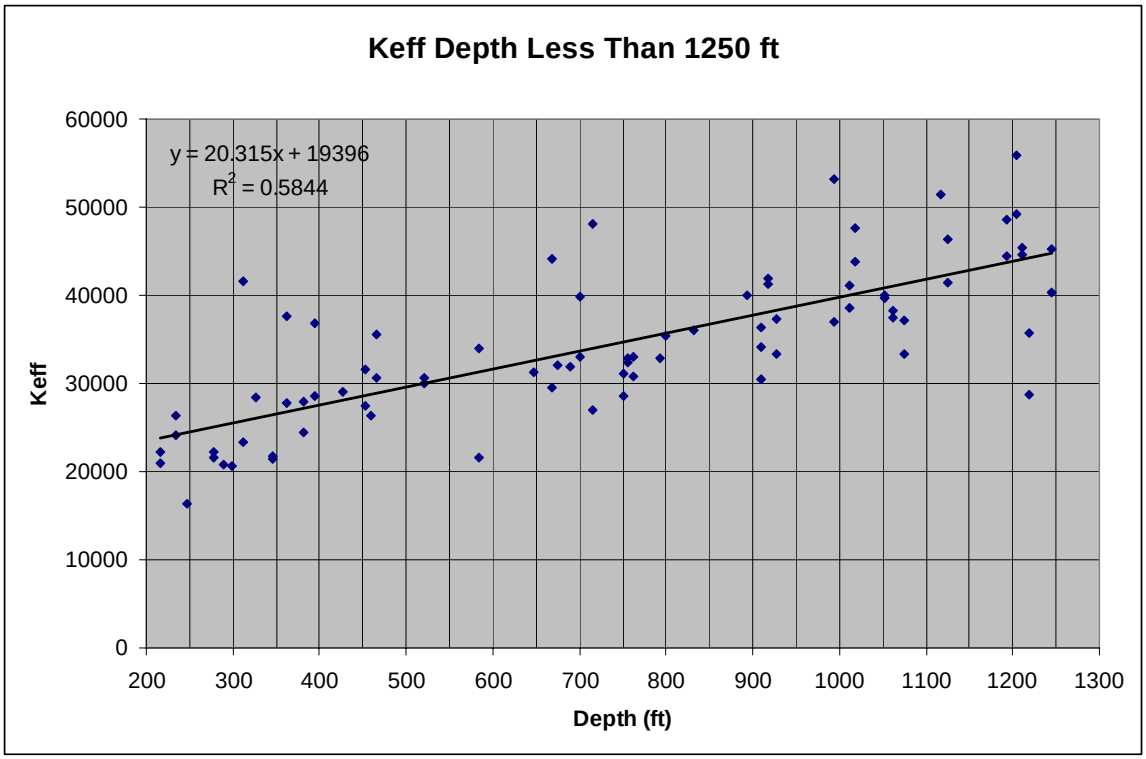

Figure 13B. Bulk modulus distribution for shallower Ugnu sands

5.1.5 Analysis of Companion Plugs

When performing a wide range of core tests, it is often necessary to test companion plugs. This is the result of 1) the desire to run tests in parallel and 2) the fact that some tests are destructive. When dealing with unconsolidated samples, even tests usually thought of as non-destructive can leave the sample modified or even unsuitable for further tests. This problem is further complicated in the case of permafrost and hydrate samples as some tests need to be run over a range of temperatures, and a sample cannot necessarily be returned to its original state by returning to its original temperature.

Companion plugs were taken for measurements in the velocity/resistivity system and the NMR system. Both sets of plugs were cleaned and dried and had porosity and permeability measured. In a few cases there are significant differences in properties of the two plugs. These differences could be in part due to tests performed on the plugs before they were cleaned and dried. Velocity and resistivity at multiple confining pressures were measured on many of the plugs when they were frozen. Most of the NMR plugs were only measured unstressed.

Porosity and permeability ratios were calculated for each companion set. Measurements at 1200 psi confining stress were used for this study. The ratio was always computed taking the velocity/resistivity sample as the numerator. **Figure 14** shows the distribution of porosity ratios. Values are grouped into bins; each bin has a half width of 0.02. For a 38% porosity rock, this corresponds to 0.8 porosity units. If all the differences were due to random factors, it would be expected that in the limit of a large number of samples, the number of companion plug sets with ratios greater than one would equal the number with ratios less than one. The distribution would not be expected to be symmetric, however. Figure 13 shows that the velocity/resistivity plugs seem biased to a lower porosity than the NMR plugs. This is likely due to the confining stress they were exposed to during velocity/resistivity measurements.

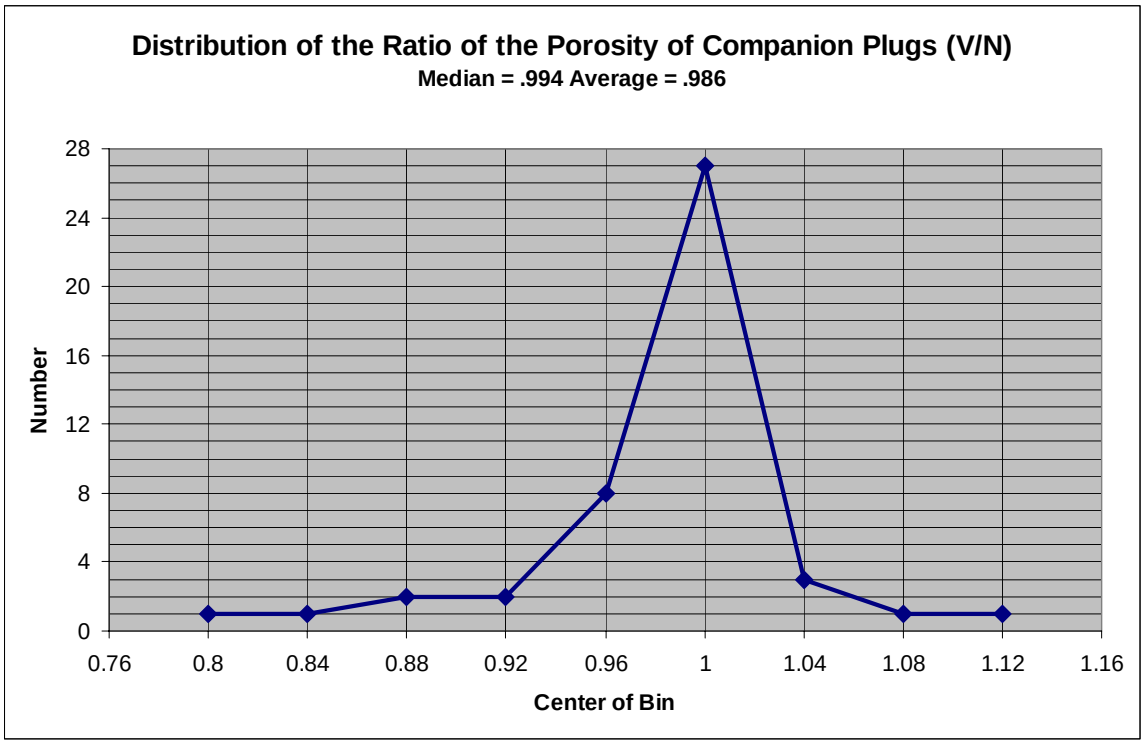

Figure 14. Plugs on which velocity was measured tend to be slightly lower in porosity

The corresponding plot for permeability ratio is given in **Figure 15**. In this case bin half-width was 0.1, which for 4000 md corresponds to 400 md. Again, distribution of permeability ratios shows that the velocity/resistivity plugs have a systematically lower permeability than the NMR plugs. This is probably at least in part due to the differences in tests on the plugs before porosity and permeability were measured.

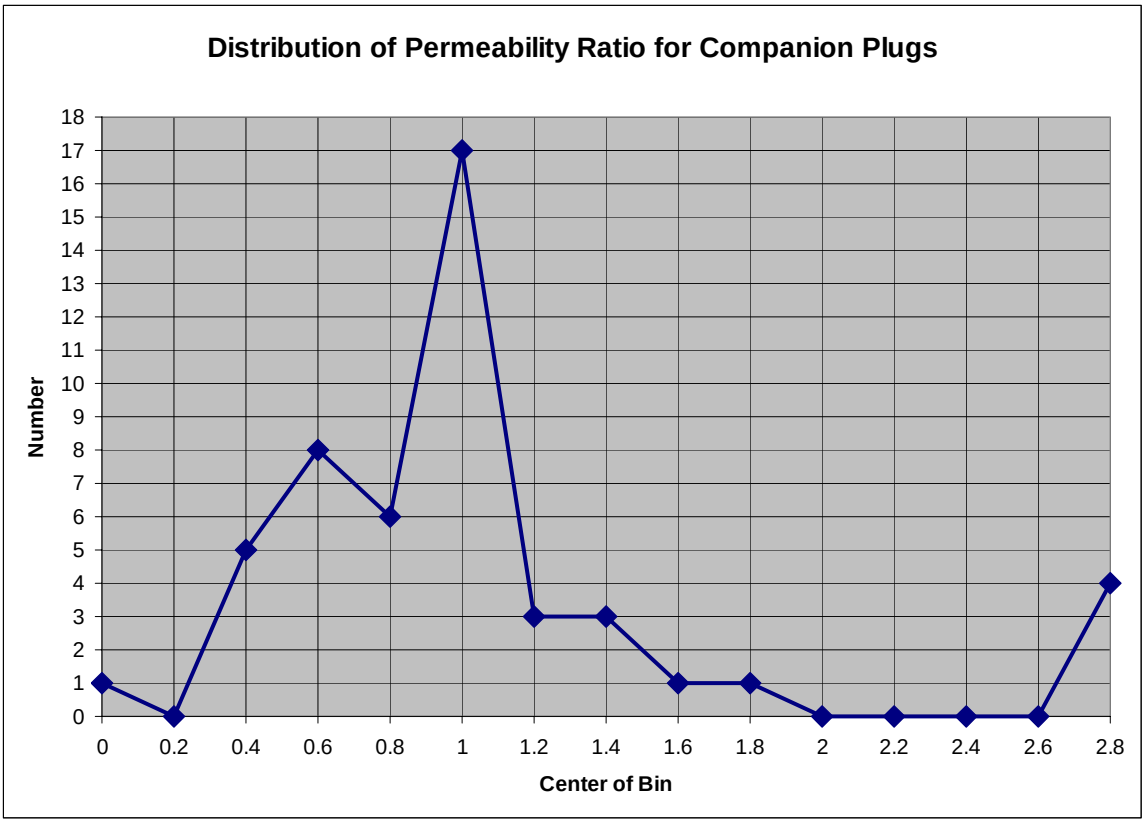

Figure 15. Permeability of velocity samples tends to be lower than for NMR samples

5.2 West Sak Formation

5.2.1 Porosity

All West Sak samples came from core taken from below the permafrost zone. The standard measurement process was to clean and dry samples before any measurements were made. With the exception of some anomalous thin beds (1-2 ft thick), "Sandstones above 1950 ft are generally soft, unconsolidated or friable. Below 1950 ft they are generally firm with occasional layers that are soft or friable." (Geological Summary). This means that above 1950 ft they are similar to the Ugnu formation. They were plugged, wrapped, cleaned and dried the same as Ugnu samples. Anomalous thin beds were scattered throughout the section. These were hard, very low porosity and low permeability zones. They had obviously undergone significant chemical diagenesis. They were not included in statistics calculated for the West Sak sands.

On average, sands in the West Sak are two porosity units less porous than the Ugnu sands. **Table 4** presents average and median porosity values for the three confining stresses. On

average, the sands lose 1.8 porosity units when stress is increased from 800 psi to 1800 psi. This is slightly less than the loss in the Ugnu. It was observed that sands above 1950 ft are less consolidated than deeper sands. Average porosity of shallow sands at 800 psi is 37.6%, while the average below is 33.6%. Because there was limited sand cored below 1950 ft, this may not be statistically significant, but is consistent with observation on consolidation. **Figure 16** plots measured porosity as a function of depth. There is no obvious trend above 1950 ft. The very low porosity samples come from cemented zones.

Table 4. Porosity of West Sak Sands

Porosity	800 psi	1200 psi	1800 psi
Average	37.2	36.3	35.4
Median	37.8	37.0	36.3

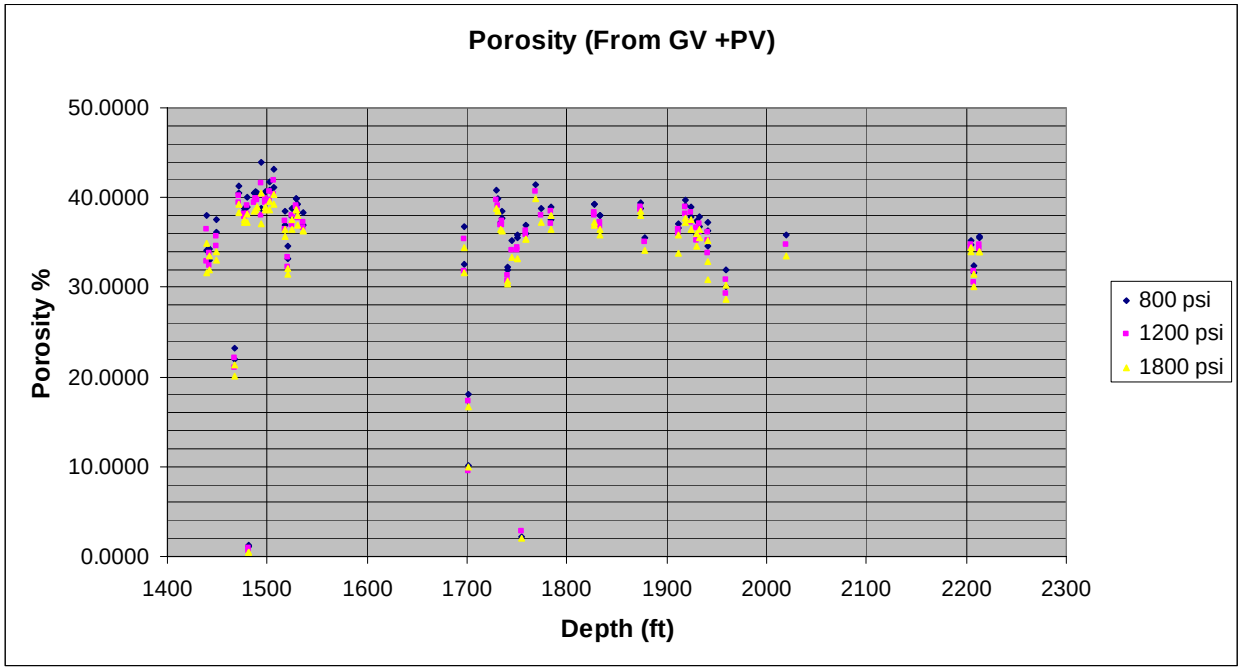

Figure 16. Porosity with confining stress and depth for West Sak sands

5.2.2 Permeability

Permeability tends to be somewhat lower in West Sak sands than the Ugnu. In the Ugnu, sands with permeability greater than 10 Darcy occur throughout the depth range. In the West Sak, only clean sand near its top has a cluster of samples with that very high permeability. **Table 5** lists geometrical mean and median Klinkenberg corrected permeabilities for each confining stress. Anomalous thin tight sand zones are not included. Permeability decreases with increasing confining stress. The geometrical mean permeability at 800 psi is 30% greater than at 1800 psi. **Figure 17** compares permeability as a function of confining stress and depth.

Table 5. Permeability of West Sak Sands

Permeability	800 psi	1200 psi	1800 psi
Geometrical Mean	633 (md)	563 (md)	486 (md)
Median	903 (md)	856 (md)	778 (md)

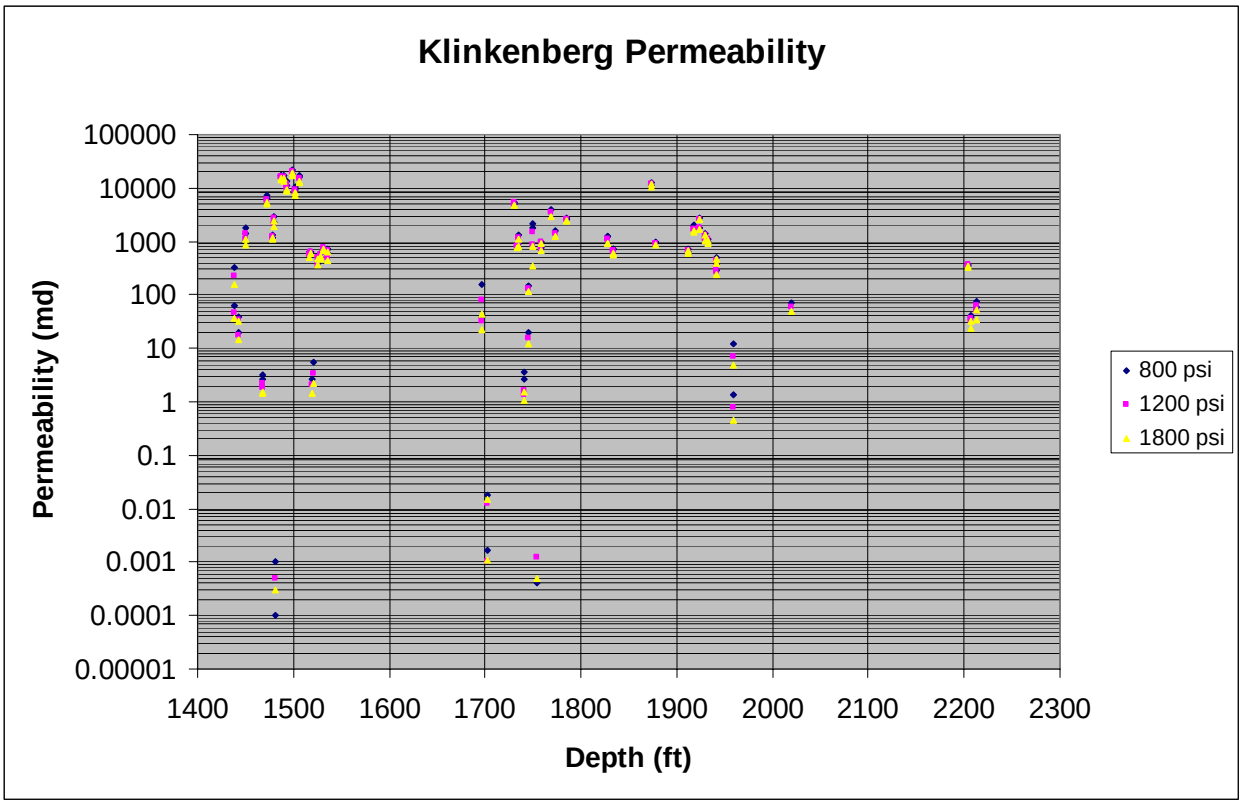

Figure 17. West Sak permeability distribution

Unlike in the Ugnu, there is a good correlation between porosity and permeability in the West Sak. **Figure 18A** shows the correlation for 800-psi confining stress. When porosity ϕ is presented as a fraction and permeability k is in millidarcys, the regression gives

$$k = 3 \cdot 10^{-5} e^{45.3\,\phi}$$

Note that this is a very sharply increasing function so a small change in porosity produces an order of magnitude change in permeability. This can make reservoir evaluation very sensitive to small errors in assigned porosity distribution. Another complication is that the correlation varies with confining stress. This is typical of formations that have a significant variation of permeability with confining stress. **Figure 18B** shows correlations for all three confining stresses. Although they are visibly similar because permeability is a strongly changing function of porosity, they give significantly different permeability at the high end of the porosity range.

Table 6 shows predicted permeability at the confining stresses for several porosity values. At the porosity of the best potential reservoir rocks, there is a difference of up to a factor of 3. Unlike error introduced by scatter in the porosity/permeability correlation, using an incorrect confining pressure correlation introduces a systematic error.

Table 6. Predicted Permeabilities from Correlations for Three Confining Stresses

Porosity	k800	k1200	k1800
0.2	0.259574	0.248285	0.327988
0.25	2.503493	2.620779	3.711632
0.3	24.14523	27.66372	42.00219
0.35	232.8715	292.0052	475.3121
0.4	2245.957	3082.27	5378.806
0.45	21661.39	32535	60868.54

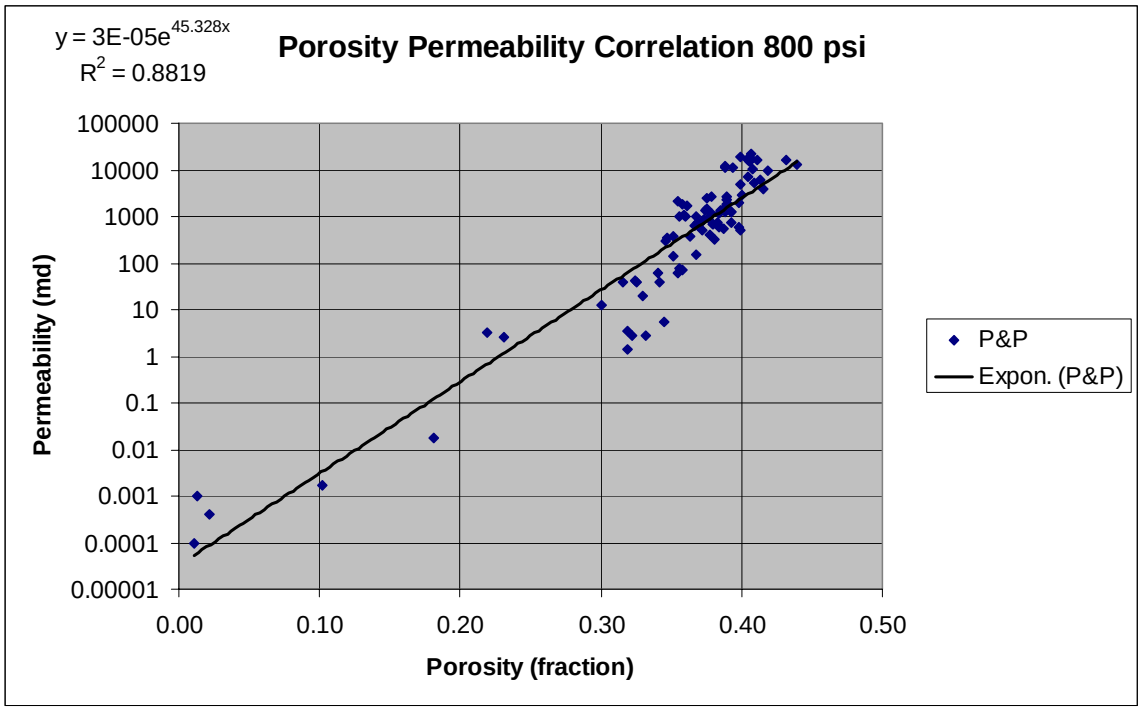

Figure 18A. West Sak porosity permeability correlation at 800 psi

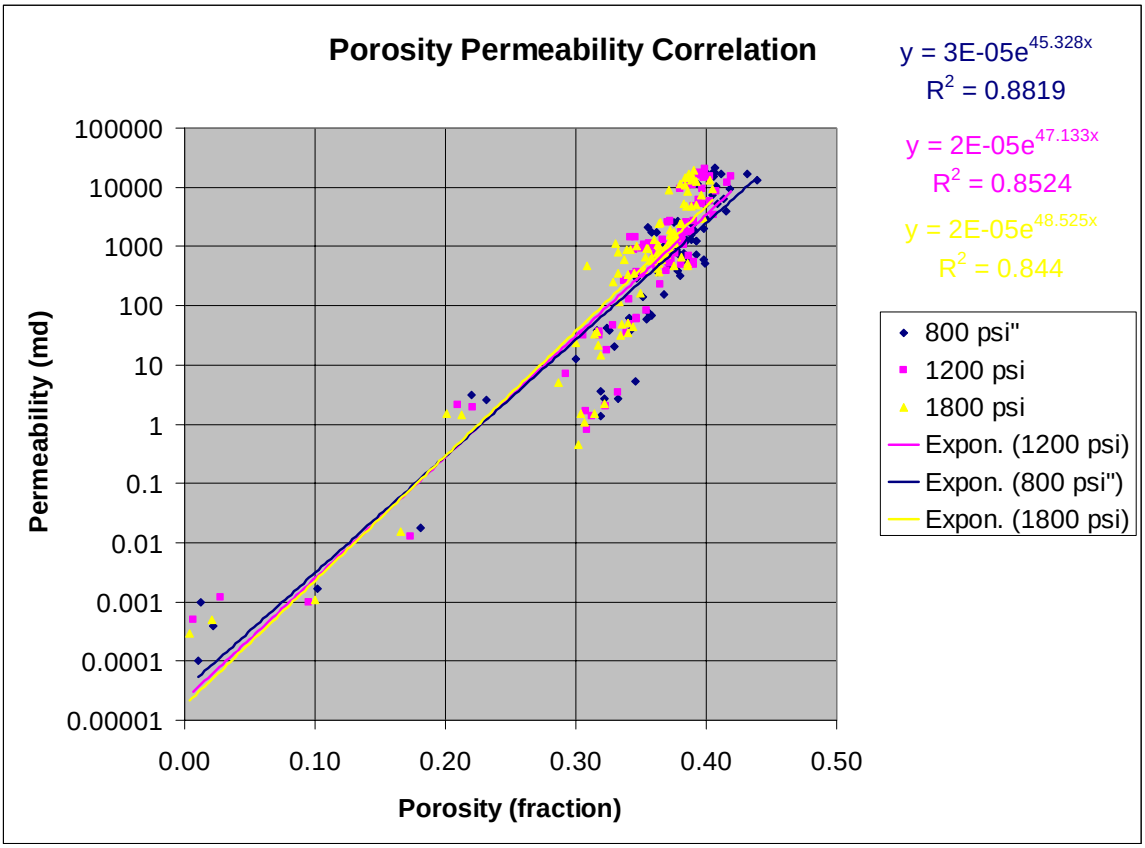

Figure 18B. Permeability correlation for three measured confining pressures

5.2.3 Grain Density

West Sak sands have an unusually high grain density. After this was first observed, we carefully rechecked experimental procedures to validate the results. (No problems were found.) Average and median grain density were measured as 2.70 g/cc. This is very high for a sand formation. The most reasonable explanation for this is the presence of heavy minerals. This needs to be confirmed by mineral and elemental analysis. **Figure 19** shows grain density as a function of depth. The shallow clean sand at about 1500 ft appears to have a grain density more consistent with what was measured in the Ugnu.

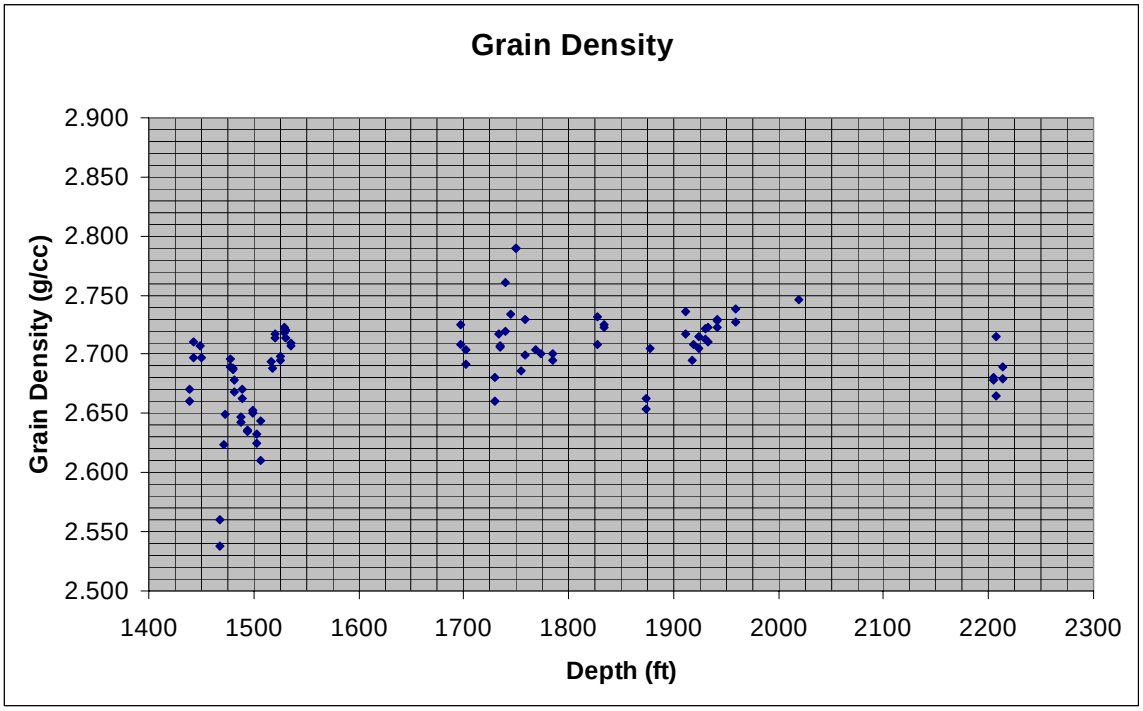

Figure 19. West Sak sand grain density

5.2.4 Bulk Modulus

Effective dry bulk moduli of the West Sak sands K_{eff} were estimated from the change in porosity with increase in confining stress using the same formalism described in the Ugnu section. **Figure 20** shows bulk modulus with depth. There is considerable scatter, but there is a trend of increasing strength with depth. Thin, hard cemented zones were not included as they do not fit well on the same scale.

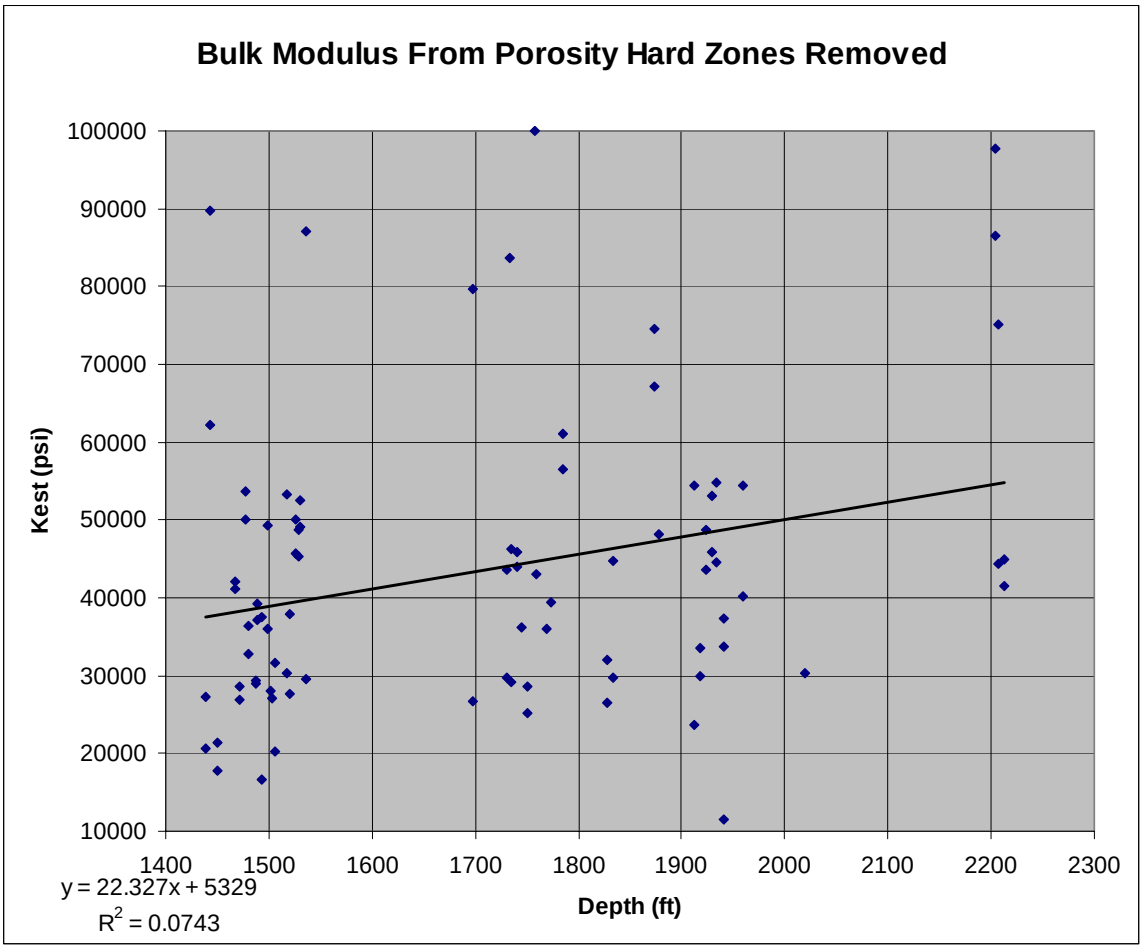

Figure 20. West Sak effective bulk moduli

5.2.5 Anomalous Thin Hard Zones

Five anomalous, thin, hard cemented sand zones were observed in the core at 1481 ft, 1701 ft, 1754 and 1756 ft, 1827 ft, and 2247 ft. Visual examination and an acid test suggests that the cementing agent is a carbonate. At each depth these zones were visible on well logs as low porosity, high density zones. They showed on the sonic as higher velocity than the sands they were encased in. The anomaly as would be expected was clearer on the shear log. In most cases they were also indicted as more resistive.

Plug samples were removed and measured from three of these zones. **Table 7** presents a list of some of their properties. Two of the sampled depths have porosity less than 3%. The samples from 1702 ft are a little more porous. They also have a very low permeability, which suggests its porosity is not well connected.

Since these samples are noticeable on the well logs from Hot Ice No. 1, similar zones (if they exist) should show up on sonic and resistivity logs in other wells. In Hot Ice No. 1 the presence of gas on the mud log and the hard appearance of the core material caused the laboratory crew to suspect hydrates the first time one of these zones were cored. Such zones in old wells with limited log curves available could be mistaken for a hydrate zone if the mud log also was

showing gas. This is not to suggest that every anomaly identified as a hydrate based on old well logs is one of these hard zones. However, the presence of these zones along with the pervasive presence of shallow gas does complicate interpretation of old logs.

Table 7. Petrophysical Properties of Samples from Tight, Hard Cemented Zones

Depth (ft)	Vgrain (cc)	Grain density (g/cc)	Pconfining (psi)	Vpore (cc)	Porosity %	Permeability (md)	Bulk Modulus (psi)
1481.4	12.5429	2.678647	828.27	0.163	1.282869	0.001	
1481.4	12.5429	2.678647	1227.61	0.084	0.665246	0.0005	
1481.4	12.5429	2.678647	1828.03	0.05	0.397049	0.0003	111,914
1481.8	12.5768	2.667849	809.76	0.139	1.093128	0.0001	
1481.8	12.5768	2.667849	1211.45	0.117	0.92171	0	
1481.8	12.5768	2.667849	1811.77	0.053	0.419642	0	147,653
1701.9	11.2488	2.692109	814.11	1.276	10.18779	0.0017	
1701.9	11.2488	2.692109	1230.56	1.189	9.559568	0.001	
1701.9	11.2488	2.692109	1844.55	1.249	9.993759	0.0011	477,486
1702.1	9.9649	2.704192	805.69	2.199	18.07808	0.0175	
1702.1	9.9649	2.704192	1216.31	2.094	17.36477	0.0126	
1702.1	9.9649	2.704192	1822.88	1.984	16.60404	0.0153	57,038
1754.8	12.2761	2.686358	820.28	0.277	2.206626	0.0004	
1754.8	12.2761	2.686358	1216.54	0.351	2.779736	0.0012	
1754.8	12.2761	2.686358	1819.44	0.258	2.058385	0.0005	659,634

5.3 Conclusions – Porosity and Permeability

Ugnu and West Sak sands of Hot Ice No. 1 are high-porosity/high-permeability formations and should make excellent reservoir rocks. As would be expected with young sediments recovered from a shallow section, they generally have porosity greater than 35%. This porosity is typical of sand packs prepared in a laboratory, and is near the maximum allowable for a generic grain supported system. In the Ugnu there is very little to no compaction observed with increasing depth. The West Sak is slightly less porous, and bottom sand cored in the West Sak shows signs of being somewhat more consolidated. Porosity in the Ugnu loses about 2 porosity units when confining stress is increased from 800 psi to 1800 psi. Increase in confining stress has slightly less effect on the West Sak.

Grain density of the sands also shows very little variation in depth in each formation. Its average value of 2.64 g/cc in the Ugnu is consistent with a quartz dominated system. The West Sak has an average grain density of 2.70. For an unconsolidated, apparently quartz-dominated sand this suggests the presence of trace amounts of heavy minerals. Ugnu sands show multi-Darcy permeability centered at about 4 Darcys. They have minimal variation with depth, and there is basically no correlation between porosity and permeability. West Sak sands are about an order of magnitude less permeable and there is a very good correlation between permeability and porosity.

Effective bulk modulus is the only parameter discussed in this report that seems to show any visible trend with depth. It increases roughly from 25,000 psi to 55,000 psi from the start of coring in the Ugnu to TD. There is, however, a very wide scatter. Some of the scatter is very likely due to the method for estimating bulk modulus.

At least two companion plugs were taken at most depths. In the Ugnu these were used in different tests after which porosity and permeability were measured. Comparison of porosity and permeability values of the companion plugs in the Ugnu shows a bias toward lower porosity and lower permeability in the plugs used for velocity/resistivity tests. This is attributed at least in part to changes produced by these tests.

6. Velocity Measurements

6.1 Ugnu Formation

6.1.1 Data Summary

Except for the deepest three plugs, all plugs cut from the Ugnu core came from the permafrost zone. Samples were taken at 62 different depths. All plugs were cut frozen, wrapped in Teflon tape and screened with stainless steel screens, and stored frozen. This was necessary as the plugs were all from unconsolidated sediments. All plugs were cut from zones identified by well site geologists as being sands. They were all taken as horizontal plugs. Plugs from all the depths except five were measured at a temperature a few degrees Celsius below freezing at a recovered state saturation. Plugs at the five other depths were measured at multiple temperatures, and had in some cases been resaturated with brines of different salinity. These measurements were mainly done as part of resistivity tests. They have been excluded from the data analysis, and the general study. Because plugs were measured as recovered in a state where most of the brine is frozen, the exact percentage of pore space filled with fluid is not known. Based on the CMR* core measurements (Schlumberger Trademark) and NMR plug measurements, most should have been between 5% and 25% of their pore space filled with unfrozen brine. That is, most samples had an “effective” porosity between 2% and 10%. The exact value depends on unfrozen porosity, brine salinity, the amount of small pores and exact temperature.

Figure 21 shows compressional and both measured shear velocities as a function of depth. Since there is very little to no difference in the two shear velocities, no attempt has been made to rotate the shear velocities into directions parallel and perpendicular to bedding. This would also suggest that these samples can safely be assumed to be elastically isotropic, making the horizontal measurements appropriate for log and seismic comparisons. There is no clear trend with depth.

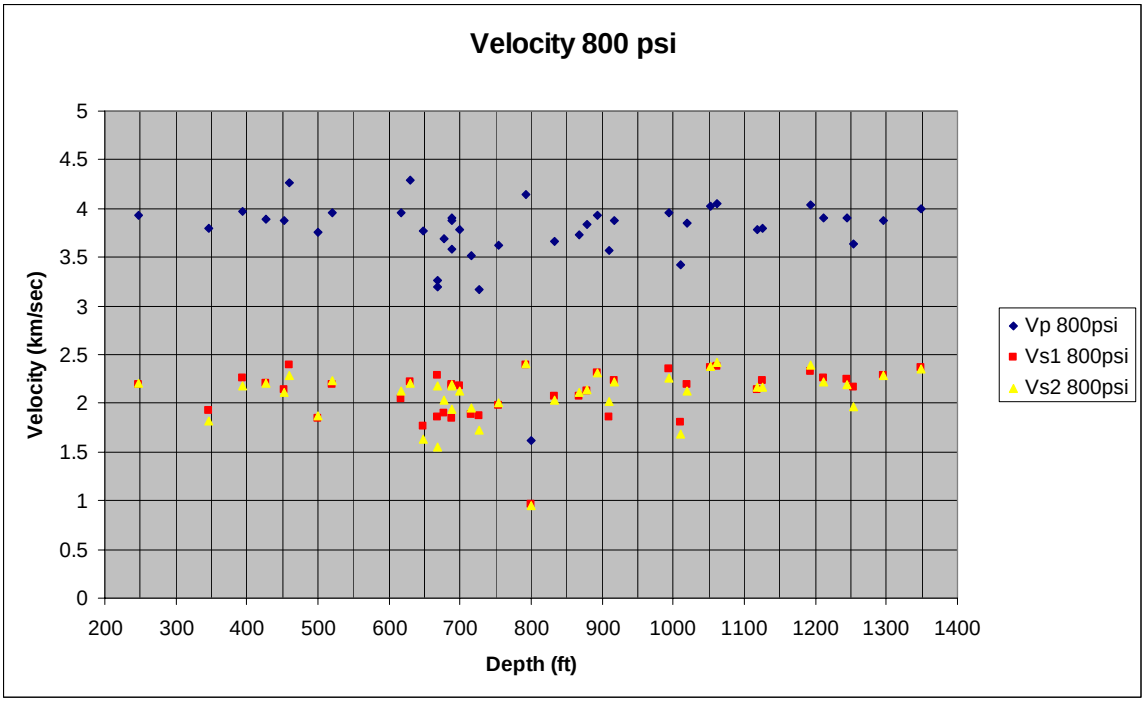

Figure 21. Compressional and shear velocity at 800 psi confining stress with depth

Figure 22 shows the ratio of Vs1 to Vs2 at 800 psi. For most samples the difference between the velocities is less than 5%. **Figure 23** shows the Vp/V2 ratio. There is some indication of a decrease with depth. This could be a reflection of a slight increase in consolidation.

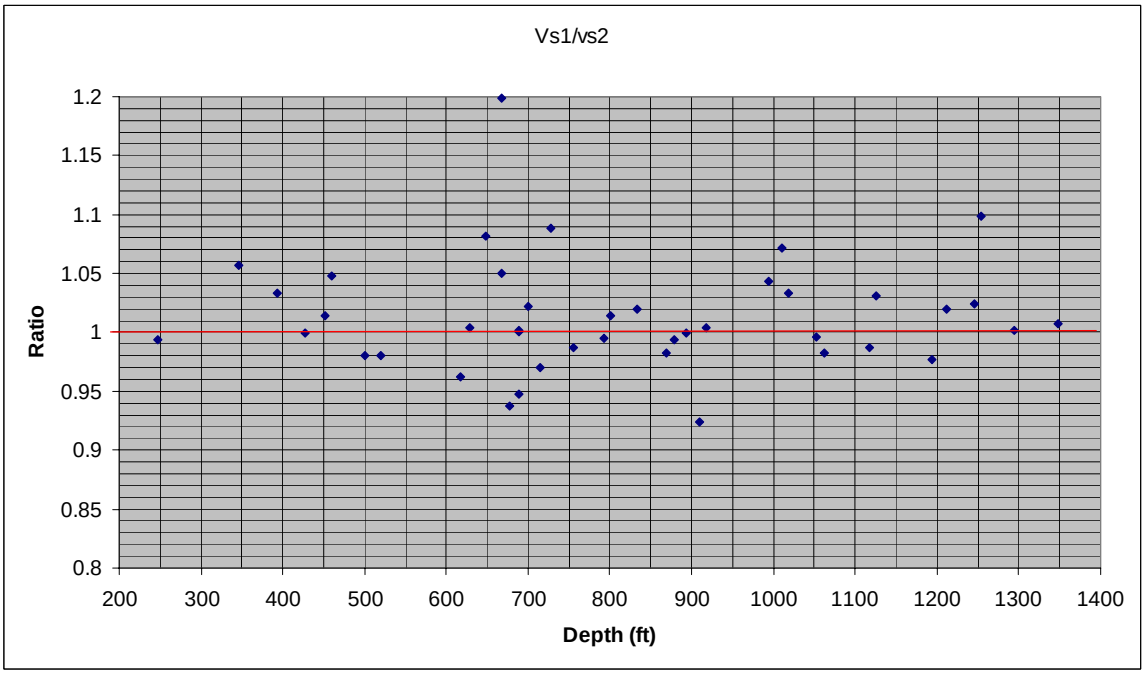

Figure 22. Ratio of Vs1 to Vs2 indicates very little anisotropy in the sands

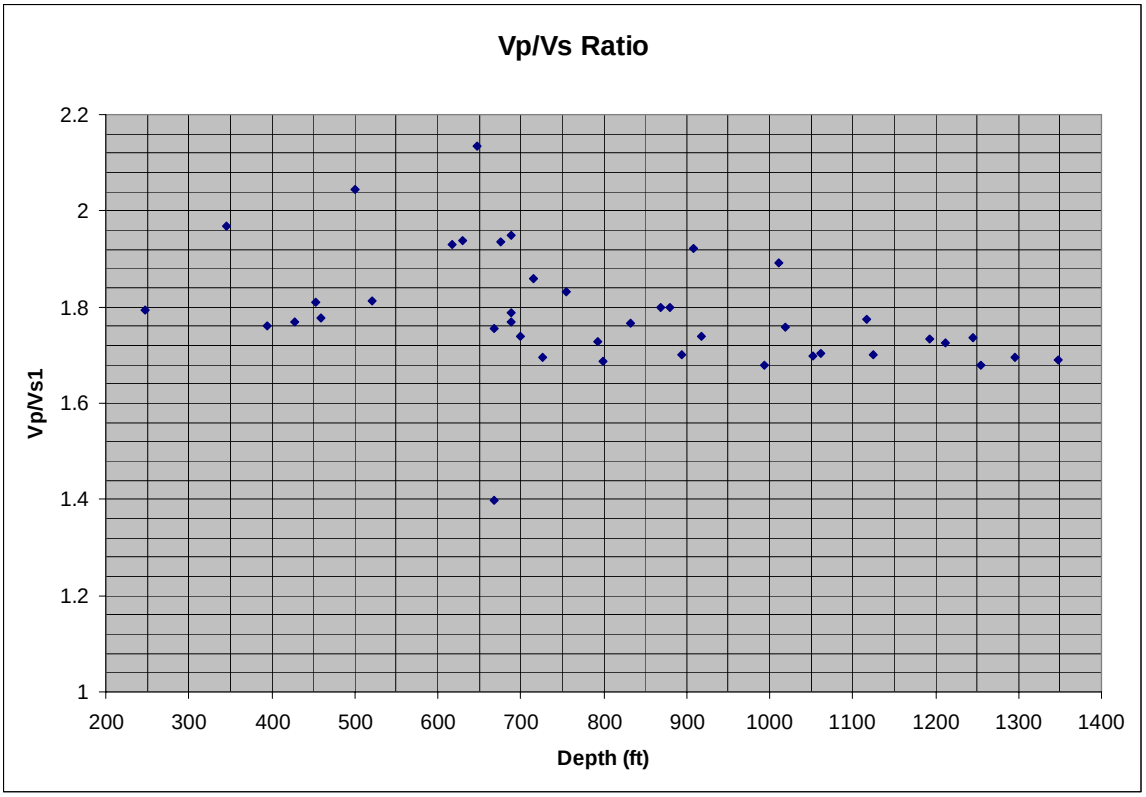

Figure 23. Ratio Vp/Vs shows some decrease with depth

The percentage of unfrozen brine is a function of temperature. Because of this it would be expected that velocity would have some temperature dependence. Since the sands in an unfrozen state are completely unconsolidated, shear velocity could have a more sensitive dependence on temperature. **Figure 24** presents compressional velocity and shear velocity as a function of measurement temperature. There is indication of a reduction in shear velocity at the warmer measurement temperatures. It is less obvious in the compressional velocity.

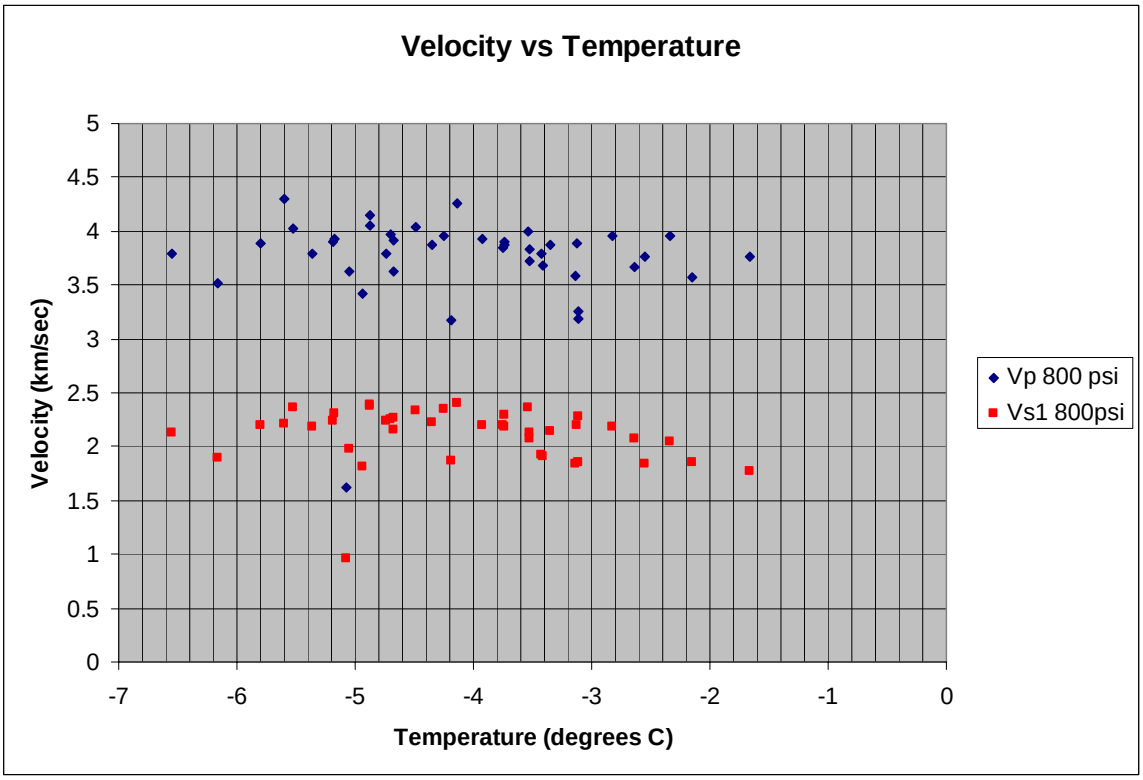

Figure 24. There is indication of shear velocity (red squares) being slower nearer the freezing point. The trend in compressional velocity is less obvious.

Velocity typically has some dependence on confining stress. **Figures 25** and **26** show compressional and shear velocity as a function of the confining stress for a selection of samples. There is some increase in velocity with increasing confining stress. It is greatest at low stress and has almost vanished by 400 psi confining stress.

Table 8 displays median and average values for velocities and ratios at 400 and 800 psi confining stress. Velocities at 400 psi are slightly less than those at 800 psi. On the other hand the Vp/Vs ratio is slightly higher at 400 psi. This is not unreasonable.

Table 8. Average and median values for measurements at 50 depth points at 400 psi and 43 depth points at 800 psi confining stress

	400 psi	800 psi
Median Vp (km/sec)	3.81	3.86
Average Vp (km/sec)	3.72	3.75
Median Vs1 (km/sec)	2.16	2.18
Average Vs1 (km/sec)	2.06	2.11
Median Vs2 (km/sec)	2.14	2.16
Average Vs2 (km/sec)	2.03	2.08
Median Vp/Vs	1.78	1.77
Average Vp/Vs	1.82	1.79
Median Vs1/Vs2	1.01	1.00
Average Vs1/Vs2	1.02	1.01

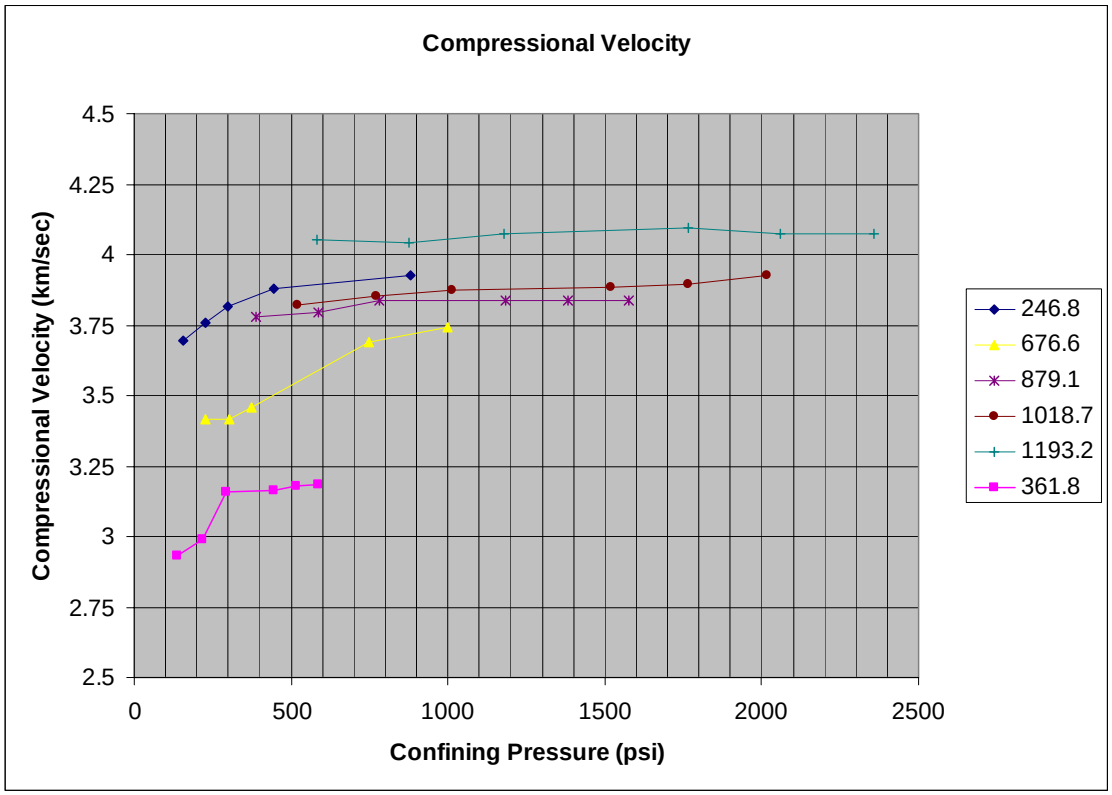

Figure 25. Compressional velocity increases with confining stress

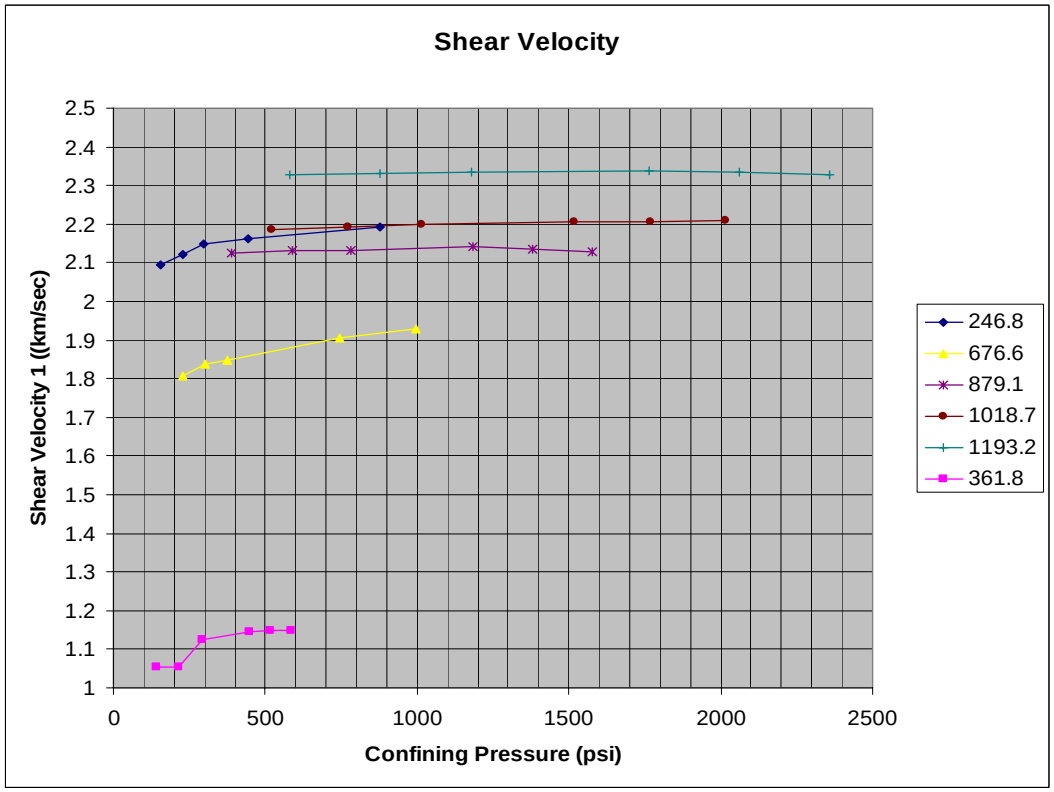

Figure 26. Shear velocity generally increases with confining stress

6.1.2 Velocity Modeling

The velocity of wave propagation in a porous media depends on the media's material composition, and distribution of component materials. The component list can in general include empty space. To model velocity requires specific assumptions about the composition and distributions, along with values of the elastic moduli of each pure material. Helgerud (2001) measured elastic moduli of pure methane hydrates and ice, and used this data to model compressional velocity for four different types of distributions of hydrates in a sandstone pore space. This work will use equivalent isotropic elastic moduli values in Helgerud's thesis, and compare measured velocities to his model results.

One class of models than can be easily investigated without specifying the arrangement of material components is the zero porosity limit, that is, a media composed of sand and ice, but no water. These models provide upper bounds on the possible velocities once composition is fixed. Since most pore space of measured sands is filled with ice, they are effectively near their zero porosity limit. The Hashin-Shtrikman Bounds (Mavko et al., 1998) provide theoretical upper and a lower bound for the elastic moduli of a solid isotropic material of specified composition. Compressional and shear velocities can be calculated from these values combined with the material's density.

The exact composition for the sands is not known as the initial study did not include either mineralogy or petrological descriptions. Primary materials in the composition are certainly quartz sand and ice, but there are probably some clays and some lithic materials. Also the exact ice percentage is not known. Measured average grain density for the samples was 2.64 gms/cc. If the system was just a sand/clay system, this places a limit on the amount of clay. Clays vary in reported density, but a reasonable value for young clays is 2.58 g/cc (the value used in Helgerud's dissertation). To obtain a grain density of 2.64 g/cc from a quartz/clay mix requires 14% clay by weight. Lithic materials would tend to increase the density, so a quartz, clay, lithic mix could have a higher percentage of clay.

Figure 27 shows compressional and shear velocities computed from the Hashin-Shtrikman Bounds on the moduli for a quartz clay system with 39.6% ice (the medium value for porosity at 800 psi in the Ugnu sands). Velocities decrease linearly with increasing clay content. It is well known this linear behavior is often observed in rocks with non-zero porosity (see for example Han (1986)).

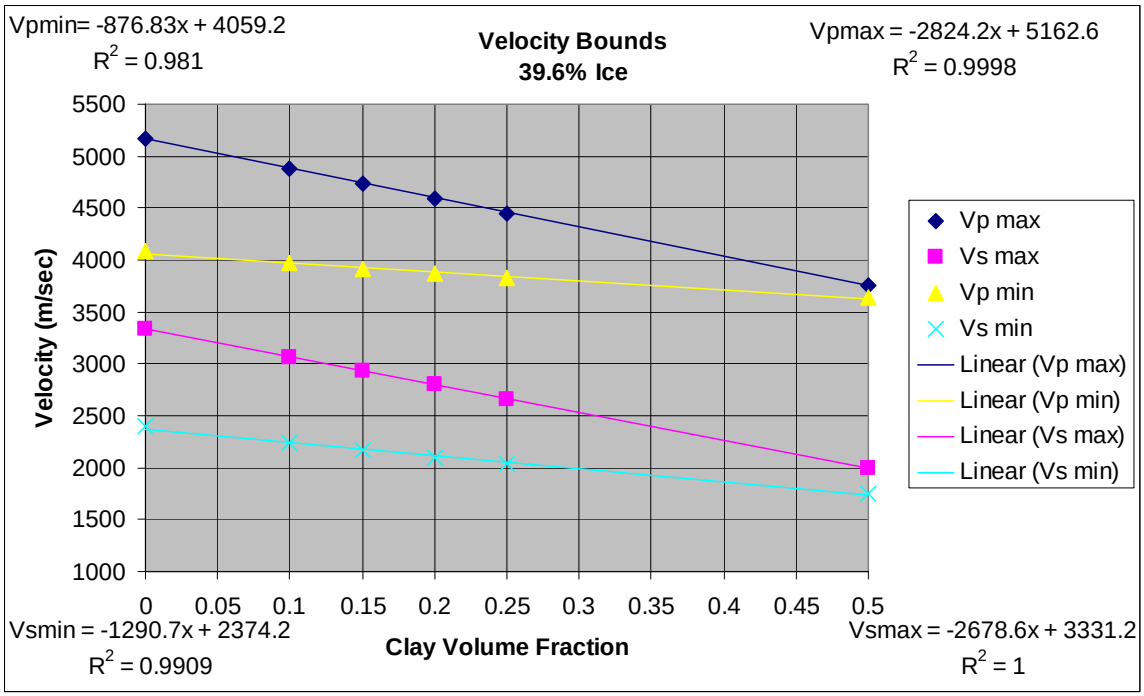

Figure 27. Upper and lower theoretical bounds for quartz sand system mixed with 39.6% ice

Figure 28 shows the velocity bounds for a quartz/ice system for a variable percentage of ice, which correspond to the porosity range observed in the samples. Dependence on porosity is linear. There is only a few percent difference in velocity over the whole porosity range.

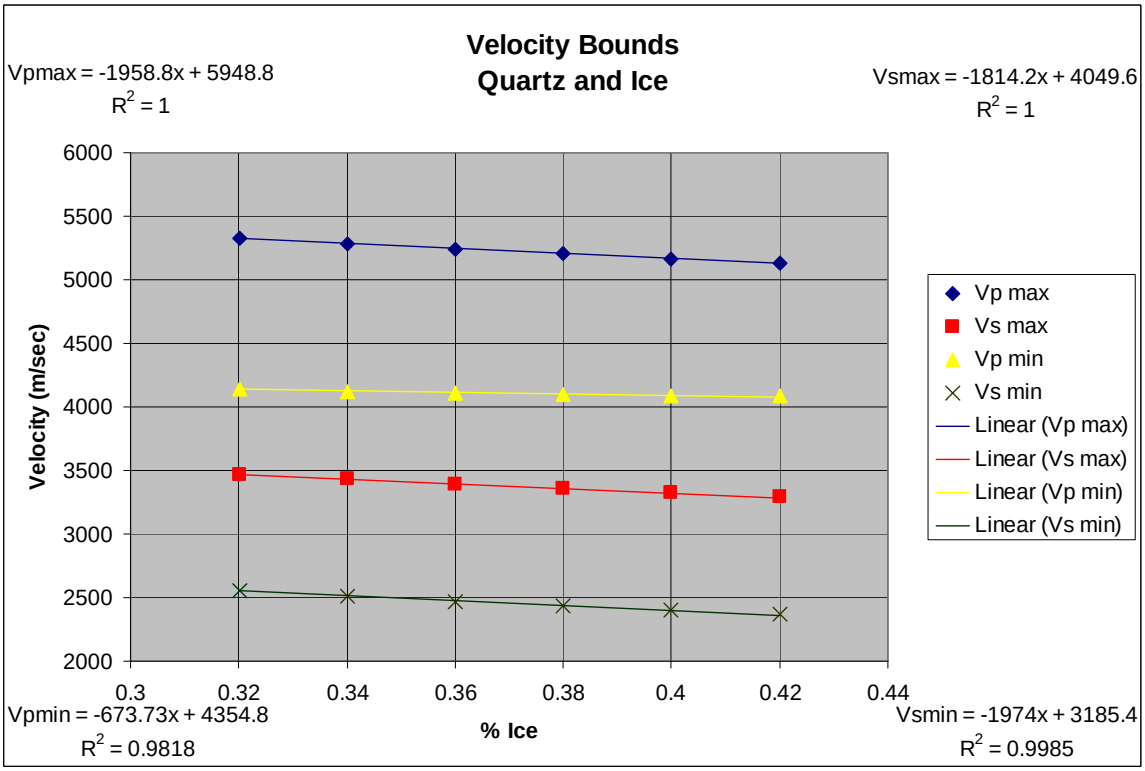

Figure 28. Velocity bounds for a quartz/ice system

For the compositions modeled or reasonable modifications the measured compressional and shear velocities must be greater than the minimum velocity bounds if all the fluid in the pore space is frozen. Unless a large amount of lithic materials acted to counter the grain density lowering of the clay component the sands must be low in clay content. The median compressional velocity is 3864 m/sec and the median shear velocity is 2185 m/sec. This is less than the theoretical minimum so implies some unfrozen water in the pore space or an unusual mineral composition.

Helgerud in his thesis modeled four types of distributions of hydrates in a 40% porosity (essentially the observed median porosity) quartz sand. The models are calculated as a function of the percent of hydrate in the pore space. Because ice and methane hydrate have very similar density and elastic properties the models are equally applicable to the ice sand samples recovered at Hot Ice No. 1. **Table 9** shows the computed Hashin-Shtrikman velocity bounds for the ice sand system and the hydrate sand system. The almost identical results justifies the applicability of the hydrate models to the ice data.

Table 9. Equivalent Isotropic Velocity Bounds using Methane Hydrate or Ice

Frozen Material	Fraction Clay	Vpmax (m/sec)	Vpmin (m/sec)	Vsmax (m/sec)	Vsmin (m/sec)
Ice	0	5173	4090	3331	2405
Ice	0.1	4879	3968	3061	2242
Hydrate	0	5162	4106	3333	2421
Hydrate	0.1	4867	3976	3036	2256

Helgerud's four models are: 1) a pore filling hydrate model in which the only effect of hydrate is to change the bulk modulus and density of the pore fluid; 2) hydrate as a frame component on equal footing with sand grains; 3) hydrate as cement at grain contacts; and 4) hydrate acting as a grain enveloping cement (see Figures 6.4 and 6.6 in his thesis). The CMR core measurements and NMR plug measurements place most of the samples as having pores filled with between 75% and 90% ice. Model 4 is limited to less than 40% frozen material in the pore space. Model 1 cannot produce the compressional velocities observed, so only models 2 and 3 are applicable to the observed data.

Model 2 has a compressional velocity of 3500 m/sec at 80% frozen material and 3900 m/sec at 90% frozen material. Model 3 predicts a Vp of 4100 m/sec at 80% frozen material and 4200 m/sec at 90%. The median measured velocity at 3864 m/sec is very close to the 90% saturation case of Model 2. Clay effects would require a higher saturation of frozen materials to fit this model.

Table 10 shows velocities for three samples where the percent of frozen material was determined by plug NMR measurements. For samples 299 and 1117.6, He porosity is close enough to 40% that the Helgerud model's values should apply. Sample 299 has a compressional velocity 5% less than predicted by the contact cement model and 1117.6 has a velocity about half way between the Model 2 and Model 3 predictions. In terms of the four models measured results suggest that at least some of the ice is acting as cement and the rest as a frame component.

Table 10. Velocity and Percent of Frozen Material for Three Samples

Sample #	Frozen Porosity	He Porosity	% Ice	Vp (Km/sec)	Vs(km/sec)
299	9.8	42.4	0.768868	3.9	1.73
1011	11.6	31.6	0.632911	3.42	1.75
1117.6	7.1	37	0.808108	3.79	2.15

Models developed by Helgerud predict values close to the measured data. These data though provide a weak test of the appropriateness of the Helgerud model set since all the data is for samples that have a high percentage of frozen materials. That places their velocities near values obtained from the Hashin-Shtrikman Bounds for the zero porosity case. Any velocity model has to have as its end point a point at zero porosity that lies between the upper and lower Hashin-Shtrikman Bound, so in the region where these data exist all acceptable models must converge.

6.2 West Sak Formation

All West Sak samples came from below the permafrost. With the exception of samples from the thin, anomalous hard, low-porosity zones, samples were unconsolidated or very weakly consolidated. To facilitate cutting plugs, the core was frozen and the plugs were cut, wrapped, and screened in a frozen state. Except for two sets of shale samples, all samples were cleaned and dried in a low-temperature vacuum oven, and then resaturated with a 3% by weight KCl brine before velocity measurements were made. In most sand locations two companion plugs were cut, and labeled V and N. V plugs were intended for velocity measurements. In a few cases the N plug was used and in a couple of cases both were used. Some samples were measured with screens on and some without. There was no obvious difference between measurements made with and without screens.

6.2.1 Ordinary Sand Samples

Unconsolidated sands were sampled at 42 locations. Velocities were measured at five confining pressures at approximately 20°C on horizontal plugs. Data quality of the signals was not as good as had been hoped for. This is probably due in part to the unconsolidated state of the plugs. The system had been optimized to measure hydrate-containing sediments which were expected to behave as consolidated samples. Velocities are determined by identifying on the measured wave train the first arrivals of the wave train for compressional and shear waves. The compressional wave, because it is always the first arrival, is fairly easy to identify. Shear wave signals always contains precursor compressional wave signals, so their first arrival is more difficult to determine and somewhat subjective. Two team members (Sigal and Sondergeld) selected all velocities. There was close agreement on compressional wave velocities, but less agreement on shear wave velocities. For consistency, Sondergeld's picks were used in all analyses.

Table 11 contains a summary of the sand data measurements at each confining stress. There is about a 6-8% increase in Vp as confining pressure increases. There appears to be no observable shear wave anisotropy.

Table 11. Sand Compressional and Shear Wave Velocities

Confining Stress (psi)	Median Vp (km/sec)	Average Vp (km/sec)	Median Vs1 (km/sec)	Average Vs1 (km/sec)	Median Vs2 (km/sec)	Average Vs2 (km/sec)	Median Vs1/Vs2	Average Vs1/vs2	Median Vp/Vs1	Average Vp/Vs1
600	2.02	2.01	1.04	1.07	1.01	1.07	0.999	0.994	1.97	1.94
800	2.04	2.06	1.08	1.04	1.08	1.02	0.998	0.999	1.96	1.98
1200	2.11	2.08	1.06	1.09	1.03	1.10	0.994	0.998	2.04	1.96
1800	2.13	2.12	1.07	1.11	1.04	1.12	1.00	1.00	1.95	1.94
2200	2.14	2.18	1.12	1.08	1.13	1.04	1.00	1.00	1.96	2.00

With soft rocks such as these it would be expected that there would be some increase in velocity with increasing confining pressure. Median and average values of compressional velocity show an increase of 6% and 8%, respectively, as confining pressure is increased from 600 psi to 2200 psi. There is no clear trend in shear velocity. Vp/Vs ratios are in the range that has been reported for poorly consolidated sandstones. The 800 psi confining stress average compressional velocity is 13% less than the calculated velocity for a water-saturated 38% porosity quartz grained Hertz-Mindlin model. This model is often used to approximate an unconsolidated granular media. Shear velocity though is 41% less. Although shear velocities were difficult to pick, it is highly unlikely that they are in error by that magnitude. Also the Hertz-Mindlin Vp/Vs ratio is much lower than is usually observer for unconsolidated sediments.

Figure 29 shows velocity distribution with depth at 800 psi for the normal sand samples and **Figure 30** shows the same distribution at 2200 psi confining pressure. In Figure 30, there are some obvious bad shear velocities selected by the authors.

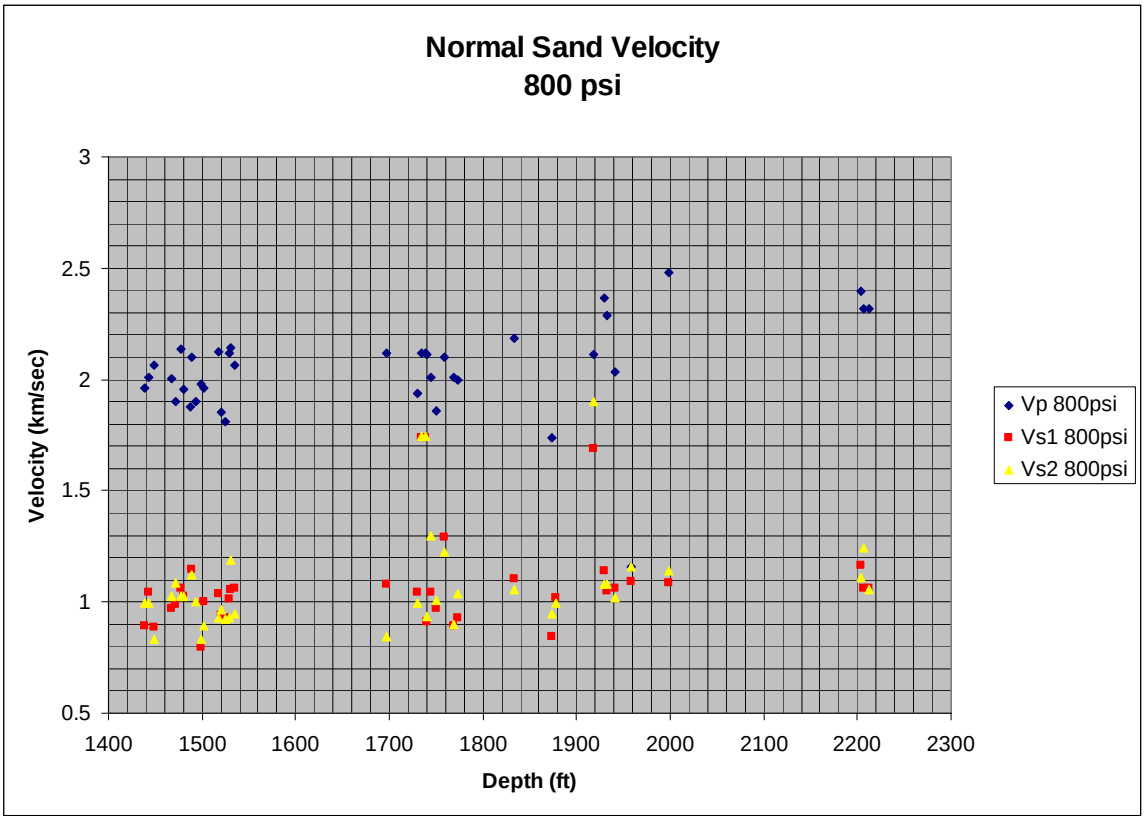

Figure 29. Compressional velocity (blue diamonds), and mode 1 (red squares), and mode 2 (yellow triangles) of shear velocity at 800-psi confining stress

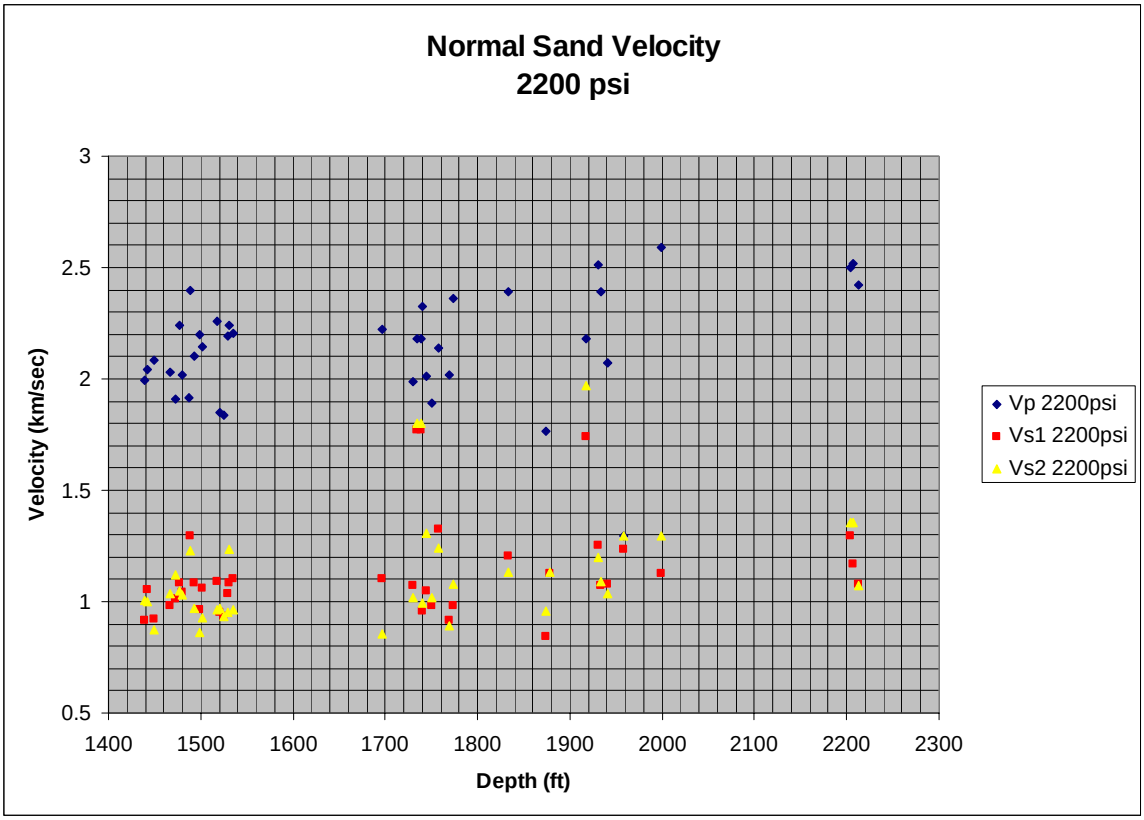

Figure 30. Compressional velocity (blue diamonds), mode 1 (red squares), and mode 2 (yellow triangles) of shear velocity at 2200-psi confining stress

Velocities deeper than 1900 ft are distinctly faster than velocities in shallower sands. This correlates with observations of the well site geologists that the deepest sands appeared to be more consolidated than shallower ones. Point to point, there are only minor differences in values of Vs1 and Vs2. Shear velocities at 1738.8 and 1918 ft appear to be anomalously fast and are probably bad picks attributable to poor signal quality.

Figure 31 shows the Vp/Vs ratio at 2200 psi confining pressure with depth. There is no obvious trend. **Figure 32** shows a cross-plot of compressional and shear velocity measured at 800-psi confining pressure against porosity measured at 800-psi confining pressure. There is no apparent correlation of velocity with porosity for the normal sands in the section.

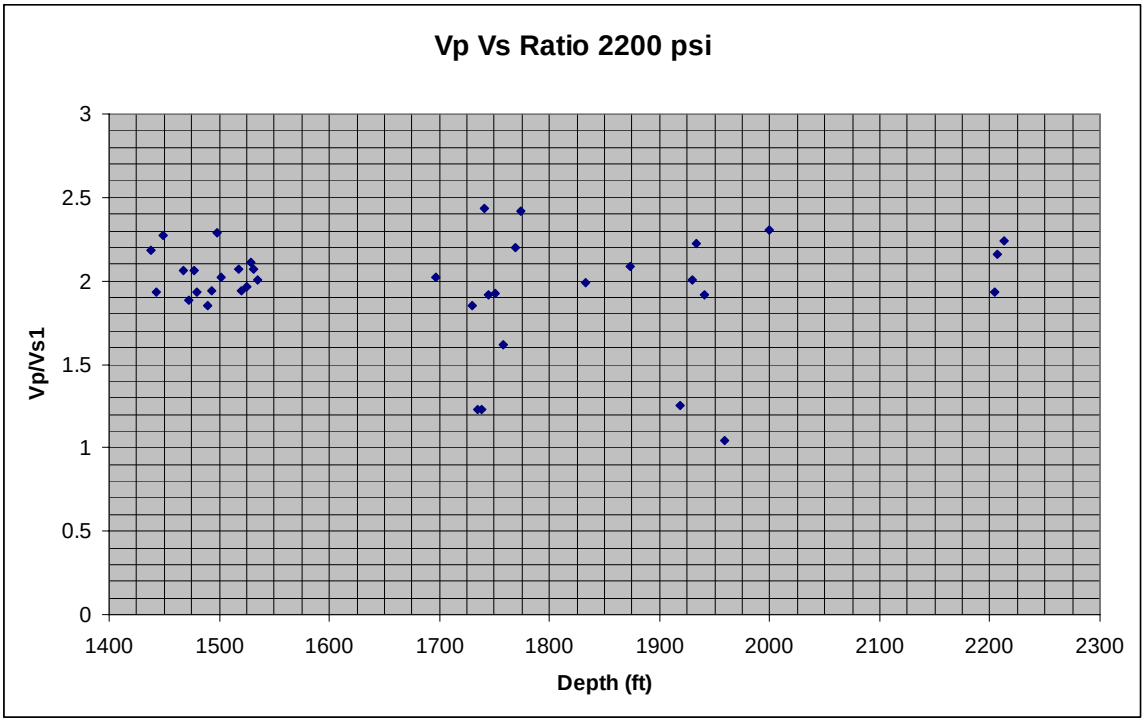

Figure 31. Vp/Vs with depth

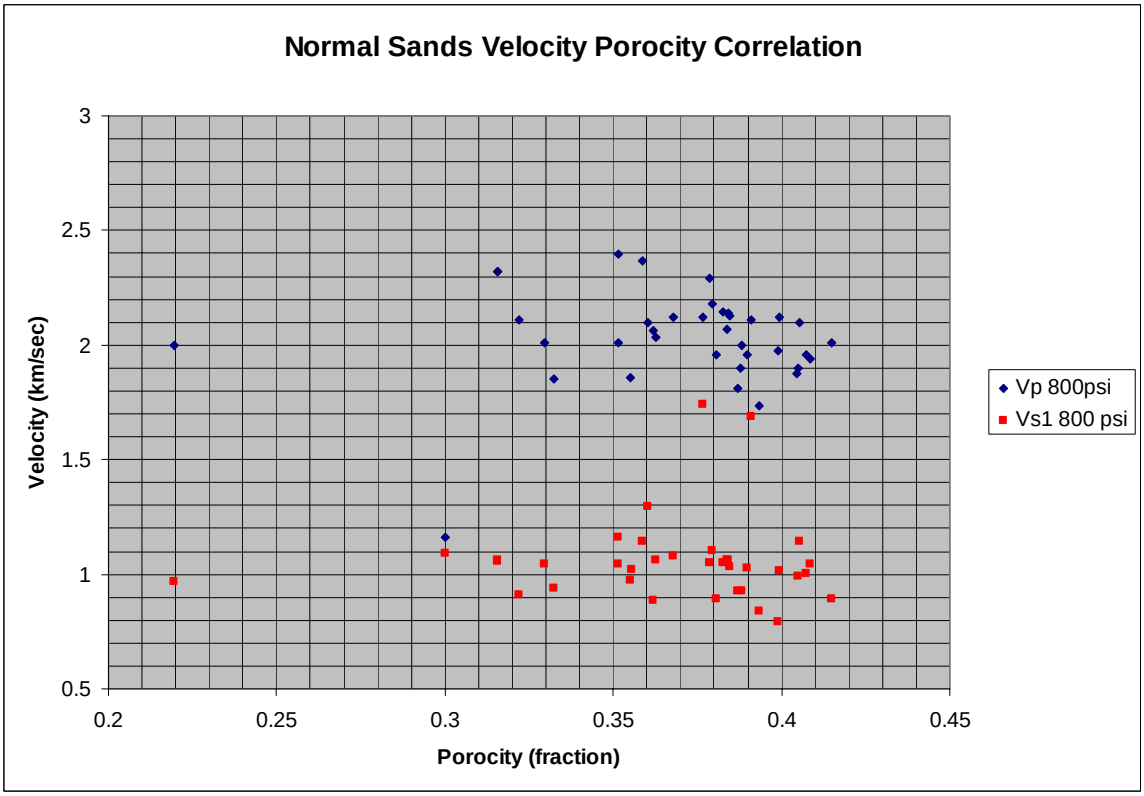

Figure 32. Compressional velocity (blue diamonds) and shear velocity (red squares) versus porosity

Velocity measurements combined with bulk density, ρ_b, can be used to calculate the dynamic elastic moduli of the wet sands assuming they are a homogeneous isotropic linear elastic media. Saturated bulk modulus, K_{sat}, and shear modulus, G, are related to velocity by:

$$V_s = \sqrt{\frac{G}{\rho_b}}$$

$$V_p = \sqrt{\frac{K_{sat} + \frac{4}{3}G}{\rho_b}}$$

Figure 33 displays dynamic shear and dynamic saturated bulk moduli as a function of depth for 800-psi confining stress. The deepest sands (which were more consolidated) have larger moduli. There are a few points that are such large outliers that they are probably experimental artifacts. The median value of K_{sat} is 5.82 GPa and the median value of G is 2.23 GPa.

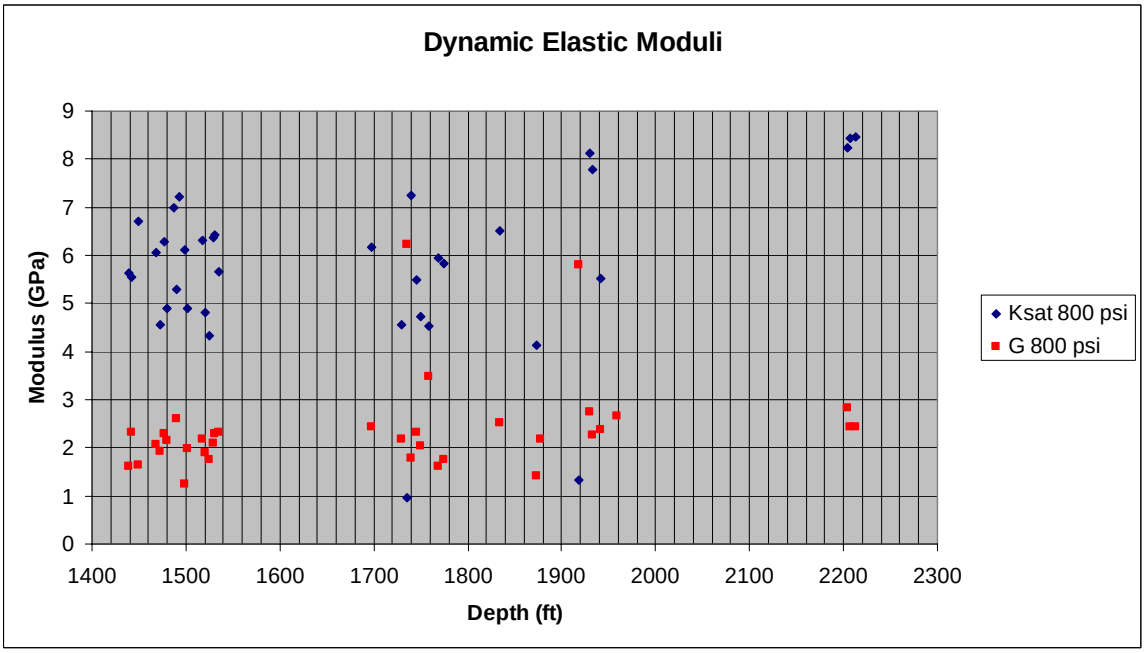

Figure 33. Dynamic elastic moduli for saturated samples calculated from velocity data

6.2.2 Shale Samples

Shales were sampled at two depths. Samples were taken at three orientations to bedding: 0°, 45°, and 90°. These samples were measured in their as-recovered state. They were wrapped and screened to help preserve them through the measurement process. Measurements on plugs at three orientations provide data to extract anisotropic elastic constants of a layered media. Because of poor quality of the shear data, that was not done for these data. **Table 12** lists velocity data at 800-psi and 2200-psi confining pressure. Horizontal compressional velocity should be larger than vertical for a layered system. In this case there is about a 10% difference. Shear wave data are not good enough to note anisotropy in it. Velocities of the sample at 1800 ft are not distinguishable from sand samples at that depth. The sample at 2030 ft is similar in

velocity to the shale sample at 1800 ft. It is, however, about 20% slower than the deepest sand velocities.

Table 12. Shale Velocity at 800-psi and 2200-psi Confining Stress

Orientations are horizontal (H), vertical (V), and 45° (45) to bedding. In general, horizontal compressional velocities for each sample are greater than the others.

Sample	Confining Pressure (psi)	Vp (km/sec)	Confining Pressure (psi)	Vs1 (km/sec)	Confining Pressure (psi)	Vs2 (km/sec)
1800.00(H)	822.8	2.095	827.7	1.024	825.2	1.021
1800.01(V)	820.3	1.878	820.3	1.017	820.3	0.982
1800.02(45)	817.9	1.915	817.9	1.064	817.9	1.011
2030.00(H)	817.9	2.111	817.9	1.022	815.5	1.052
2030.01(V)	815.5	1.856	813.0	1.015	813.0	0.992
2030.02(45)	813.0	1.709	813.0	0.972	817.9	0.948
1800.00(H)	2218.6	2.108	2218.6	1.036	2216.2	1.034
1800.01(V)	2213.7	1.899	2213.7	1.017	2213.7	0.986
1800.02(45)	2211.3	1.942	2211.3	1.068	2211.3	1.034
2030.00(H)	2213.7	2.144	2208.8	1.040	2208.8	1.057
2030.01(V)	2208.8	1.863	2206.4	1.013	2206.4	1.000
2030.02(45)	2208.8	1.726	2206.4	0.972	2206.4	0.955

6.2.3 Anomalous Hard Zones

Velocity measurements were made on samples from three of the anomalous thin hard low-porosity sand zones encountered. **Table 13** lists data for measurements at 800 psi and 2200 psi. There appears to be no observable pressure dependence. Compressional velocity is twice as fast as in the normal sands. The two shear velocities are essentially equal and also about twice as fast as normal sand velocities. These velocities are similar to those seen on frozen samples from the Ugnu. The thin hard zones also appear fast on the velocity logs, so they clearly appear to be a hydrate zone when the velocity logs are viewed.

Table 13. Velocity Data for Thin, Low-Porosity, Hard Sandstone Formations

Sample	Confining Pressure (psi)	Vp km/sec	Confining Pressure (psi)	Vs1 (km/sec)	Confining Pressure (psi)	Vs2 (km/sec)	Vs1/Vs2	Vp/Vs1
1481.8	810.5	4.895	808.1	2.542	808.1	2.414	1.053	1.926
1702.1	773.8	4.511	773.8	1.850	771.4	1.897	0.975	2.438
1753.8	800.8	4.505	795.9	1.614	800.8	1.664	0.970	2.791
1481.8	2196.6	4.895	2199.0	2.566	2203.9	2.414	1.063	1.908
1702.1	2154.9	4.615	2154.9	1.906	2152.5	1.901	1.002	2.421
1753.8	2181.9	4.551	2179.4	1.629	2179.4	1.677	0.971	2.794

6.3 Conclusions – Velocity

Velocity measurements were made on frozen samples from the permafrost zones and on brine-saturated samples from sands below the permafrost. Velocities of the frozen samples are very similar to low-porosity cemented sandstones. They are (as expected) much faster than the

unfrozen sand samples. The frozen samples, when cleaned and dried, are very similar in porosity to samples taken from below the permafrost.

The similarity of elastic properties of pure methane hydrate and ice imply that the velocities of a rock with ice replaced exactly by hydrate would have essentially the same velocities as ice-filled rock. That is, ice can be used as a surrogate to understand how hydrates affect measured velocities. Observations on the permafrost samples should be analogous to what would be seen in hydrates formed near the base of permafrost. Velocities measured on frozen samples are consistent with models that have ice acting as part of the "rock" frame and probably also as a cement. Helgerud (2001) concluded from modeling sonic log measurements that hydrates seen at the Eileen State Well #2 were grain supporting but did not act as cement. This could mean that hydrates in the Tarn-type accumulations play a different structural role than the deeper hydrates at Eileen State.

Brine-saturated normal sand samples had poor quality velocity signals, making it very difficult to pick shear velocities; however, most attempts produced values near 1000 m/sec. Compressional velocities were easier to pick, and hence are of superior quality. Most were about 2000 m/sec. These velocities are on the low end of typical velocities reported for unconsolidated sandstones. Samples taken from the deepest sands had about 20% higher velocities. This is consistent with visual observations that they seemed more consolidated. Sands and shales had similar velocities.

Hard anomalous zones had velocities about twice as fast as velocities in surrounding normal sand zones. They were similar to velocities measured on frozen samples. They also showed up as fast zones on the sonic logs run in Hot Ice No. 1. Under some conditions, these zones could be mistaken for hydrates.

7. Resistivity Measurements

7.1 Ugnu Formation

Almost every sample from the Ugnu was taken from sands in the permafrost zone. With the exception of a few samples used for equipment tests, all samples were cut from frozen core, kept frozen, and measured in a frozen state. They were not, however, true native-state plugs since they had not been maintained at reservoir temperature and pressure, and the measurements were not conducted at reservoir temperature and pressure. It is generally expected that the state of a frozen sample depends not only on its current temperature and pressure but on its temperature and pressure history. Due to various details of the measurement process, the samples were not all measured at the same temperature.

Each sample was measured at five different confining stresses. Pore pressure was laboratory air pressure. There was very limited temperature variation as confining stress was varied on a single sample.

7.1.1 Formation Factor and Porosity

Electrical measurements of Ugnu samples are not straightforward to interpret. Because they were made in a "native state," neither resistivity of the unfrozen brine nor volume of unfrozen brine is known. Also, since measurements were not performed at native formation temperature for that sample, they do not represent the resistivity that an electrical log would measure. To extract information from them requires adopting a series of assumptions.

The basic assumption made is that, for a plug containing both ice and unfrozen brine, the unfrozen brine has a salinity that is the lowest value needed to keep it from freezing at that temperature. This assumption is only an approximation since capillary forces also suppress the freezing point of brine in a rock. These sands though are very high permeability, so this effect is expected to be small. This assumption allows the frozen rock's formation factor to be calculated. If the frozen rock is them considered to have a matrix made up of ice and standard matrix materials, the liquid filled porosity can be estimated from Archie's Law.

Required information on the freezing point of brines as a function of salinity and the electrical conductivity of the brine at that temperature can be extracted from the website of Dr. Rick Chapman of The Johns Hopkins University Applied Physics Laboratory. (The calculator on the website implements the UNESCO International Equation of State (IES 80) as described in Fofonoff (1985). Equations and data used in the calculator have only been checked to -2°C, so there could be some error introduced by extrapolating them to -6°C.)

Figure 34 displays salinity of brine at its freezing point as a function of temperature. A linear regression is an excellent fit to the data over this temperature range.

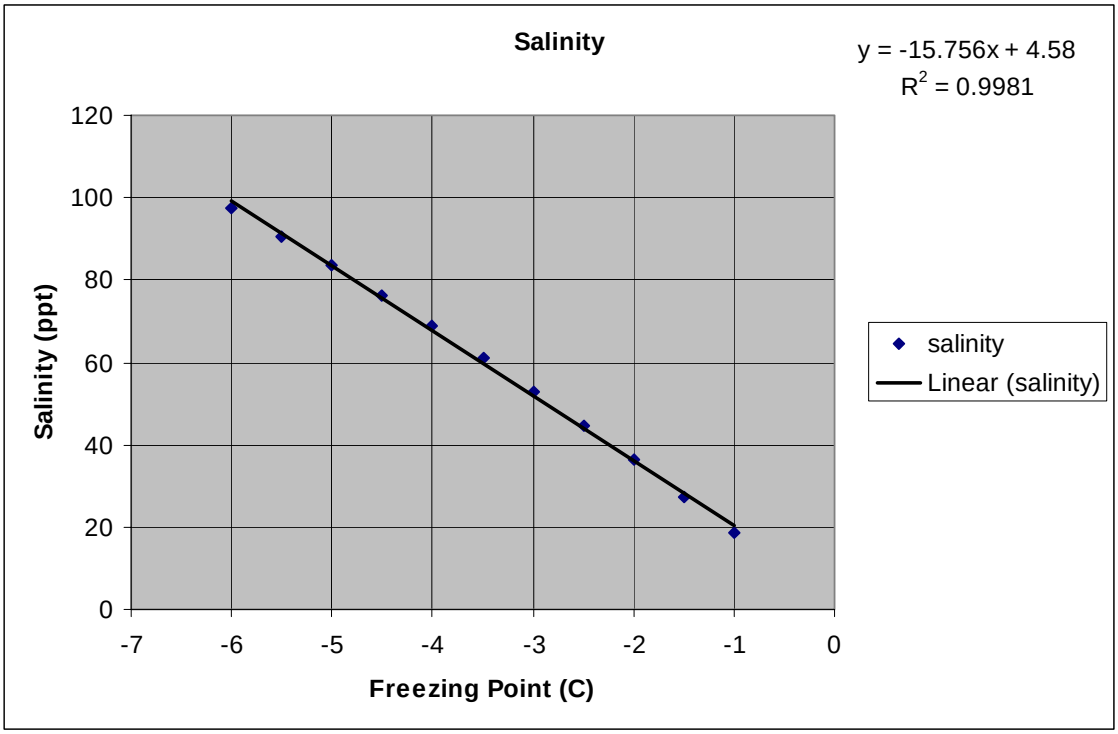

Figure 34. Salinity exactly at the freezing point for a brine at each temperature

Figure 35 shows electrical conductivity of brine at its freezing point salinity. A quadratic curve provides an excellent fit to the data over the temperature range of interest.

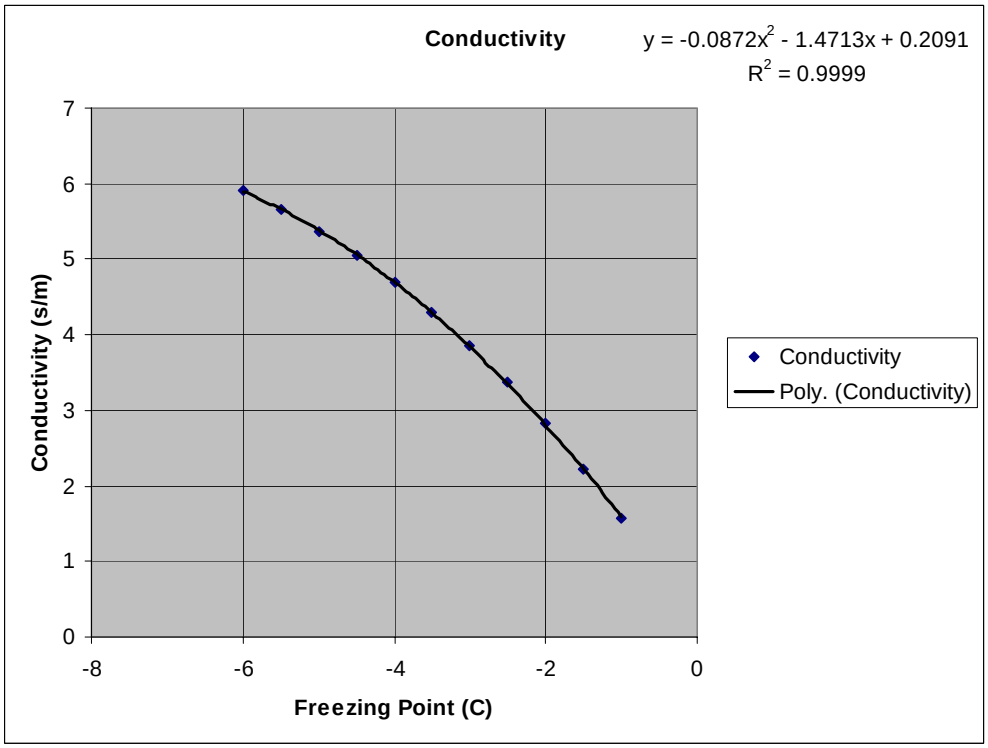

Figure 35. Electrical conductivity of brine at its freezing point for required temperature range

Archie's law in its simplest form for a brine saturated sample is:

$$R = R_w \phi^{-m}$$

where R is measured resistivity, R_w is resistivity of the saturating brine, ϕ is porosity, and m is cementation factor. The formation factor is ϕ^{-m}. Modeling the velocity data and NMR plug data (see Sections 6 and 8) along with physical observation of the samples show that the ice mostly acts as another element of the rock frame and to a lesser extent as a cement. NMR data on the frozen samples look like that of a low porosity small pore sandstone, that is, in many ways the frozen rocks resemble a standard low-porosity sandstone. For such rocks a value of m of 2 is appropriate. Previous assumptions allow calculation of the fraction of the rock volume ϕ_m filled with fluid at the temperature at which the electrical measurement was made from the formula

$$\phi_m = \sqrt{\frac{R_w}{R}}$$

Figure 36 shows measured electrical conductivity (1/R) as a function of measurement temperature. The measurement used was that recorded at a confining stress closest to 800 psi. There is no limited variation in porosity in these samples. As such it is very likely that the five most conductive measurements represent experimental artifacts.

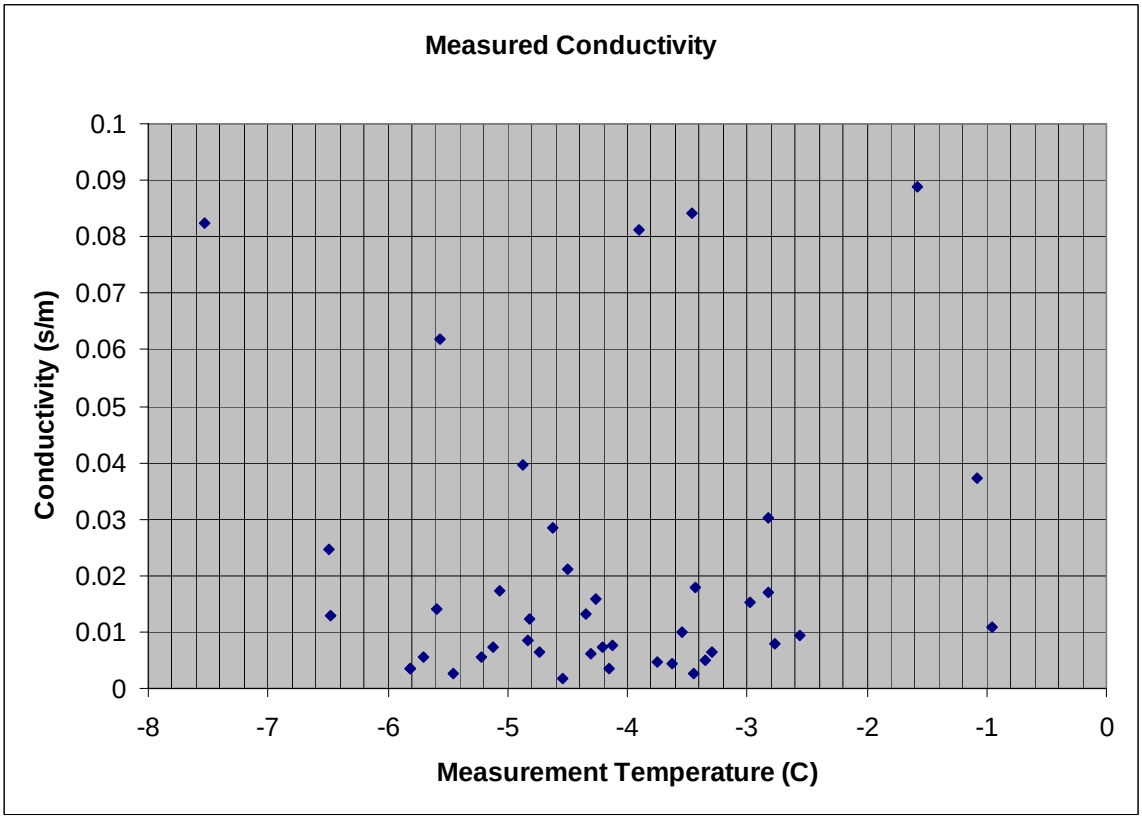

Figure 36. Electrical conductivity versus measurement temperature

Figure 37 shows porosity ϕ_m against temperature. **Figure 38** presents the same data normalized by the porosity of the sample measured on the cleaned and dried sample at 800 psi

confining stress. In Figure 37, the five most anomalous measurements have been removed. There is probably a fair amount of error in either the measurements or due to the assumptions made in the analysis. The general picture is consistent, however. Percentage of unfrozen brine increases as temperature increases, and the values of ϕ_m are in the same range as those observed in the CMR core measurements.

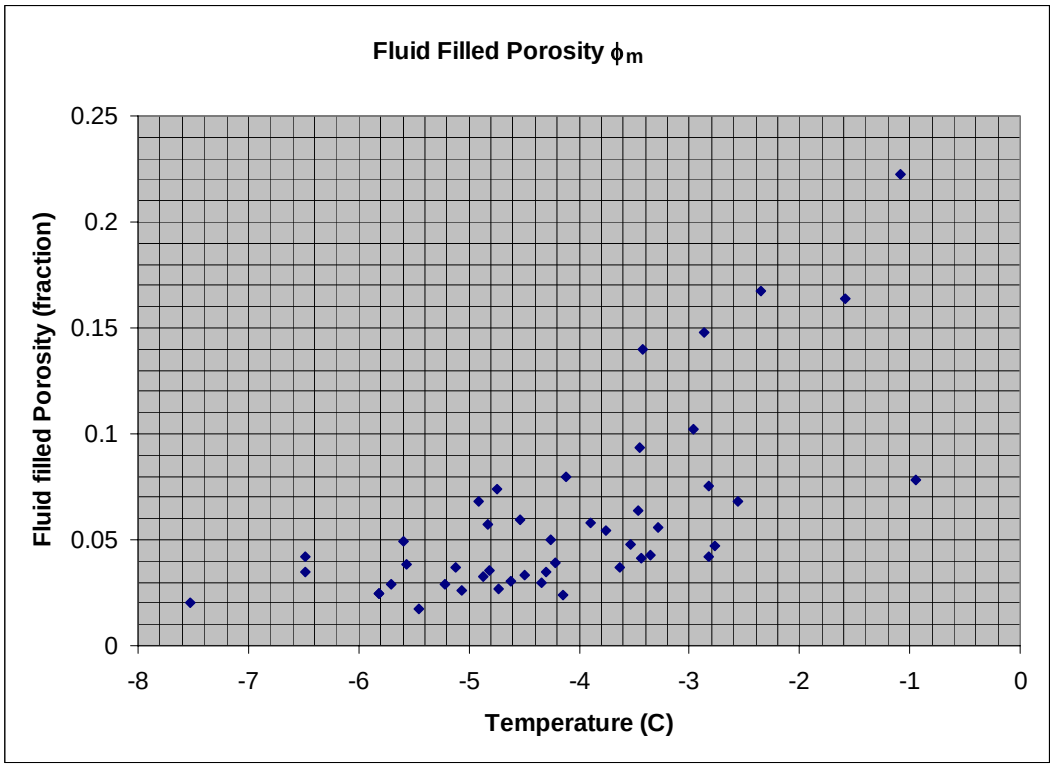

Figure 37. Fluid-filled porosity versus measurement temperature

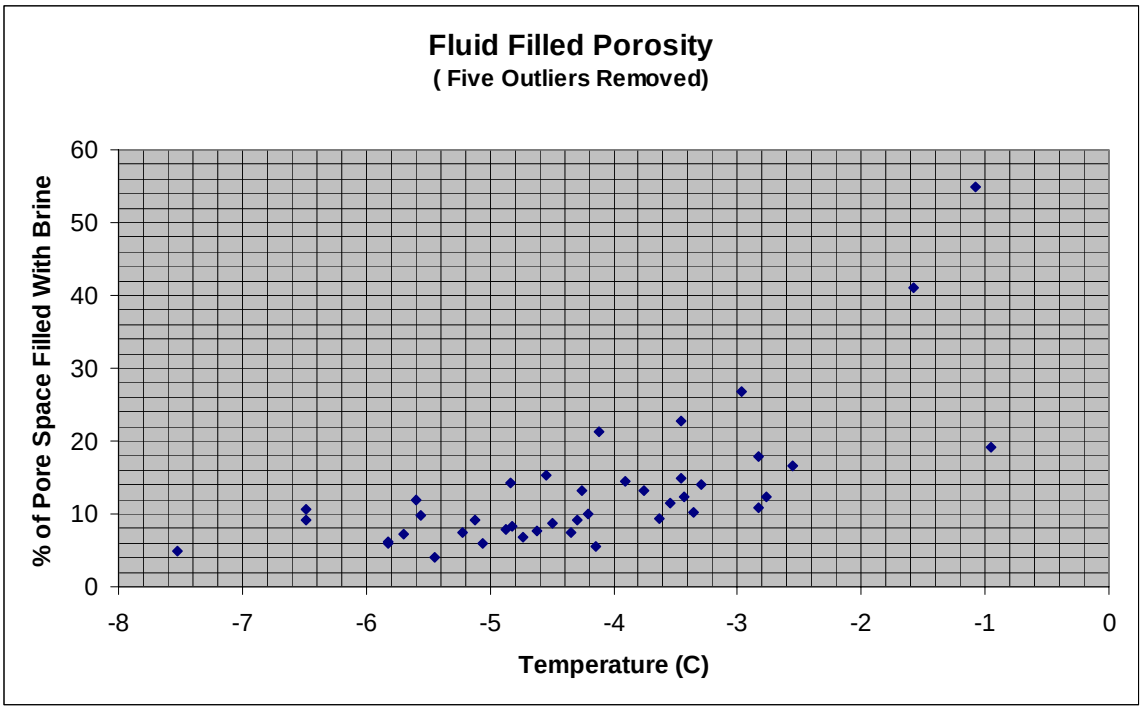

Figure 38. Percent of pore volume filled with liquid versus temperature

7.1.2 Salinity of in-Situ Brine Before Freezing

The previous analysis can be extended to calculate salinity of the formation brine before the rock froze. Two assumptions are necessary for this calculation. The first is that unfrozen brine in the pore space did not have its salinity altered by diffusion processes. The second is that all the salt in the initial brine was expelled from the ice when it froze. It has been reported for ocean water this is not exactly correct (Shcherbina et al., 2003). Using these assumptions

$$S_o = S_m \frac{\phi_m}{\phi}$$

where S_m is the calculated salinity at measurement temperature.

Figure 39 compares estimated brine salinity at each depth. The five highest values are the samples corresponding to the most anomalous conductivity measurements. All values show a low salinity brine. With the five anomalous points removed, median value of salinity is 7100 PPM. This is close to the value obtained from core water extracted from an Ugnu sample taken from a sand just below the base of the permafrost. Consistently of estimated salinity and agreement with other estimates of formation salinity suggests that the assumptions are (to the first order) reasonable.

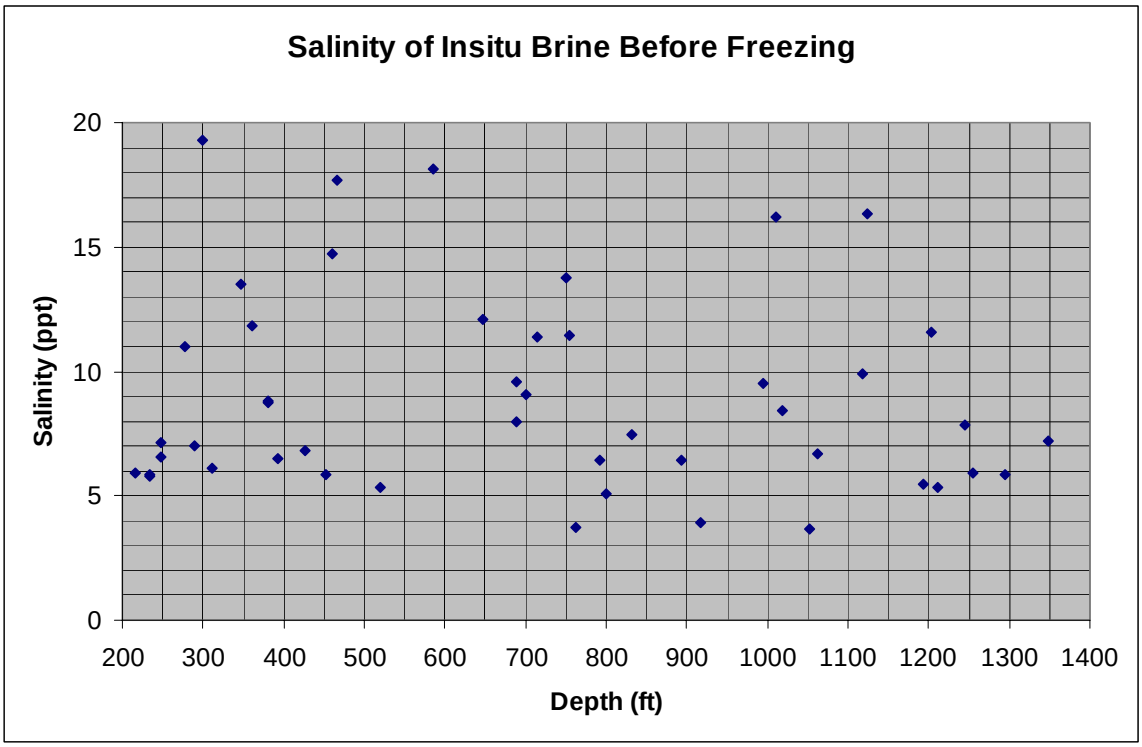

Figure 39. Estimated salinity before freezing pore water in the sample

7.1.3 In-Situ Sand Resistivity

Formation resistivity is a function of formation temperature and formation brine resistivity. If it is assumed that median salinity is a good estimate of formation salinity throughout the permafrost, then, using the same assumptions as before and using the thermal gradient in the permafrost at Hot Ice No. 1 (0.0142°F/ft), a resistivity profile as a function of depth can be constructed (**Figure 40**). The trend of decreasing resistivity as the base of permafrost is approached agrees with what is observed on resistivity logs in the area.

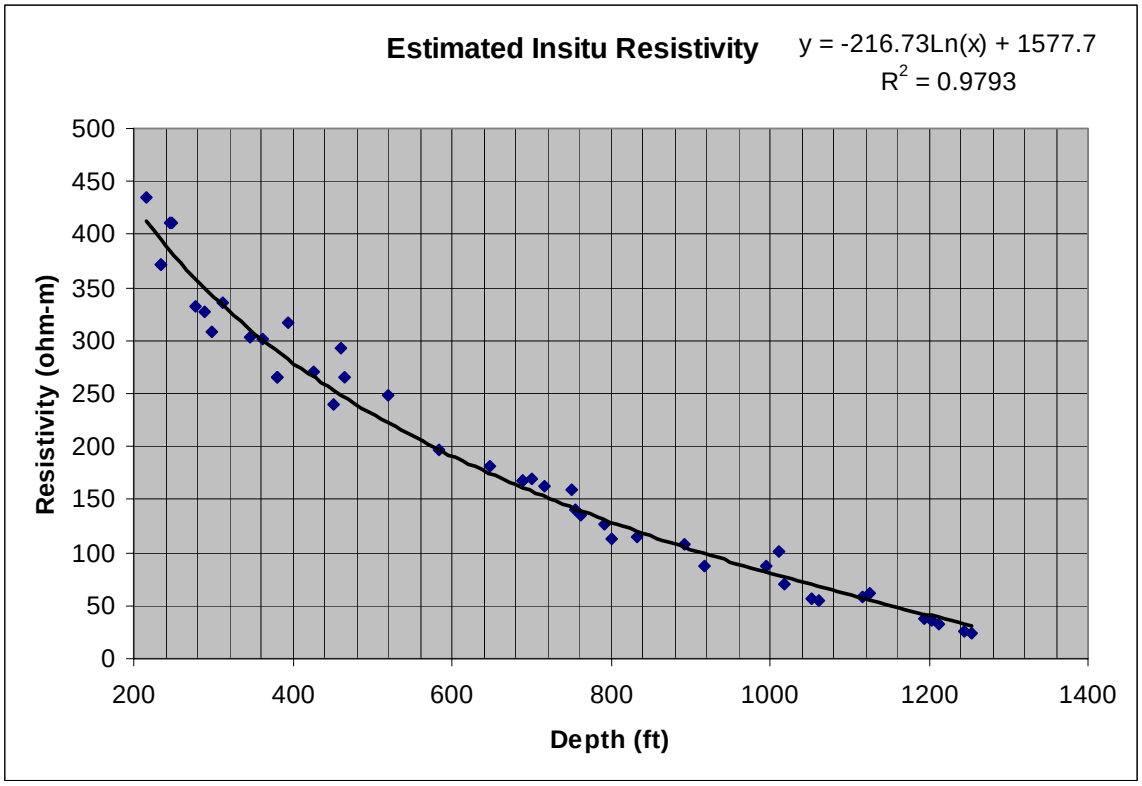

Figure 40. Calculated formation resistivity in permafrost zone at Hot Ice No. 1

7.1.4 Conclusions – Resistivity in Ugnu Formation

Although there appears to be more experimental "noise" in the electrical measurements than is desirable, the general analysis is consistent with measurements made using the CMR and water salinity estimates made by several means. The assumption that salinity of the unfrozen brine as a function of temperature is only that necessary for the brine not to freeze, seems to give reasonable results. Salinity of the unfrozen brine seems to be reasonably well calculated by simple volumetric considerations. Finally, frozen rock pore geometry behaves like a typical low porosity sandstone with m equal to 2.

7.2 West Sak Formation

All West Sak samples were recovered from below the permafrost. With the exception of the deepest sands, they were completely unconsolidated. Resistivity R was measured on 52 samples from the West Sak. Two samples from the sand section were measured in their recovered state to provide information on the salinity of the brine saturating West Sak sands. Six "shale" samples from two different depths were also measured in their recovered state. These measurements provide a comparison to the resistivity logs in shale and information on resistivity anisotropy. The 44 remaining samples were all horizontal plugs that were cleaned and dried in a low temperature vacuum oven, and on which He porosity ϕ and permeability k at three confining stresses (800, 1200, and 1800 psi) had been measured.

The samples were then resaturated with a 3% by weight KCl solution and resistivity was measured at five confining stresses (600, 800, 1200, 1800, and 2200 psi) at a temperature of 20°C. At this temperature the brine has a calculated resistivity (R_w) of 0.223 Ohm-meters. (Salinity was converted to an equivalent NaCl salinity using chart Gen-8 from the 2000 Edition of *Schlumberger Log Interpretation Charts*. It was then converted to a resistivity using a JavaScript calculator available on a website provided by Dr. Rick Chapman of The Johns Hopkins University Applied Physics Laboratory. The calculator implements the UNESCO International Equation of State (IES 80) as described in Fofonoff, *JGR*, Vol 90 No. C2, pp 3332-3342, March 20, 1985.)

7.2.1 Cementation Exponent

For the three confining pressures at which ϕ was measured, a cementation exponent, m, was calculated using Archie's Law. m was calculated for each sample and confining stress from the formula:

$$m = \frac{\log \frac{R_w}{R}}{\log \phi}$$

Table 14 lists average and median values for m at the three confining pressures.

Table 14. Cementation Exponents for West Sak Sands

m	800 psi	1200 psi	1800 psi
Average	1.99	1.96	1.92
Median	1.94	1.91	1.87

One sample with an m value of 6.74 was excluded in making the table. This is not a physically reasonable value for a high-porosity, high-permeability sample. Values from the anomalous hard zones have been included along with five other samples with an m value that is far higher than would be expected from high-porosity, high-permeability sands.

Values of m are generally higher than expected based on the team's past experience with unconsolidated high-porosity samples. However, the average and median are well within a reasonable range for sandstones. There is a tendency for m to decrease with confining stress. This has been observed previously. **Figure 41** shows m at 800 psi plotted against depth. Measurements made in the two different measurement systems (NER1 and NER2) are plotted with different symbols. There are no obvious systematic differences between them.

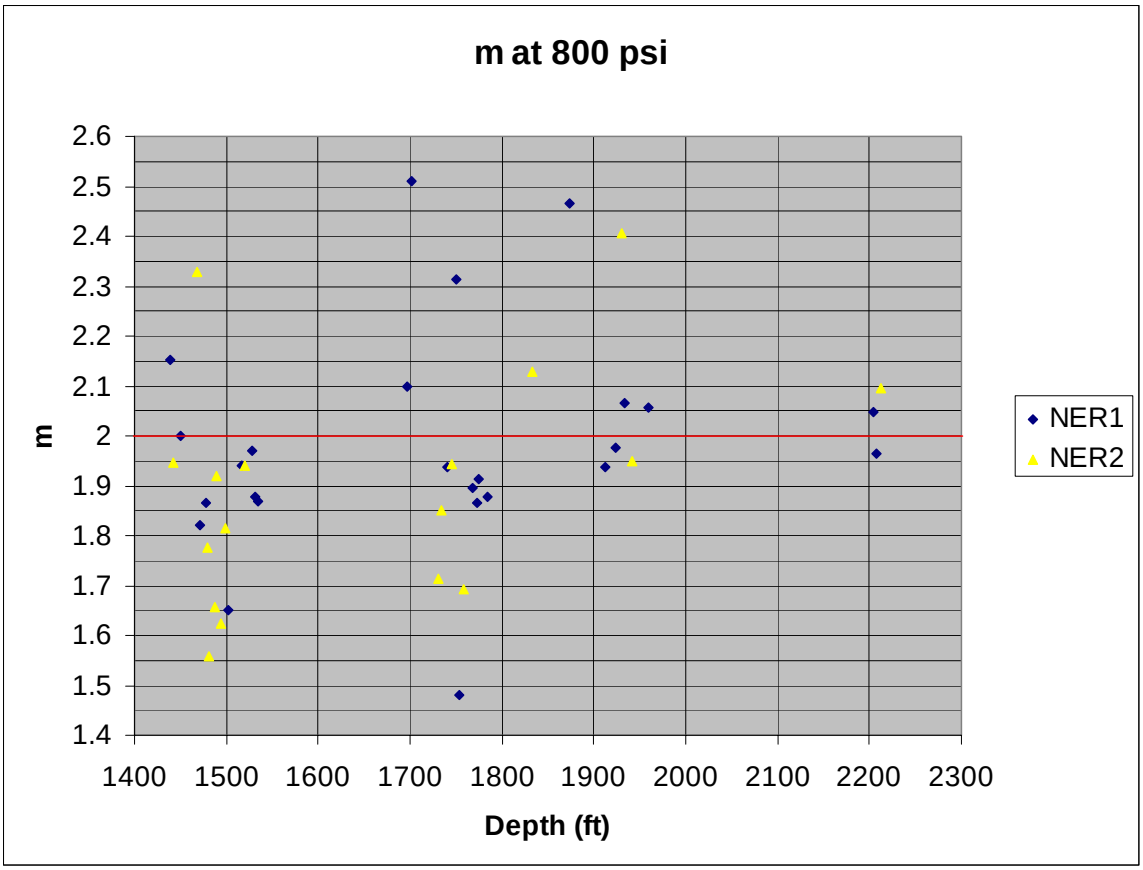

Figure 41. Archie's cementation exponent m versus depth

The two most anomalous values of m (6.74 and 3.66) are not plotted in Figure 41 to provide a less compressed scale. Both these samples are high-porosity, high-permeability samples (38.7%, 527 md and 39.1%, 1899 md) that cannot be associated with these values of m. These are clearly experimental errors. Three other good sands have values of m between 2.31 and 2.47. These values are suspicious. Of these five, laboratory documentation suggests problems with two of them. Two other values above 2.3 may be reasonable. The 2.33 value of m at 1467.6 ft is from a 21% porosity 3-md sand. Both this porosity and permeability are also very low for sands in this section, so a large m value is consistent with this. The value 2.51 at 1701 ft is from one of the low-porosity, hard cemented zones. The two lowest values of m (1.48 and 1.56) also come from low-porosity, hard cemented zones. The remaining low values of m are from high-porosity, high-permeability unconsolidated sediments, and thus are reasonable.

Figure 42 presents values of m at all three confining stresses plotted against depth; **Figure 43** displays m against porosity; and **Figure 44** against grain density. There is no clear correlation with porosity. There is perhaps a slight tendency for m to increase with increasing grain density.

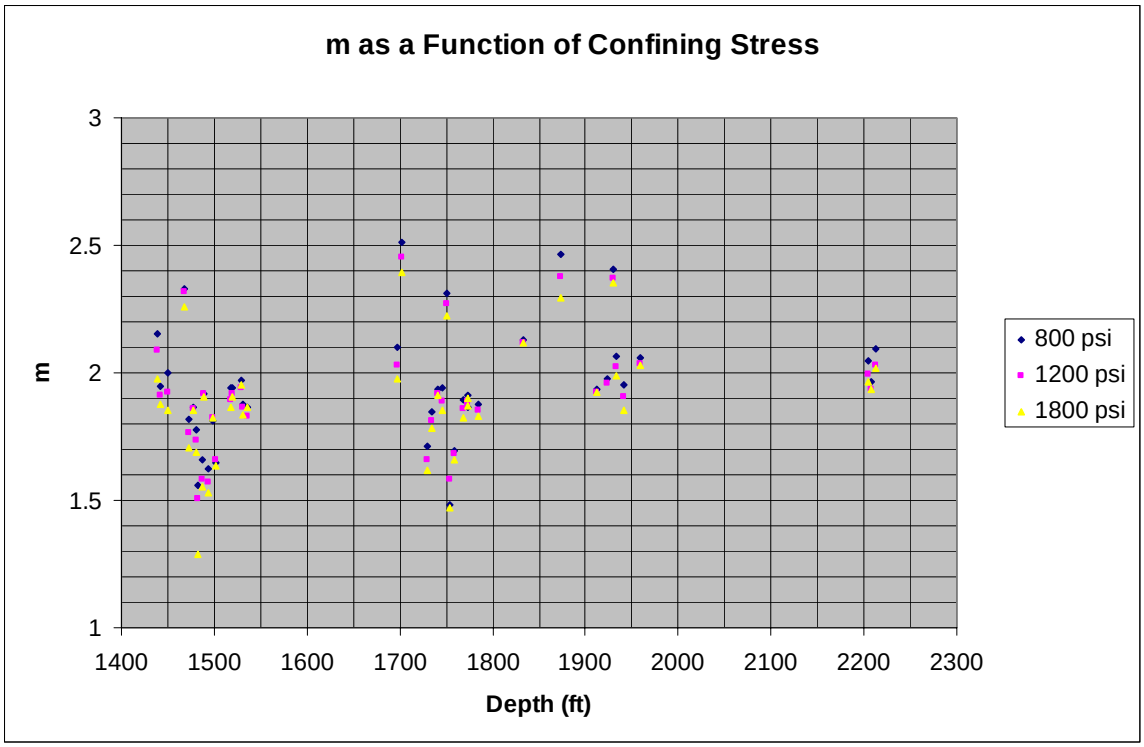

Figure 42. Archie's cementation exponent m versus depth

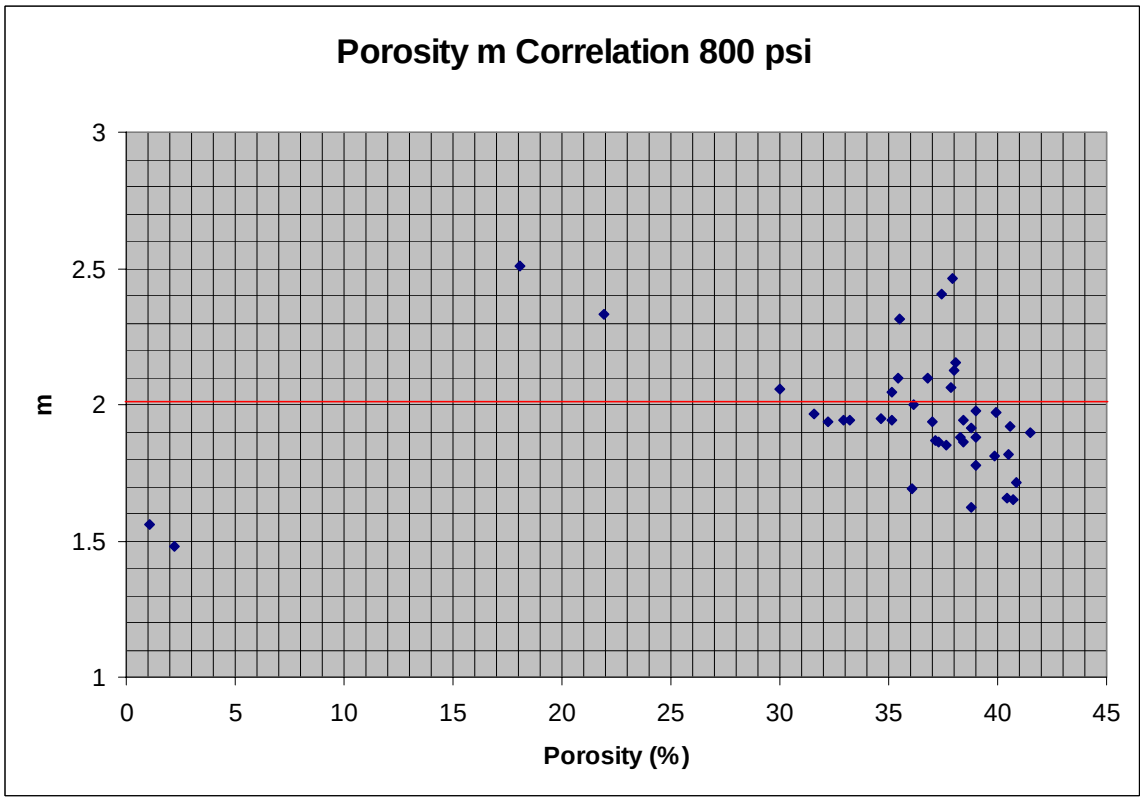

Figure 43. Archie's cementation exponent m versus porosity

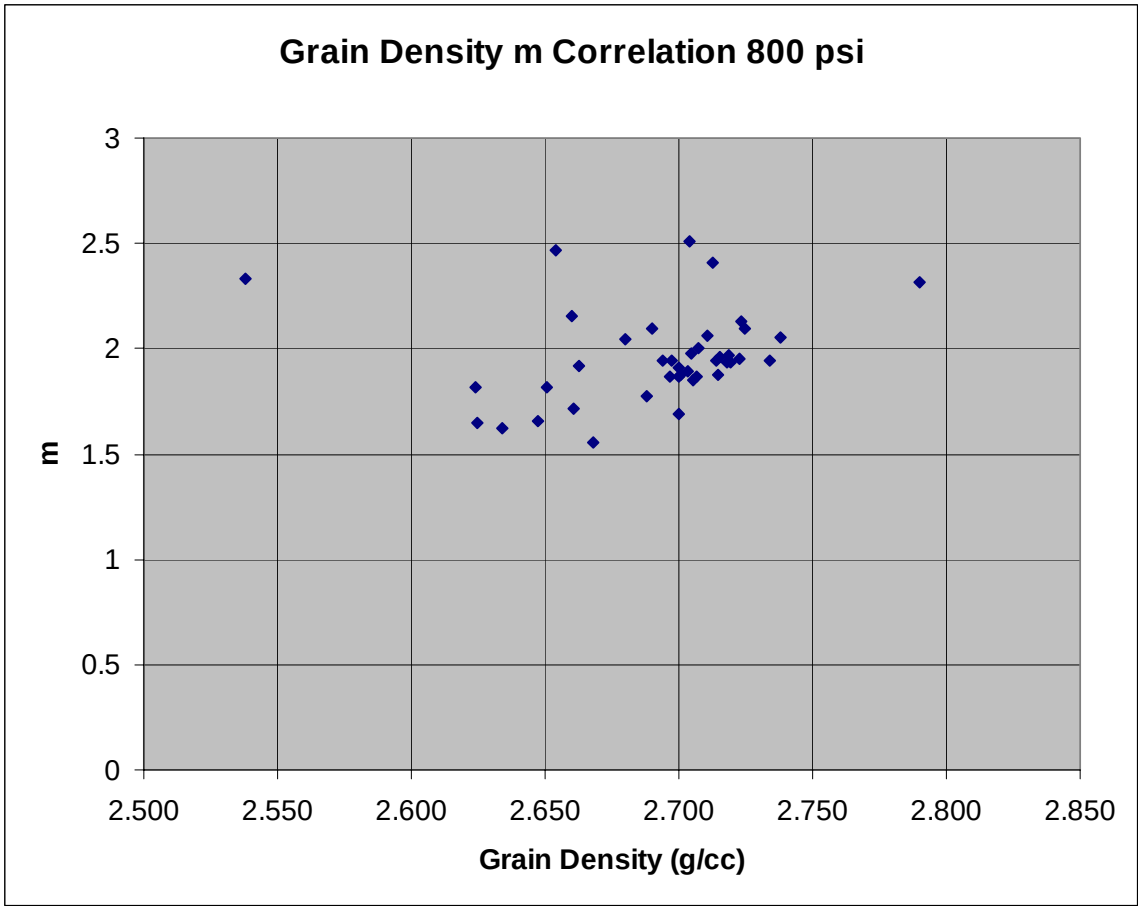

Figure 44. Archie's cementation exponent m versus grain density

7.2.2 Fresh-State Sand Samples

Two sand samples (A1877.8V and A1999.0V) were measured for resistivity as recovered. These measurements (along with reasonable assumptions) allow an upper bound to be set for in-situ pore water salinity. The drilling mud was 18% KCl by weight, and thus any mud invasion would produce an increase in estimated salinity. Pore fluid loss during handling would produce an underestimate of salinity, but that effect is small and would not affect the basic conclusion.

For sample A1887.8V, porosity was available from a companion plug A1877.8N. No companion plug porosity was available for A1999.0V. Because of the lack of a measured value for m on sample A1877.8V and m and ϕ on A1999.0V, R_w for the pore fluid was calculated for a range of possible values of m and ϕ. R_w was converted to salinity using Dr. Rick Chapman's JavaScript calculator. From Archie's Law for a measured value of R, the estimated value of R_w increases as ϕ increases and decreases as m increases.

Examination of the values of m in the deeper part of the section (see Figure 41) shows its range to be bounded by 1.93 and 2.09, with 1.97 being close to a best estimate. **Table 15** displays the range of salinity allowed by this range of m values for sample A1877.8V.

Table 15. Salinity Estimated from Resistivity on Sample with Known Porosity

Sample	Resistivity (Ohm-m)	Porosity (%)	m	Pore Brine Resistivity	Salinity (PPM)
A1877.9	8.901	35.5	1.93	1.21	5133
A1877.9	8.901	35.5	1.97	1.16	5366
A1877.9	8.901	35.5	2.09	1.03	6133

For sample A1999.0V a range of possible porosities must be assumed (**Table 16**). For these deeper sands, 32% to 40% adequately bounds the porosity, and 38% is an approximate best estimate.

Table 16. Salinity Estimated from Resistivity on Sample with Unknown Porosity

Sample	Resistivity Ohm-m	Porosity %	m	Pore Brine Resistivity	Salinity PPM
A1999.0V	3.48	0.4	1.93	0.594	11007
A1999.0V	3.48	0.38	1.97	0.517	12860
A1999.0V	3.48	0.32	2.09	0.322	21640

It is possible that pore water salinity is very low. Even the highest estimated value is only 2/3 that of typical ocean water. The most reasonable value is less than 1/3 of typical ocean salinity. Pore water at 1999 ft appears to be about twice as saline as water at 1877.9. This could be due to differences in the amount of mud filtrate invasion. The sands are separated by a significant thickness of shale so the difference could be real. These low salinity values are consistent with salinity estimated from a water sample extracted from an Ugnu sand at 1260 ft. These low values can produce at most only minor modifications in the zone of hydrate stability that was assumed for this project.

7.2.3 Fresh-State Shale Samples

Shale samples were cut from the core at 1800 ft and 2030 ft. At each depth samples were taken parallel to bedding, perpendicular to bedding and at 45° to bedding. These three orientations allow a complete set of elastic constants to be determined from velocity measurements in a layered media. **Table 17** provides a summary of the resistivity measurements at 800-psi confining stress. These were measured in their recovered state.

Table 17. Resistivity of Shale Samples at Three Orientations Relative to Bedding

Sample	Resistivity Ohm-m 800 psi	Resistivity Ratio Parallel to Perpendicular
1800 parallel	3.26	0.542
1800 45°	3.32	
1800 perpendicular	6.02	
2030 parallel	3.25	0.429
2030 45°	3.14	
2030 perpendicular	7.57	

Resistivity parallel to bedding is remarkably consistent. The value of 3.3 Ohm-m is very close to that measured on the fresh-state sand sample from 1999 ft (3.5 Ohm-m). For a layered media, resistivity parallel to bedding is always minimum and that perpendicular is maximum. For the sample from 2030 ft the 45° orientation sample has a resistivity slightly less than the parallel orientation. This is most likely experimental error. There is about 20% difference in the vertical resistivity measurements. The average ratio of parallel to perpendicular resistivity is 0.49.

7.2.4 Conclusions – Resistivity in West Sak Formation

West Sak sands are saturated with fresh brine probably with salinity less than 10,000 ppm. The fresh-state samples showed that shale and sand zones are not strongly distinguishable by their resistivity measurements. The cementation exponent mostly ranges from 1.8 to 2 with the majority of the samples between 1.9 and 2. This is higher than many unconsolidated samples. The thin, hard cemented zones either have anomalously high or low values of m. In all cases measured, they are much more resistive than the unconsolidated sands they are embedded in.

8. NMR Measurements

8.1 Introduction

NMR logs were measured on 49 plugs from the Ugnu formation and 46 plugs from the West Sak recovered from zones identified as sands by well site geologists. These sands are potential reservoir rocks in the cored section. On samples taken from permafrost zones in the Ugnu formation, measurements were made on recovered-state samples both in frozen and after they were allowed to thaw. Measurements were also made on cleaned, dried and resaturated samples. For samples from the West Sak, only resaturated samples were measured. For the Ugnu samples, four samples were measured frozen at a temperature of approximately -5°C. All four of these samples were also measured at room temperature after thawing. Three of the four were also remeasured after resaturation. A total of 45 recovered state plugs were measured after thawing. Of these, 17 were also measured after resaturation. Four Ugnu samples were only measured after resaturation.

Sands in the Ugnu section were observed to be completely unconsolidated after they were cleaned and dried. Sample porosities were at the upper range of porosities typically observed in sand packs. This indicates that even physical compaction has not been completed. When frozen, the sands had the appearance of hard rocks. This suggests the ice is acting either as a cementing agent or providing a structural framework for the grains. Ice acting as part of the frame would have tended to preserve the sands at a higher porosity, and is consistent with very high measured porosity of the samples. Sands in the West Sak were also unconsolidated, except for the deepest zones. They were slightly less porous than Ugnu sands.

8.2 Procedures and Sources of Error

Interpretation of NMR data from the Ugnu proved to be much more difficult than expected. A primary reason is that differences between thawed and resaturated decay spectra were much greater than anticipated. At this time, no model has been found that explains the differences via a well supported physical mechanism, although possible explanations have been investigated.

Some of the interpretation complexity is related to the unconsolidated nature of the samples. It does not appear, however, that all features and differences of the decay spectra can be explained by the consolidation state of the samples and the difficulty in handling such samples. It is possible that some aspect of the experimental procedures produced the effect. It has been suggested that the drying process (Kleinberg, private communication) could produce some of the differences. Other procedures have been carefully reviewed and samples with known properties were measured using the same procedures by a different investigator than the original measurements. This review and calibration test found no error in the other procedures, but until a completely satisfactory theory for the observations has been found, an unidentified experimental effect cannot be completely discounted.

Handling and measurement of unconsolidated samples present special problems. All stages of preparation are more difficult, there are more sources of error in handling, and measurements are more prone to error and more ambiguous in meaning.

The Ugnu samples were cut from frozen core with cold 20% KCl brine. This brine had approximately the same salt content as the planned formula for the drilling mud. Later changes to the drilling mud resulted in lower brine content during the 2003 season. The same plugging procedure was used for the West Sak formation except the core was not hard frozen. To keep the samples intact during measurement, they were frozen (if not already frozen), wrapped in Teflon tape and screened with two steel screens at each end. (These screens had to be removed before NMR measurements.) Dimensions of each sample were measured with calipers before they were wrapped and screened. This measurement is the only direct measure of bulk volume of the sample. Volumes and weights of all wrapping and screening materials were measured and tracked to provide information needed to correct measurements made on the wrapped and screened samples.

Samples were cleaned and dried to measure permeability and porosity. Drying was done in a low-temperature vacuum oven. Porosity of a sample is defined as the ratio of its pore volume to its bulk volume. There are multiple sources of error and ambiguity in this measurement. He pore volume was measured on cleaned and dried samples at three confining stresses (800, 1200, and 1800 psi). For samples from the Ugnu and to some extent the West Sak, this is greater confining stress than they experienced subsurface. This measurement was to quantify pressure dependence of porosity and permeability and to obtain an estimate of bulk modulus of the sample. For these samples pore volume measurably decreases with increase in confining pressure. The unconsolidated samples are not completely elastic so there is some irreversible change in pore geometry introduced by the measurement process. An independent measure of pore volume was obtained from the NMR measurement. This was performed at ambient pressure. (The system in the laboratory will allow NMR measurements under confining pressure, but those measurements are much more time consuming and were left for follow-up studies.)

Grain volume was measured on cleaned and dried samples in a high pressure porosimeter. For unconsolidated rocks at confining stresses under consideration, grain volume can be considered constant. Bulk volume of the samples can be computed from the sum of grain and pore volume. This bulk volume along with pore volume measured at a given confining pressure provides the best measure of cleaned and dried porosity at that confining stress. Unless there is sample loss, this bulk volume underestimates bulk volume of the frozen and thawed recovered state samples, as well as resaturated samples when at ambient stress.

There are two different sources for underestimation of bulk volume. The first is that bulk volume is a function of confining stress. This can be corrected from measurement of bulk modulus. The more serious problem is that ice appears to have acted (at least to some extent) as part of the rock frame. That could make bulk volume of the rock in the frozen state greater than the sum of pore and grain volume measured on cleaned and dried samples even after correction for compression due to stress. The previous considerations lead to small uncorrectable systematic errors in the NMR porosity of thawed samples and frozen samples.

Another source of error in measured NMR plug porosity is sample loss. The steel screens need to be removed from each sample before it is measured. Even with extreme care, removing the screens sometimes causes a loss of pore fluid and grains. There is no effective way to quantify this loss. Experimental procedures were conducted to minimize this loss.

Another source of error in NMR porosity was the saturation state of the samples. For resaturated samples there is always a possibility they did not achieve 100% saturation in the saturation cell. For consolidated samples, measuring a before and after weight will check this.

Pore volume is an uncertain percentage larger than stressed pore volume, so the only check is qualitative. Fines can also be lost during saturation, which further confuses the situation.

Saturation state of thawed samples is an even more difficult problem. These samples started as some mixture of water, ice and rock grains. In the case where the sample is completely grain supported, saturation state can be calculated assuming the frozen pore space was completely filled with ice or water. In this case, total pore volume V_p is given by

$$V_p = V_{Ice} + V_{wi}$$

where V_{Ice} and V_{wi} are initial ice and water volumes.

After thawing, final water volume, V_w, is given by

$$V_w = V_{wi} + V_{wt}$$

where V_{wt} is the volume of water from the ice.

$$V_{wt} = \frac{\rho_{ice}}{\rho_w} V_{Ice}$$

Densities of ice and water are given by ρ_{Ice} and ρ_w.

Water saturation in a thawed sample, S_w, is

$$S_w = V_w/V_p$$

So that

$$S_w = \frac{V_{wi}}{V_p} + \frac{\rho_{ice}}{\rho_w} \frac{V_{ice}}{V_p} = S_{wi} + \frac{\rho_{ice}}{\rho_w} S_{Ice} = S_{wi} + 0.917 S_{Ice}$$

S_{wi} is water saturation in the frozen state, S_{Ice} ice saturation and 0.917 the density ratio $\frac{\rho_{ice}}{\rho_w}$.

Measurements on frozen state samples indicated about 25% unfrozen water. This would produce a water saturation of 94% in the thawed samples. Ice provides some frame support in the frozen samples so that grains may fill a larger part of the volume in thawed samples than in frozen. That is, calculated S_w is a minimum value.

A final concern in measuring NMR pore volume is the hydrogen index of the pore fluid. Amplitude of the NMR signal is proportional to the number of hydrogen atoms in a fluid state in the instrument's measurement volume. This amplitude is converted to a fluid volume by taking its ratio to a calibration sample of known volume and hydrogen index HI. As long as saturation fluid and calibration fluid are the same, HI cancels out. In measurements on permafrost sections, the calibration fluid was a 5% by weight KCl solution. This was the same solution used to resaturate samples.

HI of brine in frozen and thawed samples is not known. Analysis of logs in adjacent wells and a water sample recovered from the core at 1265 ft just below the base of the frozen zone show

that pore water is less than 1% salt. (See **Section 9** describing the base of the hydrate stability zone.) If there is no invasion from mud, frozen brine would have a salinity less than 4% by weight assuming 25% unfrozen water in the pore space. Actual salinity could be less than 1% if over geological time scales pore water in the frozen section is in diffusional equilibrium with the unfrozen sections, or water in the clay stone zones.

Drilling mud used to drill the Ugnu was mixed with 10% KCl by weight. If there were significant mud filtrate invasion into the core, the recovered sample at 1265 ft would have been much more saline than it was. Although differential pressure driving invasion was larger in shallower sections of the well, the unfrozen section is a multi-Darcy zone while the frozen section is a low permeability zone. It is likely there was limited mud filtrate invasion in the frozen zones. The West Sak was drilled with 18% KCl mud. Low salinity of the sample from 1265 ft also implies limited mud filtrate invasion in the West Sak core.

Density of the 5% brine used as a calibration fluid for the Ugnu samples is 1.036 g/cc. This results in a calculated HI for the 5% brine of 0.984. For typical porosities measured in thawed samples, this would cause an overestimation of porosity of about half of a porosity unit. This is insignificant. The 18% KCl mud filtrate has a calculated HI of 0.9. NMR measurements on the 18% filtrate are discussed below. HI of the mud could distort the NMR logs in the West Sak since by the time logging was conducted, significant invasion into the formation would be expected.

8.3 Ugnu Formation

8.3.1 Frozen Plugs

Four frozen plug samples were measured in the NMR system. The type of NMR measurement made on the plugs is sensitive only to hydrogen atoms in the pore fluid, not to hydrogen atoms in the rock matrix or in the ice. NMR porosity measured and reported is the ratio of volume of unfrozen brine to bulk volume of the plug.

The nominal measurement temperature was -5°C. The NMR probe magnet was maintained at 85°F, and the cooled pressure vessel is inside the probe. Temperature sensors in the pressure vessel must be situated outside the NMR measurement zone, so precise temperature of the core plug was not known. A change in plumbing and location of temperature sensors in 2004 showed there is a temperature gradient of a few degrees C along the axis of the pressure cylinder. Radial temperature gradient is not known. From the data it is clear that the plug was below the freezing point of water. General considerations suggest that the percentage of frozen brine could be a sensitive function of both temperature and pore geometry.

The four frozen samples have very similar NMR responses. **Figure 45** shows the decay curve for the sample from 465.5 ft.

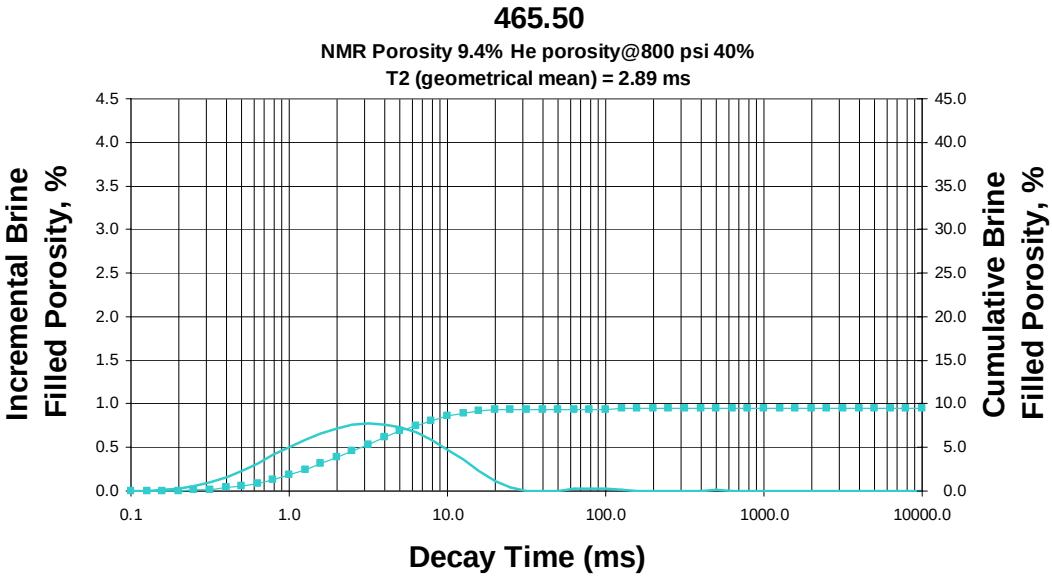

Figure 45. Typical frozen plug NMR response

All four of these decay curves are presented in **Appendix C**. The cumulative porosity curve above (curve with square symbols) shows the sum of all pore volumes in porosity units from 0.1 ms up to each decay time shown. The incremental saturation curve (curve without symbols) displays pore volume in porosity units associated with each decay time. All curves are single mode with slightly more pore volume on the faster decaying (smaller pore) side of the mode. This sort of decay spectrum is generally associated with pore size found in shale. That size identification assumes a certain value range for surface relaxivity. Correlation to permeability discussed below suggests that effective surface relaxivity of these sands may be unusually large and variable, so pore size distribution represented here may be larger than first examination would suggest.

NMR responses of the plugs compare reasonably well with measurements made in the laboratory on frozen whole core using a CMR by Robert Kleinberg (see **Appendix D**). **Table 18** summarizes data for frozen plugs and comparison to CMR data.

Table 18. Comparison of Bench Top Plug NMR Measurements to CMR Measurements

Plug Depth, ft	NMR Frozen Porosity, %	Plug T_{2gm}, ms	Plug He Porosity 800 psi, %	CMR Depth, ft	CMR Porosity, %	CMR T_{2gm}, ms
299	9.8	5.48	42.4	296.93	10.6	0.9
465.5	9.4	2.89	40	464.33	4.1	1.51
1011	11.6	1.95	31.6	1011.76	14	3.93
1117.6	7.1	4.15	37	1117.3	5.7	1.4

There is some deviation between CMR whole core measurements and plug measurements. Differences of this magnitude are most likely due to different volumes of investigation combined with differences in NMR processing. Some differences may be due to temperature variations. The CMR core measurements sampled considerably more frozen zones than did the plug study. It shows greater variability than might be inferred from the four frozen plug samples. The most

significant part of the variability is in the percent of unfrozen brine. The CMR measurements show many zones with a lower percentage of unfrozen material than the four plug samples. Median porosity for zones measured by CMR is 5%. This includes both sands and clays. Mud and clay stones on the CMR log tend to have a higher porosity than sands, but it is not as distinct as might be expected.

Comparison of NMR decay spectra on frozen samples with measurements made on unfrozen samples leads to conclusions about how water and ice are distributed in the pore space. There are many conceivable ways in which brine and ice could be distributed in the rock. Some of the simplest are: 1) large pores are completely frozen and small ones unfrozen; 2) all pores contain the same percentage of frozen and unfrozen water; 3) ice is pore filling with a layer of liquid between the ice and pore walls; 4) ice is pore lining with unfrozen brine in the center of the pores. Under reasonable assumptions NMR response for each of these cases can be studied and shown to not fit the observed data.

8.3.2 Small Unfrozen/Large Frozen

In examining decay spectra of the frozen samples, in each case there is a time T_{max} beyond which there is no signal. In a model in which a small pore contains only liquid and a large one only ice, cumulative porosity for time less than T_{max} in the saturated decay spectrum should be equal to frozen porosity. **Table 19** shows T_{max} for each frozen sample and cumulative porosity up to the decay time T_{max} for corresponding thawed and resaturated spectra. Although neither of these probably exactly represents the frozen sample with all ice melted, they are close enough to allow conclusions.

Table 19. Comparison of NMR porosity in frozen plugs to predicted porosity with cutoff model

Plug Depth, ft	NMR Frozen Porosity, %	T_{max}, ms	Thawed Porosity decaying faster than T_{max}, %	Resaturated Porosity decaying faster than T_{max}, %
299	9.8	40	28.8	10.1
465.5	9.4	30	22.3	14.8
1011.0	11.6	10	17.1	
1117.6	7.1	40	18.4	17.8

In all cases thawed samples have significantly more pore volume in pores smaller than T_{max} than there is porosity in frozen samples. To a lesser extent this is also true of the resaturated samples. **Figure 46** shows porosity distribution for sample 465.5 for the frozen, thawed, and resaturated states.

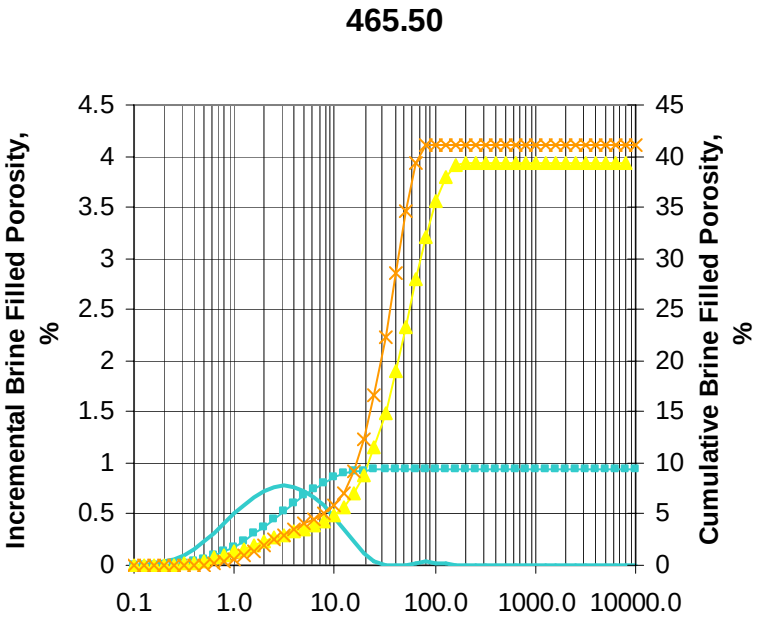

Figure 46. Porosity distribution for frozen (aqua), thawed (orange), and resaturated (yellow) measurements

The cumulative frozen curve (aqua squares) has more porosity at times less than 10 seconds than the cumulative resaturated curve (yellow triangles) or the cumulative thawed curve (orange crosses). That is, there is less total porosity in the frozen sample than in the small pores of the water saturated sample, but faster decaying parts of the frozen sample contain more porosity than water saturated samples. *The most straightforward interpretation of these observations is at least some pores contain both water and ice.* **Appendix C** includes comparable plots for the other samples for which all three saturation states were measured.

8.3.3 Constant Percentage of Ice and Water

Examining this case along with the last two requires quantitative modeling. Sample 1117.6 was used here since for this sample there is only a slight difference between thawed and resaturated NMR responses. **Figure 47** shows NMR response of sample 1117.6 in the frozen state. **Figure 48** shows the thawed and resaturated cases. They are almost identical. For simplicity only the resaturated curve will be used in the modeling.

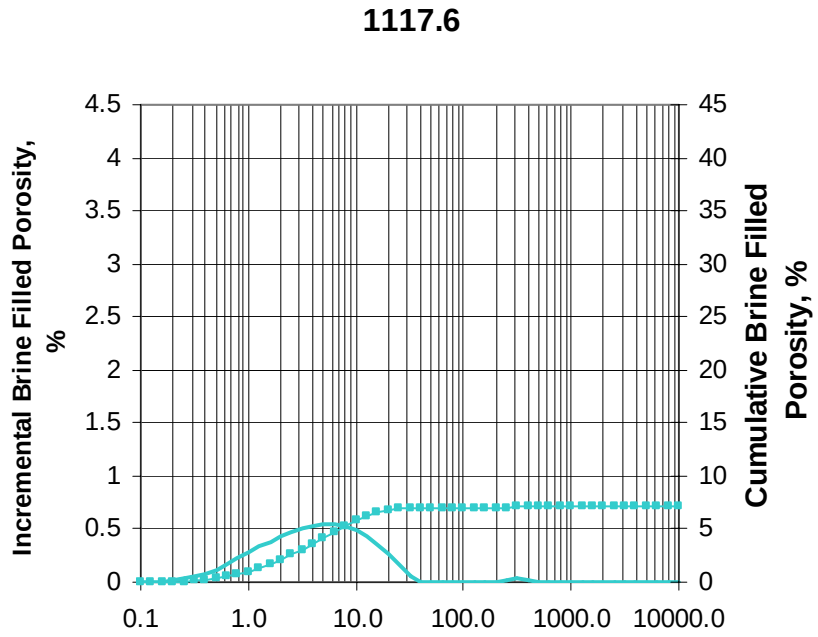

Figure 47. Frozen porosity distribution

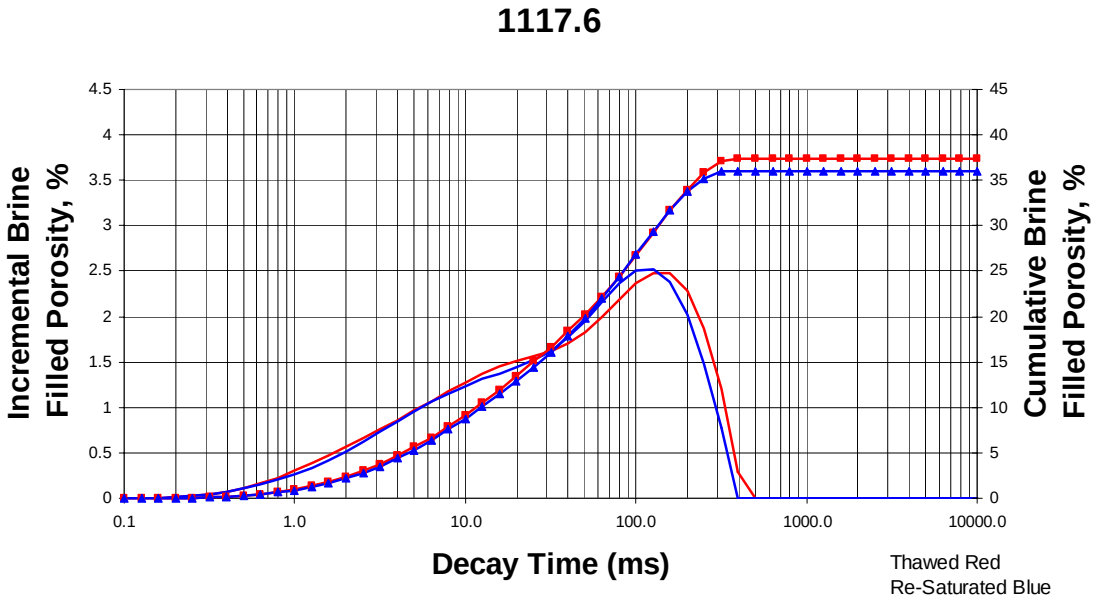

Figure 48. Thawed and resaturated porosity distributions

A weighting function was used to model pores that are partly frozen. Weighting function w(T) represents the fraction of pore volume at each decay time (pore size) T that is liquid filled. For sample 1117.6 the liquid filled porosity is about 20% of total pore volume. w(T), which was assumed to be constant for this case, equals 0.2.

For a totally liquid filled pore, time T for the NMR signal from that pore to decay is given by

$$\frac{1}{T} = \rho_S \frac{S}{V}$$

Where S is surface area of the pore wall, V is volume of fluid in the pore and ρ_s is surface relaxivity. (A good introduction and review of the basic principles of NMR as applied to rock petrophysics is found in Coates (1999).) If one assumes ice is in the center of the pore so that the liquid layer is in contact with the pore wall, and that all liquid in the pore is in fast diffusional equilibrium, then the complete surface area of the pore acts to relax the liquid volume V_L. The ice surface area S_I also forms a second relaxing surface with enclosed volume V_I and surface relaxivity ρ_I. One then has

$$V_L = w\, V$$

$$\frac{1}{T_F} = \rho_S \frac{S}{V_L} + \rho_I \frac{S_I}{V_L}$$

$$V_I = (1\text{-}w)\, V$$

To derive an estimate for S_I/V_L, one assumes both pore and ice volume are spheres of radius r_p and r_I. For this assumption

$$\frac{S}{V} = \frac{3}{r}$$

$$r_I = (1\text{-}w)^{1/3}\, r_p$$

Also assuming

$$\rho_I = c\, \rho_s$$

then

$$\frac{1}{T_F} = \frac{1}{w} T\ (1 + c(1\text{-}w)^{2/3})$$

Liquid pore volume and its decay time for each pore size can now be directly calculated from the saturated decay spectrum. The assumption of a spherical pore and ice ball is not as restricting as it might seem since deviation from this would only change c, which is a parameter that must be adjusted to fit data constraints. The frozen spectrum calculated in this way is also an approximation as it gives a spectrum in terms of a different set of exponential basis functions than the original processing.

To transform a saturated decay spectrum into a frozen decay spectrum requires that there is no porosity in the frozen spectrum for times greater than 40 ms. Examining Figures 47 and 48 shows that the 400-ms bin in the resaturated spectrum needs to be transformed to 40 ms; that is, T_F must equal 40 when T equals 400. This fixes c to be 1.16. Although relaxivity of ice is not well known, it is probably not larger than that for the rock surface so this value is suspicious. Using this value of c produces the modeled frozen decay spectrum shown in **Figure 49**.

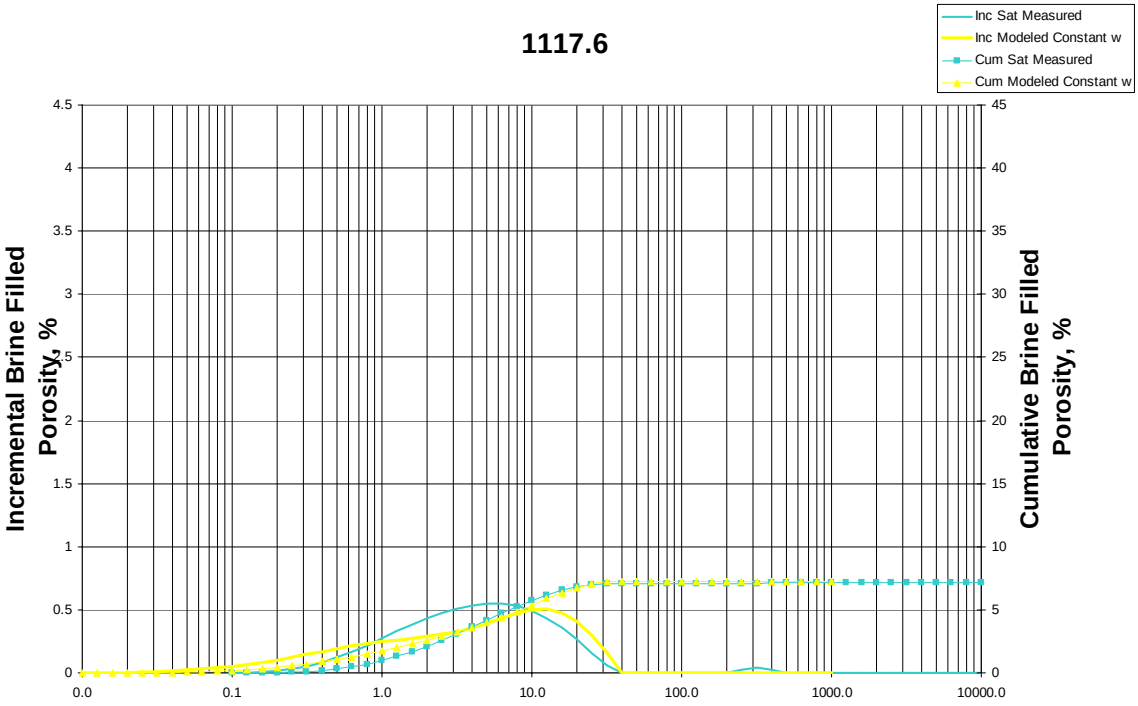

Figure 49. Comparison of measured frozen decay spectrum to modeled spectrum assuming pore filling ice and a constant fraction of liquid

It is clear that the modeled spectrum (yellow curve) has the wrong shape and is not a good approximation to the observed frozen spectrum.

8.3.4 Pore Filling Ice with Variably Weighting

Data from sample 1117.6 was again modeled for this case. To model the case of the fraction of frozen material being a continuous function of pore size, a weighting function needs to be specified. Issues in this case are similar to earlier work done to model pore saturation under the capillary displacement of water by a hydrocarbon fluid. One proposed model that seems particularly appropriate (Coates et al., 1998) has the weighting function w(T) given by

$$\frac{1}{w} = m\,T + b$$

Parameters can be determined by fixing a value of w at two relaxation times. It seems reasonable to take w=1 at 0.1 ms (the smallest pores observable are taken as completely unfrozen). In fixing the second value of w it is necessary to satisfy the constraint that w(T) convolved with the unfrozen incremental porosity distribution, giving a frozen sample porosity of 7.1%. Fixing

$$w(1000\ ms) = 0.0454$$

provides the necessary weighting function. For this choice m = 0.2193 and b = 0.9781.

Volume of liquid $V_L(T)$ in a pore class that relaxes with time T and has a saturated volume V(T) is given by

$$V_L(T) = w(T) \cdot V(T)$$

This pore relaxes at modeled time T_F

$$\frac{1}{T_F} = \rho_S \frac{S}{V_L} + \rho_I \frac{S_I}{V_L}$$

In this case ρ_I will be taken as zero since a non-zero value produces an even faster relaxation time, and modeled relaxation times are too fast even with the zero value. T_F is then given by

$$\frac{1}{T_F} = \frac{1}{w(T)} T$$

Figure 50 compares the modeled spectra to that measured; the match is poor. This figure may be slightly confusing. The clearest comparison is between the cumulative distribution curves. The modeled incremental distribution curve has its basis elements compressed into a shorter time range so, if it were resampled to have the same basis elements as the frozen sample, each resampled point would contain more porosity, and the yellow curve would be above the aqua curve.

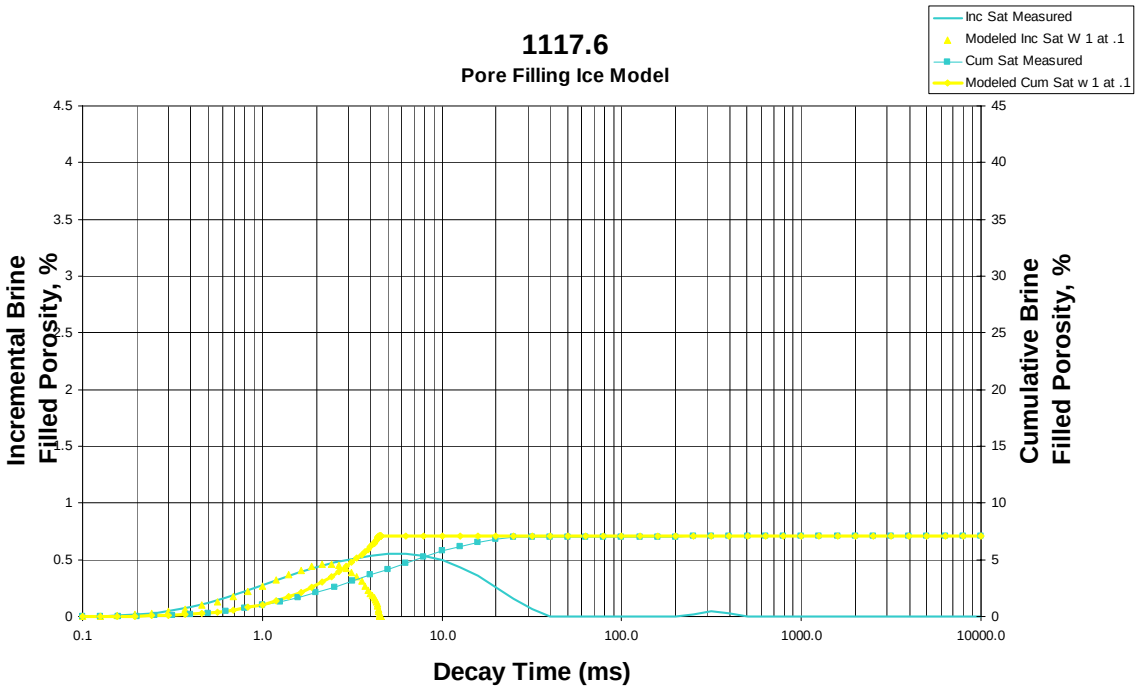

Figure 50. Continuous weighting function and pore filling ice model

8.3.5 Pore Lining Ice Continuous Weighting Function

Sample 1117.6 is again used for this case. Since saturation is the same as in the previous case with only the location of the brine being different, the same weighting function needs to be used. The brine has no contact with the rock surface so the only source for relaxation is the ice surface:

$$\frac{1}{T_F} = \rho_l \frac{S_l}{V_L}$$

To estimate $\rho_l * S_l$ it is again assumed that pore and water volumes are spherical. To match the frozen distribution requires all incremental porosities to be zero for decay times greater than 40 ms. This gives

$$\frac{1}{T_F} = \rho_l \frac{S_l}{V_L} = \frac{w^{1/3}}{c} T = \frac{w^{1/3}}{2.235} T$$

Figure 51 shows modeled distribution in this case. Again, the match is not good.

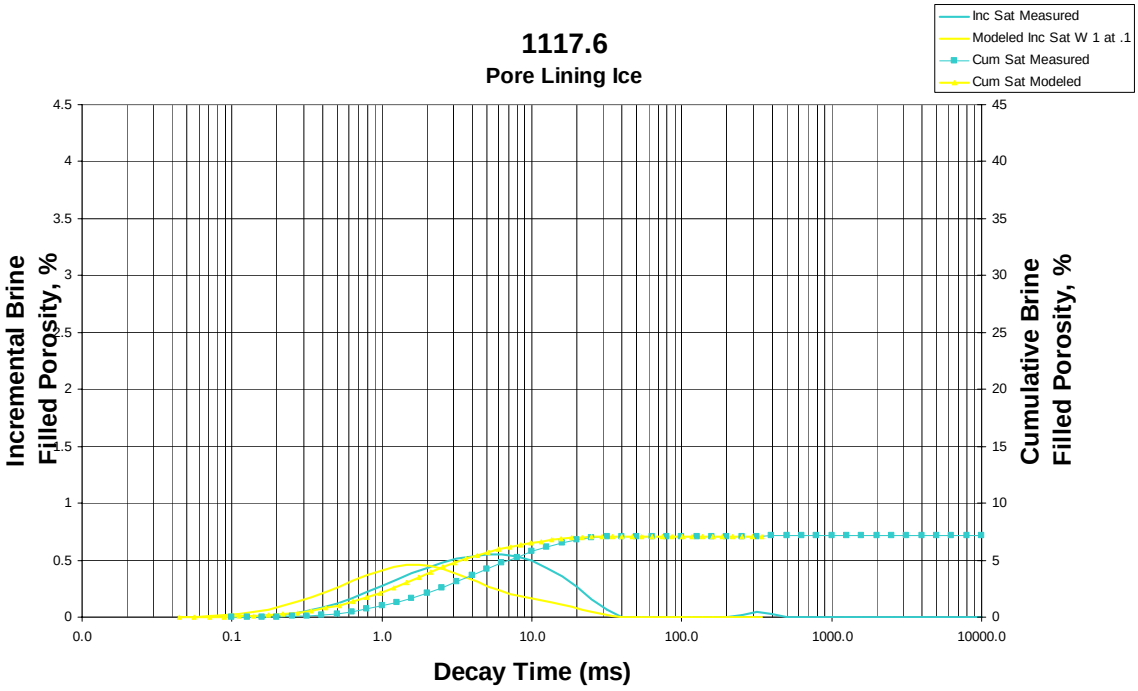

Figure 51. Continuous distribution and ice lining model

All models discussed have one common feature. Remaining liquid is assumed to be in fast diffusional equilibrium over the time of the NMR measurement. Breaking this assumption allows ice to create isolated small pores in a larger pore. Although all possible permeations and combinations of connected liquid models have not been investigated, it is unlikely that a good match to frozen NMR spectra lies in this direction. It seems more likely that the best model to fit the data will be a combination of very small pores being unfrozen along with separated unfrozen voids in the larger pores. Such models depend much more strongly on the particular pore geometry of the sample and probably depend on the history of the freezing and melting.

8.3.6 Thawed and Resaturated Sample Comparison

In planning the core analysis program, it had been thought that the closest model of the frozen samples with ice replaced by water would be recovered state samples that were allowed to

thaw. Since ice seems to form part of the frame, no real completely fluid saturated sample can have the same rock grain distribution and thus pore geometry as the frozen sample in which the ice volume is just replaced by water occupying the complete volume that ice occupied. The most obvious problem with the thawed samples is they should not be 100% saturated, although grain rearrangement should make them more saturated than the 94% saturation previously calculated assuming a rock grain supported frozen sample.

These resaturated samples were resaturated after the samples had been cleaned, dried, and measured at confining stress for permeability and porosity. The stressed measurements almost certainly modified pore geometry of the samples. NMR measurement on these samples should be the best measurements to combine with He porosity and permeability measurements.

Differences between thawed and resaturated NMR measurements are not easily understood in terms of what should be differences in pore geometry and saturation. To a first approximation thawed and resaturated samples seem to differ by a simple shift along the time axis. In seven of the fourteen samples, resaturated samples have a higher percentage of porosity located in the faster decaying part of the spectrum. As decay time is displayed on a logarithmic scale, a shift along the time axis is achieved by multiplying each bin time in the resaturated spectrum by a constant designated as the shift. **Figures 52A, 52B, 53A and 53B** show typical examples of thawed and resaturated spectra both with and without the shift in the resaturated curve.

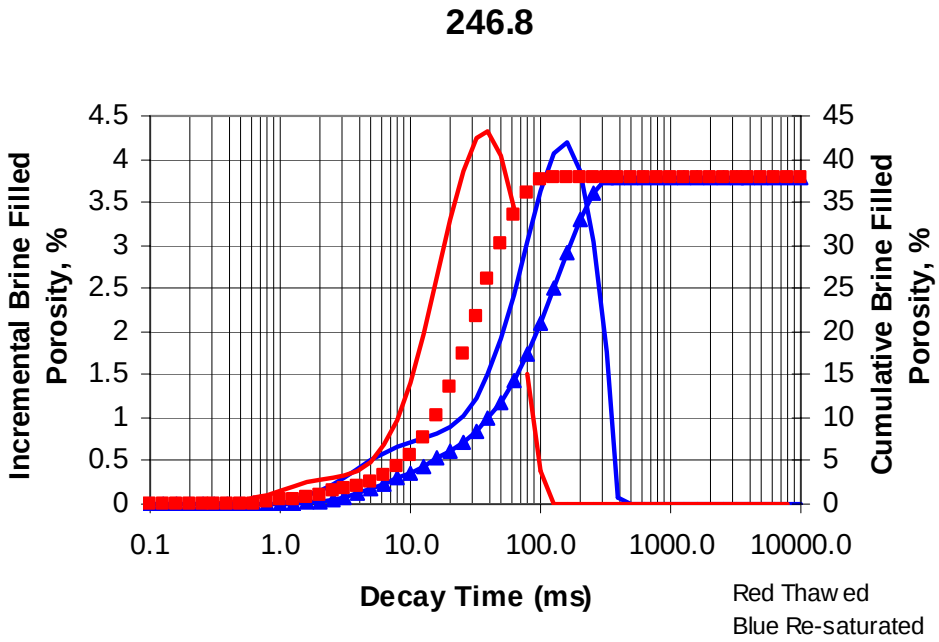

Figure 52A. Thawed sample decays four times faster than resaturated sample

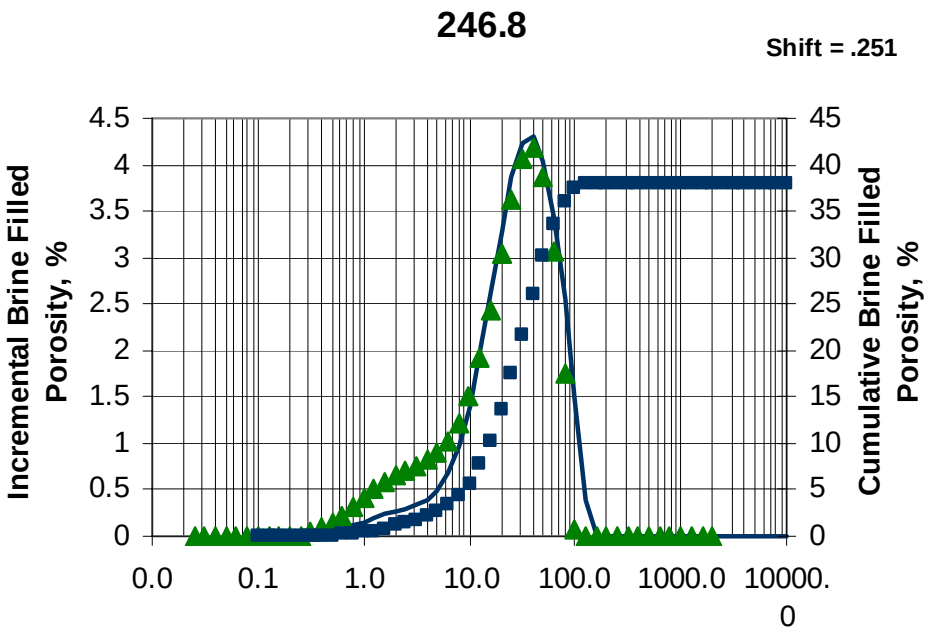

Figure 52B. Resaturated sample (green triangles) has larger percentage of fast decaying pores

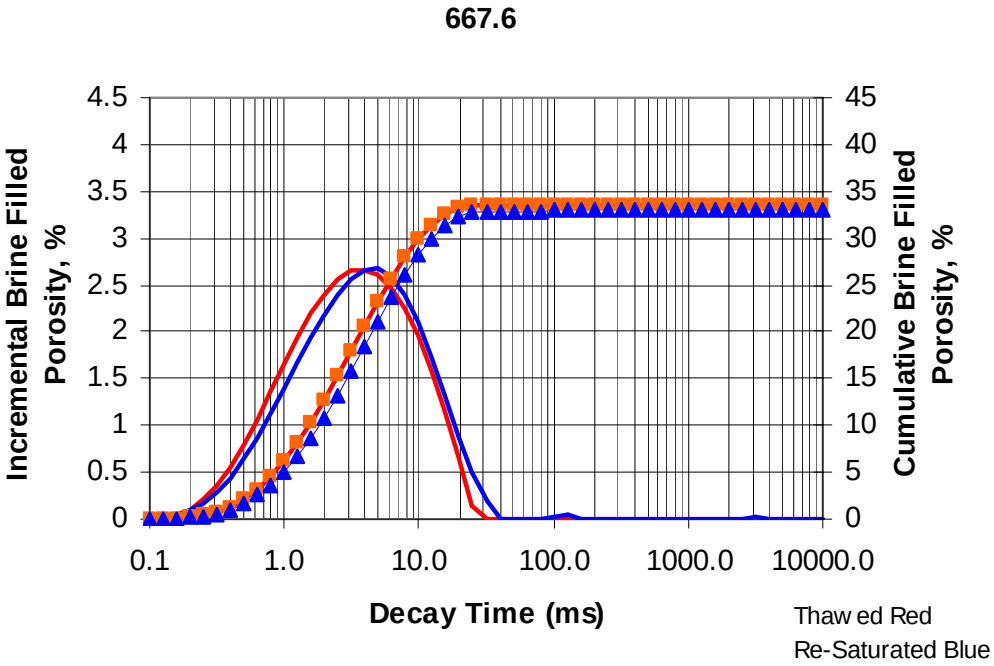

Figure 53A. There is minimal difference between two decay curves

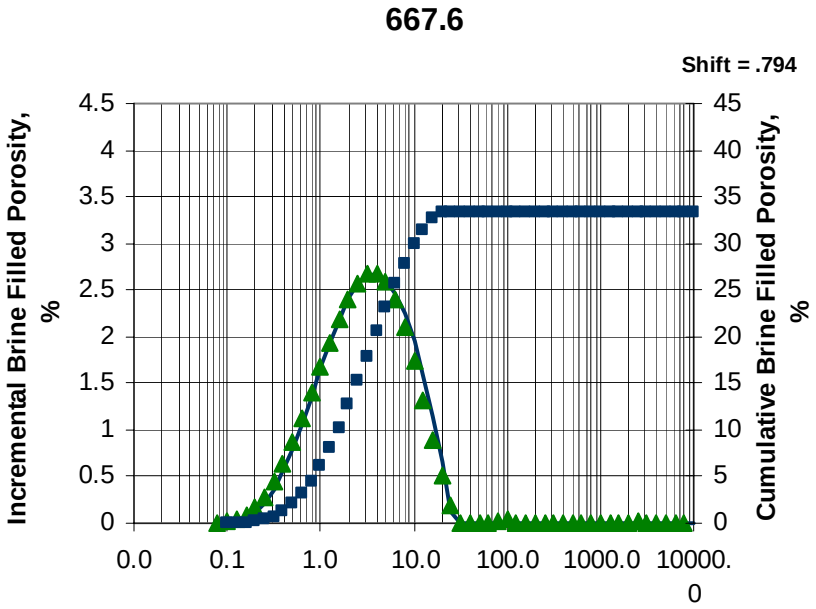

Figure 53B. After a shift, resaturated (green triangles) and thawed curves are identical

The complete set of plots of thawed and resaturated decay curves are presented in **Appendix C**. **Figure 54** plots shift value as a function of sample depth. Most significant shifts occur at shallower depths.

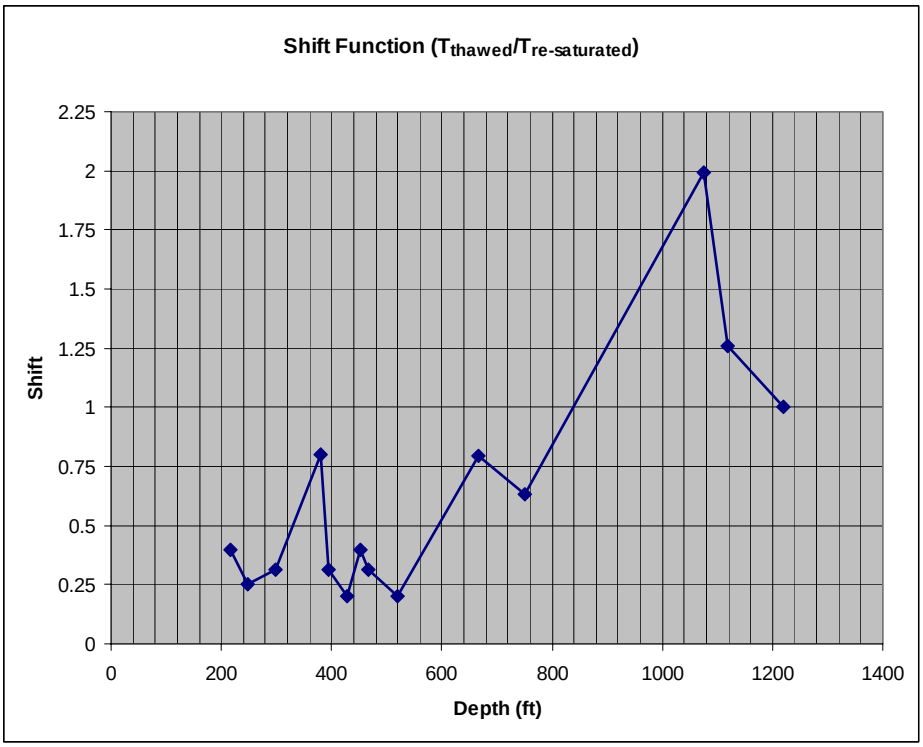

Figure 54. Identical curves have a shift of 1. Shifts between 0.75 and 1.25 are insignificant. Shifts less than 1 represent thawed samples that relax faster than resaturated samples.

As was stated, it is not clear what produced these differences. There is no obvious difference in fluid-filled porosities, although sample loss and estimates of correct bulk volume could account for a few porosity units of difference. The most obvious cause of a difference in the measurements is between the thawed measurement and resaturated measurement the sample was cleaned, dried, and subjected to 1800 psi confining stress.

Cleaning and drying could alter clays, as drying was in a low-temperature vacuum oven, not a humidity oven. Kleinberg (private communication) pointed out that, in the thawed state, expanding clays (if present) could hold more water than the same clays after drying and resaturation with a KCl solution. If clays were fairly uniformly distributed, pore-lining, and in fast diffusional equilibrium with the brine in the body of the pore, this mechanism would appear as equivalent to an increase in surface relaxivity.

In unconsolidated samples, subjection to confining stress causes irreversible rearrangement of grains and should cause a small irreversible porosity loss. Grain rearrangement is a reasonable explanation for the observed increase in percentage of faster decaying pores in some of the resaturated samples. The observation that it is more common in the samples from shallower depths also supports this hypothesis. Confining stress rearrangement though would have been expected to cause the resaturated samples to relax slightly faster. Sample 1117.6 (see Figure 48) has a resaturated decay curve that is slightly faster than the thawed curve. This is what might have been expected to be observed in all cases.

If one accepts that the change in the fast relaxing part of the spectrum is explained as a stress effect, then the rest of the difference (i.e., a shift to slower relaxation) can be produced by reducing surface relaxivity of the resaturated pore walls by a factor equal to the shift. It is tempting to ascribe this to the cleaning and drying process. Under some conditions, pore-lining clays (since they increase surface area) can mimic a change in surface relaxation. A petrographic study combined with further NMR measurements and experiments using various drying methods could help determine if this is an appropriate mechanism.

As was seen in modeling frozen sample response, a partially saturated sample and or one with some ice in the pores can give the appearance of having an increased surface relaxivity. This is another possible source for the observed effect. A constant weighting function model with an ice surface relaxivity produces a shift to faster times without distorting curve shape. Saturation is determined by the weighting function. Once a saturation is chosen, the rest of the shift is supplied by ice relaxivity. **Figure 55** shows a model that produces the correct shift for sample 465.5. Modeled data are plotted as a green curve. For this model

$$w = 0.9$$

$$\rho_l = c\ \rho_s$$

$$c = 1.981$$

465.5

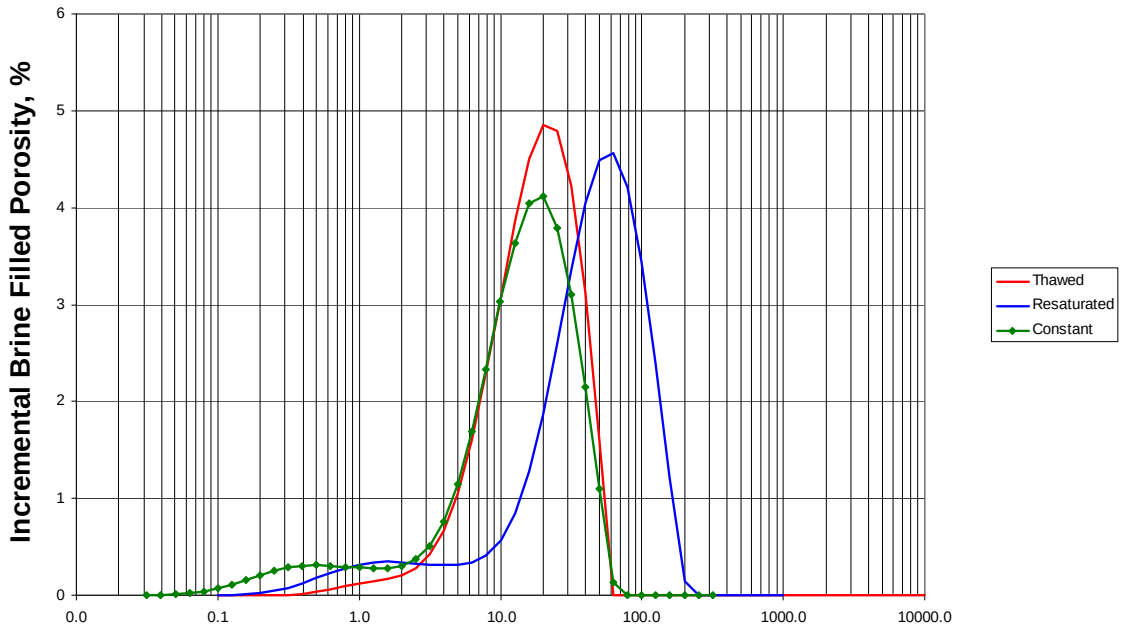

Figure 55. Shift produced by assuming 10% ice at center of each pore

Although this model successfully reproduces the shift it is physically suspect due to the required size of the ice surface relaxivity relative to the surface relaxivity of the rock.

Another type of model would be to use a variable weighting function. This class of models has

$$\frac{1}{w} = m\,T + b$$

The thawed sample has to be close to 100% saturation. This limits the range of possible parameters. For this study w=1 is forced at 1 ms decay time and w=0.1 at 1000 ms. This produces a thawed sample porosity of 28%. **Figure 56** shows models for c=0, c=0.2, and c=1. None of them produces a satisfactory map from the resaturated measurement to the thawed measurement.

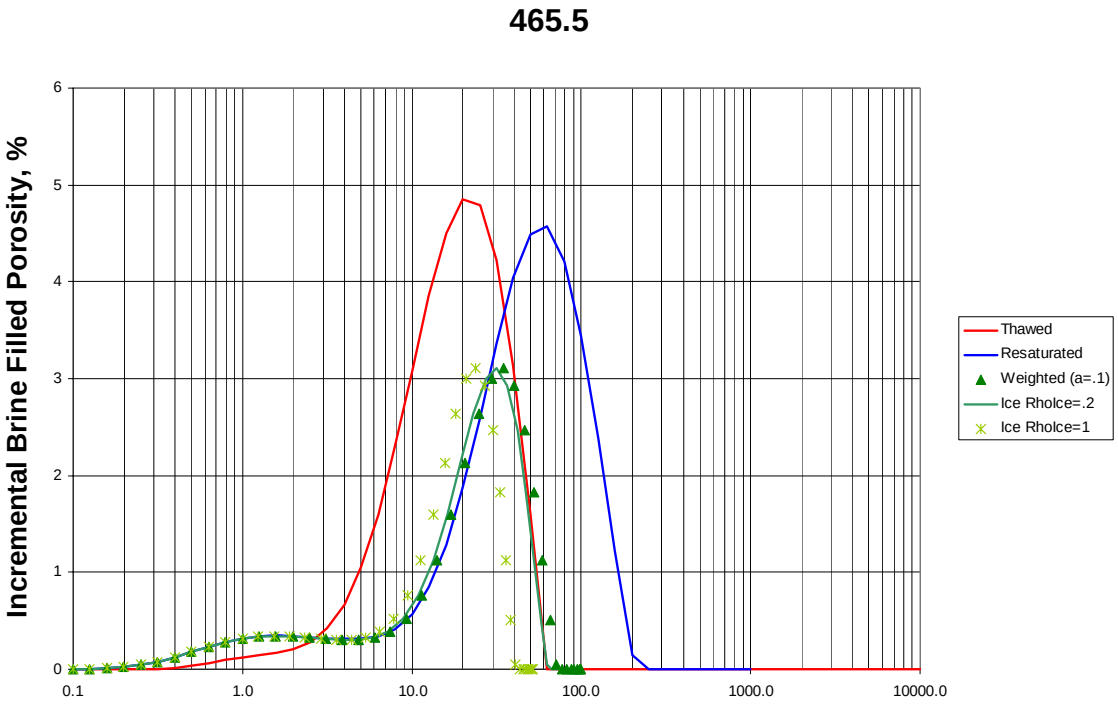

Figure 56. None of the variable weight models successfully transforms a resaturated measurement to a thawed measurement

8.3.7 Ugnu Rock Typing from NMR

Traditional petrophysical rock typing is performed using capillary pressure curves. Well-documented correlations between a rock's NMR spectrum and its capillary pressure curve suggest that rock typing using NMR curves is also useful. Rock typing was performed using both resaturated and thawed samples. In both cases depth sorting was preserved in each rock type, although there was an attempt to place transition curve types at the end or beginning of the group. As with any typing, class types are clear but there are spectra that seem to fall between types.

Thawed sample measurements were divided into five rock types based primarily on the shape of the decay spectrum. Rock Type 1 has 16 members. Most come from the shallow part of the section. **Figure 57** shows an example of a Type 1 rock.

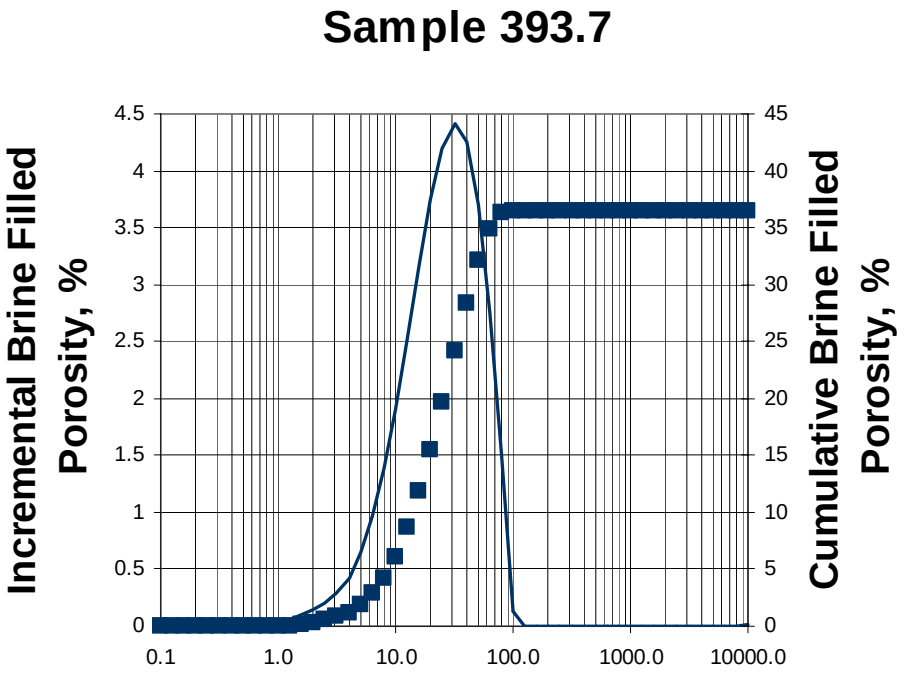

Figure 57. Example of Rock Type 1, thawed measurements

Rock Type 2 has 15 members. They seem to be approximately uniformly distributed throughout the depth range. Type 2 spectra differ from Type 1 by appearing to have a better defined fast decay mode. **Figure 58** shows a typical Type 2 spectrum.

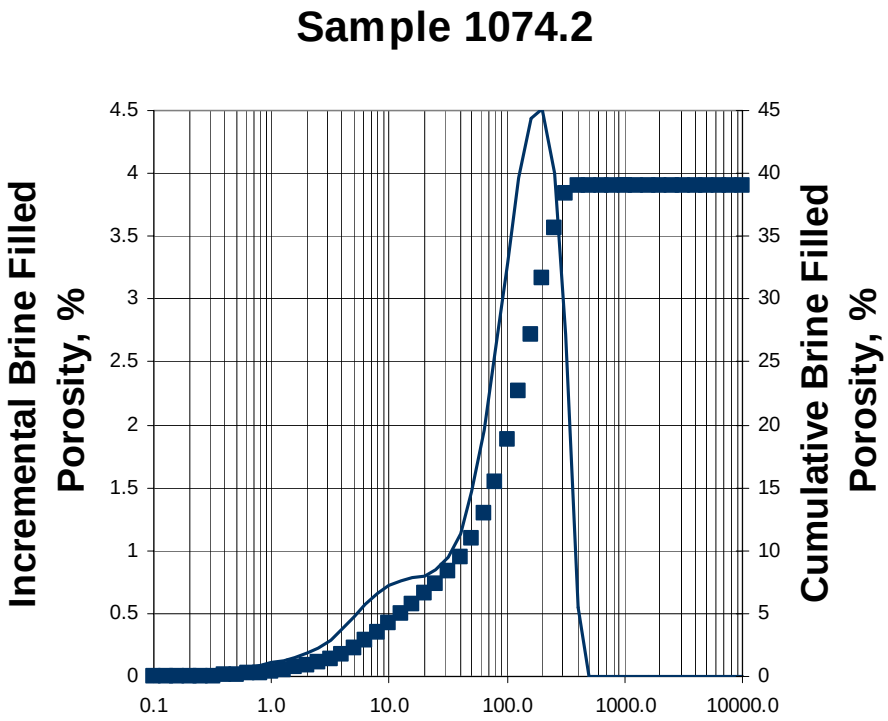

Figure 58. Example of Rock Type 2, thawed measurements

Rock Type 3 is found only in the deeper part of the section. There are nine plugs with this type. **Figure 59** shows an example.

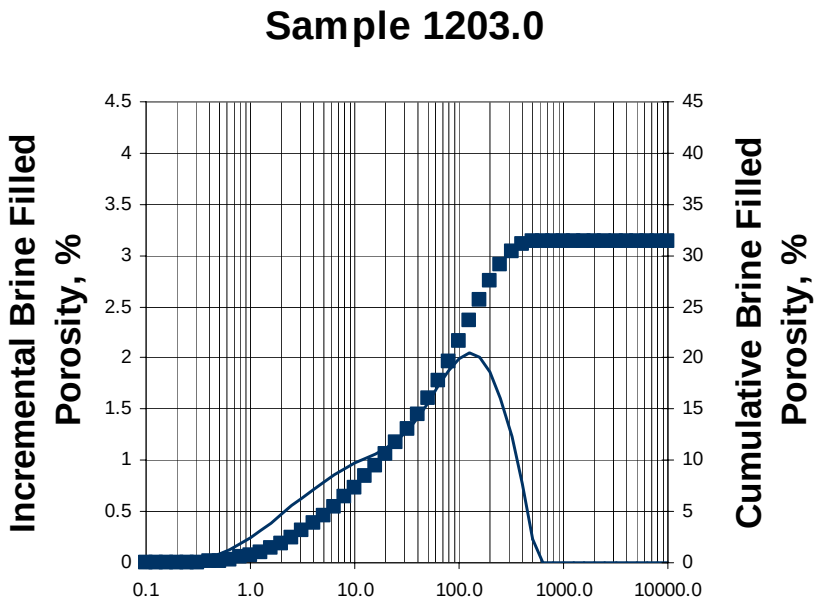

Figure 59. Example of Rock Type 3, thawed measurements

There are only three examples of Rock Type 4 and only two of Rock Type 5. Both types are found in the deeper part of the section. Rock Type 4 perhaps could have been placed with Type 1 rocks. Rock Type 5 is distinctly different from others in that it is the only one with a tail of slowly relaxing pores. It is a mirror image of the Type 3 spectrum. **Figures 60** and **61** show examples of Type 4 and Type 5, respectively.

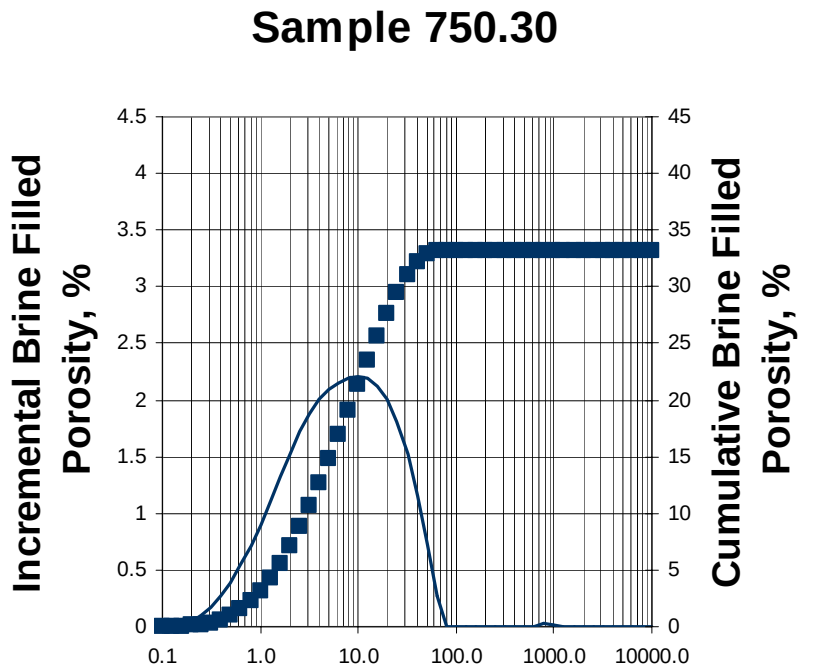

Figure 60. Example of Rock Type 4, thawed measurements

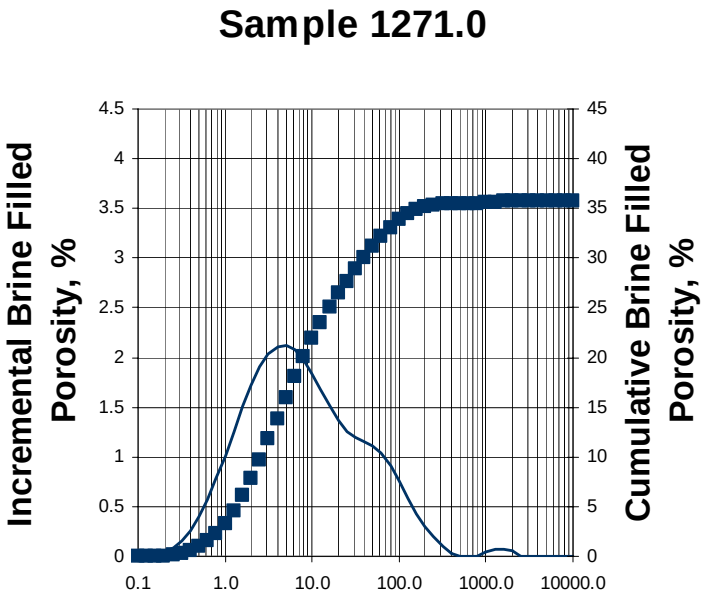

Figure 61. Example of Rock Type 5, thawed measurements

Resaturated measurements have the same rock types except for Type 5. There are 11 Type 2 spectra, three Type 1 spectra, two Type 3, and two Type 4. Some of the differences in the percentage of the different types may be due to sampling, but there does seem to be a tendency to have better developed fast decaying pore space in the resaturated spectra. For samples measured both as resaturated and thawed, one thawed Type 1 became a Type 2. Two of the three resaturated Type 1 samples could have been called Type 2 and one Type 4, if they had not have been Type 1 in the thawed measurement. If only resaturated measurements had been available, no Type 1 rock type would have been identified.

8.3.8 Permeability Estimation

One of the primary uses for NMR logs is to provide an estimate of permeability. Core data (when available) are used to build correlations. Core permeability measurements were made on cleaned and dried samples under confining stress, and as is expected for unconsolidated rocks, permeability noticeably decreases with pressure. There is roughly a 20% decrease when confining stress increases from 800 psi to 1800 psi. The best way to build a permeability relationship would be to use NMR measurements under confining stress, but because of time constraints measurements under stress were not performed in the field. This should not be a serious problem as the most common industry practice even for unconsolidated samples is to use NMR measurements taken without confining stress.

The most natural way to build the correlation is to use samples that are as close to comparable as possible. Here that means using NMR measurements on the resaturated samples as they were made after the samples were cleaned and dried. Permeability at 800 psi confining stress has also been used. To the extent that the samples have similar elastic moduli, a correlation built using one confining stress can be translated to other stresses. Stress dependence of permeability will cause some deterioration of the correlations, however. A more serious question is the significant differences between the decay spectra of the thawed measurements

and resaturated measurements. A correlation to thawed spectra would be different than to resaturated data.

Usually very good permeability estimators can be built from NMR decay curves. There are two standard default formulas used in the NMR literature to estimate permeability k in millidarcys from an NMR measurement of porosity ϕ_{NMR} and the decay spectrum. For 100% brine-saturated samples they give very similar estimates, and a reasonably good correlation to measured permeability. The formula developed by Schlumberger uses NMR porosity as a fraction and the geometrical mean of the T_2 decay spectrum T_{GM}. Schlumberger's default formula is

$$k = 16\,(T_{GM})^{0.2}\,(\phi_{NMR})^{4}$$

When measured data are available a custom regression is often constructed. One approach that works very well is to develop a relationship of the form

$$\log k = A + B \log[(T_{GM})^{0.2}\,(\phi_{NMR})^{4}]$$

Usually such a relationship has an R^2 value somewhat greater than 0.9.

NMR data in the shallow section are anomalous in two ways. The default formula greatly underestimates measured permeability, and the custom-built regression is poor by NMR standards. On average, the default formula underestimates measured permeability by a factor of six. Such a large difference cannot be due to permeability being measured under confining stress and NMR decay not being measured under stress. In fact, NMR measurements under confining stress would only make the default estimate smaller. Using thawed spectra would have the same effect.

A much more serious anomaly is the relatively poor regression fit to the data. **Figure 62** shows logarithm of measured permeability plotted against logarithm of $(T_{GM})^{0.2}\,(\phi_{NMR})^{4}$. Also shown is the value from the default equation.

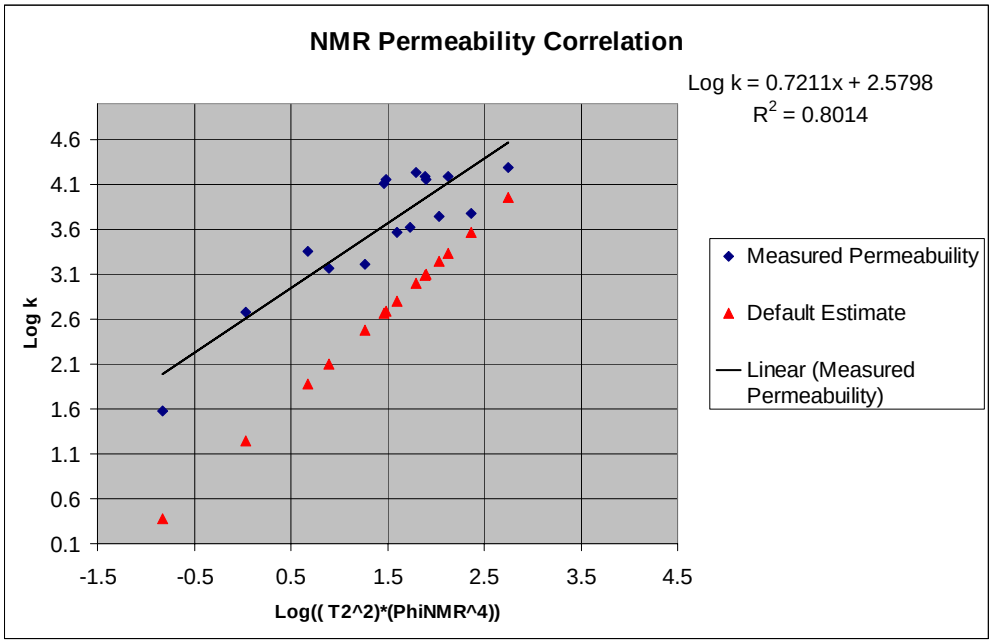

Figure 62. Measured permeability versus $(T_{GM})^{0.2}$ $(\phi_{NMR})^4$

One possible explanation for both anomalies is that surface relaxivity of the rocks is both larger than the typical rock surface, and somewhat more variable. These sediments are relatively young sediments that are sourced in the Brooks Range. They could easily have a higher percentage of paramagnetic materials which would increase their relaxivity. Pore lining clays might also produce such an effect. Follow-up work is needed on mineralogy and elemental composition of these rocks to see if this is the cause for the observations.

8.4 West Sak Formation

Since only resaturated samples were measured for the West Sak rocks, the analysis needed is much less extensive. It is restricted to rock typing, permeability estimation, and NMR response of the mud filtrate.

8.4.1 West Sak Rock Typing

NMR rock types seen in the West Sak are very similar to NMR rock types in the Ugnu. The differences are there are no Ugnu Type 1 spectra and a new rock Type 6 is introduced to account for low porosity cemented sandstones. Bench-top measurements were made on 46 resaturated plugs from the Ugnu. For two of the samples, the data seem corrupted so only 44 have been included in the study. All samples were taken from sandstone formations. With the exception of the tightly cemented samples, all are potential reservoir rocks. There were 16 Type 2 samples, 13 Type 3 samples, five Type 4 samples, six Type 5 samples, and four Type 6 samples. The Type 2 and Type 3 classes form a continuum so it is a subjective decision on where to place the boundary. A complete summary of decay spectra arranged by depth is presented in **Appendix C**.

Figure 63 shows an example of a decay spectrum that is clearly Type 2 and **Figure 64** one that is a transition between Type 2 and Type 3.

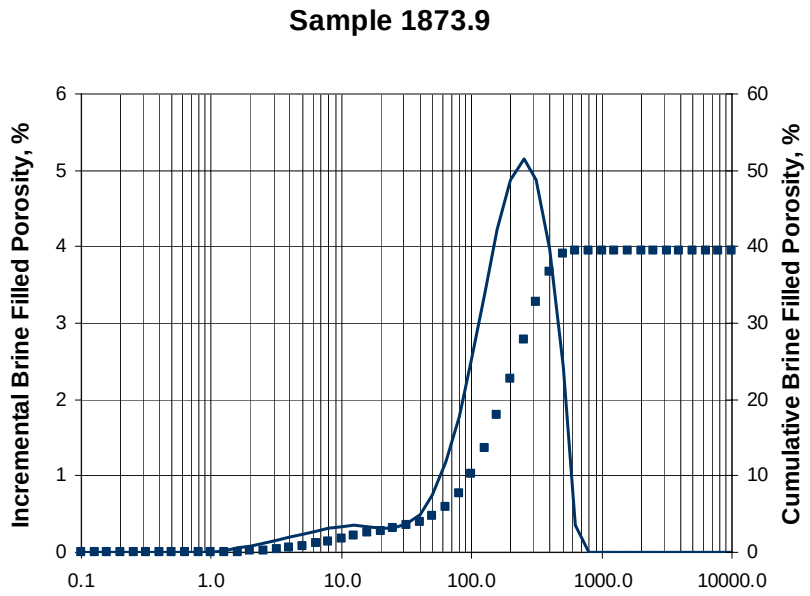

Figure 63. Example of Type 2 decay spectrum

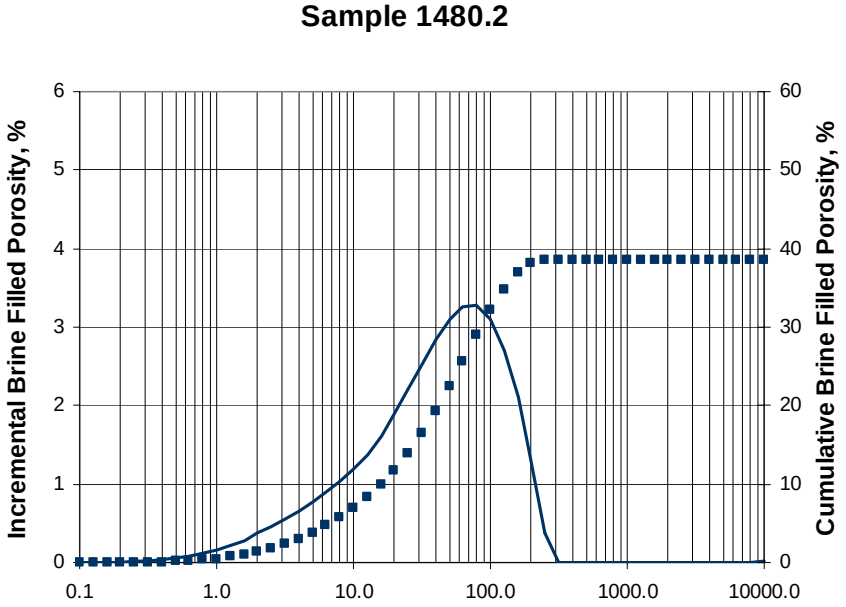

Figure 64. This sample was classified as Type 2 but could have been called Type 3

A typical Type 3 spectrum is shown in **Figure 65**.

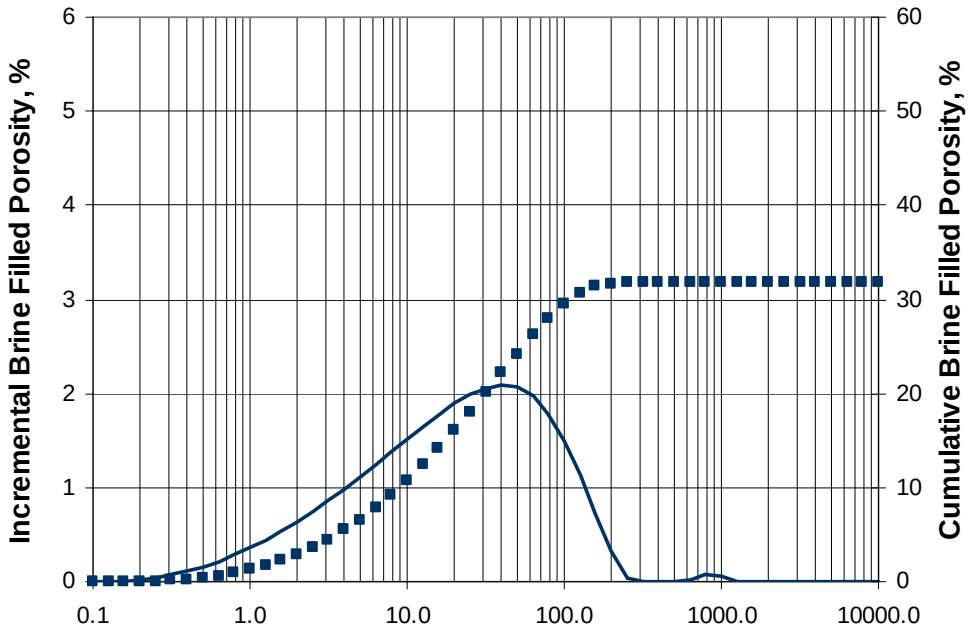

Figure 65. Example of Type 3 decay spectrum

The distinction being drawn between Type 2 and Type 3 spectra is in Type 2 rocks small and large pores have at least some hint of forming a bi-modal distribution, while in Type 3 there is no break to separate the fast decaying tail from slower decaying pores. In both cases there is no slow decaying tail made up of larger pores.

Type 4 rocks have a more symmetric spectrum (**Figure 66**).

Sample 2313.1

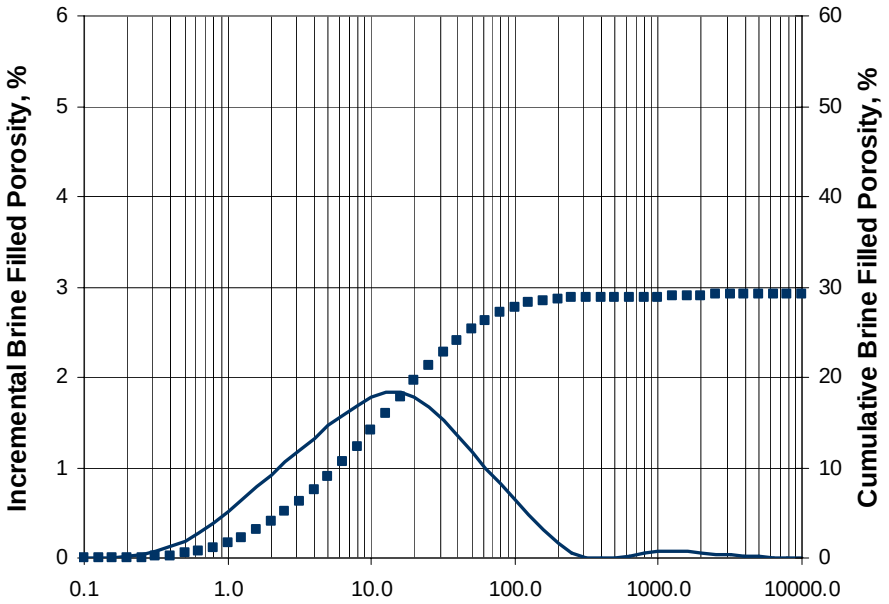

Figure 66. Example of Type 4 decay spectrum

Type 5 spectra have a have a slow decaying tail. They are essentially a mirror image of Type 3 rocks. **Figure 67** shows a typical Type 5 spectrum.

Sample 1438.7

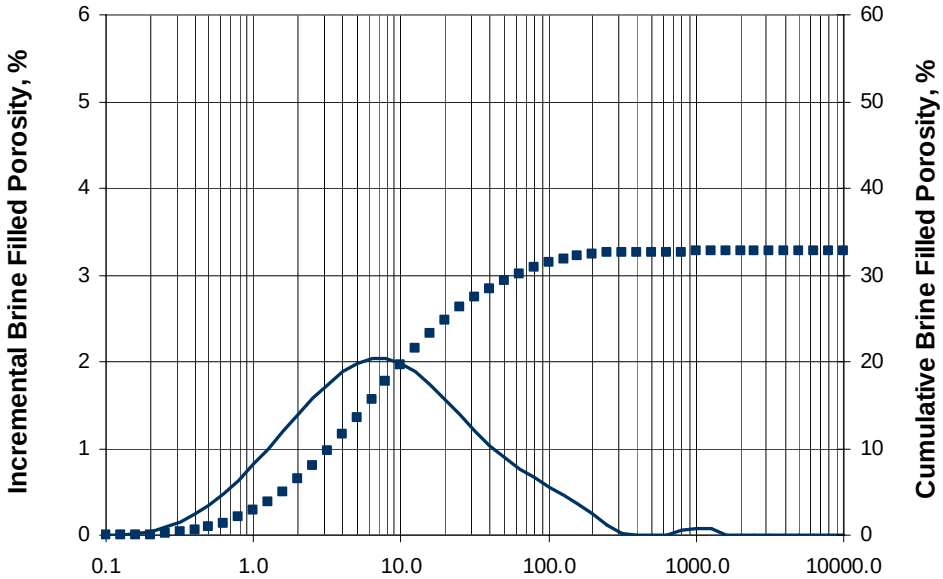

Figure 67. Example of Type 5 decay spectrum

The tightly cemented samples are different from any other sand encountered in the Hot Ice No. 1 well. They are low to very low porosity and have permeabilities well under a millidarcy. They are the only formation seen that exhibited signs of extensive chemical diagenesis. **Figure 68**

presents an example of their spectral type. The large pores in this sample probably do not form a connected set.

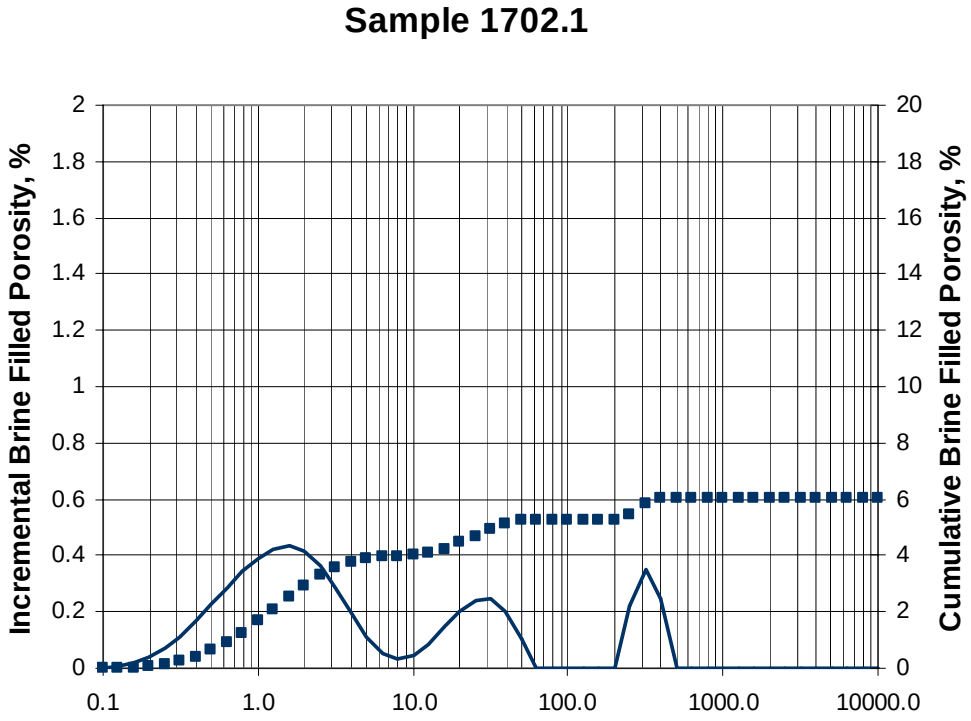

Figure 68. Rock Type 6 represents an anomalous tightly cemented formation

8.4.2 Permeability Estimation

West Sak samples seem to form a better-behaved set than Ugnu samples. A small modification in the Schlumberger formula provides a very good permeability formula. For this case porosity as a fraction of ϕ at 800 psi has been used rather than NMR porosity due to the uncertainty in NMR porosity introduced by not having a sufficiently accurate bulk volume. Permeability, k, is in millidarcys and the geometrical mean T_2 T_{2gm} is in milliseconds. The permeability formula

$$k = 50\ (T_{2gm})^2\ \phi^4$$

provides an excellent match (R^2 = 0.95) to measured data (**Figure 69**). It differs from the Schlumberger formula by having a leading factor of 50 rather than 16. This difference can be explained by assuming surface relaxivity of West Sak sandstones is 1.77 times the average surface relaxivity in the rock sample set that was used to establish the default formula. The four lowest permeability samples are Rock Type 6.

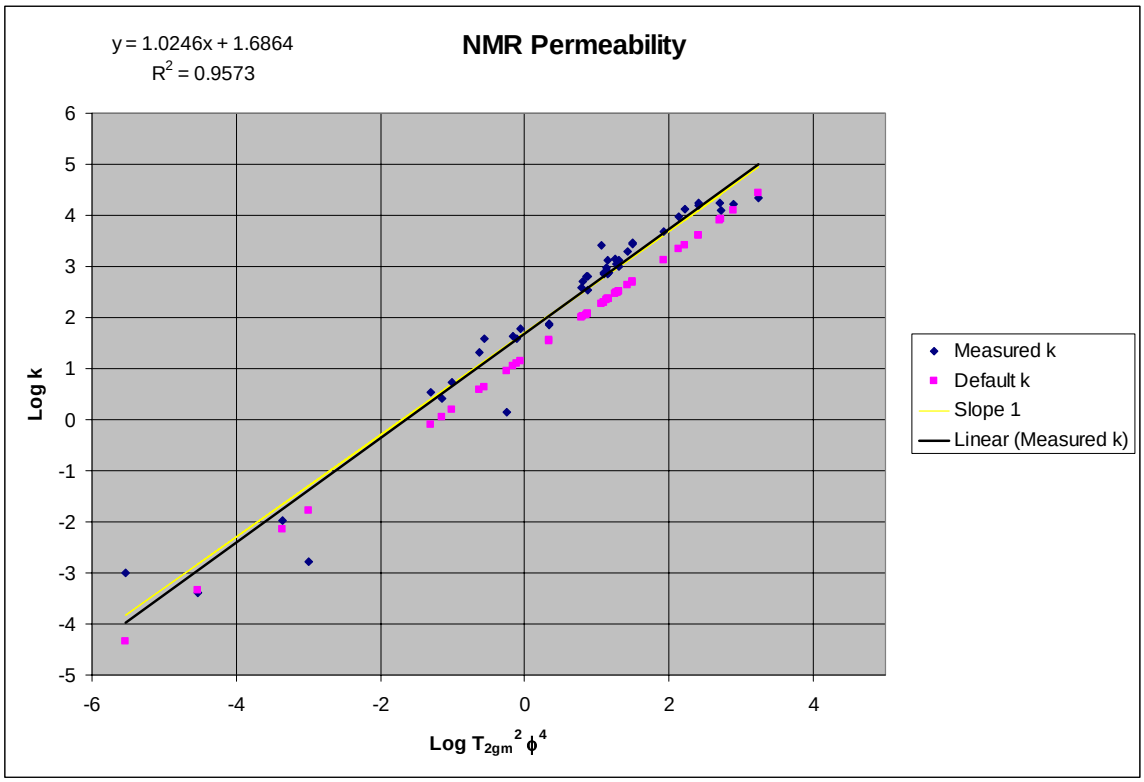

Figure 69. Permeability at 800 psi versus $(T_{2gm})^2\ \phi^4$

Data in Figure 69 fit a linear regression very well. The yellow line, which is almost identical to the regression line, is based on the formula $k = 50(T_{2gm})^2\ \phi^4$. Permeability is in millidarcys, porosity is expressed as a fraction and time is in milliseconds.

8.4.3 Mud Filtrate

Mud filtrate relaxes somewhat faster than fresh water and has a smaller hydrogen index mainly due to its 18% KCl concentration. Its density was 1.107 g/cm^3. Decay of both fluids can be fit by a single decaying exponential. Distilled water samples measured at the laboratory temperature of near 20°C had an average decay time constant of 2630 ms. The mud filtrate decayed with a characteristic decay time of 1130 ms.

Hydrogen index for the mud filtrate was 0.906 based on measured ratios of NMR amplitudes produced by equal volumes of fluid. Since there appears to have been little mud invasion into the core, the mud filtrate hydrogen index should not have affected NMR sample porosity. On the other hand, it would be expected that in high permeability West Sak sands, the CMR logging tool was sensing the flushed zone so its porosity measurements are probably 10% too low. The neutron porosity tool should also be affected to some extent.

In this case the rocks have fairly rapid decays produced from surface relaxation. The faster decay time of the mud filtrate will not affect interpretation. For high permeability sandstones with smaller surface relaxivity or for a typical carbonate, reduction in bulk decay time of the fluid in the pore space would produce an incorrect interpretation on the log if it was not corrected.

8.5 Conclusions – NMR

A series of NMR measurements was made on sands identified in core in the Ugnu and West Sak formations. Almost all the Ugnu formation at the Hot Ice No. 1 location is in the permafrost zone. Ugnu measurements were made on frozen and thawed recovered state samples along with samples that had been cleaned, dried and resaturated. Brine-saturated samples for both the Ugnu and West Sak formations showed decay spectra that fell into four primary rock types (with a few exceptions) that varied in the percent of fast decaying pores. In the West Sak an extra rock type had to be added to account for the thin, tightly cemented sandstone zones that were found.

A study investigated deposition of the frozen material by modeling a frozen spectrum using an unfrozen spectrum as a starting point. The most reasonable conclusion of the study is that the ice in the larger pores acts to partition the unfrozen brine into isolated, non-communicating pockets, that is, individual pores separated by pore throats. Only the smallest pores could be completely ice-free.

The primary issue unresolved in the study of the Ugnu is the difference between decay spectra in the thawed and resaturated state. This issue is extremely important and needs to be resolved for NMR measurements to be used to their full potential in evaluating hydrate resources. In any hydrate production project, repeat logging will almost certainly be used to evaluate production processes. NMR logs should be an important tool for this analysis. To make ideal use of it will require better understanding of NMR response through the entire thawing process.

Correlation of NMR measurements in the Ugnu to permeability was poorer than past experience led the project team to expect. This needs to be further investigated. This also is an important issue for hydrate production processes, as NMR measurements have potential to help quantify permeability and relative permeability throughout the thawing process. In the West Sak formation NMR measurements provide a very good estimate of permeability. The reason for this difference is not clear.

9. Base of Hydrate Stability Zone

One objective of drilling Hot Ice No. 1 was to obtain continuous core through to the bottom of the hydrate stability zone (HSZ). This required determining the depth to the base of the HSZ. Phase I drilling at Hot Ice (i.e., the 2003 season) ended at a shale zone below a thick, high-porosity, multi-Darcy permeability sand. This sand contained a sharp, well-defined boundary between frozen and unfrozen material. This boundary was consistently identified on well logs, CMR measurements on the core, and by well site geologists describing the core. It occurred at a depth of 1262 ft below KB. If standard assumptions are considered (i.e., the hydrate is a methane hydrate, and the section is normally pressured), then the bottom of the HSZ is determined by the temperature at the base of the frozen zone and average thermal gradient below it.

Temperature at the base of the frozen zone can be estimated by calculating the freezing point of brine in the sand zone at which the transition occurs. Brine was extracted from a sand sample just below the boundary. Extraction and subsequent measurements were performed by Dr. Craig Woolard of the University of Alaska, Anchorage. Woolard's results were reported as:

- Moisture content of soil sample = 16.7%
- Mass of soil used = 50.07 g
- Volume of DI water with conductivity of 0.63 µS/cm = 100 ml
- Soil sample and DI water were mixed to a slurry. A sample was filtered with a 0.45 micron filter. Conductivity of slurry sample was 1477 µS/cm (i.e., conductivity of original soil pore water after dilution with DI water).

Measured conductivity of the diluted solution was converted to a salinity of 0.8207 PSU using a JavaScript calculator available on the internet by Dr. Rick Chapman of The Johns Hopkins University Applied Physics Laboratory. (The calculator implements the UNESCO International Equation of State (IES 80) as described in Fofonoff, JGR, Vol 90 No. C2, pp 3332-3342, March 20, 1985.) This salinity translates back, after conductivity of the DI water is corrected for, to 10.06 PSU salinity in the sample taken from the sand. The JavaScript calculator provides a freezing point for brine recovered in the sand of 30.6°F.

Salinity of the sample obtained from the sand could differ from salinity of the brine before freezing. The largest uncertainty is probably due to the possibility of drilling mud filtrate invading the sample. The drilling mud was mixed with a high concentration of KCl (10%), so this would lead to overestimating salinity and thus underestimating the freezing point of the in-situ brine. A second possible influence could arise from the permafrost just above it. When the frozen zone forms, there is always some unfrozen brine left in the rock. This brine starts out much more saline than original brine since salt is concentrated in it during the freezing process. Over time diffusional processes could have redistributed this salt and thus increased the salinity of brine immediately below the base of the frozen zone where the sample was taken. This would also cause the actual freezing point to be higher than the estimated freezing point. There is also a depression of freezing point in a sand due to capillary forces. However, in sand as permeable as the present case, this effect should be negligible.

Because of these uncertainties, the freezing point used to estimate the depth to the base of the HSZ was rounded up to 31°F. This is 3°F higher than the regional value calculated by Collett et al. (1988).

The second factor that impacts the estimation of depth to the base of the HSZ is the thermal gradient below the base of permafrost. The regional value at the Hot Ice No. 1 location calculated by Collett et al. (1988) is 1.65°F/100 ft. Newsham et al. (see **Appendix E**) used bottom-hole temperatures at three wells adjacent to Hot Ice No. 1 to estimate a local thermal gradient. Bottom-hole temperatures were corrected using a diffusion model from the literature. The local value obtained was 2.22°F/100 ft. This gradient is still within the range of values reported by Collett et al. but would correspond to a location north of Hot Ice No. 1 on their maps.

Figure 70 summarizes results of investigations to estimate the base of the HSZ at Hot Ice No. 1.

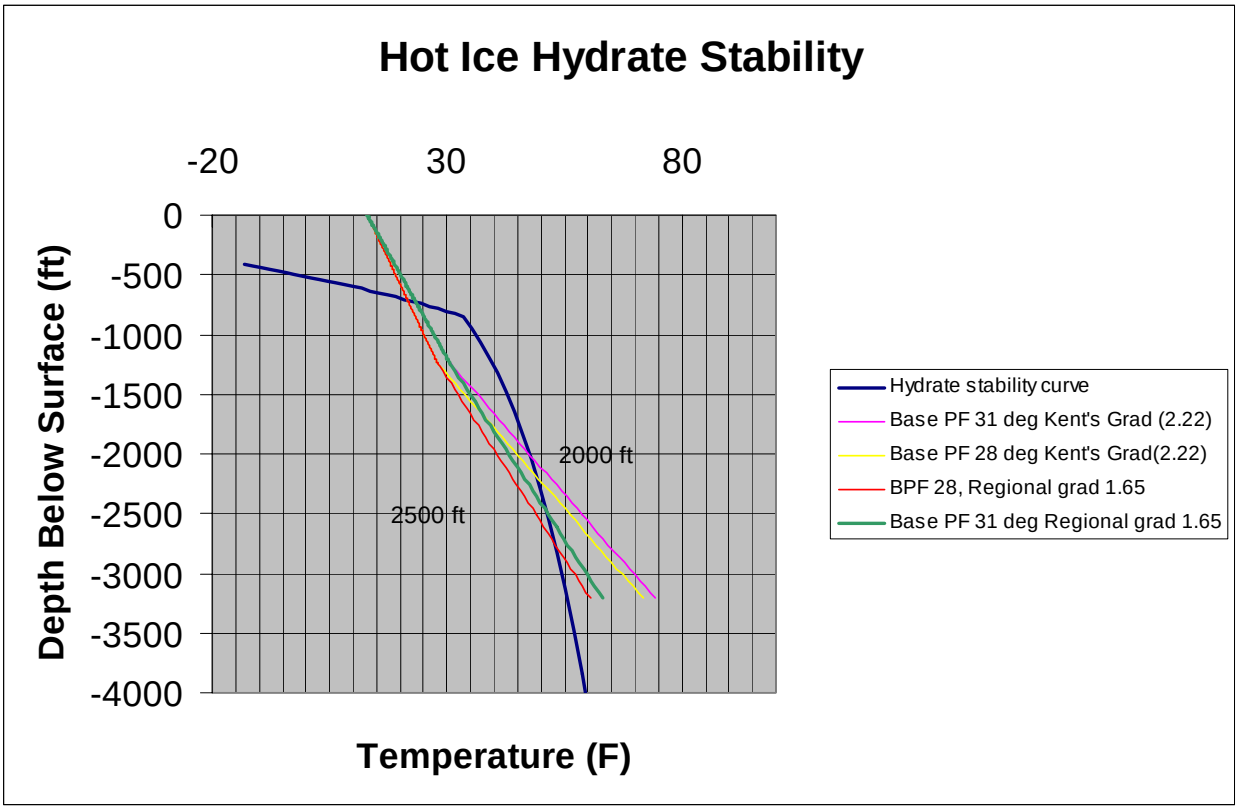

Figure 70. Hydrate Stability Zone at Hot Ice No. 1

Temperature at the base of the frozen zone is well constrained by the salinity measurements, so the most important lines (green and violet) are the two that use 31°F as starting temperature. They represent the two different thermal gradient estimates – regional (green) and violet (local). The local gradient gives a base of HSZ at 2000 ft below the surface, whereas the regional value produces a depth of 2500 ft below surface. (Note that these depths are below surface not KB, which is 26 ft above ground level.) Both calculations of the gradient probably contain more sources of uncertainty than the simple salinity measurement used to estimate temperature. In light of this information, a depth of **2300 ft below KB** was taken as a reasonable total depth to core to at Hot Ice No. 1.

10. Conclusions

10.1 Summary of Core Analysis

10.1.1 Scope

The Hot Ice No. 1 well was drilled from the surface to a measured depth of 2300 ft. There was almost 100% core recovery from the bottom of surface casing at 107 ft to total depth. Based on the best estimate of the bottom of the methane hydrate stability zone (which used new data obtained from Hot Ice No. 1 and new analysis of data from adjacent wells), core was recovered over its complete range. Approximately 580 ft of porous, mostly frozen, sandstone and 155 of conglomerate were recovered in the Ugnu Formation and approximately 215 ft of porous sandstone were recovered in the West Sak Formation. There were gas shows in the bottom part of the Ugnu and throughout the West Sak. No hydrate-bearing zones were identified either in recovered core or on well logs. The base of the permafrost was found at about 1260 ft.

The whole core was briefly described by well site geologists William Zogg and James Ebanks as soon as it was extracted from the wireline-retrievable core barrel. A graphic lithology log was produced from the description. Photographs and a surface gamma ray log were also recorded for the full length of core. During 2003 operations, a CMR logging tool located in the mobile laboratory was used to make NMR measurements on a 6-inch section from each 40-inch length of core. The tool was donated for use by Schlumberger and operated by a Schlumberger team (Robert Kleinberg and Douglas Griffin). This measurement provided an estimate of the amount of unfrozen brine in the “frozen rocks” from the permafrost section. The median value for “unfrozen porosity” in the permafrost zone was 0.051. For rocks in this section, this translates to about 13% of the pore space being filled with unfrozen brine. All whole-core measurements were performed in a laboratory module maintained at a temperature below the freezing point of water.

One-inch plugs were cut from all rock intervals that were of potential reservoir quality as identified by the well site geologists, whether these were from above or below the base of the permafrost. For thick sand sections, several plugs were cut. At a later stage, the plugs were cleaned and dried. Next, porosity, permeability, and grain density of each plug were measured. Other procedures performed on the plugs followed two paths, depending on whether they came from the “permafrost zone” or from the deeper section. For samples from the permafrost zone, velocity and resistivity was measured on samples as they were recovered at subfreezing temperatures. NMR measurements were made on a few frozen plugs, on thawed plugs, and on some resaturated samples. For samples taken from unfrozen formations, the complete suite of measurements was made after cleaning and drying.

10.1.2 Measurement Results

With the exception of the deepest sands in the West Sak and some anomalous thin, tight zones, all sands recovered (after thawing) are unconsolidated with high porosity and high permeability. At 800 psi, Ugnu sands have an average porosity of 39.3% and geometrical mean permeability

of 3.7 Darcys. Average grain density is 2.64 g/cc. West Sak sands have an average porosity of 35.5%, geometrical mean permeability of 0.3 Darcy, and average grain density of 2.70. There were several 1-2 ft intervals of carbonate-cemented sandstone recovered from the West Sak. These intervals have porosities of only a few percent and very low permeability. On a well log they appear as resistive with a high sonic velocity. In shallow sections of other wells these usually are the only logs available. Given the presence of gas in Hot Ice No. 1, if only resistivity and sonic logs and a mud log had been available, tight sand zones may have been interpreted as containing hydrates. Although this finding does not imply that all previously mapped hydrate zones are merely tight sands, it does add a note of caution to the practice of interpreting the presence of hydrates from old well information.

Velocity data from the Ugnu section is consistent with high-porosity sands with most of its pore space filled with ice. Median compressional velocity at 800 psi confining stress is 3864 m/sec. Median shear velocity is 2185 m/sec. Compressional velocity is 75% of the maximum possible velocity for a mixture of quartz with 39.6% ice. Median shear velocity is 66% of the maximum possible velocity. These values are consistent with ice acting as part of the frame and probably to some extent as a cementing agent.

West Sak velocities (being from unconsolidated unfrozen samples) were much slower than frozen Ugnu samples. The median Vp was 2000 m/sec and median Vs 1000 m/sec. Sands and shales have similar velocities.

Ugnu sample resistivities were measured on the “native state” samples. If assumptions are made regarding the percentage of unfrozen brine in the samples, salinity of the brine before freezing can be estimated from the data. The percentage of unfrozen brine found in this way is consistent with values obtained from core CMR measurements. The median pre-freezing salinity of the brine is 7100 PPM.

Most West Sak sand samples were resaturated with a 3% KCl solution after drying in a low temperature vacuum oven. Resistivity was then measured and fit to a standard Archie’s Law relationship. The median value of m, Archie’s cementation exponent, for the unconsolidated sands was 1.94. Two sand samples were measured in their recovered state. These measurements provided an estimate of pore fluid salinity. Pore fluid in the West Sak appears to have a salinity less than about 1/3 that of ocean water. This is consistent with salinity measured on a water sample extracted from the core at the bottom of the Ugnu.

NMR measurements on plugs in the Ugnu raise some interesting unanswered questions. There are significant differences between measurements made on thawed samples and those made on the same samples after resaturation. As of yet, no completely satisfactory model has been found to explain these differences. Observed relaxation times for samples are somewhat faster than usually observed for rocks with such high permeability. Finally, NMR measurements do not provide a good estimate of permeability. Modeling of NMR response of the frozen samples from the unfrozen samples shows that the ice restructured the pore geometry so that what appeared as a single pore in the unfrozen rock appears as multiple smaller pores in the frozen NMR spectrum.

NMR measurements on West Sak samples are more nearly what would be expected from past experience. A very good permeability estimator could be developed from the NMR data. Possibly due to trace minerals in the West Sak rocks, the formula differs from the default formula by a factor of three, so that West Sak samples appear have a relaxation rate 1.7 times that of samples used to develop the default formula.

In summary, the methane hydrate stability zone below the Hot Ice No. 1 location includes thick sections of sandstone and conglomerate which would make excellent reservoir rocks for hydrates and below the permafrost zone shallow gas. The Ugnu formation comprises a more sand-rich section than does the West Sak formation, and the Ugnu sands when cleaned and dried are slightly more porous and significantly more permeable than the West Sak.

10.1.3 Future Work

The characterization that has been performed is only the first stage in a complete characterization of the core recovered from Hot Ice No. 1. The complete core (except plugs removed for the initial analysis) is currently stored frozen at the University of Alaska at Fairbanks. This core is a unique resource on shallow North Slope formations. A second more complete description of the core after slabbing should be completed. This would provide among other things valuable stratigraphic data.

NMR results and the high 2.70 g/cc grain density suggest the need for detailed mineralogy analysis and thin section studies. As these are unconsolidated samples, grain size should be analyzed. This information will be essential for any production planning in the future. Capillary pressure measurements are very desirable on potential reservoir rocks. The anomalous NMR results require a careful follow-up study. Further velocity measurements combined with a more complete modeling study are needed to better define the structural role of the frozen material. In addition, velocity measurements from the shale zones, which were not extensively studied in the first stage analysis provide, would provide valuable calibration for surface seismic surveys. Additional velocity data in the sands along with the new NMR data would allow a joint data interpretation. These second-stage studies would allow complete extraction of information that the Hot Ice No. 1 core can provide. This will provide a more sound basis for any commercial development of the North Slope hydrate or shallow gas resources.

10.2 Occurrence of Hydrates at Hot Ice No. 1

Continuous core was recovered throughout the **hydrate stability zone (HSZ)**. It had been predicted before drilling began that the location would have significant sands in the HSZ and gas in the system. As no shallow seismic data were available, and the cost of acquiring such data was too expensive, it was not known if any traditional hydrocarbon traps existed. Hydrates were established as existing in wells to the northwest in sands that would be cut by Hot Ice. Core showed in the HSZ (as predicted) good high-porosity, high-permeability reservoir sands, and gas shows on the mud log. Despite this, no hydrates were recovered in this well.

Modeling of hydrate dissociation indicates that, if significant hydrates were cored, they would not completely dissociate before reaching the surface. There was no evidence on well logs for hydrates existing in-situ. Information on formation brine extracted from samples and resistivity measurements showed it to be somewhat less saline than seawater; therefore, there is no reason to believe that the HSZ had been incorrectly calculated. Experience at Hot Ice No. 1 further establishes what was already clear from earlier studies: *even in very good reservoir rocks, more is required beyond correct thermodynamic conditions and gas in the system to produce a hydrate reservoir.*

Numerous wells drilled on the North Slope of Alaska have reported drilling through hydrates. Hydrates were definitely recovered at the Northwest Eileen Well 2. Thus, there is no question that hydrates exist at some locations on the North Slope. It is also clear that they are not everywhere. The question then becomes: *What is the nature of the geographic distribution?* The most optimistic model is that they exist as continuous sheet-like deposits. For this case, detection of hydrates in isolated wells can be used to contour the existence of hydrates between the wells. At the other extreme, the most conservative model states that hydrates only exist where there were shallow gas reservoirs before temperatures cooled a few million years ago. The first model makes hydrates a very large potential resource, the second at best a marginal one. Wells in which hydrates have been detected or inferred from well logs were generally drilled based on the expected existence of a deeper trap containing oil. Such traps often imply the existence of traps in shallower formations. For such a scenario, drilled wells form a biased set, not a random sampling of shallow formations.

It is well known that hydrate plugs can form in pipelines. In addition, ocean floor hydrates seem to form without the presence of traditional hydrocarbon traps. These observations show that, given a sufficient methane flux and proper temperature/pressure conditions, hydrates are a self-trapping system. It would follow that, if no trapped gas already exists, the size of the gas flux through the system is probably a critical parameter. Lack of hydrates at Hot Ice No. 1 implies that this critical flux was not achieved there. One question then arises: *Does or did a large enough gas flux exist in some areas on the North Slope?* If so, sheet-like accumulations should exist.

If gas fluxes everywhere on the Slope are below the critical value, a traditional trapping mechanism seems to be necessary. Under these conditions, fields could still be larger than the gas volume the trap can hold. This is because after trapped gas is converted to hydrate it could act as a seed reservoir that grows by converting gas passing by into hydrate. It is therefore essential to obtain quantitative bounds on the gas flux passing through North Slope reservoirs in the last few million years.

11. References

Coates, G., Marschal, D., Mardon, D., Galford, J., 1998, "A New Characterization of Bulk-Volume Irreducibility using Magnetic Resonance," paper QQ, 38th Annual SPWLA Logging Symposium Transactions.

Coates, G.R., Xiao, L., and Prammer, M.G., 1999, *NMR Logging Principles & Applications*, published by Halliburton and distributed through Gulf Publishing.

Collett, T.S., Bird, K.J., Kvenvolden, K.A., and Magoon, L.B., 1988, "Geologic Interrelations Relative to Gas Hydrates Within the North Slope of Alaska," *USGS Open-file Report 88-389*.

Fofonoff, 1985, *Journal of Geophysical Research*, Vol 90 No. C2, pp 3332-3342, March 20.

Han, D.H., 1986: *Effects of Porosity and Clay Content on Properties of Sandstones and Unconsolidated Sediments*, Ph.D. Dissertation, Stanford.

Helgerud, Michael, 2001: *Wave Speeds in Gas Hydrate and Sediments Containing Gas Hydrate: A Laboratory and Modeling Study*, Ph.D. Dissertation, Stanford, April.

Mavko, G., Mukerji, T. and Dvorkin, J., 1998: *The Rock Physics Handbook,* Cambridge University press, Cambridge.

Shcherbina, A.Y., Talley, L.D., Rudink, D.L., 2003: "Direct Observations of North Pacific Ventilation: Brine Rejection in the Okhotsk Sea," *Science*, December.

Sigal, R. F., 2002, "The Pressure Dependence of Permeability," *Petrophysics,* pp. 92-102.

Appendix A:
On-Site Geologic Core Analysis Using a Portable X-Ray Computed Tomographic System

Barry M. Freifeld and Timothy J. Kneafsey
Lawrence Berkeley National Laboratory, Berkeley, CA, USA

Frank Rack
Joint Oceanographic Institutions, Washington DC, USA

Abstract

X-ray computed tomography (CT) is an established technique for nondestructively characterizing geologic cores. CT provides information on sediment structure, diagenetic alteration, fractures, flow channels and barriers, porosity, and fluid-phase saturation. A portable CT imaging system has been developed specifically for imaging whole-round cores at the drilling site. The new system relies upon carefully designed radiological shielding to minimize the size and weight of the resulting instrument. Specialized x-ray beam collimators and filters maximize system sensitivity and performance. The system has been successfully deployed on the research vessel *Joides Resolution* for Ocean Drilling Program's Leg 204 and 210, within the Ocean Drilling Program's refrigerated Gulf Coast Core Repository, as well as on the Hot Ice No. 1 drilling platform located near the Kuparuk Field, Alaska. A methodology for performing simple densiometry measurements, as well as scanning for gross structural features, will be presented using radiographs from ODP Leg 204. Reconstructed CT images from Hot Ice No. 1 will demonstrate use of CT for discerning core textural features. To demonstrate the use of CT to quantitatively interpret dynamic processes, we calculate 95% confidence intervals for density changes occurring during a laboratory methane hydrate dissociation experiment. Field deployment of a CT represents a paradigm shift in core characterization, opening up the possibility for rapid systematic characterization of three-dimensional structural features and leading to improved subsampling and core-processing procedures.

Table of Contents

Introduction

Radiographic imaging has been used since 1947 [Boyer et al.] to determine oil saturation in cores and to investigate fluid flow [Morgan et al., 1950]. Development of x-ray computed tomography (CT) by Hounsfeld [1972] sparked a revolution in x-ray imaging by enabling nondestructive estimation of density with high spatial resolution, based on reconstruction of a series of radiographs. Currently, x-ray CT is used to nondestructively characterize geologic samples and investigate dynamic processes. Computed tomographic images reveal sediment structure, diagenetic alterations, fractures and flow paths, and permit a large range of other properties to be inferred from quantitative densiometry. CT also allows intelligent selection of appropriate subsampling locations by revealing the internal structure of a whole core.

Early pioneering x-ray CT work for soil science applications was performed by Petrovic et al. [1982] looking at bulk soil density, and Hainsworth and Aylmore [1986], studying water saturation distribution. In the petroleum engineering field, Vinegar [1986] and Wellington and Vinegar [1987] laid a comprehensive foundation for performing petrophysical characterization of oil-bearing units, enhanced oil recovery experiments and multiphase relative permeability measurements using x-ray CT. To date, most work performed on geologic core characterization has been performed using medical scanners, which are designed for imaging the human body and not optimized for core characterization.

The portable CT system described herein has been designed specifically for core characterization. Unlike medical systems that require the user to exit the room during system operation, a novel radiological shielding arrangement minimizes the weight and volume of the system and permits operation of the x-ray in close quarters. To produce the highest-quality three-dimensional images, we have designed an x-ray compensator, similar in purpose to compensators used in early medical systems, that reduces image saturation beyond the edge of the core and improves system sensitivity.

The new system has been used on the *JOIDES Resolution* during the Ocean Drilling Program's (ODP) Leg 204 and Leg 210 to image whole-round cores, as well as within ODP's refrigerated Gulf Coast Core Repository. The system was also used at Hot Ice No. 1, a methane hydrate research drilling project on the North Slope of Alaska. At the Hot Ice No. 1 drill site, the system was operated in a room at subfreezing temperatures to stabilize permafrost cores and reduce the rate at which any recovered hydrate would decompose. This paper details the portable x-ray CT system design, shows examples of acquired data, and uses a methane hydrate dissociation experiment to demonstrate the system's quantitative capabilities. Suggestions on future research activities, and areas needing attention for improving x-ray CT core analysis, are presented in the conclusions.

System Description

A schematic layout and photograph of the portable CT installed on the Bridge Deck of the *JOIDES Resolution* are shown in **Figure 1**. The core is installed vertically in the instrument and rotated around its vertical axis. A horizontal gantry holding the x-ray source and detector is raised and lowered by a belt-driven actuator to facilitate imaging selected regions of the core. The x-ray source has a tungsten target and a 250-µm thick beryllium window, delivering up to 130 kV at 0.5 mA, with a variable focal spot size that increases from 5 microns at 4 watts to 100 microns at 65 watts. Computer control permits adjustment of both anode voltage and current. To be able to efficiently capture the cone-beam projection of the core, we used a dual-field 100 mm/150 mm cesium iodide image intensifier. The image intensifier exhibits some geometrical distortion (commonly referred to as pin-cushioning) and lacks the dynamic range of available

solid-state x-ray detectors, but rapidly acquires images and has high sensitivity. Rapid imaging is important for imaging large numbers of cores and for performing transient studies.

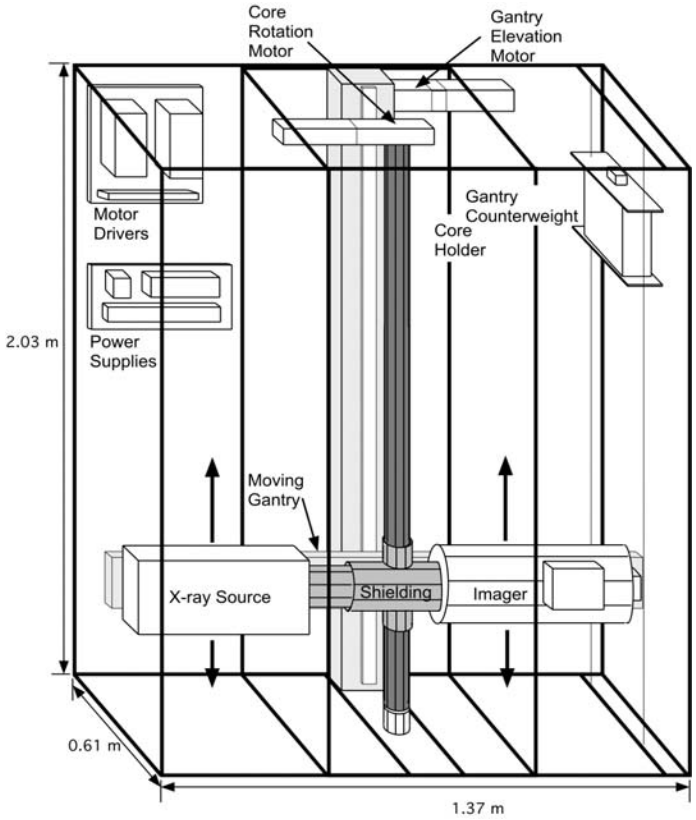

Figure 1. (a) Schematic layout of portable x-ray CT system. (b) CT system installed in Bridge Deck Joides Resolution core laboratory for ODP Leg 210.

Resolution of the CT system is dependent on numerous system parameters, including x-ray source focal spot size, image intensifier phosphor properties, location of the core between the x-ray source and the image intensifier, CCD camera resolution, and the image intensifier field of view. For CT images shown in this paper, x-ray spot size varied from 60 to 100 µm depending

on power setting, the image intensifier input window was kept fixed at 150 mm in diameter, and the camera resolution was 768 × 494. With these settings, pixels on the acquired radiographs were approximately 200 μm^2, resulting in reconstructed voxels (200 µm on a side) that have a volume of 8 nanoliters.

To reduce noise and increase the dynamic range of the system, great care was taken to optimize the x-ray beam path for core imaging. A beam collimator mounted on the x-ray source was used to minimize albedo, which degrades image quality. To reduce camera noise, multiple frames are acquired and averaged without moving the object, leading to a noise reduction proportional to the square root of the number of frames. Ten frames acquired over a 0.4-second period was considered a reasonable trade-off between speed and image quality for the images acquired in this paper, although that number can be adjusted to match the requirements of the user's particular application.

As part of the beam collimator, a computer-controlled copper shutter mounted in front of the beryllium exit window can optionally be used to reduce the soft x-ray content of the beam. This is normally only performed at energies above 100 kV to reduce the influence of the effective atomic number on x-ray attenuation, and lead to more precise density estimates. Below 100 kV, there is a significant component of photoelectric absorption, which is proportional to effective atomic number. Reducing x-ray voltage (softer x-rays) results in increased photoelectric absorption and serves to highlight contrasting media and differences in fluid-phase saturation. This also leads to greater uncertainty in the density estimates because of increased beam-hardening effects (filtering of soft x-rays). A concise discussion of the effects of spectral energy, including implications for core analysis, is provided by Wellington and Vinegar [1987].

An aluminum compensator (**Figure 2**), installed between the sample and x-ray imager, reduces the dynamic range of the x-rays incident upon the image intensifier and increases sensitivity to attenuation variations within the sample. Because of the geometry of passing a cone-shaped beam through a cylindrical object, x-rays passing beyond the outside edge of the coreholder are not attenuated by the object; thus, the compensator is thickest in this region. By greatly attenuating the x-ray beyond the edge of the core holder, the aluminum compensator eliminates image blooming, an image defect that involves pixels on a CCD approaching their electron charge capacity and spilling over into nearby pixels, washing out the image. Where the core is thickest, in the center, the attenuator is thin, providing minimal additional attenuation of the x-rays. The result is an image of fairly uniform intensity striking the image intensifier. The aspherical compensator is designed using a fan-beam x-ray path simulation, assuming a core of uniform density. The slight variation in attenuation that occurs along the vertical axis of the core (as x-ray cone-beam angle increases) is ignored.

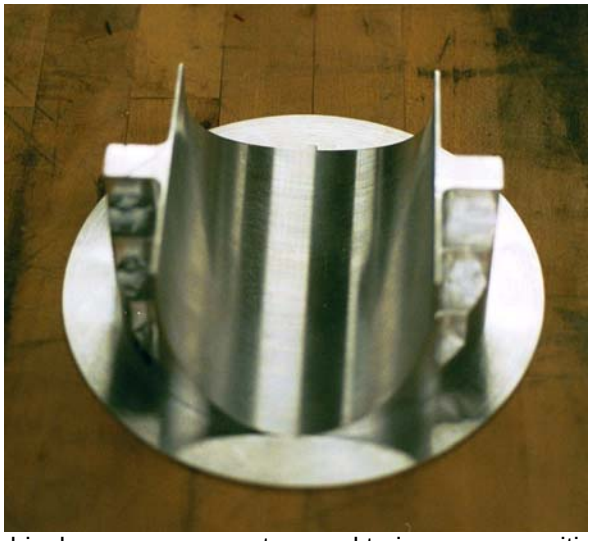

Figure 2. Aluminum acylindrical x-ray compensator used to increase sensitivity of x-ray CT by reducing variation in intensity of image striking image intensifier. Flat regions at edge of compensator provide reference area on each radiograph for normalizing variations in x-ray intensity.

While the qualitative benefits of using the compensator have been mentioned above, **Figure 3** provides a quantitative example of how density resolution can be improved by using the compensator, without having to resort to cameras with increased dynamic range. For this discussion, it should be mentioned that every radiograph is composed of pixels with an intensity spanning a range that can be digitally represented, i.e., 10 or 12 bits. Similarly, a dynamic range, or bit depth, can be assigned for any region of interest. Dynamic range of a region of interest will be less than or equal to that of the whole image. As noted previously, without the compensator in place, a large variation in intensity occurs, from outside of the core image to the inside. With the compensator in place, dynamic range across the image is reduced, and greater contrast can be seen in any particular region of interest.

Figure 3 shows radiographic images of sandstone cores taken with the x-ray energy set below the threshold at which significant image blooming occurs, along with a histogram of pixel intensity for the region of interest enclosed in the white rectangles. The image taken without using the compensator was taken with the x-ray source set to 90 kV and 250 µA, whereas the image with the compensator was taken at 110 kV and 300 µA. For the region of interest without the compensator, the histogram reveals an image bit depth of 6 bits. The image with the compensator has a bit depth of 7.7 bits, representing a more than three fold increase in the x-ray attenuation resolution. The increased performance provided by the compensator is significant.

The aluminum compensator also contains milled flats that extend beyond the edges of the acylindrical region, used for correcting for fluctuations in x-ray tube intensity. By normalizing each image by the average image intensity in the reference region, one source of errors in density estimates is eliminated. This is particularly important for experiments that span long time periods, such as petroleum core floods, which can span several weeks duration. Note that large variations in x-ray current can be corrected for using this method, but because of photoelectric absorption, changes in x-ray voltage beyond small ripples produce nonlinear changes in the image intensity. Thus x-ray tube current can vary over a broad range and all of the images can be normalized to each other. Any change in the voltage setting, however, will require an independent system calibration for each selected voltage.

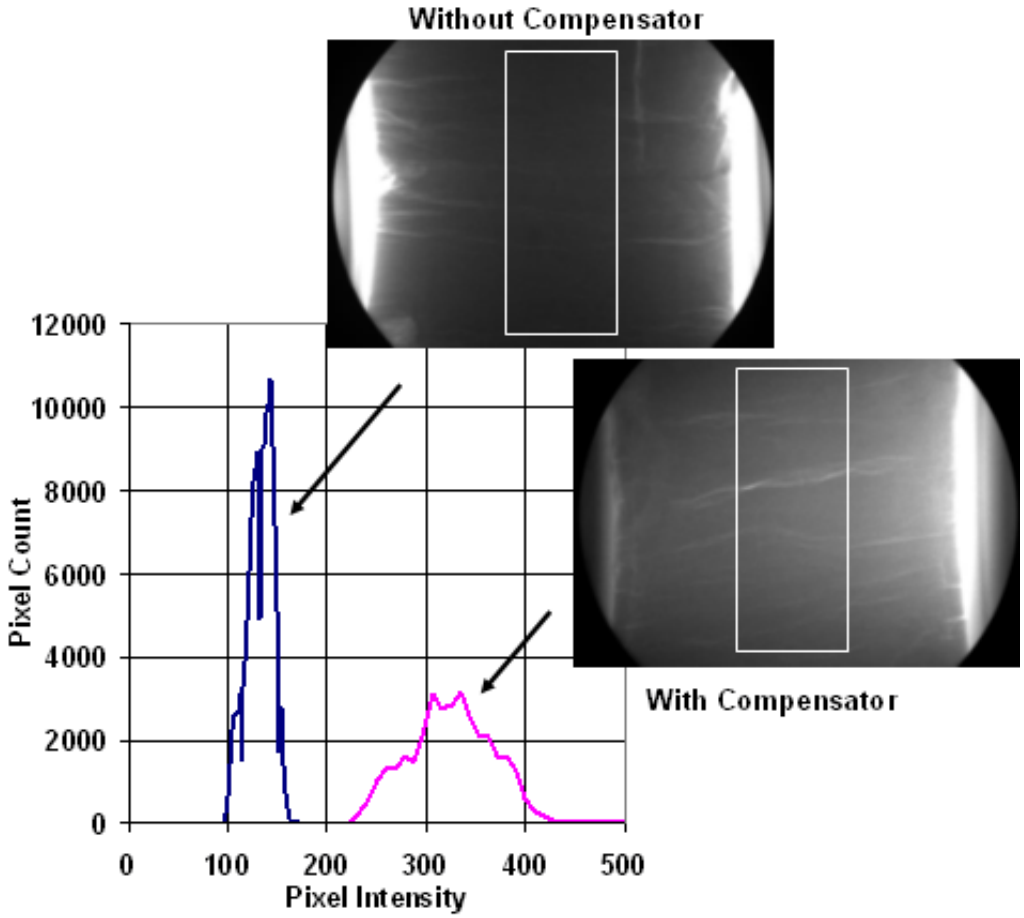

Figure 3. Radiographs taken with and without aluminum x-ray compensator. Histograms for mid-region of each image show how the compensator permits use of greater x-ray energy resulting in broader distribution of pixel values. This translates into CT reconstructions with greater density resolution.

Image reconstruction software, Imgrec (developed at Lawrence Livermore National Laboratory), was employed to perform fan-beam convolution back projection (CBP) and Feldkamp reconstruction of the acquired cone-beam radiographs [Feldkamp et al., 1984]. The CBP algorithm is used for rapid reconstruction of acquired radiographs to verify correct parameter settings (only a few seconds are required to reconstruct a single horizontal slice), but does not account for the divergent cone-beam projection geometry. This limits CBP to the region near the radiograph's mid-plane. The Feldkamp algorithm corrects for the divergent cone beam geometry and can be used to accurately reconstruct images with x-ray projection angles up to 6 or 7°. However, beyond that point, the approximations that make the Feldkamp algorithm computationally tractable result in noticeable geometric distortions. The images shown in this paper have used cone-beam angles from 6° to 10°. Reconstruction of 180 radiographs into a 10 cm three-dimension volume data set takes approximately 10 minutes on a 3 GHz PC. For either the CBP or the Feldkamp algorithm, it is important to acquire both a dark image from the camera (an image with the x-ray beam off) and a background image (where no object is in the beam path), which is subtracted from subsequent images of the object to account for x-ray intensity variations across the imaging plane.

Several innovations in the CT system make it both portable and radiologically safe for use in a core laboratory. The key to transportability is minimizing the volume enclosed within lead shielding. The usual shielding method for a fixed system, encapsulation of the entire unit or room within a lead enclosure, would have resulted in a unit of limited portability. We minimized

the shielding required to enclose the x-ray path, by forming a cross that translates along the core axis (**Figure 1**). One arm of the cross encompassed the main x-ray beam, and the other arm reduces radiation scattered along the core axis. To permit loading and unloading of the core, we split the vertical arm of the cross, allowing it to open and close by telescoping back over the horizontal arm. The entire system is designed to meet the United States radiological requirements for a cabinet safe system (U.S. Title 21 Code of Federal Regulations §1020.40). Redundant safety interlocks are located both on the access door and the shielding, to prevent energizing the x-ray unit while personnel are manipulating the core.

To convert x-ray attenuation to density, we scan the reference materials and perform a three-dimensional CT reconstruction. A slice from a CT reconstruction of a calibration standard containing a variety of materials is shown in **Figure 4**. This standard consists of a 7.62 cm diameter PVC cylinder with a series of vertical holes, each of which contains a rod of different materials. For this standard, **Figure 5** shows density versus attenuation, along with regression analysis of the data. The data for PVC are not used for creating the calibration curve, because the high atomic number of the chlorine contributes to a significant photoelectric absorption component in the x-ray attenuation, resulting in an overestimated density.

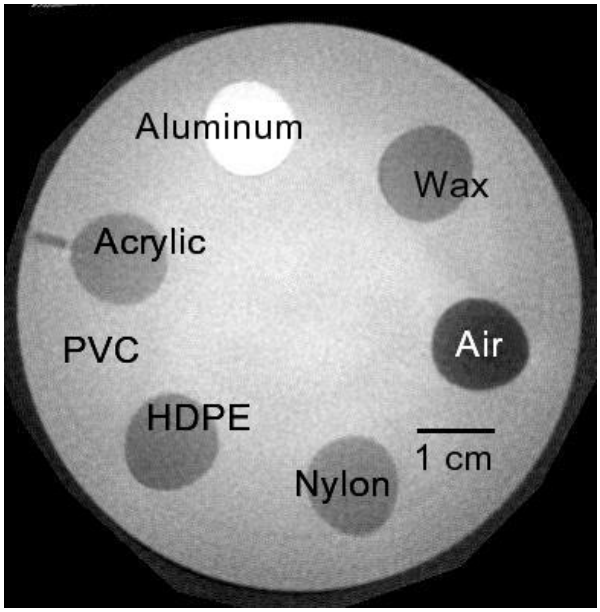

Figure 4. Single horizontal slice from a CT reconstruction of a cylindrical density reference standard

The CT reconstructed image of the calibration cylinder displays artifacts and aberrations that are worth noting. Geometrically, because of image intensifier pin-cushioning, there is some visible elongation of the reference rods, which should appear circular. This aberration can be removed by remapping the pixels on each radiograph to eliminate the distortion prior to performing CT reconstruction. Quantitatively, there are negligible changes in the estimated material densities due to geometrical distortion. Beam-hardening, due to the polychromatic nature of the x-ray beam, is a reconstruction artifact responsible for the PVC cylinder appearing brighter in the center than at the edges. Unlike typical beam-hardening that make the outer edges of an object appear more dense (since it attenuates soft x-rays) and the center appear less dense (due to interaction with harder x-rays), the aluminum compensator adds a counterintuitive beam-hardening aberration. This is because the background correction image used to normalize for intensity variation across the image intensifier suffers from beam-hardening effects, making the image appear disproportionately dark at the edges and bright at

the center. The background corrected CT core images thus appear bright (less dense) at the edges, and dark (more dense) in the center.

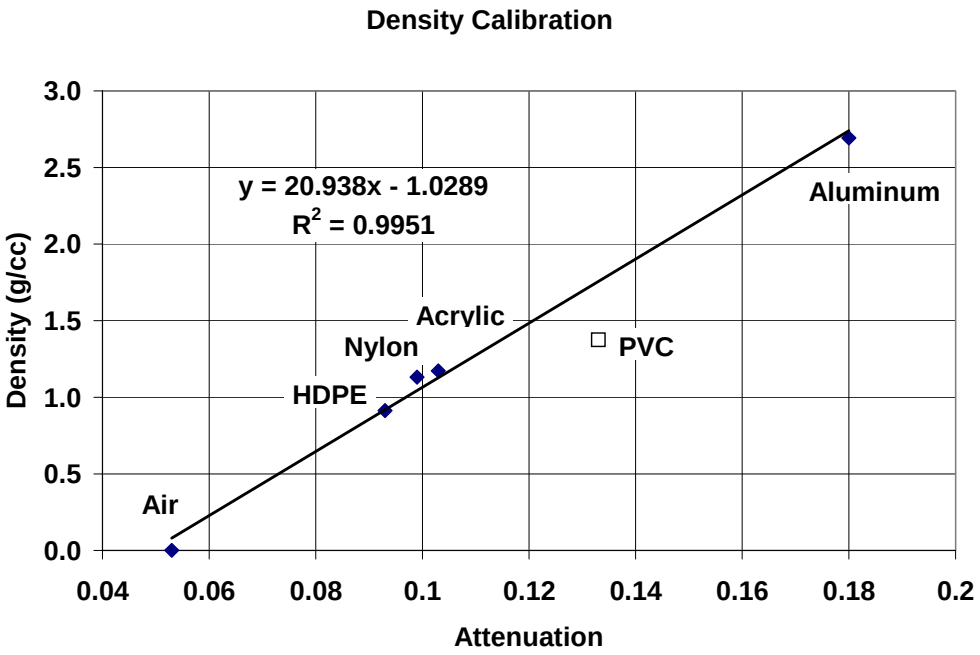

Figure 5. Linear regression of mean attenuation values obtained using a density reference standard containing an assortment of materials. PVC data point is not used in regression because the high effective atomic number of chlorine atoms increases attenuation.

There are several ways to eliminate or correct for beam-hardening effects when using the compensator. The simplest method is to perform a polynomial correction to the radiographs that removes the beam-hardening trend. This is the method that has been applied to images in this paper. The second method, which will be carried out in the future, is to design the compensator using a polychromatic ray-path simulation.

Deployment on Ocean Drilling Program Leg 204

The portable x-ray CT system was first deployed on the *Joides Resolution* for Ocean Drilling Program Leg 204, Drilling for Hydrates at Hydrate Ridge, Cascadia Continental Margin, approximately 50 nautical miles from the Oregon Coast. A radiation safety check was performed to verify that no hidden damage occurred to the radiation shielding during transport, and *Joides Resolution* technical staff were trained. Both portability and ease of use of the CT system were demonstrated by the CT system's set-up and operation within a 12-hour period.

During Leg 204, the CT system was used in two different modes: 1) to linearly scan the core, taking two images at 90° orientation to each other at 10 cm intervals along the length of the core and 2) in CT mode, which acquires 180 images with a 2° core rotation between each image. In less than two minutes, the linear imaging mode captures gross structural features along the entire length of a 1.5 m core. These data can be used to perform high resolution densiometry. Over 12,000 radiographs from more than 500 cores were acquired during Leg 204, with the images available for both real-time viewing and electronic archival storage. The CT imaging mode takes between one and three minutes to image a 10 cm core section, depending on the final desired resolution.

The radiographic images provide quantitative densiometric measurements with high spatial resolution. An alternative measurement technique for performing systematic density measurements from whole cores, which is part of the *Joides Resolution*'s multi-sensor core logging system [Blum, 1996], is Cs^{137} gamma ray densiometer (GRD). GRD provides an integrated average density along the mid-line of the core over a 1 cm^2 area, with a typical sample frequency of one data point every 2.5 cm. Spacing of GRD data points is limited because it takes several seconds (e.g., 4 seconds for a 7 cm OD core) to acquire each measurement. The x-ray radiographs provide a two dimensional data set with a resolution of 200 μm. By acquiring two images at 90° orientation to each other, the x-ray provides some indication as to gross structural inhomogeneities that may be ambiguous from a single image.

The radiographs taken during linear scanning reveal more than just gross structural features and densiometric data. Small heterogeneities with enough density contrast are apparent, particularly if the supporting matrix is fairly uniform. As an example, a radiograph taken from ODP Leg 204 Site 1251B15 showing dark sulfide deposits filling in former bioturbation features is shown in **Figure 6**. The bright horizontal fractures are created by gas evolution during core recovery, which results in significant changes in the core fabric.

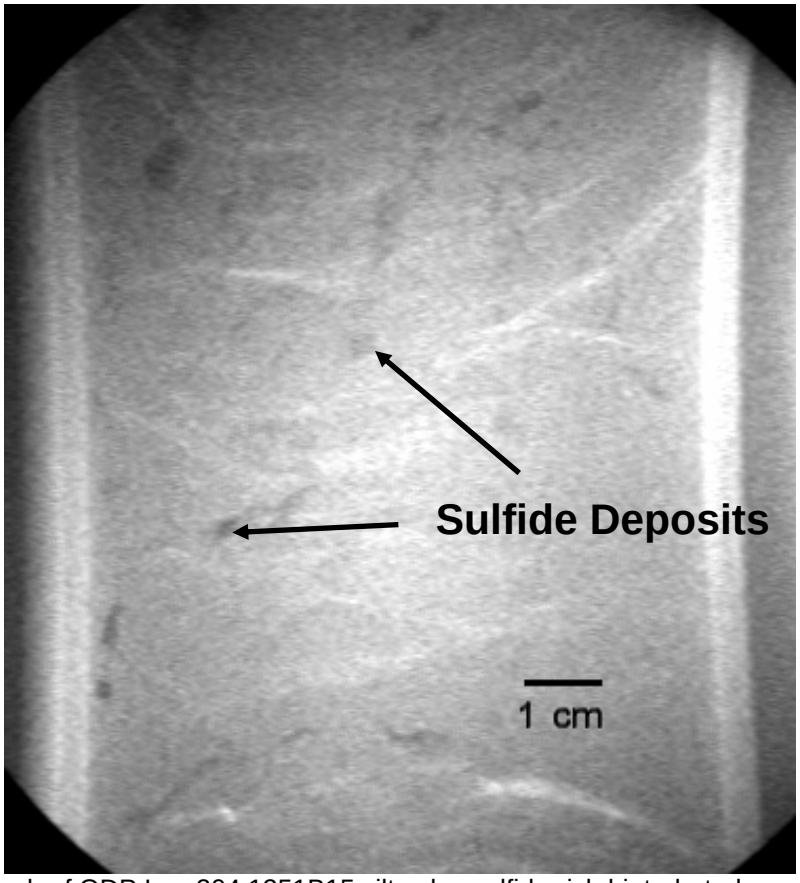

Figure 6. Radiograph of ODP Leg 204 1251B15 silty-clay sulfide-rich bioturbated core. Bright horizontal features result from disturbance of core during recovery caused by exsolution of gas.

To estimate density using the x-ray radiographs, three processing steps are performed. The first step is to correct for fluctuations in the energy emitted from the x-ray source using the reference region from the aluminum compensator. Second, geometrical effects (scanning through the cylindrical core and compensator using a divergent cone-beam) are corrected by normalizing each acquired radiograph by an ideal image generated by a homogeneous core.

This image can either be calculated theoretically or obtained experimentally. For this paper, an experimentally obtained image from a homogeneous sediment core was used to normalize the radiographs. Finally, the normalized data are converted from corrected attenuation to density, using a linear calibration like the one shown in **Figure 5**.

Figure 7 shows radiography data from ODP Leg 204, Site 1251B37 compared to GRD, gravimetric-based moisture and density measurements, along with logging-while-drilling (LWD) density logs taken in nearby ODP Leg 204 1251A [Tréhu et al, 2003]. Density estimates using the x-ray radiography, GRD, and LWD data are plotted every 2 mm, 2.5 cm and every 15 cm, respectively. The x-ray radiography density estimate is calculated using average attenuation measured for the 100 pixels contained within a 2 × 2 mm region.

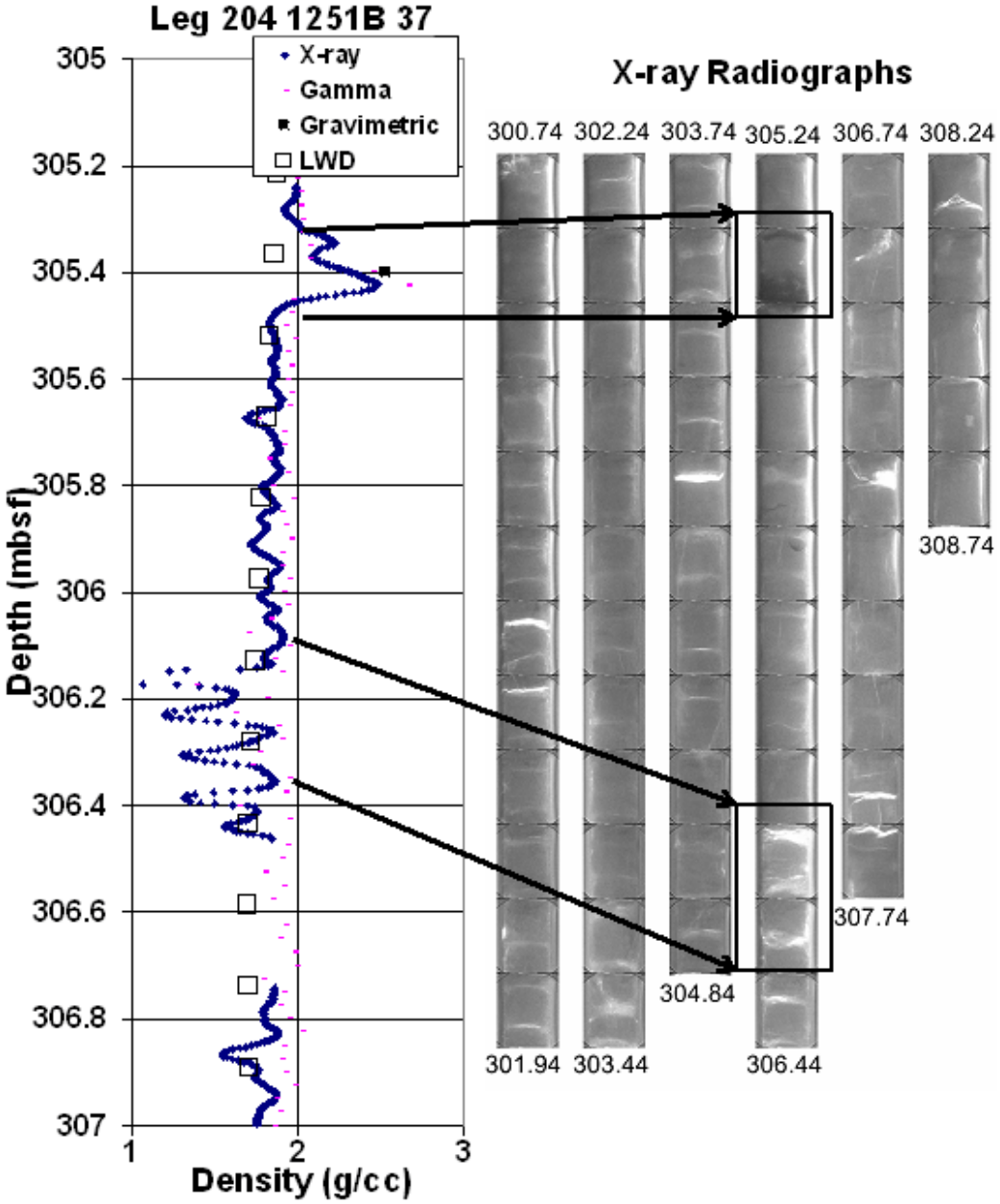

Figure 7. A comparison of different methods of estimating bulk density for ODP Leg 204 1251B 37. The graph shows data from x-ray radiography, Cs^{137} gamma ray densiometry, gravimetric density measurements, and logging-while-drilling density measurements.

All three core based methods are able to identify a dense carbonate-rich feature a few centimeters in length at 305.45 mbsf. Only the x-ray radiographs are able to reveal lateral extent of this feature across the core, as well as the presence of another thin dense feature at 305.32 mbsf. Since the LWD was not taken in the same borehole, a direct comparison for this particular feature is not possible. The radiographic data (i.e., between 306.4 and 306.5 mbsf) show very-well-defined areas of core disturbance interspersed between regions of intact core. Because of the limited spatial resolution of the GRD measurements, areas of the core that are heavily disturbed by gas exsolution appear as increased noise in the data. As expected, the LWD measurement displays none of the artifacts that arise from core recovery. It is encouraging that all of these methods offer very good overall agreement for both density trends and absolute estimated value.

Hot Ice No. 1 Methane Hydrate Research Well

Methane hydrate is a naturally occurring clathrate compound, commonly found within deep oceanic or permafrost regions. In methane hydrate, crystalline water encages a gas molecule. Interest in naturally occurring gas hydrates is increasing because of their energy resource potential, as well as their role in climate variability [Kvenvolden, 1988]. An exploratory hydrate drilling program, Hot Ice No. 1, targeting the Sagavanirktok Formation was drilled down to 427 m in April 2003, and completed February 2004 to a total depth of 701 m. The portable x-ray CT was operated as part of a mobile laboratory to nondestructively image cores recovered during both drilling operations. The room in which the x-ray CT was operated was kept at temperatures between -10°C and -5°C, to prevent deterioration of the permafrost cores and to minimize dissociation of any recovered hydrates. Dissociation of hydrate is the phase-change transformation from crystalline hydrate to distinct water (either liquid or solid) and gas phases.

Prior to the initial mobilization to Hot Ice No. 1, hydrate dissociation studies were conducted, using the x-ray CT scanner, to spatially and temporally track the conversion of methane hydrate to methane and water ice using synthetic methane hydrate samples. **Figure 8** shows a simplified schematic of the hydrate dissociation experiment. The synthetic hydrate was manufactured by the method detailed in Stern et al. [1996] and combined with water ice and sand in a sealed pressure vessel. Hydrate dissociation, stimulated by allowing the room air to warm the sample in the pressure vessel, was monitored by measuring the temperature and pressure and periodically acquiring CT data [Freifeld and Kneafsey, 2003]. The goal was to determine how sensitive CT imaging is to spatial and temporal changes that occur during the hydrate dissociation process, so that these measurements can be applied to natural hydrate-bearing samples recovered during the Hot Ice No. 1 coring operation.

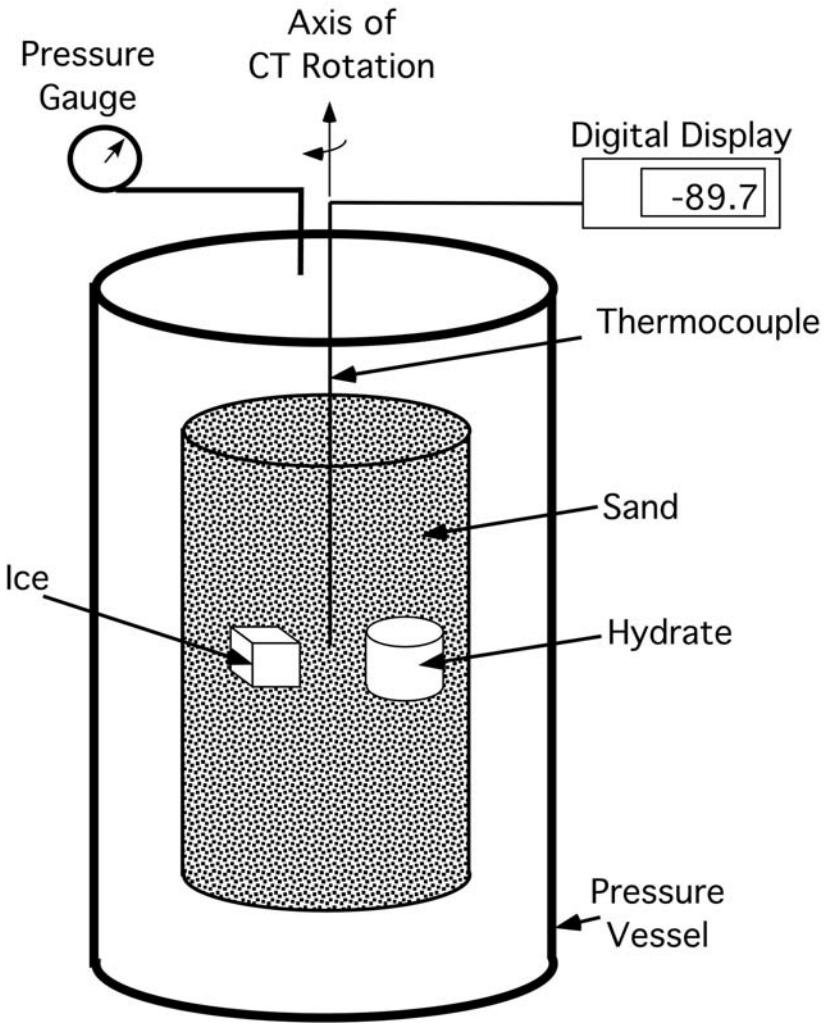

Figure 8. Simplified schematic of a hydrate dissociation experiment

Figure 9 shows a sequence of reconstructed CT slices tracking the progression of dissociation of the synthetic methane hydrate. Differential images, created by subtracting the baseline image from subsequent images, are used to highlight relatively subtle changes in density as dissociation progresses. The difference in the images taken prior to the start of the dissociation process, and after dissociation is complete (as verified by the pressure in the vessel), yields estimates of total hydrate saturation and spatial distribution. Quantifying hydrate dissociation changes in the CT data depends on accurate system calibration, and high resolution densiometry. Since any one voxel has considerable noise, confidence in density estimates can be increased by averaging multiple voxels, assuming that the region averaged over is homogeneous, and any variation in measured attenuation results from normally distributed noise. The 95% confidence interval for an estimate can be expressed as

$$\rho_{0.95}(x) = \rho(x) \pm t_{0.95,n} \frac{\sigma}{\sqrt{n}}$$

where n is the number of voxels, σ is the standard deviation of density estimates, and t is Student's t distribution. Water ice is used as a reference material because its density will remain constant throughout this experiment.

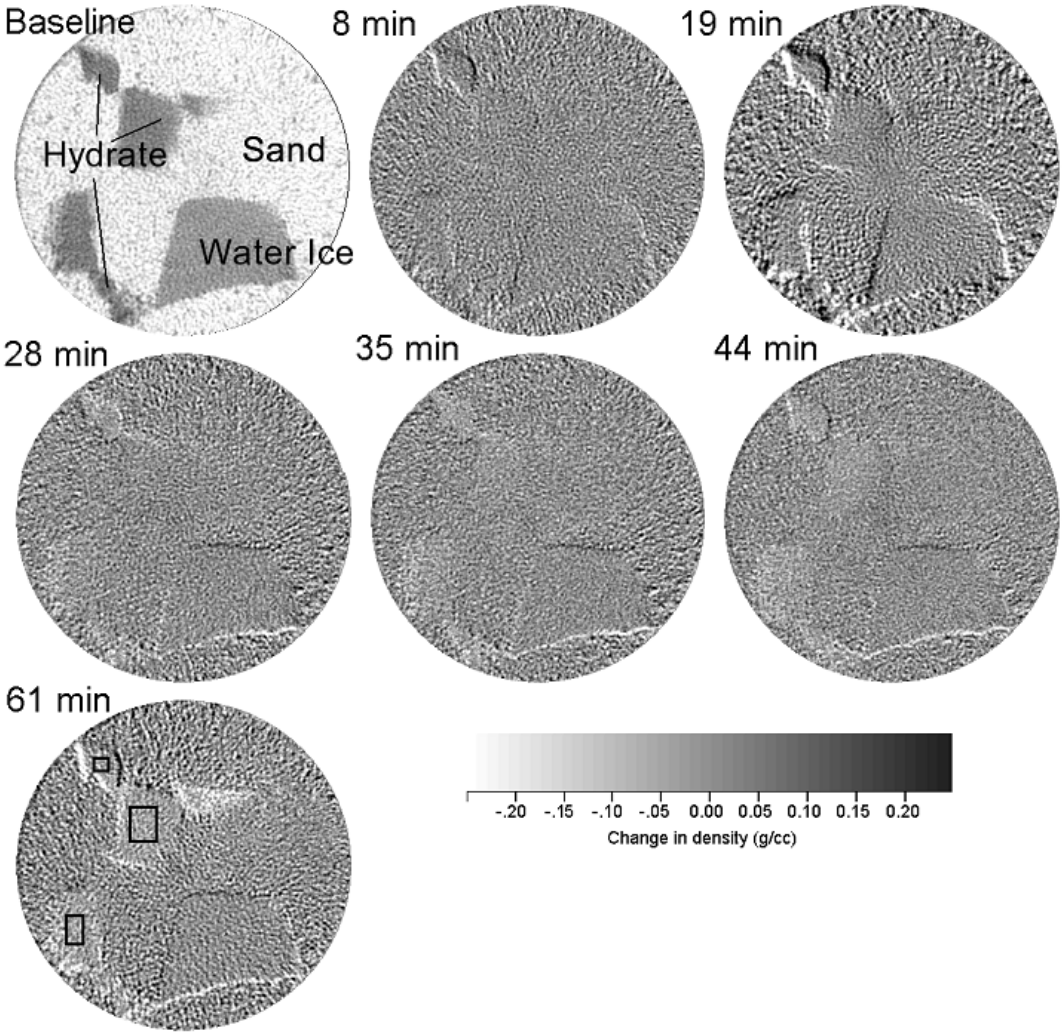

Figure 9. X-ray CT images of a synthetic hydrate dissociation experiment. Baseline image shows location of hydrate and water ice in a sand matrix. Difference images reveal the progression of dissociation within hydrate nodules. Gray scale bar only applies to the difference images. Rectangular highlighted regions in difference image at 61 minutes were used to calculate changes in hydrate density.

The 95% confidence interval for estimating density change for the water ice is shown in **Figure 10(a)** as a function of length of a cubical region of interest. As the cubic region of interest is increased to a few millimeters in length, uncertainty declines to ±0.01 g/cc.

Figure 10(b) shows 95% confidence intervals for hydrate density changes during dissociation as a function of cubic region of interest, taken at three different times after the start of the experiment. As the hydrate dissociates and methane gas evolves, density of the hydrate is seen to decrease. At the start of the experiment, density of the methane gas encaged in the porous hydrate is calculated to be 0.084 g/cc, based on the stoichiometric ratio between water and methane. Density reduction as calculated from the x-ray images at 44 minutes, after dissociation concluded, is 0.088 g/cc. These density changes rely on an initial baseline CT calibration curve, using regions of interest containing sand, hydrate and ice and their known densities. **Figure 10(b)** shows that even though x-ray CT system resolution may be 200 µm, if the objective is to determine small changes in hydrate saturation, then the smallest region of interest that yields reasonable confidence has a minimum spatial dimension of approximately a 2.5 mm cube, or roughly 2,000 voxels.

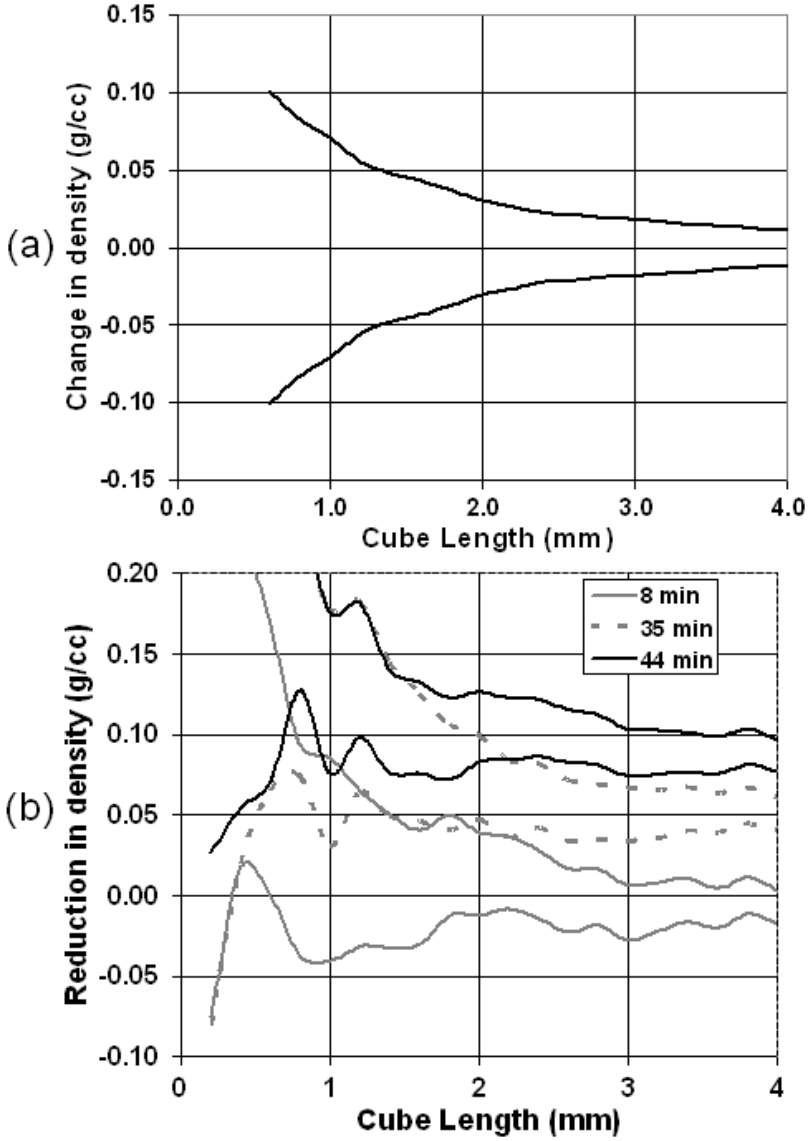

Figure 10. (a) Estimated change in density for water ice used as a reference material in hydrate dissociation experiment, showing upper and lower 95% confidence intervals as a function of region of interest size. Density changes were calculated using the difference between baseline CT data set and a data set acquired after 44 minutes. Expected change is 0.0 g/cc. (b) Time progression for changes in density of hydrate as dissociation progresses, expressed with upper and lower 95% confidence intervals as a function of region of interest size. Final data set, taken at 44 minutes, was acquired after dissociation was determined to be complete by independent pressure measurements.

The sedimentary structure at Hot Ice No. 1 contains thick sequences of conglomerates, sandstones, mudstones, and coals. Coring operations recovered no hydrates, which was corroborated by standard geophysical logs and the general absence of finding significant gas bearing formations. X-ray CT images were acquired of more than 200 one-meter long core tubes. Operationally, the only problem to note from work at the Arctic Platform Mobile Laboratory, in a space maintained at -5°C to -10°C, was failure of a coating on one of the objective lenses in the image intensifier. The coating appeared to delaminate, causing a slight distortion in one portion of the image. This problem did not occur when the system was operated at the warmer, 2°C to 6°C temperatures within the Ocean Drilling Program's Gulf Coast Core Repository.

A CT image of permafrost sandstone recovered at Hot Ice No. 1 (210.7 mbgs) is shown in **Figure 11**. The slice shown from the three dimension data set is a midcore vertical plane, resulting from averaging five 200-µm thick slices. The core displays numerous interbedded laminae, ranging from wispy millimeter-sized fining layers, as shown in the upper detail, to organic interbeds containing small claystone clasts. The dark subhorizontal feature near the top of the core is an ice lens that has formed near a set of fine sand laminae. Changes in bedding strike and dip are clearly visible and can be used to define strike set thicknesses for various sedimentary layers.

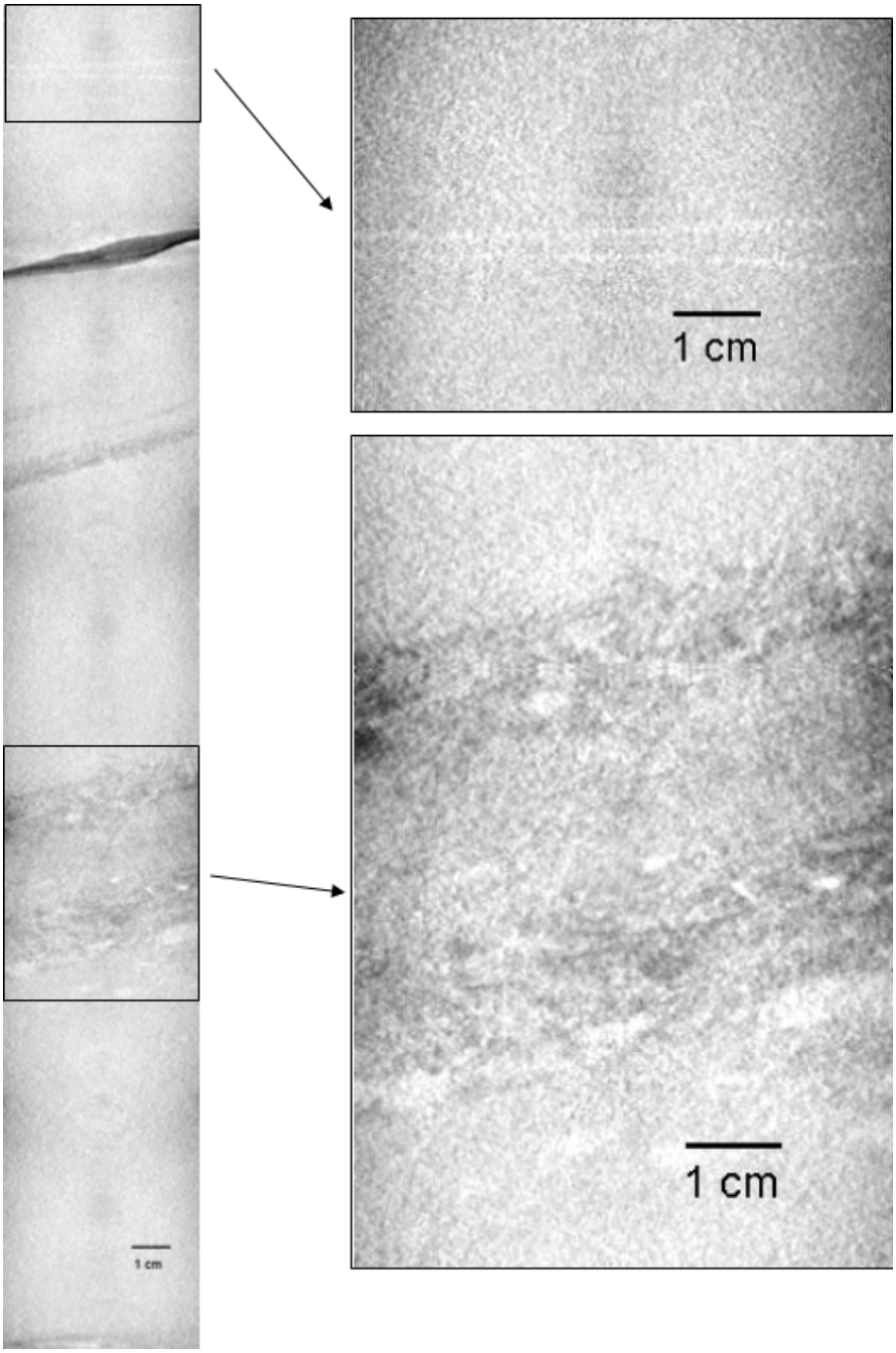

Figure 11. X-ray CT image of an interbedded sandstone from Hot Ice No. 1. The upper detail reveals wispy submillimeter planes of fine sand, while lower detail shows interbedded organic laminae and small claystone clasts. Dark subhorizontal feature located approximately 10 cm below top of core is an ice lens.

Figure 12 shows vertical and horizontal CT images taken of three different core samples collected at Hot Ice No. 1. **Figure 12(a)** shows vertical CT images of an unlithified sand (570.3 mbgs) with interspersed, rounded mollusk-shell fragments. The dense (bright) region near the top of the core is an iron claystone concrete. **Figure 12(b)** shows horizontal CT images of a conglomerate cemented in a sand/ice matrix bearing numerous ice lenses. Individual gravel-sized fragments and small claystone clasts are visible. In **Figure 12(c)**, horizontal CT images reveal abundant intact mussel fossils contrasting with the fine sand matrix.

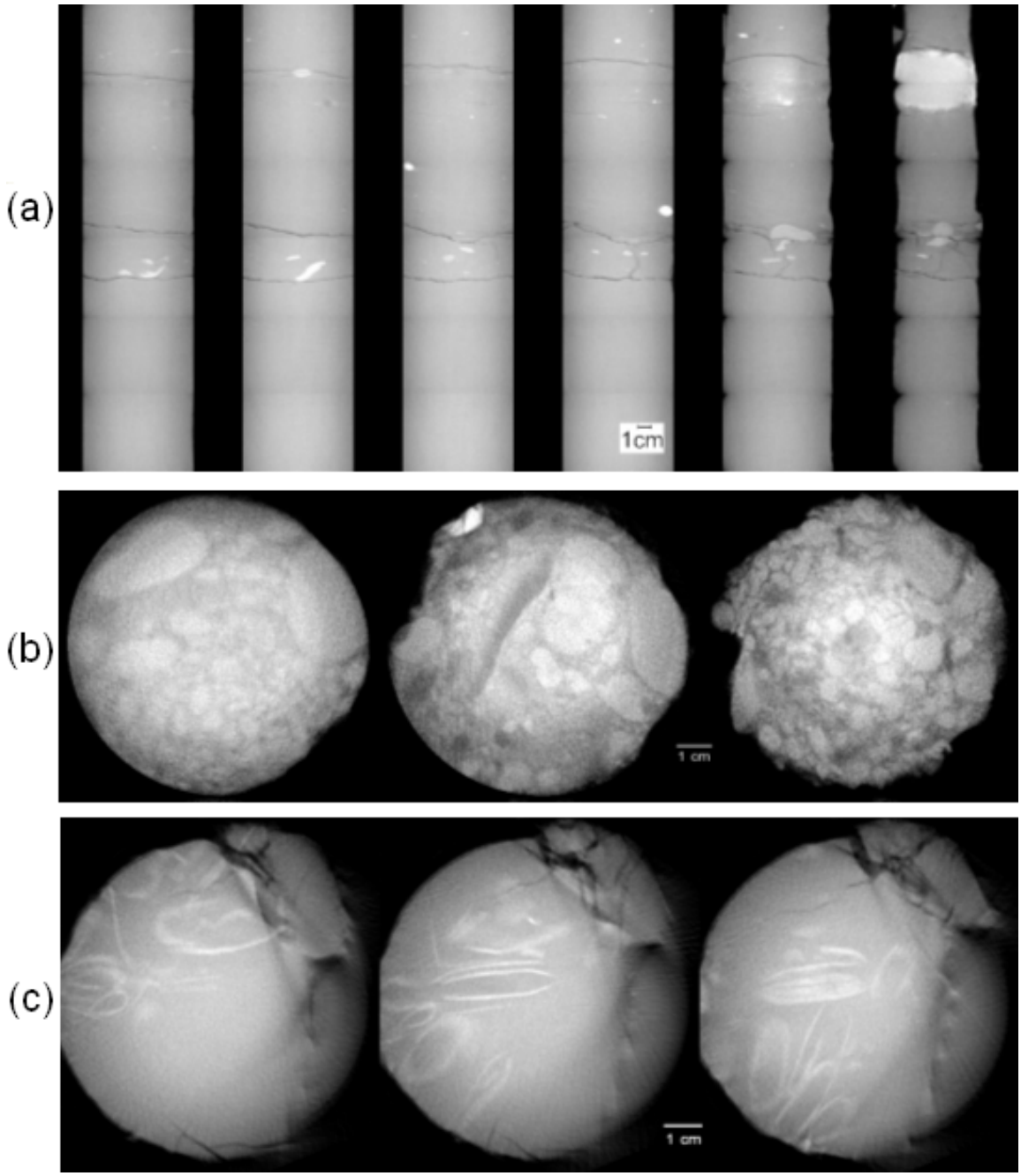

Figure 12. X-ray CT images of core recovered at Hot Ice No. 1 (a) Vertical slices through an unlithified sand, with abundant fossil shells. The large bright region is a clay ironstone concrete. Rounded dense objects are quartz pebbles. (b) Horizontal images of a permafrost conglomerate cemented together by a sand/ice matrix. (c) A sandstone core with abundant mussel fossils.

Conclusions

X-ray CT imaging of recovered core adds significantly to the amount of information that can be systematically obtained in the field. Structural information, porosity, and phase-saturation can be obtained. High-resolution images of whole-core permit intelligent subsampling locations to be chosen so that they either intersect or avoid specific features. The portable system detailed here offers significant improvements in image quality over previous x-ray CT systems by incorporating specially designed collimators and filters to optimize the x-ray beam path.

By minimizing the sample volume enclosed by radiation shielding, carefully selecting ruggedized components, and by severely limiting infrastructure requirements, the x-ray CT we developed is able to be easily transported and operated. The vertical core orientation minimizes the footprint of the instrument, so that it can be easily incorporated into working lab space. By performing imaging at the drilling location, the highest quality data can be obtained before transport and storage lead to core degradation. This is especially important when looking at ephemeral properties, such as gas hydrate saturation.

While the portable CT system shown here represents a paradigm shift from previous systems, numerous areas are open for continued development. These areas include incorporation of dual-energy techniques for mineral identification and improved density estimation, data mining software for identifying particular features or structures, and integration of the CT system into multiproperty measurement systems. The interface for accessing the enormous volume of data acquired in high-resolution three-dimensional imaging needs improvement, requiring advances in data handling and interpretation software.

Acknowledgments

This work was supported by the Assistant Secretary of the Office of Fossil Energy, Office of Natural Gas and Petroleum Technology, U.S. Department of Energy under Contract No. DE-AC03-76SF00098. The authors would also like to thank Dan Schneberk for making the CT image-processing code, Imgrec, available to us and Jacob Pruess for assistance in data analysis. In addition, we would like to thank Liviu Tomutsa for his careful review.

References

Blum, P., Physical properties handbook: a guide to the shipboard measurement of physical properties of deep-sea cores. Chap. 3 Gamma-Ray Densiometry, (1997) *ODP Tech. Note,* 26 [Online]. Available on World Wide Web: <http://www-odp.tamu.edu/publications/tnotes/tn26/INDEX.HTM>.

Boyer, R., Morgan, F., and Muskat, M., “A new method for measurement of oil saturation in cores,” *Petroleum Transactions*, AIME, (1947) 170, 15-33.

Feldkamp, L.A., Davis, L.C. and Kress, J.W., “Practical cone-beam algorithm,” *J. Opt. Soc. Am. A* (1984) 1, 612-619.

Freifeld, B.M. and Kneafsey, T.J., “Investigating methane hydrate in sediments using x-ray computed tomography,” in *Advances in the Study of Gas Hydrates*, (2004) Kluwer Academic/Plenum Publishers, New York

Hainsworth, J.M. and Aylmore, L.A.G., “The use of computer assisted tomography to determine the spatial distribution of soil water content,” *Aust. J. Soil Res.* (1983) 21, 435-443.

Hounsfield, G.N., "Computerized transverse axial scanning (tomography): Part I, Description of system," *British Journal of Radiology* (1973) 46, 1016-1022.

Kvenvolden, K.A. "Methane hydrate – a major reservoir of carbon in the shallow geosphere," *Chem. Geol.* (1988) **71**, 41-51

Morgan, F., McDowell, J., and Doty, E., "Improvements in the x-ray saturation technique of studying fluid flow," *Petroleum Transactions*, AIME, (1950) 170, 183-184.

Petrovic, A.M., Siebert, J.E. and Rieke, P.E., "Soil bulk density in three dimensions by computed tomographic scanning," *Soil Sci. Soc. Am. J.*, (1982) 46, 445-450.

Stern, L.A., Kirby, S.H., and Durham, W.B., "Peculiarities of methane clathrate hydrate formation and solid-state deformation, including possible superheating of water ice," *Science*, (1996) 273 (5283), pp. 1843-1848.

Tréhu, A.M., Bohrmann, G., Rack, F.R., Torres, M.E., et al., 2003. *Proc. ODP, Init. Repts.,* 204 [CDROM]. Available from: Ocean Drilling Program, Texas A&M University, College Station TX 77845-9547, USA.

Vinegar, H.J., "X-ray CT and NMR imaging of rocks," *J. Pet. Tech.*, (1986) 38, 257-259.

Wellington, S.L. and Vinegar, H.J., "X-ray computerized tomography," *J. Pet. Tech*., (1987) 39, 885-898.

Appendix B:
Coring for Methane Hydrate in Shallow Sands of the Sagavanirktok Formation, North Slope, Alaska – Phase I: Progress and Geologic Description

W.J. Ebanks, Jr. (PTS Labs)

W.D. Zogg (CORPRO)

Introduction

Most known subsurface North Slope gas hydrates occur in lower Tertiary sandstones and conglomerates overlying the eastern part of the Kuparuk River oil field and the western part of the Prudhoe Bay oil field (Collett, 1993). On the North Slope, the methane hydrate stability zone is areally extensive beneath most of the coastal plain province. The presence of methane hydrate has been inferred from numerous North Slope wells on the basis of well log responses calibrated to the response of an interval in a well where gas hydrates were recovered in a core by ARCO and Exxon (Collett, 1993).

Recognizing the potential importance of this untapped source of natural gas, Anadarko Petroleum Corp. is taking cores of sedimentary deposits in the subsurface of the North Slope that will provide material for experimentation leading to further evaluation of this resource. The location chosen for drilling and coring of a well, "Hot Ice No. 1", is on acreage leased earlier by Anadarko, about two miles south of the present boundary of Kuparuk River Unit and five miles east of the Meltwater development, in NW/4, Sec. 30-T9N-R8E, Umiat Meridian, on the North Slope of Alaska (Figure 1). This location was chosen to maximize the chance of encountering gas hydrates beneath Anadarko's leases.

Hot Ice No. 1 has surface conductor pipe set in permafrost at 107 ft MD. The well was drilled out of this casing on April 1, 2003. Original projected total depth was 2600 ft. Due to delays in the project commencement and subsequent early onset of spring thaw conditions on the North Slope, drilling was halted on April 13, 2003. The well was cored continuously from 107 ft to a total depth of 1,400 ft. Surface casing was set at this depth, and the well was placed in "suspended" status. Coring is to resume during the next drilling season.

Geology

Geology of the North Slope of Alaska has been the subject of numerous earlier reports (Morgridge and Smith, 1972; Jamieson et al., 1980; Carman and Hardwick, 1983; Molenaar et al., 1986; Werner, 1987; Gryc, 1988; Collett, 1993). The general setting of the location where the Hot Ice No. 1 well is being drilled is one of surface and near-surface gravels overlying a section of Cenozoic to Upper Cretaceous sedimentary deposits, which dip east-northeastward at a rate of approximately 100 ft per mile (Runyon, 2003). No faulting is known to affect these deposits in this local area.

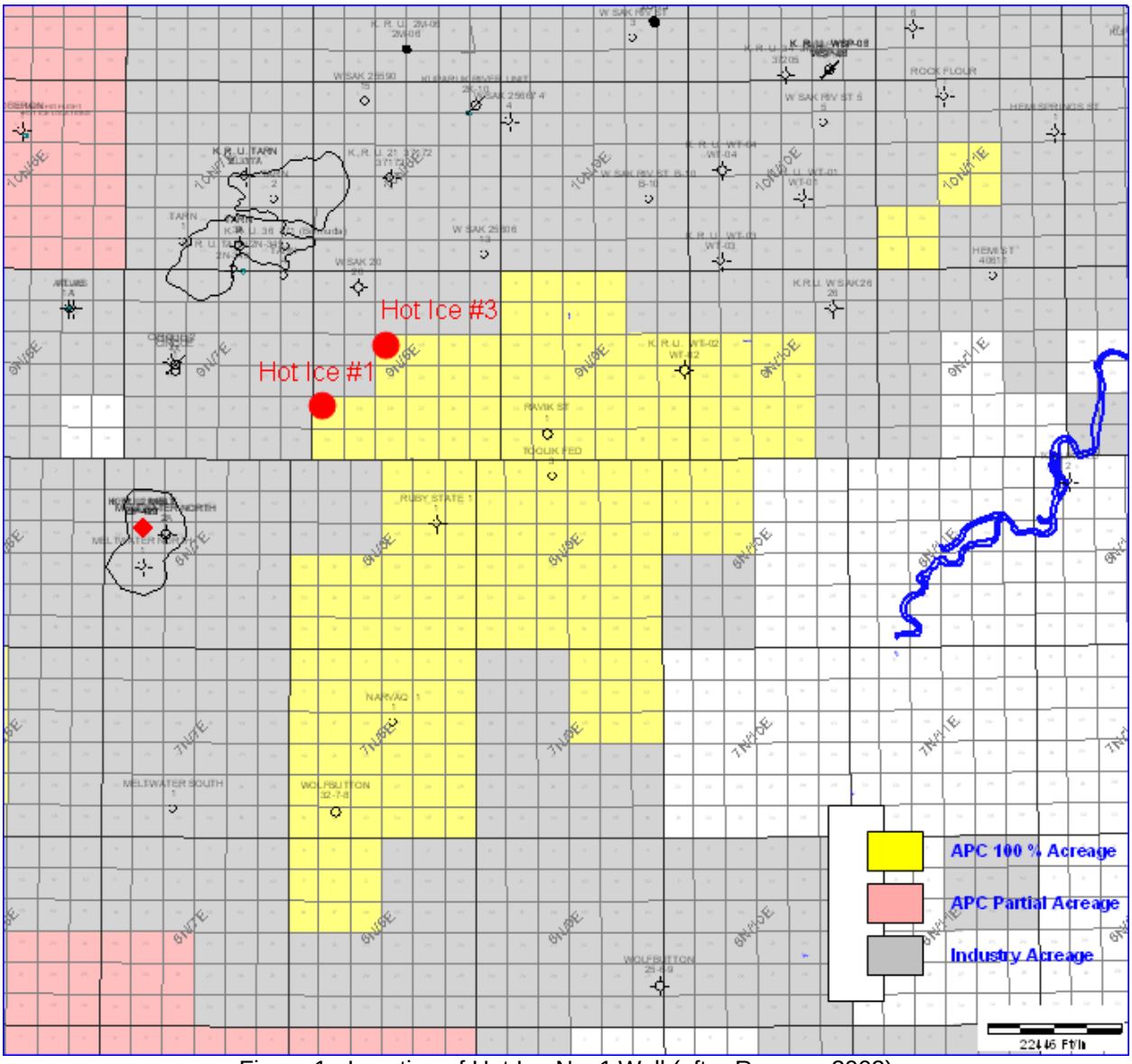

Figure 1. Location of Hot Ice No. 1 Well (after Runyon, 2002)

Ice-bearing permafrost varies somewhat in thickness from well to well, and the base of this interval has been found to occur at measured depths ranging from about 1100 ft to almost 1500 ft in wells nearest Hot Ice No. 1 (Newsham, 2003). In the Hot Ice No. 1 well, base of ice-bearing permafrost has been found at about 1260 ft. No methane hydrate has been found within the permafrost zone in this well. Observation of retrieved cores indicates that the chilled drilling mud, rapid coring rate, and wireline retrieval, contributed, as planned, to maintaining the frozen condition of sediments from the permafrost interval. It is expected that similarly frozen, gas-hydrate-bearing intervals that may be encountered below the permafrost zone will likewise remain frozen when brought to the surface, using this coring system. This will facilitate the recognition, sampling and preservation of these gas hydrates.

Sediments in which gas hydrates occur in this area of the North Slope comprise parts of the Sagavanirktok Formation, a thick succession of Late Cretaceous to Early Tertiary age (Molenaar, 1986; Collett, 1993) that comprises sandstones, mudstones, conglomerates and

coal. This includes the informal units, the Ugnu and West Sak sands (Collett, 1993), which are reservoirs containing heavy oil farther north (Werner, 1987). The Hot Ice No. 1 well began coring in frozen surface gravels at 107 ft, probably the Gubik Formation. After 7 ft of these gravels were cored, it passed into the Sagavanirktok Formation, but penetrated only as deep as the mudstone between the lower Ugnu sands and the West Sak sands (Werner, 1987; Runyon, 2003). No gas hydrates were encountered during the first phase of the coring operation.

The sediments above 1360 ft in the Hot Ice No. 1 well were deposited in environments that ranged from fluvial to marginal marine and upper deltaic. Alternations of sandstone, mudstone, conglomerate and coal form sequences that indicate an overall progradation and shallowing of environments of deposition with time. There is considerable vertical variability in these shallow sediments, implying lateral variability of the surface environments in which they were deposited. This variability is common in flood plain and deltaic or other nearshore environments. Although sharp lithologic contacts are not uncommon, there are no obvious unconformities within the sediment sequences cored.

Lithologic Logging

The graphic lithologic log prepared for this project (see companion Topical Report on Logging Operations) is the primary means of communicating information about composition of the sediments in the cored interval (107-1400 ft). This information provides a context for understanding variations in reservoir properties found during analysis of core. This lithologic log will be complemented by selected photos of whole core and of plugs taken for analysis, as well as measurements of porosity, permeability and other petrophysical properties and displays of curves from downhole wireline logs.

This log was compiled by rapid visual examination of each 10-ft segment of the 3.25”-diameter continuous core shortly after it was brought to the surface. This macroscopic core examination was necessarily brief because of the need to prevent the cores from thawing. After reaching the surface, each 10-ft segment was further subdivided into three 40-inch sections and part of the drilling mud scraped from one side. These sections were scanned for natural gamma ray radiation to compare with downhole wireline logs, for imaging in infra-red light, for white light photography and for logging by a surface-mounted CMR logging tool. Plugs (1 inch diameter) were taken from selected lithologies, and end pieces of some of these were examined microscopically for texture and mineralogy. The 40-inch sections were then placed in transparent plastic tubes, the open ends capped, and stored at sub-freezing temperature. Core recovery through the ice-bearing permafrost interval and to the total depth of the first phase of drilling, 1400 ft, was excellent – about 95%.

The aspect of core description that has been minimized here is the observation of sedimentary structures. Because core could not be slabbed and cleaned for extended examination, only a quick appraisal of those features that could be seen on the outside of scraped core surfaces was logged. Trace fossils other than root casts were not observed, possibly because of this limitation on the logging methods. Samples were not taken for micropaleontologic analysis, so there is no information of this type to contribute to interpretation of environments of deposition. However, these continuous cores of the shallow formations provide a far more accurate representation of the lithologies drilled and their variability than can be obtained from logs of only cuttings.

Lithologic Description

Subdividing the lithologic section for description is based on recognition of changes in predominant rock types, on gradations in grain size within short intervals, the nature of contacts between rock types, and on correlation to nearby well logs. The sediments are given equivalent rock names, even though they are mostly unconsolidated except for the ice cement. **Table 1** summarizes the occurrences of each lithology logged. Below the table are summaries of each major section of core.

Table 1. Lithologies represented in each interval described

INTERVAL	Measure	Conglomerate	Sandstone	Mudstone	Coal	Lost Core
114'-143'	Thickness	6.20	1.00	28.20	0.00	0.40
	%	21.38	3.45	97.24	0.00	1.38
143'-252'	Thickness	1.60	52.00	28.50	27.10	0.00
	%	1.47	47.71	26.15	24.86	0.00
252'-446'	Thickness	8.00	142.60	26.80	12.70	3.80
	%	4.12	73.51	13.81	6.55	1.96
446'-649'	Thickness	131.85	43.50	26.30	0.15	0.80
	%	64.95	21.43	12.96	0.07	0.39
649'-760'	Thickness	13.40	60.20	24.90	5.60	4.30
	%	12.07	54.23	22.43	5.05	3.87
760'-951'	Thickness	0.00	67.90	97.80	3.50	21.40
	%	0.00	35.55	51.20	1.83	11.20
951'-1187'	Thickness	0.00	67.30	125.10	33.50	9.90
	%	0.00	28.52	53.01	14.19	4.19
1187'-1358'	Thickness	0.00	131.70	32.00	0.00	6.90
	%	0.00	77.02	18.71	0.00	4.04
1358'-1400'	Thickness	0.00	0.10	39.70	0.10	2.70
	%	0.00	0.24	94.52	0.24	6.43
TOTAL	Thickness	161.05	566.30	429.30	82.65	50.20
	%	12.46	43.80	33.20	6.39	3.88

114’ – 143’

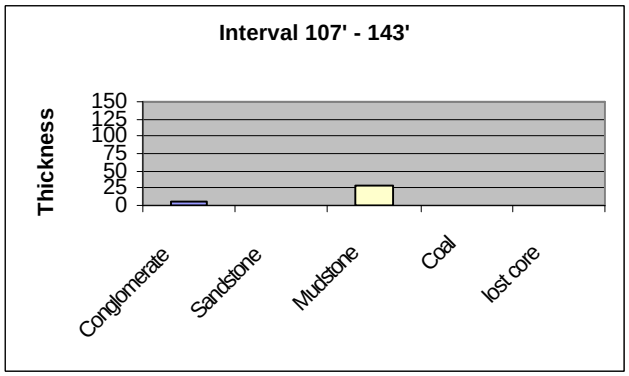

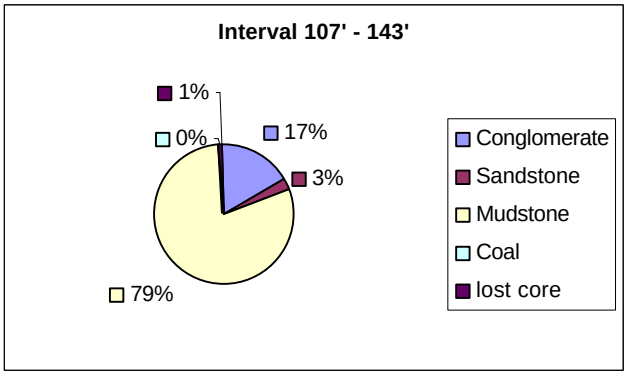

Beneath the surface gravels is a thick (29 ft) section of horizontally laminated mudstone, which contains a few silty laminae. This mudstone probably is the uppermost part of the Sagavanirktok Formation in this area. Without the aid of paleontology or palynology, its age and environment of deposition is in doubt. The same may be said for the rest of the cored interval; except that correlation with wireline logs of nearby wells may help in determining approximate age, as well as analogy with sediments in other areas may help interpret environments of deposition.

143' – 252'

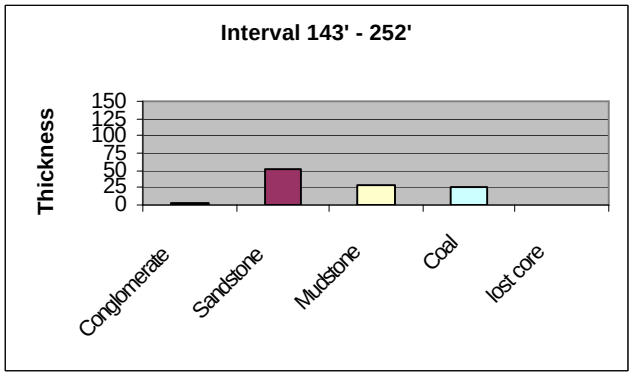

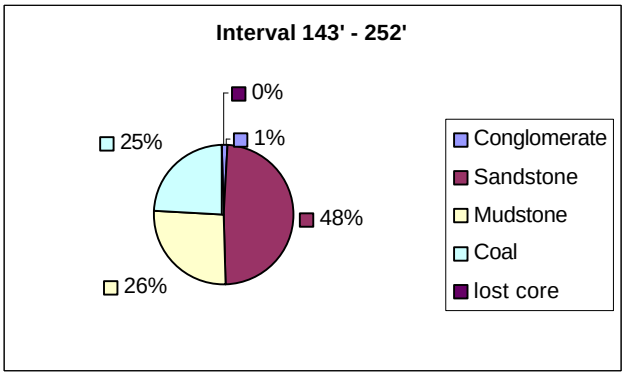

From a depth of 143 ft to 252 ft is an interval of sediments consisting of an overall fining-upward sandstone-mudstone sequence overlain by thick coal. The 49 ft of sandstone at the base is medium- to coarse-grained and contains carbonaceous fragments and disseminated organic matter probably eroded from a coal below. The sandstone becomes fine to medium grained upward and, at the top, includes scattered pebbles and a few shaly laminae. At the top, the sand is interbedded with a few thin mudstones and is overlain by 18 feet of mudstone that is silty and sandy, becoming carbonaceous just below the overlying coal. The 36 feet of coal is actually four distinct beds separated by thinner, very carbonaceous mudstones. The coal is black, soft and impure lignite containing argillaceous and sandy streaks.

252' – 446'

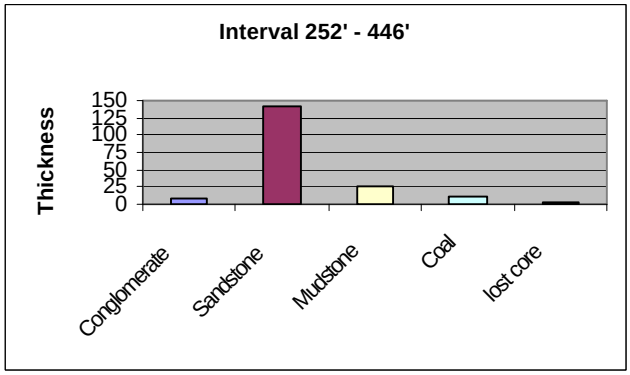

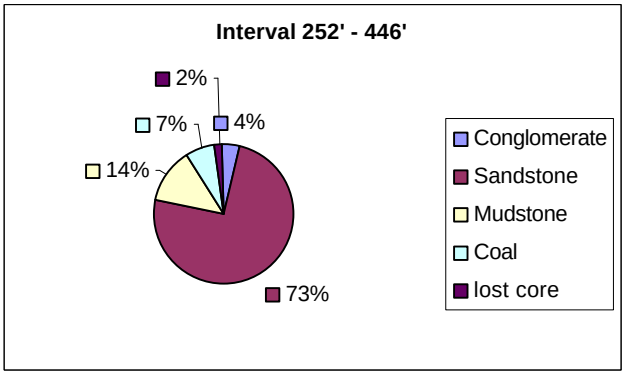

A similar sequence, sandstones below mudstone, below thick coal, is present in the interval 252-446 ft. There are significant differences in this interval from that above. At the base are two sequences with a basal conglomerate grading upward into pebbly sandstone, then sandy mudstone. Above this is a thick interval, 110 ft, in which sandstone is the main lithology. This

sandstone interval, however, comprises numerous thinner intervals in which medium-to-coarse grained sand grades to fine-to-medium sand. The coarser sandstone has low-angle cross bedding, while the finer grained sands have mostly horizontal bedding. Most of the thin sands grade upward into sandy mudstone. The mudstones commonly have carbonaceous particles on bedding planes. The sandstones at the top of this interval are argillaceous. Those at the base are very carbonaceous.

Above this interval of sandstones and thin mudstones is dark gray or brown and black mudstone in which lenses of ice have formed along bedding planes. Above this mudstone is a black or dark brown lignitic coal, which also includes several ice lenses.

446' – 649'

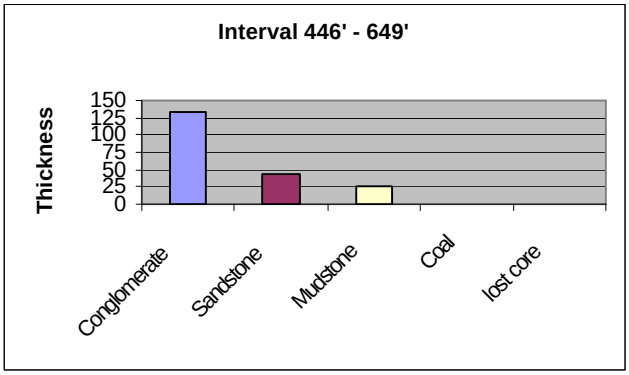

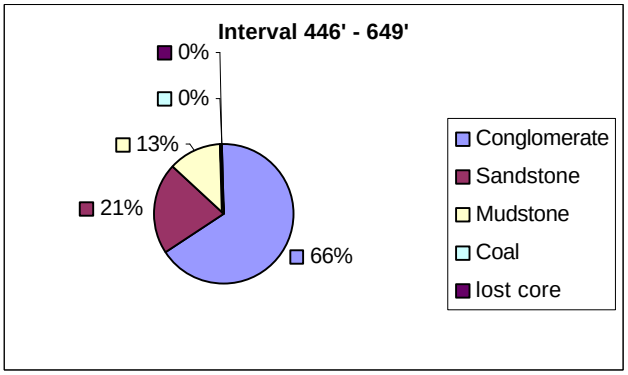

The next deeper interval, 446 ft to 649 ft, is distinctive in comprising mostly conglomerate in beds as thick as 21 ft. Conglomerate beds are separated by thinner pebbly sandstones or sandy mudstones. Carbonaceous material is commonly present. The conglomerates consist of clasts of quartz, chert and lithic fragments of various types. Mudstone intraclasts also are common, most notably angular intraclasts of tan mudstone that probably are rip-up clasts, as they resemble some of the interbedded mudstones. Most of the conglomerates are clast-supported, but some more poorly sorted layers have sandy matrix support. Ice lenses are numerous in the interval 510-540 ft.

649' – 760'

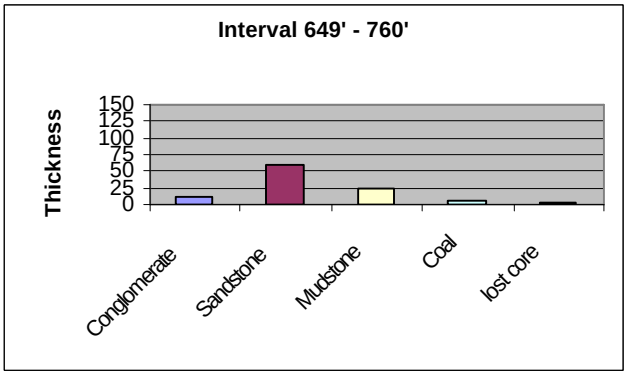

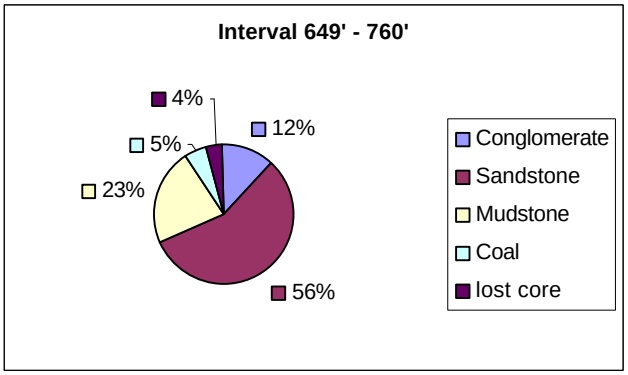

The interval 649-760 ft is very different from the interval above. This is the most complexly interbedded interval in the core. It is marked by numerous thinner sequences consisting of

conglomerate or sandstone grading upward into mudstone. This variability is reflected also in the thin sandy interbeds in the mudstones and thin mudstone layers in the sands. Above 730 ft, carbonaceous matter is very common, accentuating wispy horizontal laminations and low-angle cross beds in the sandstones. The interval is capped by a 9-ft thick mudstone and 6 ft of argillaceous lignite coal with ice lenses.

760' – 951'

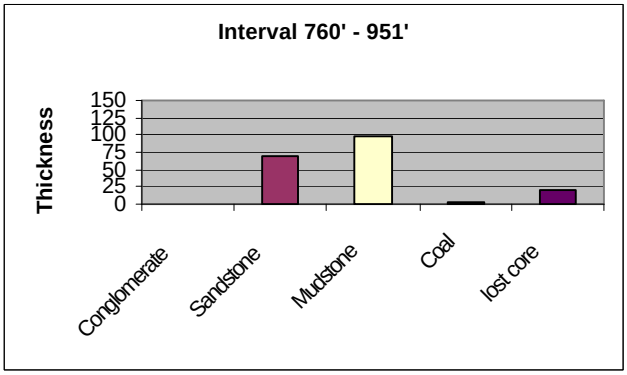

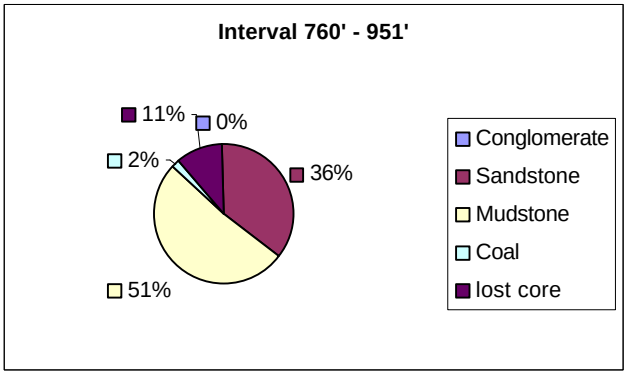

The interval 760-951 ft includes several sequences of carbonaceous sandstone that become more argillaceous and grade into sandy mudstone above. In this aspect, the interval is similar to others above. One distinctive feature is the thin 5-ft oil-bearing sandstone beneath a 1-ft thick coal at the top of the interval. The oil in this sand is a heavy oil that does not "cut" with toluene solvent. Nevertheless, this occurrence is of interest, because it is the only such oil-bearing sand in the section cored.

Beneath a 3-ft thick coal at 835 ft is a 48-ft thick, carbonaceous, sandy mudstone which contains fossil plant rootlets. Within this unit are several thin sandstone beds that have horizontal lamination or low-angle cross bedding. Numerous ice lenses occur in this mudstone.

In the deepest 50 ft of this interval (901-951 ft) is a sequence that is important because it marks a change in style of sedimentation. At the base of this unit is a mudstone that grades from slightly silty claystone below to sandy, silty mudstone, then upward to argillaceous, carbonaceous, very fine-to-fine grained sand and finally, to fine-to-medium grained sand with low-angle cross bedding at the top. This is the first sequence of sediments exhibiting this motif of coarsening and "cleaning" upward that was encountered during coring. It may signify an important change in the environment of deposition.

951’ – 1187’

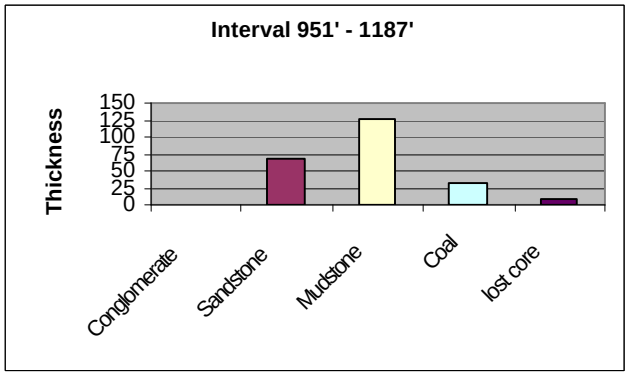

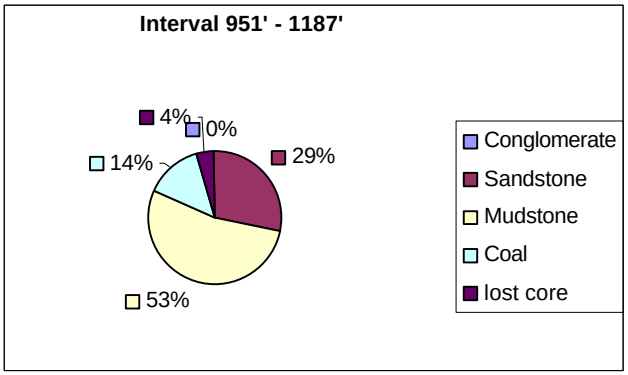

In this interval are several fining-upward sandstone/mudstone/coal sequences, as described above, but with occasional coarsening-upward sequences intervening. Intervals of each lithology tend to be thicker than the alternations cited above.

At the top of the interval is a very thick 28-ft lignitic coal. At the top, this coal is argillaceous with numerous ice lenses, and at its base are interbedded, carbonaceous mudstones and thinner coals. Below this, other sandier sediments and coal are present.

Between 1000 ft and 1076 ft, two prominent sandstones grade upward into sandy mudstones with thin coals. These sandstones are carbonaceous, and even contain small fragments of fossil wood. They have lenticular bedding and wavy laminae as well as horizontal bedding. Below thin coals the sediment commonly contains root traces.

The lower half of this interval, 1076-1187 ft, is predominantly mudstone. The few sandstones are very argillaceous. Very carbonaceous intervals of mudstone are common, and some exhibit color-mottling and root traces.

1187’ – 1358’

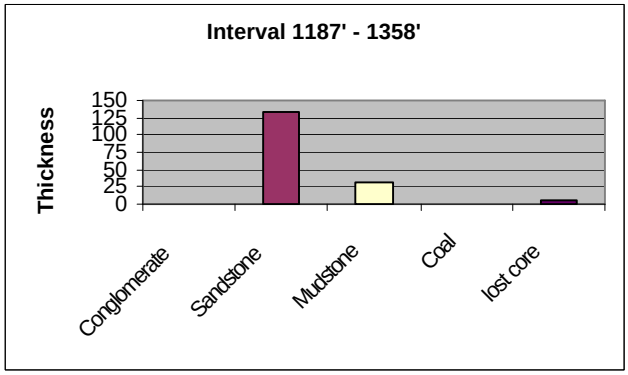

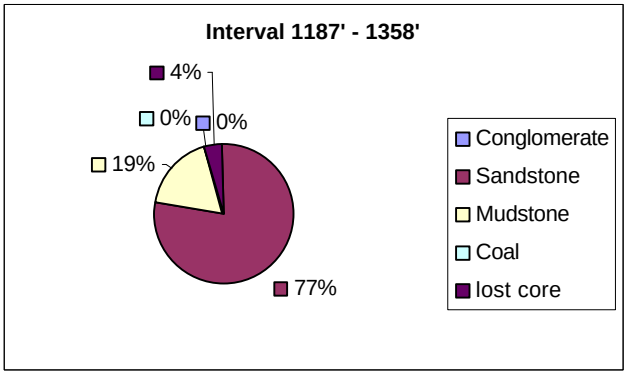

The interval 1187-1358 ft, in contrast to the one above it, consists mainly of sandstone. One prominent mudstone, 1226-1242 ft, is present, but otherwise, the frequent mudstones are very thin and sandy. The sandstones typically are fine-to-medium grained. They have horizontal or low-angle cross lamination. The sands are usually argillaceous, with occasional carbonaceous

intervals. Some sands appear finer grained and more argillaceous upward, as others appear to coarsen and become less argillaceous upward.

An important aspect of this interval is that it includes the base-of-permafrost in this well, at about 1260 ft. This coincides with a noticeable change in mechanical properties of the cored rocks, as well as changes in resistivity and acoustic wireline log responses.

1358' – 1400'

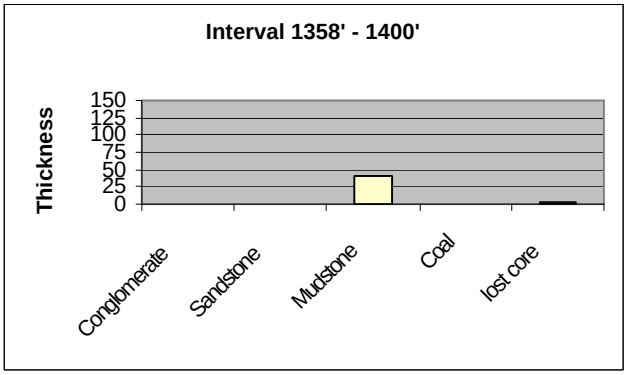

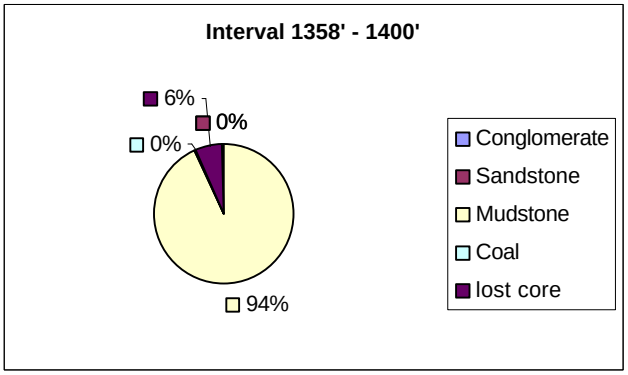

The top of this deepest interval cored is recognized as the base of the Ugnu sands, the informal stratigraphic unit described earlier. This interval is correlated widely as the unnamed mudstone unit between the Ugnu and underlying West Sak sands (Runyon, 2003). The core of this interval comprises only monotonous, slightly silty mudstone with only a very thin coaly bed near the top.

The well had not completely penetrated this interval of mudstone when coring was halted at the end of Phase I and surface casing set to protect the permafrost. The well was placed in suspended status.

Summary and Interpretation (Phase I)

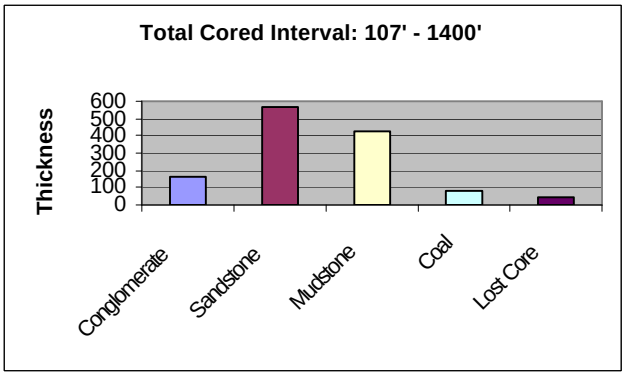

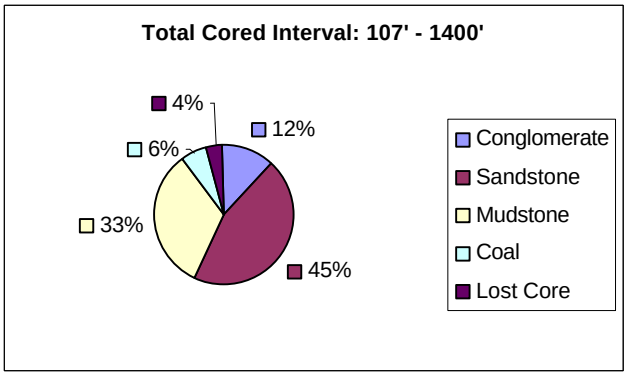

A thick section of sandstones, mudstones, coals and conglomerates was cored continuously in the Anadarko Hot Ice No. 1 well during Phase I (the 2003 drilling program) from 107 ft to total depth of 1400 ft. At this depth the well was temporarily suspended because of early thaw beginning to occur on the North Slope. Surface protective casing was set at this point, just

below the base of the ice-bearing permafrost. No gas-hydrate-bearing sediment had been encountered as of the suspension of coring.

Correlations with wireline logs and descriptions of cuttings taken in nearby wells lend support to the idea that frozen sediments cored in this well are part of the Sagavanirktok Formation. The cored sediments are part of a thick sequence of rocks that are probably of late Cretaceous to early Tertiary age. Paleontologic evidence of this age is lacking, but stratigraphic position of these units and absence of tectonic complications in this area of the North Slope support this age assignment. Like similar sequences studied in nearby outcrops of the North Slope, they have characteristics of marginal marine or deltaic deposits. Some authors refer to these sequences as the "Deltaic Unit" of the Brookian Sequence (Molenaar, 1983), referring to their origin as part of the deposits transported from the south and southwest to fill the tectonic basin that formed with uplift of the Brooks Range. If these correlations are correct, then the bottom of the cored interval at 1400 ft was in the mudstone that separates the Ugnu sands from the underlying West Sak sands, informal members of the Sagavanirktok Formation.

The thick mudstone at the base of the cored interval, 1358-1400 ft, may be a marine tongue of fine-grained sediment representing a brief transgression of the late Cretaceous sea over the mostly terrestrial environments of this area. Sandy sediments above this mudstone are thin sequences that form alternations of fining-upward and coarsening-upward units. They become very carbonaceous upward and are capped by a thick coal and mudstone interval. This overall interval includes a prominent, very sandy and carbonaceous, mudstone unit more than a hundred feet thick. These sequences, from 951 ft to 1358 ft, probably represent the attempted, repeated progradation of several wedges of sandy sediment from the southwest into a more marine environment to the northeast. These progradations culminated in the persistent presence of coal-forming environments in this area, such as coastal marshes and delta-top swamps, which resulted in the thick coals at the top of the sequence.

Following this time of coal formation, sand and mud sedimentation resumed, and the first 50 ft of deposits above the coal was a coarsening-upward sequence of sandy mudstone and sandstone. Following deposition of these units, however, the alternations of finer grained and coarser grained sediments mostly followed the pattern of fining-upward. These patterns suggest deposition of distributary mouth bars and crevasse splay sediments, which prograded over a subsided area of coastal swamp environments. These deposits were then buried by deltaic distributary and overbank sediments as shallow water deltas worked over the prograding coastal plain. Another coal, 6 ft thick, was deposited at the top of these sediments, attesting to the natural variability inherent in coastal plain deposits. This sequence of events is represented by the sediments cored from 649 ft to 951 ft.

After this period of sedimentation when alternations of coarser and finer grained sediments were so common, a thick sequence of mixed-clast conglomerates was deposited in this area, seen in the sediments from cores of the interval 446 ft to 649 ft. This would seem to represent a time of maximum progradation of the onshore, terrestrial environments of deposition, such as when short-headed, high energy streams could have crossed a very narrow deltaic shelf and/or when there was increased tectonic activity in the source area to the south and southwest, as suggested by Molenaar (1983). This would have resulted in very coarse sediment being delivered to this area of deposition.

The next phase of sedimentation in this area resulted from return of more typical upper deltaic environments, with fluvial sequences being dominant over the area, represented by cores from 143 ft to 446 ft. The earlier of these sediments may have been deposited by braided streams,

as they contain basal units of pebbly, coarse sand, grading upward into finer grained sediment. Higher in the section, sandstones are fine-to-medium grained, also grading upward into sandy mudstones. Two prominent coals occur within and at the top of this interval of fluvial sediments, again suggesting the shifting nature of environments of deposition and re-establishment of peat swamps and lakes or other very low energy environments in this area.

Finally, just above the uppermost coal, is a thick mudstone, from 114-143 ft, which may represent another incursion of marginal marine conditions over the low-relief, coastal or freshwater swamp environments represented by the underlying coal. Above this mudstone are a few feet of conglomerate, stained dark by carbonaceous material from above, that probably represents the near surface gravel of the Gubik Formation, of Tertiary age.

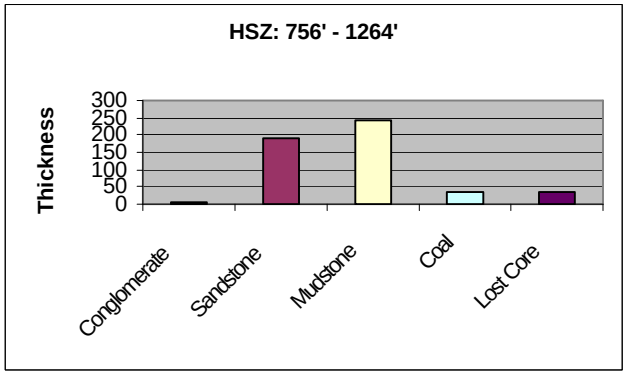

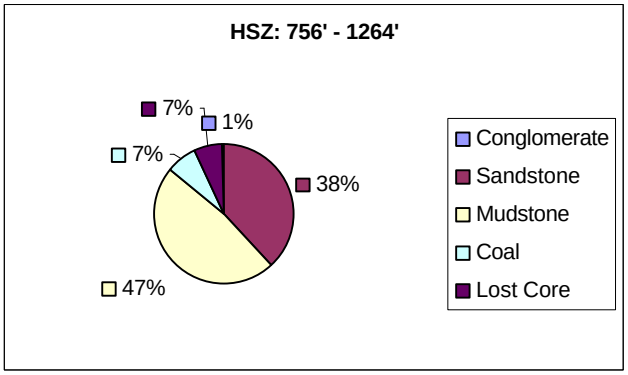

Coring for Methane Hydrate in Shallow Sands of the Sagavanirktok and Canning Formations, North Slope Alaska – Phase II: Geologic Description

W. J. Ebanks, Jr. (PTS Labs)

W. D. Zogg (CORPRO)

Introduction

Continuous coring in the Hot Ice No. 1 well resumed during January 2004 following suspension of coring in April 2003 (see Figure 1). Cores were recovered from the interval 1403 ft to total depth of 2300 ft during this Phase II of the operation.

Background on the purpose of the project, location of the well, and geology of the cored interval are provided in the previous Phase I report. Methods of obtaining cores and handling them following retrieval, as well as methods of describing and logging the cores are also discussed in the Phase I report. *(Note: Phase I report is attached.)*

Geology

Sediments cored during Phases I and II of the Hot Ice No. 1 project comprise the Sagavanirktok Formation and part of the underlying Canning Formation, of Tertiary and latest Cretaceous age. Two informal units, the Ugnu Sands and West Sak Sands, which occur near the base of the Sagavanirktok, are separated by a regionally extensive unnamed mudstone (Collett, 1993; Werner, 1987; Runyon, 2003). Coring during Phase I ceased in this mudstone at 1403 ft, and casing was set at 1358 ft. The base of the permafrost was found at about 1260 ft.

Coring during Phase II resumed at 1403 ft. Coring penetrated the remainder of the unnamed mudstone, the underlying West Sak Sands, and part of the Canning Formation mudstones and sandstones. The sediments, though unfrozen and somewhat unconsolidated, are competent enough to have afforded excellent recovery – 94.5% of the cores taken.

Sediments cored during Phase II, from 1403 ft to 2300 ft, are not as variable in character as those encountered during Phase I. This reduction in variability, overall more fine-grained texture of the sediments, and common occurrence of layers of shell fragments and whole bivalve shells, indicate deposition of these sediments in shallow marine shelf environments. Once again, support for this conclusion from paleontology or from the study of sedimentary structures and trace fossils (ichnology) is lacking because of the limited means available to analyze the cores.

Conglomerate and coal, which are so common in cores from Phase I, are not present in cores from Phase II. In later cores, alternations of sandstone and mudstone, across a range of scales, are common. Contacts between sandstones and mudstones are almost all gradational changes of texture, or they occur as alternations of thin beds of contrasting texture. Unlike earlier Phase I cores, the pattern or motif that is most often seen is one of grain size coarsening upward. Sandstones are only occasionally as coarse as medium-sand size. Silt-size particles

are very common in beds that are predominantly sandstone or mudstone, acting as part of the matrix in sandstones and forming thin laminae in the mudstones. No obvious unconformities occur within the cored interval.

Minor shows of heavy oil were found in thin sandstones between 2100-2250 ft, and very minor shows of gas were seen as bubbles breaking out of the split core tube or bleeding from tight sandstones or fractured mudstones; however, no gas hydrates were encountered during this phase of the coring operation.

Lithologic Logging

The graphic lithologic log of the sediments penetrated is the primary means of communicating information about the composition of the sediments in the cored interval (1403 ft-2300 ft). This is presented in the companion Topical Report "Logging Operations." This graphic information provides a context for understanding variations in physical properties of the cores found during petrophysical analysis.

The same methods of handling and brief description have been used in Phase II as were used in Phase I, with the exception that no logging by a surface-mounted CMR logging tool was attempted. Although X-Ray imaging of selected intervals of core was performed, results of this were not available at time of reporting.

Lithologic Description

1,403' – 1,462'

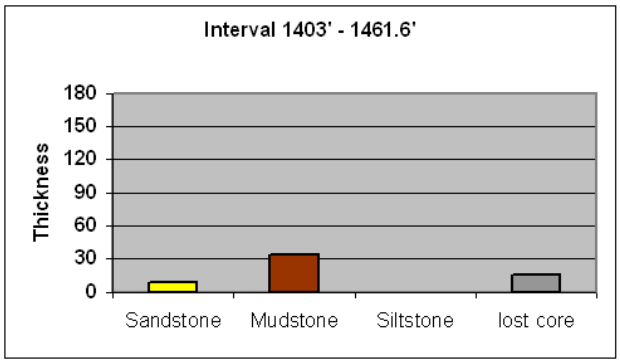

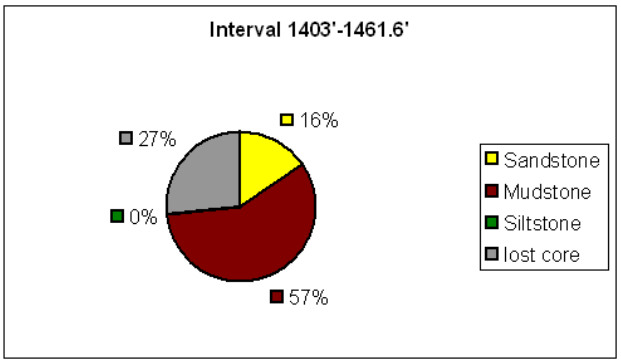

This shallowest interval cored in Phase II is a downward continuation of the mudstone occurring from 1358 ft to 1403 ft in Phase I cores. Only a very silty, argillaceous sandstone from 1436 ft to 1444 ft breaks the monotony of the thick mudstone. This mudstone is the unnamed unit that separates the Lower Ugnu Sands above from the Upper West Sak Sands below (Runyon, 2003).

1,462' – 1,537'

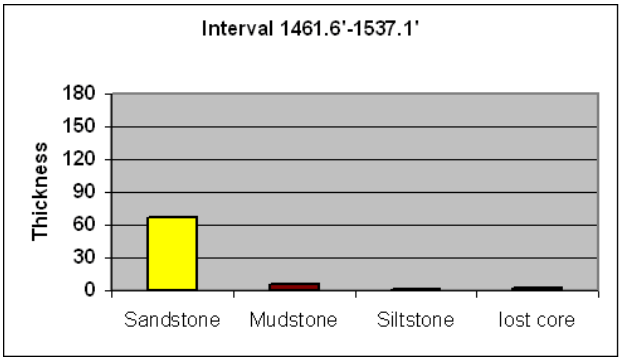

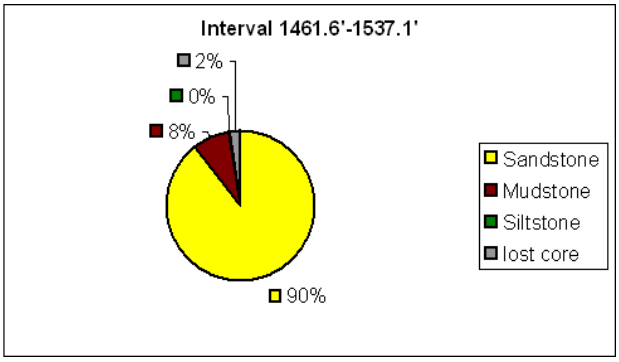

This uppermost of the sandstone intervals cored is also the thickest sandstone. Transition to the overlying mudstone is a series of three thin beds of sandstone, each underlain by carbonaceous, silty mudstone. The sandstones are fine- to very fine-grained, and contain broken shell fragments. Below this, from 1476-1509 ft, is a fine- to medium-grained sandstone that becomes cleaner and coarser upward, and which includes several thin beds of shells. This cleaner, coarser part of the sandstone overlies several alternations of sandstone, siltstone and mudstone, which form thin, fining-upward units above the mudstone below. A hard, calcite-cemented bed at 1482 ft has a characteristic response on wireline logs, which, like others below, is useful for calibrating the logs to the core. A coaly lamina occurs at 1468 ft. The most common sedimentary structure throughout this sandstone is horizontal or very slightly inclined parallel laminae. Between 1510-1520 ft, gas shows were noted in the siltstones and mudstones.

1,537' – 1,727'

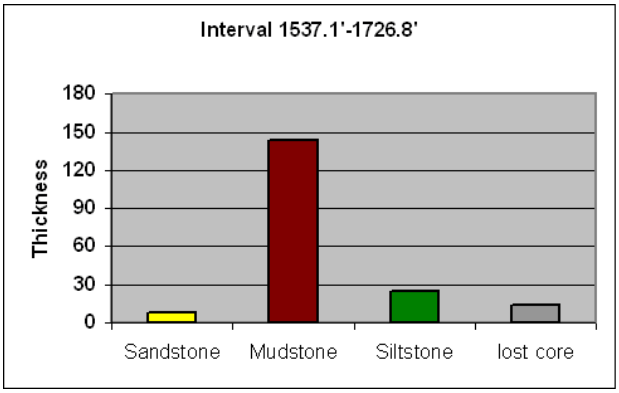

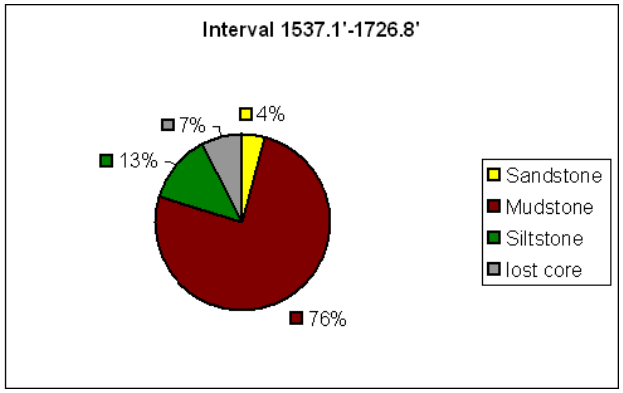

The sandstone from 1462-1537 ft caps a lengthy interval of mostly silty mudstone from 1537-1727 ft. Correlation of wireline logs suggests that the upper part of this mudstone section is equivalent to sandier intervals in nearby wells, that is, the lower part of the West Sak Sands. Here, coarser intervals are merely slightly sandy siltstones.

These siltstones cap upward-coarsening units of varying thickness. The uppermost unit contains abundant carbonaceous matter, which imparts a very dark color and horizontal lamination to the sediment. Other thin, upward-coarsening units below this one contain layers of shell fragments within the siltstones and whole or fragmented shells within the silty mudstones. Beneath the siltstone, which occurs at 1609 ft to 1620 ft, is the thickest continuous

mudstone interval cored (1620-1692 ft). Scattered throughout this variably silty mudstone are whole and fragmented shells of mollusks, probably bivalves. Horizontal lamination is the only sedimentary structure observed in this unit.

Beneath this mudstone interval, from 1692-1703 ft is a very fine-grained sandstone with sandy siltstone interbeds. At 1701 ft is one foot of calcite-cemented, very fine-grained, very silty sandstone, whose expression on wireline logs, like the one at 1482 ft, is a useful marker for calibrating logs and core. Beneath this sandstone is an interval of thin, fining-upward, sandy and silty mudstones that is a transition from the sandstone below into the lengthy mudstone above.

1,727' – 1,825'

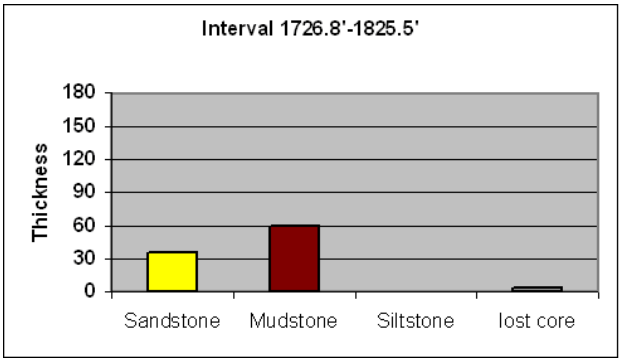

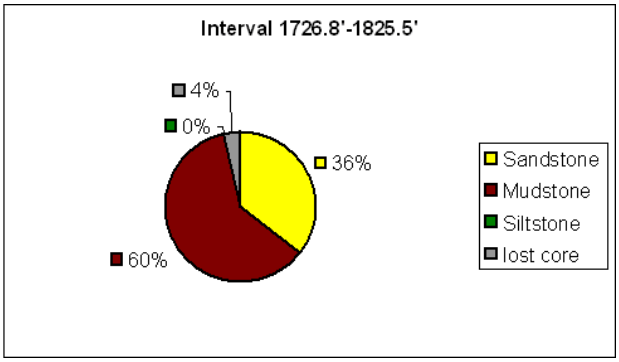

This next deeper interval comprises about equal thicknesses of sandstone and mudstone, forming a coarsening-upward pair of lithologies. The uppermost sandstone, from 1727-1788 ft, is very porous, being 9 ft of well-sorted, fine-grained, friable sand. The rest of the sandstone is very fine- or fine-grained, very silty, and includes scattered carbonaceous matter and shell fragments. The mottled color and texture of the sandstone suggests the presence of burrowing. At 1753-1760 ft are three cemented sandstones similar to those mentioned above. Beneath these hard sandstones are interbedded, shelly, silty, sandstone-mudstone couplets forming a gradation from the mudstone below.

From 1788-1825 ft is another continuous silty mudstone with horizontal or inclined, parallel laminae and scattered shell fragments. Color of the mudstone ranges from olive-gray to dark gray, depending on the silt content. There is a gradational contact with the sandstone below.

1825' – 1908'

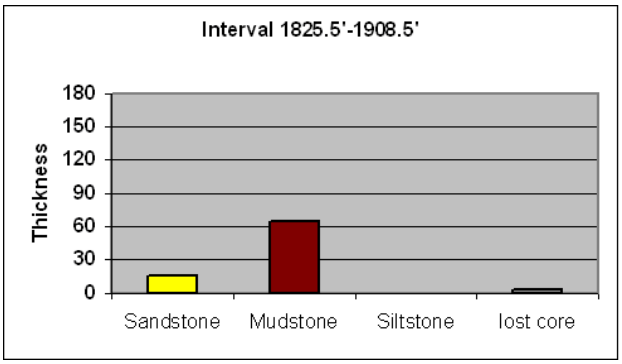

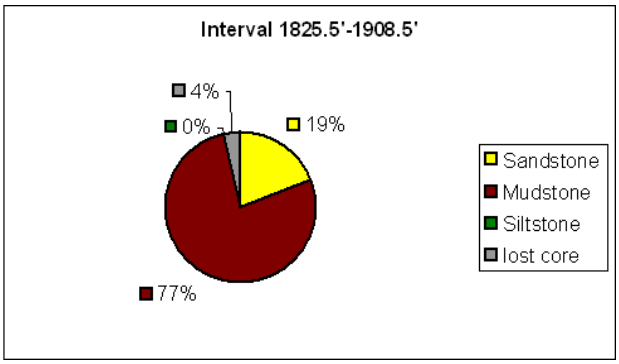

This interval comprises two very similar sequences of sandstones above thicker mudstones, forming coarsening-upward couplets. The sandstones are medium-to very fine-grained, silty and contain numerous shell fragments. They include several thin mudstone beds. The mudstones are slightly silty, with distinct horizontal or low-angle cross laminae of very fine-grained sand and silt. A thin, hard, calcite-cemented sandstone occurs at 1906 ft.

1,908' – 1,998'

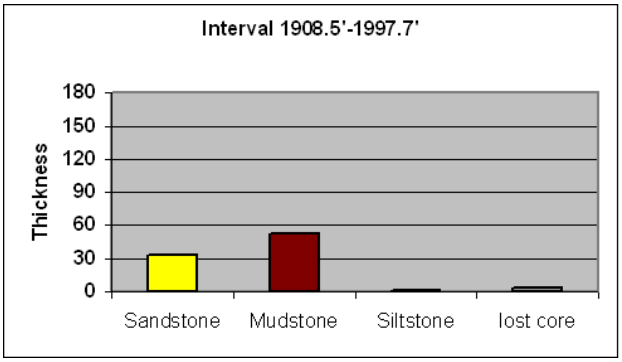

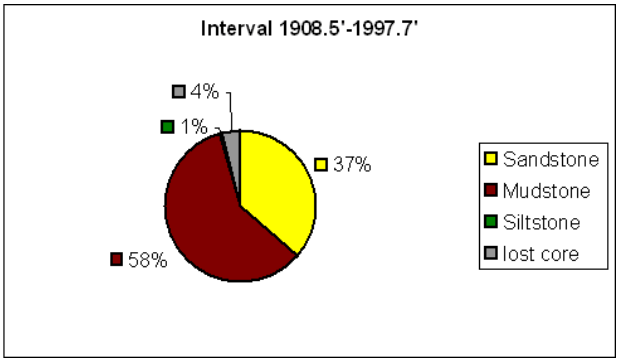

This interval, like the ones above, consists of alternations of sandstone and mudstone, the sandstones of greater thickness and number above, and mudstones thicker and more continuous downward. The sandstones are dark gray, fine- or very fine-grained, silty and argillaceous, and they include numerous thin beds of silty mudstone and shell fragments. Horizontal lamination is the most common structure. A thin (<0.5 inch) layer of granule-size particles is present at the contact of the top sandstone and its underlying mudstone.

The mudstones are olive gray to dark gray, silty and slightly sandy, with scattered shell fragments being common. Carbonaceous laminae are dark gray. Thin, cemented claystone laminae at 1997 ft are tan in color.

1,998' – 2,201'

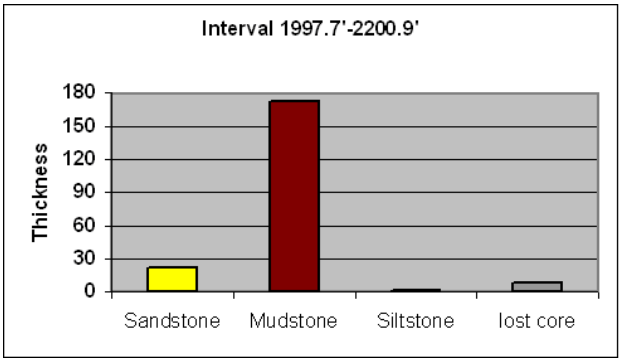

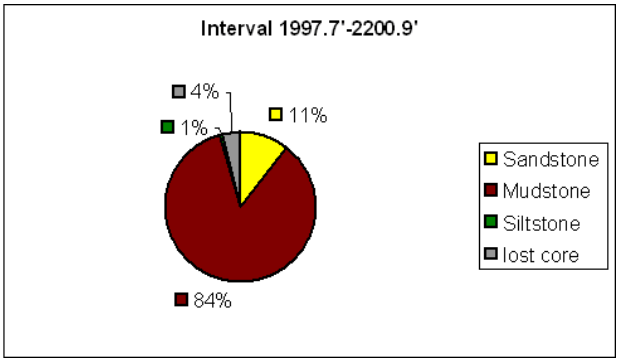

This lengthy interval includes numerous thin sandstones interbedded with thicker mudstones in repeated patterns of coarsening-upward sediment couplets. Sandstones are no thicker than 3 ft, but mudstones are much thicker. Sandstones typically are very fine- to medium-grained, horizontal or low-angle cross-laminated, and they contain carbonaceous debris. Oil stain and odor are present in sandstone at 2117-2120 ft. The oil appears to be very viscous and immobile.

Mudstones in this interval are similar to those in other intervals. They range in color from olive gray to dark gray and contain abundant silty laminae as well as disseminated silt, especially as they grade upward into sandstone. Horizontal lamination is most common. A cemented sandstone layer occurs at 2169 ft in a thick interval of mudstone.

2,201' – 2,300'

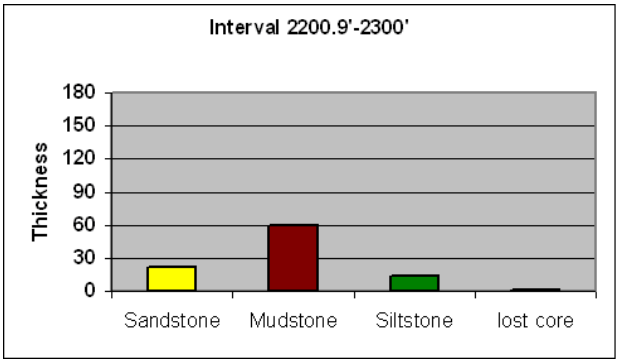

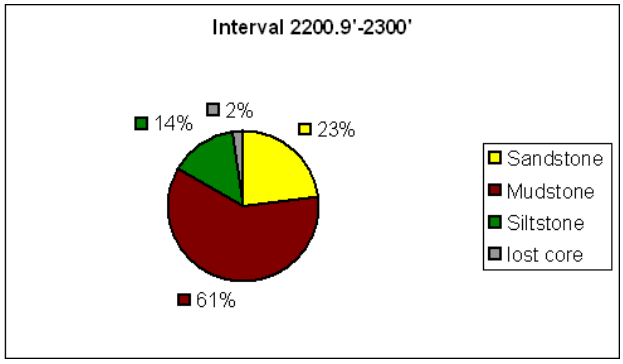

This interval comprises three smaller intervals that, together, form an upward-coarsening sequence. The top unit, 17 ft thick, is a series of amalgamated, thin sandstones. These sands are fine- to medium-grained, and individual sands vary in thickness from 1.5 ft to 3 ft. Each sand coarsens and becomes cleaner upward. More argillaceous sandstone occurs at the base, interbedded with sandy, carbonaceous siltstone. The middle unit is a 22 ft-thick siltstone. This siltstone includes numerous sandy and argillaceous laminae and abundant shell fragments.

The deepest unit is mainly mudstone, which extends from 2240 ft to the total depth of the well, 2300 ft. Mudstone is interbedded with thin sandstones at the top, and includes one bed of sand lower in the interval. The mudstone is silty throughout and contains dark, carbonaceous debris. Two of the thin sands in this interval contain weak shows of heavy oil, at 2235.5 ft and at 2243.5 ft. Horizontal laminae are the main structure, but contorted laminae occur at 2278 ft. Thin sands interbedded at the top of this mudstone include a thin layer of granule-size particles at 2245 ft. A clay-lined burrow occurs at 2143.6 ft and a thin, calcite-cemented sandstone is present at 2246 ft. The mudstone from about 2240 ft downward is firmer, or harder, than that at shallower depths and of a darker brownish-gray color than most of the mudstone above.

Summary and Interpretation (Phase II)

A thick section of mudstones and sandstones, with occasional siltstones, was cored continuously in the Anadarko Hot Ice No. 1 well during Phase II of the drilling program. Phase II of the operation began at 1403 ft. Total depth of the well was 2300 ft. Despite minor indications of gas being present in some low-permeability units, no gas hydrates were found.

Correlations with wireline logs and descriptions of cuttings taken in nearby wells indicate that the interval cored in Phase II is part of the lower Sagavanirktok and upper Canning Formations of Late Cretaceous age. The sequences of sediments cored probably comprise the marine equivalents of marginal marine or deltaic units of the Brookian Sequence in nearby outcrops farther south (Molenaar, 1983).

The shallowest interval cored is a continuation of the thick mudstone being cored at the end of the Phase I operation. Beneath this mudstone interval is the informal unit known as the West Sak Sands.

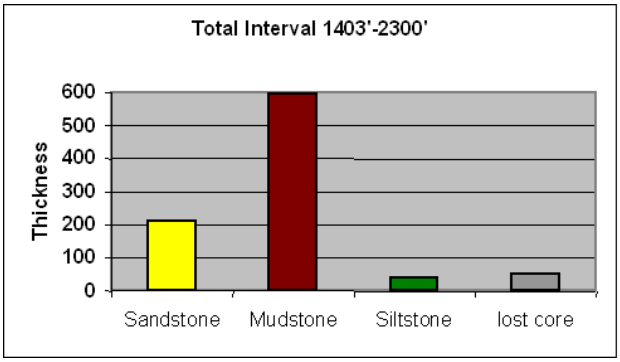

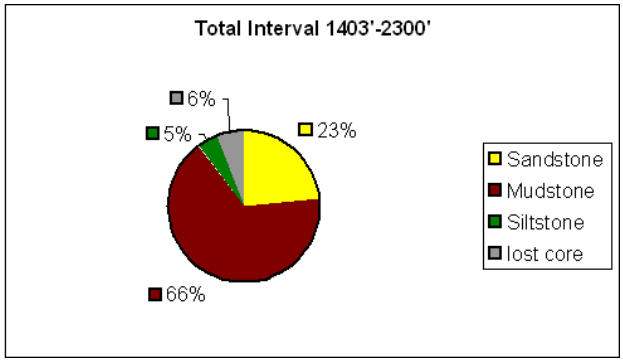

Sediments cored from 1462-2300 ft are a series of coarsening-upward mudstone-sandstone intervals. They may be grouped for descriptive purposes into four major intervals: 2300-2201 ft, 2201-1908 ft, 1908-1727 ft, and 1727-1462 ft. Each of these major subdivisions of the cored interval begins with a thick, somewhat silty, fossiliferous mudstone and is capped by a very fine- to medium-grained, upward-coarsening, fossiliferous, silty sandstone. Each major, capping sandstone, in succession upward, is thicker than the next one below it.

Within each of these major sequences are numerous smaller subdivisions, each with a prominent sandstone that lies above a silty mudstone and each of which exhibits greater or lesser degrees of interbedding of finer and coarser sediments within its interval. The mudstones and sandstones commonly have gradational contacts and there is frequent occurrence of fossil mollusk shells and thin beds of shell debris in both kinds of sediment.

These characteristics support the interpretation that sediments of the entire Phase II cored interval were deposited in a shallow marine shelf environment. They probably owe their cyclic variability to differences through time in activity and location of deltaic complexes in the south and southwest, which were active at the same time (Molenaar, 1983). As coarser-grained sediment was delivered to the marine environment, it was reworked and re-distributed by marine waves and currents into offshore bars and sheets of sand, some of which may be continuous laterally with their shoreline or river mouth equivalents. Between episodes of coarser-grained sedimentation, longer periods of deposition of finer-grained sediment allowed accumulation of silt and clay burying and enclosing the sandier deposits from the last progradation of the coastal environments.

References

Carman, G.J., and P. Hardwick, 1983, “Geology and regional setting of Kuparuk oil field, Alaska,” *AAPG Bulletin*, v. 67, no. 6, p. 1014-1031.

Collett, T.S., 1993, “Natural gas hydrates of the Prudhoe Bay and Kuparuk River area, North Slope, Alaska,” *AAPG Bulletin*, v. 77, no. 5, p. 793-812.

Gryc, G., 1988, “Geology and exploration of the National Petroleum Reserve in Alaska, 1974 to 1982,” U. S. Geological Survey Professional Paper 1399, 940 p.

Jamieson, H.C., L.D. Brockett, and R.A. McIntosh, 1980, "Prudhoe Bay – a 10 year perspective," in M.T. Halbouty, ed., *Giant oil and gas fields of the decade 1968-1978*, AAPG Memoir 30, p. 289-314.

Molenaar, C.M, K.J. Bird, and T.S. Collett, 1986, "Regional correlation sections across the North Slope of Alaska: U. S. Geological Survey Miscellaneous Field Investigations Map," MF-1907, 1 plate.

Molenaar, C.M., 1983, "Depositional relations of Cretaceous and Lower Tertiary rocks, Northeastern Alaska," *AAPG Bulletin*, v. 67, no. 7, p. 1066-1080.

Morgridge, D.L., and W.B. Smith, 1972, "Geology and discovery of Prudhoe Bay Field, eastern Arctic Slope, Alaska," in R.E. King, ed., *Stratigraphic oil and gas fields – classification, exploration methods, and case histories*, AAPG Memoir 16, p. 489-501.

Newsham, K.E., 2003, "Shallow sand study in the Hot Ice gas hydrate area," Anadarko Petroleum Corp., internal report, 22 p.

Runyon, S., 2003, "Base Map w/ structural contours, Top of West Sak," Anadarko Petroleum Corp., internal report, one map and personal communication.

Sigal, R., 2003, Data reduction of sample analyses, Anadarko Petroleum Corporation, personal communication.

Werner, M.R., 1987, "Tertiary and Upper Cretaceous heavy-oil sands, Kuparuk River area, Alaskan North Slope," in I.L. Tailleur and P. Weimer, eds., *Alaskan North Slope Geology: Bakersfield, California, Pacific Section, Society of Economic Paleontologists and Mineralogists and the Alaska Geological Society*, Book 50, v. 1, p. 109-118.

Appendix C:
Supplemental NMR Measurement Results

Decay Curves for Plugs from Ugnu Formation

299.00

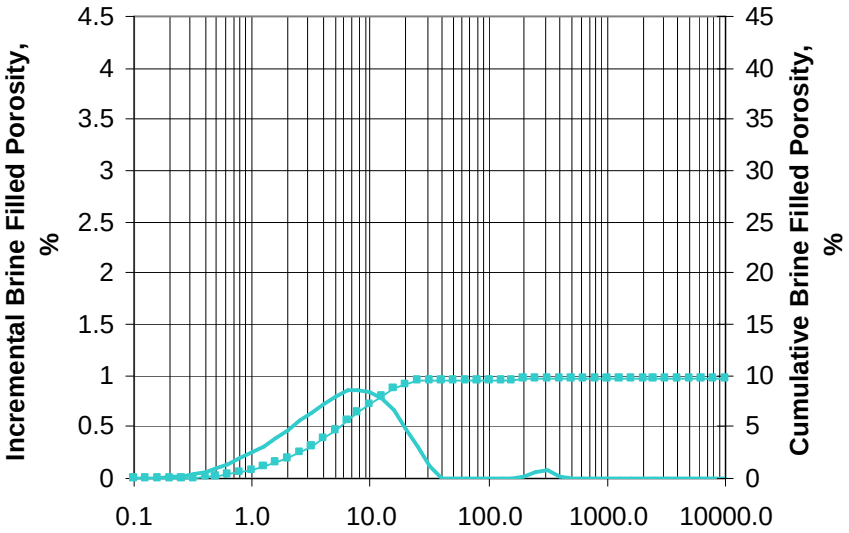

465.50

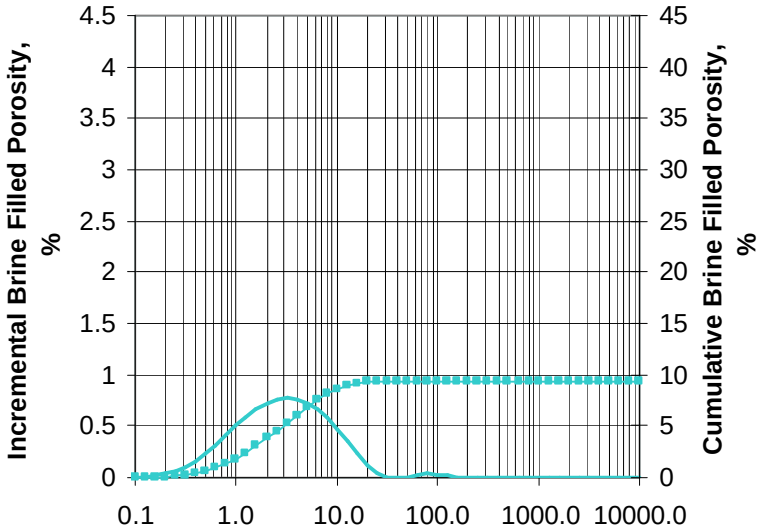

1011.00

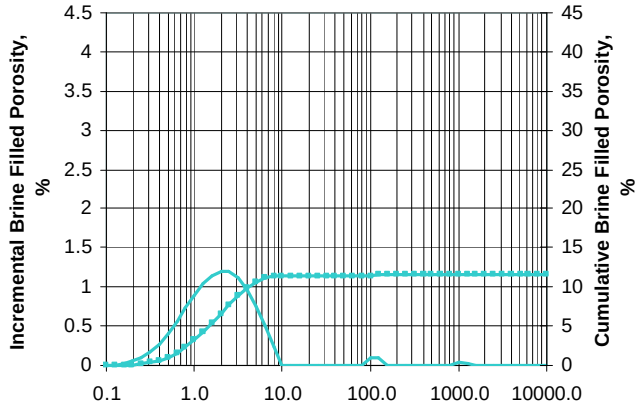

1117.6

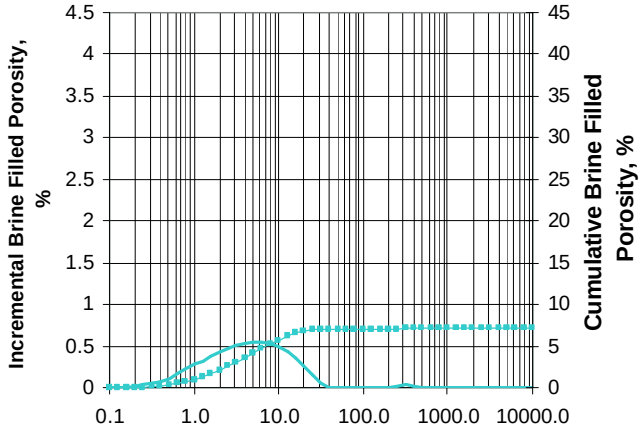

Porosity for Frozen and Saturated Plugs from Ugnu Formation

299.00

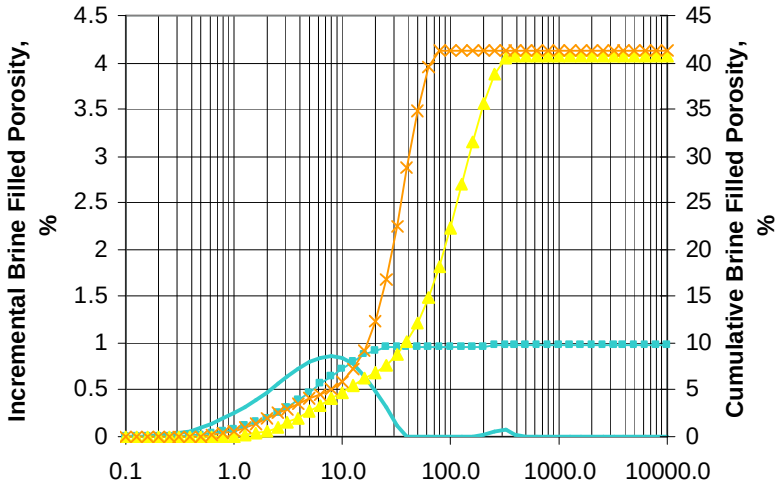

465.50

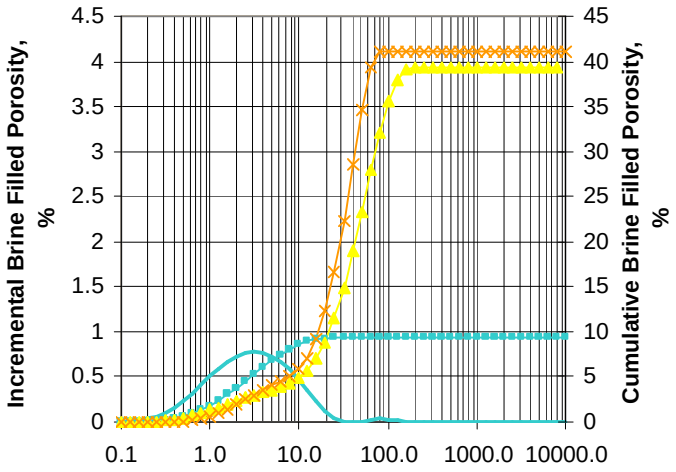

1117.6

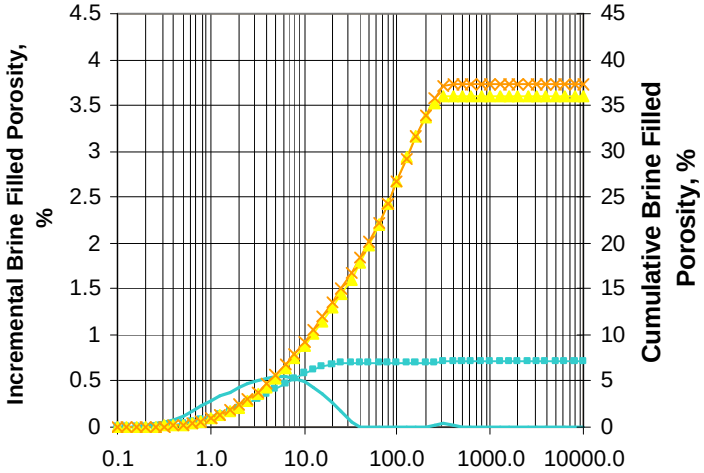

Decay Curves for Thawed and Resaturated Plugs from Ugnu

Sample 216.6

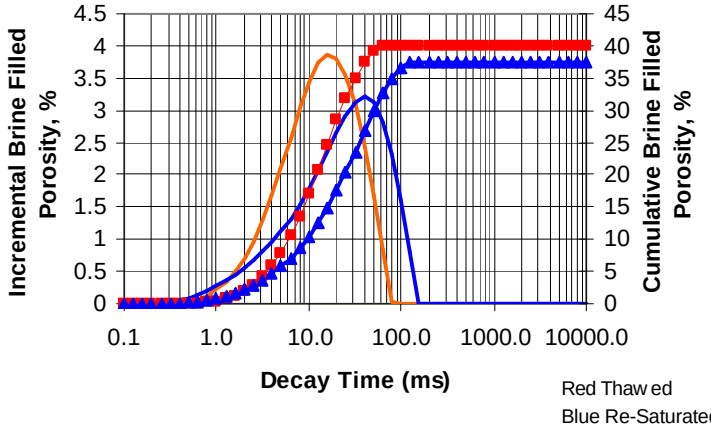

246.8

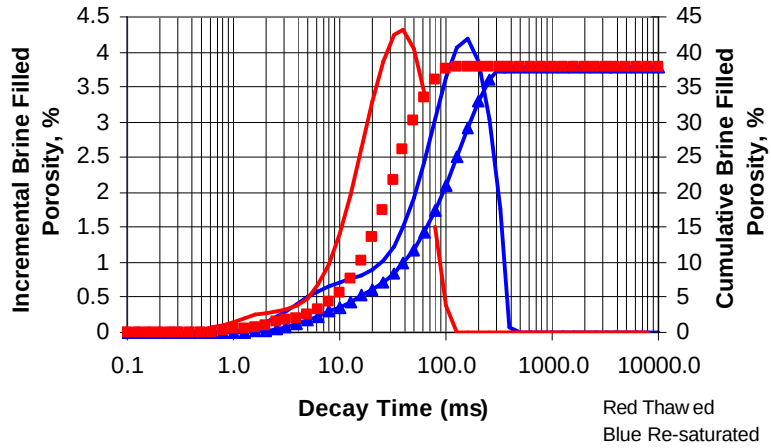

299.0

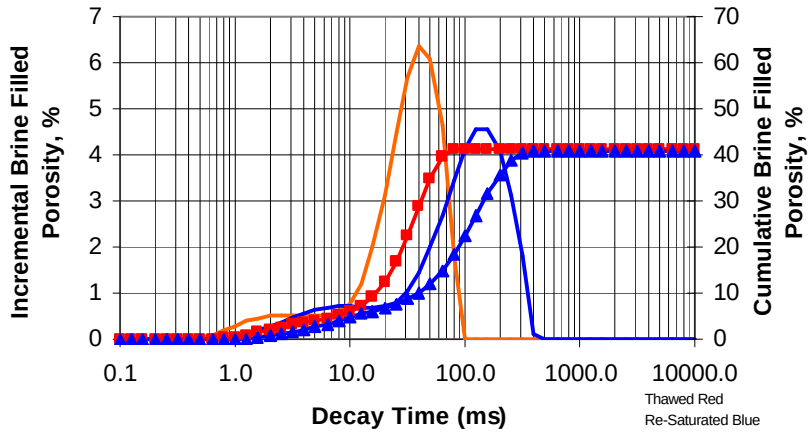

381.1

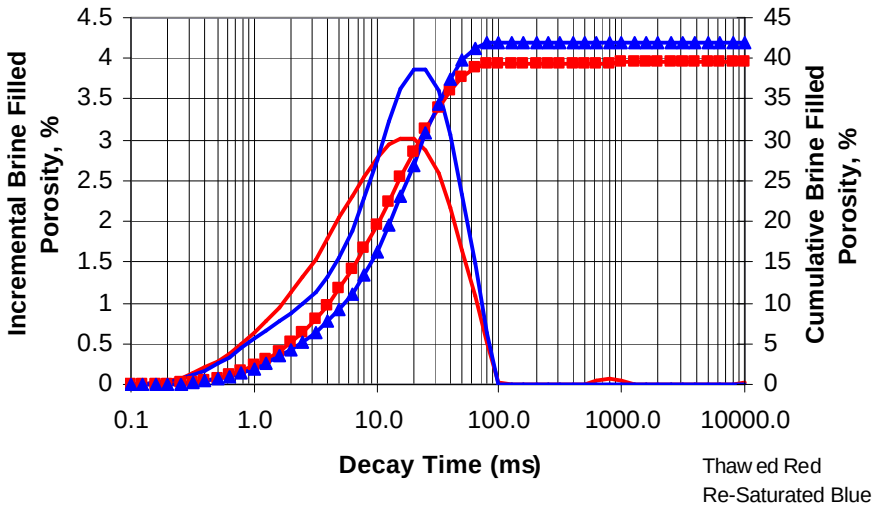

393.7

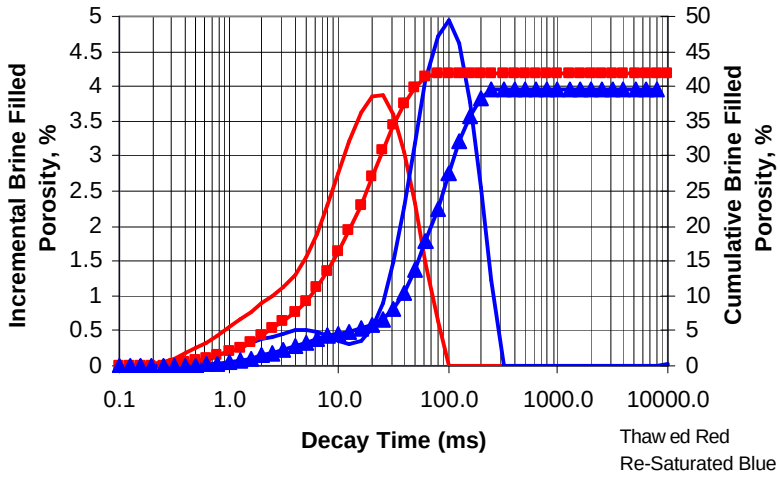

427.4

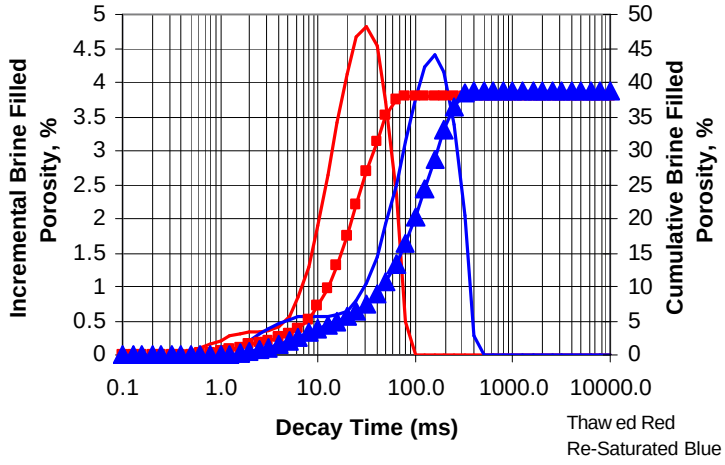

452.3

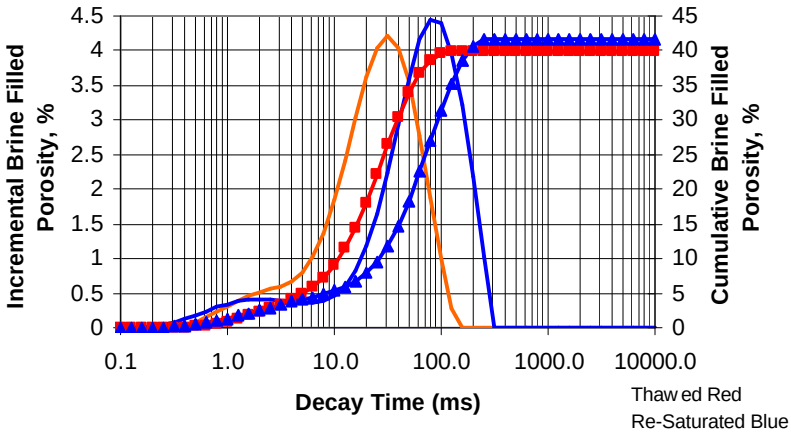

465.5

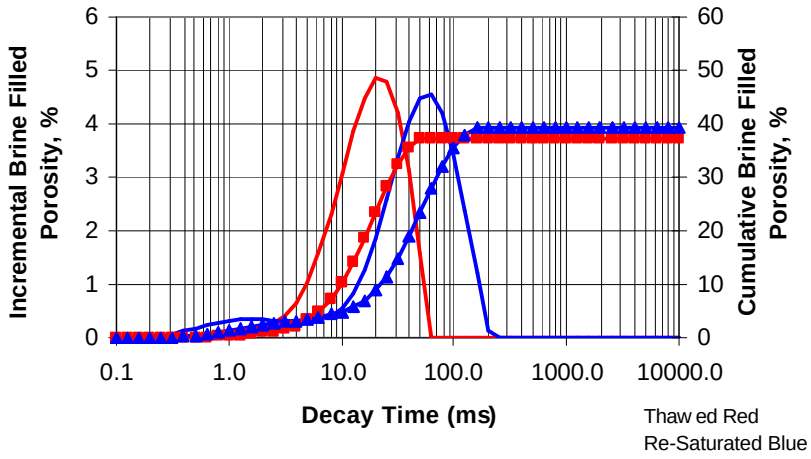

520.5

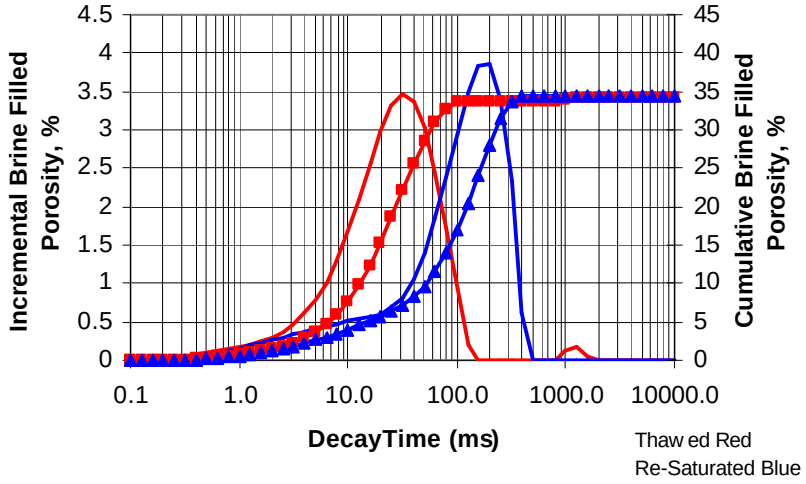

667.6

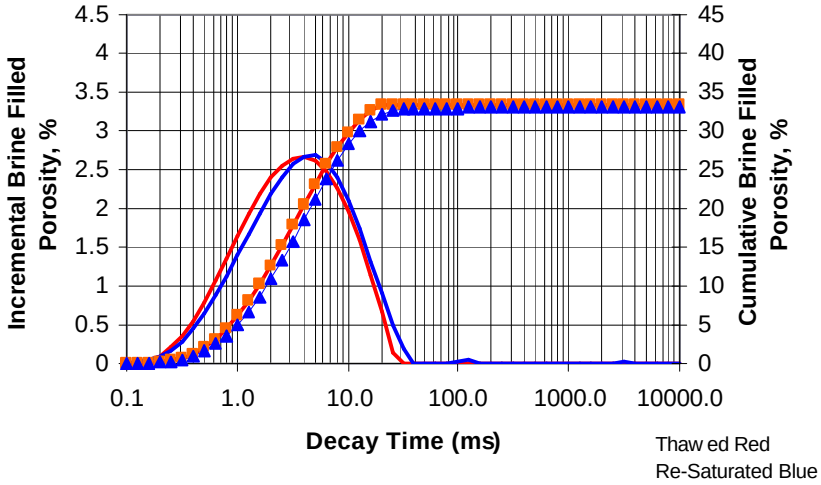

750.3

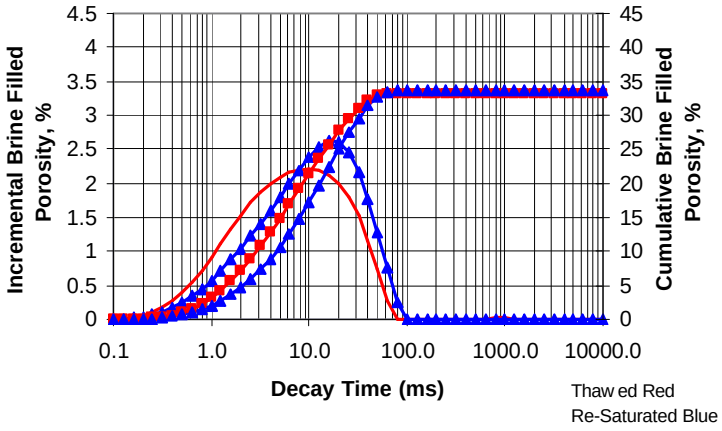

1074.2

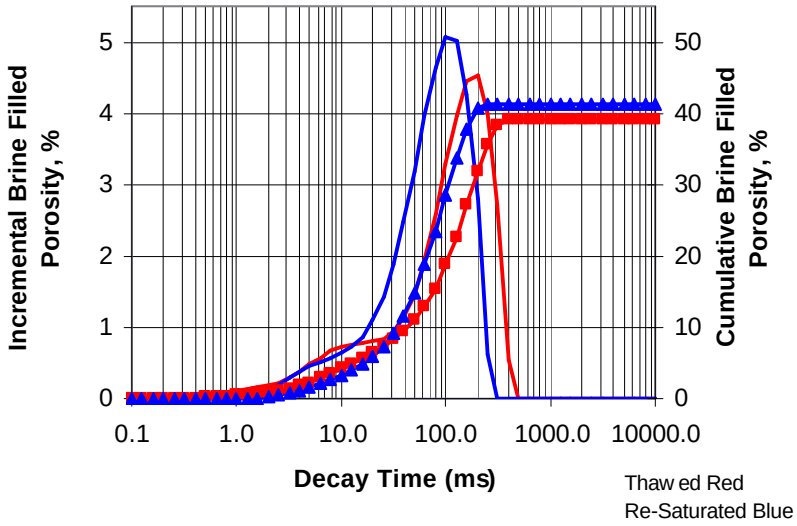

1117.6

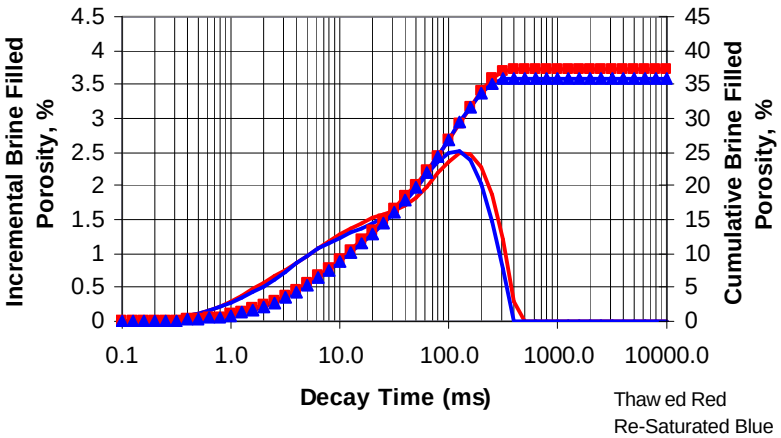

1219.9

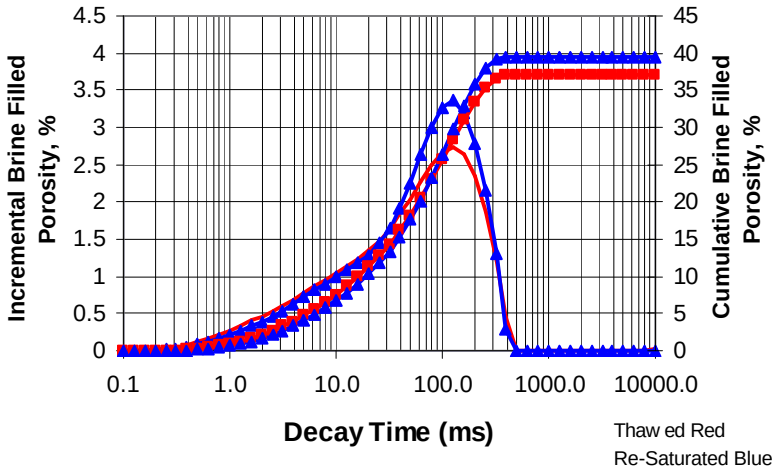

Decay Curves for Plugs from West Sak Formation

Sample 1438.7

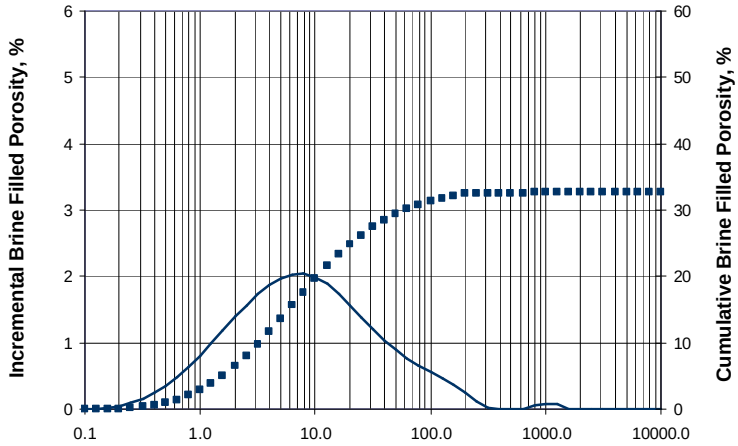

Sample 1442.7

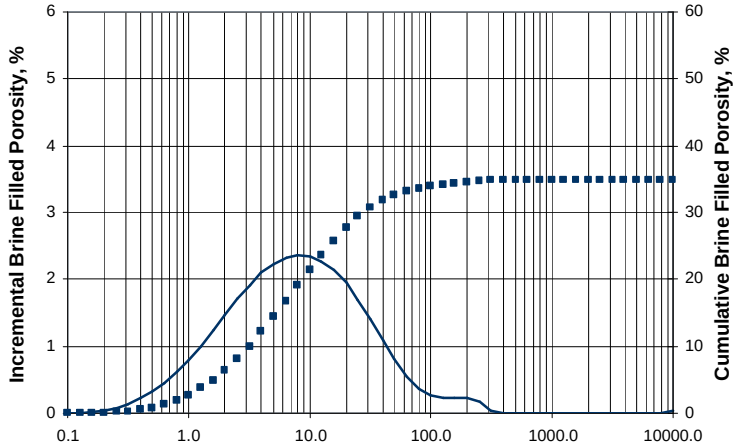

Sample 1449.6

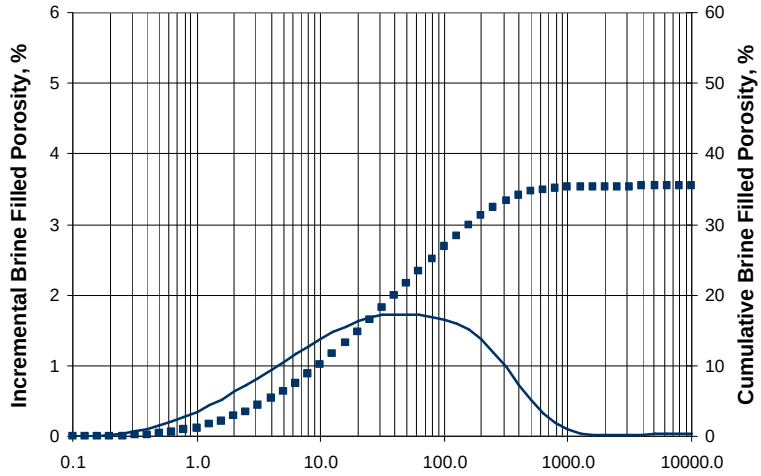

Sample 1467.7

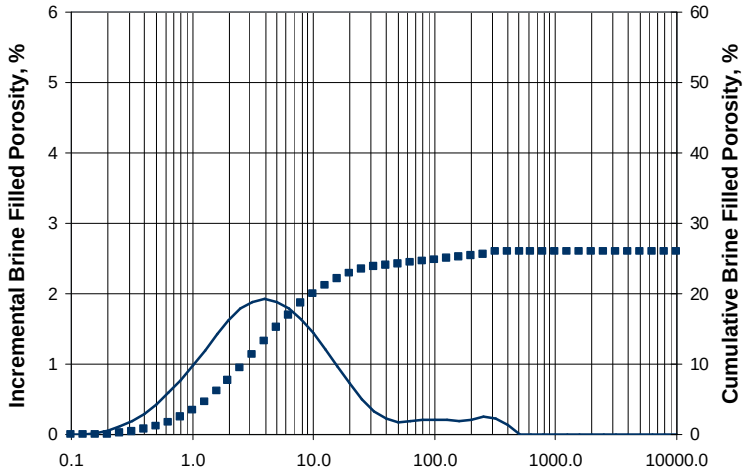

Sample 1477.7

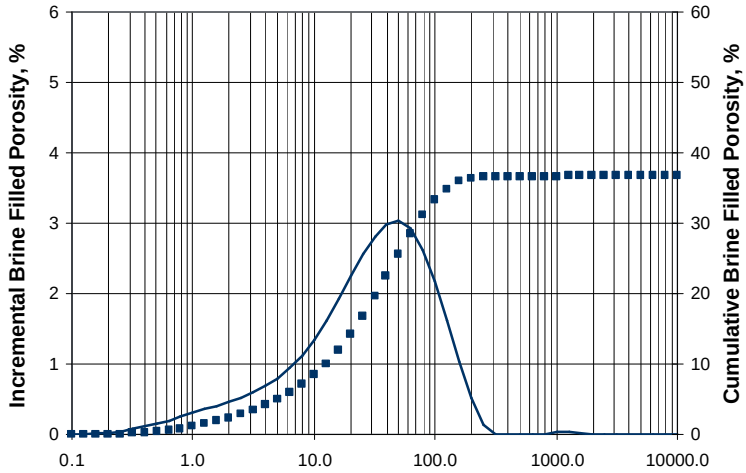

Sample 1480.2

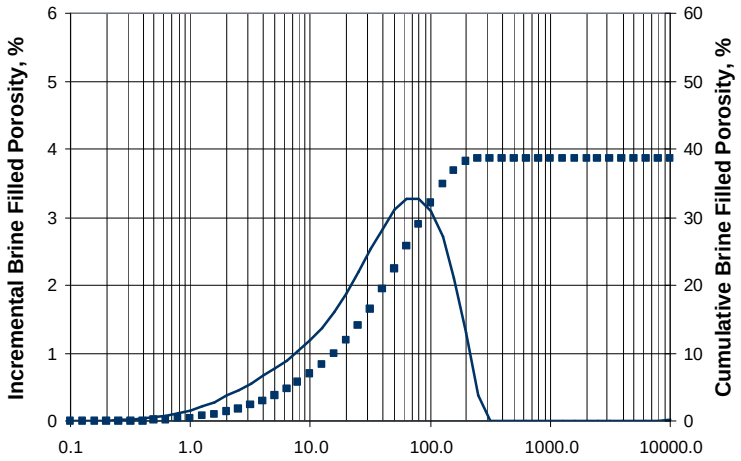

Sample 1481.4

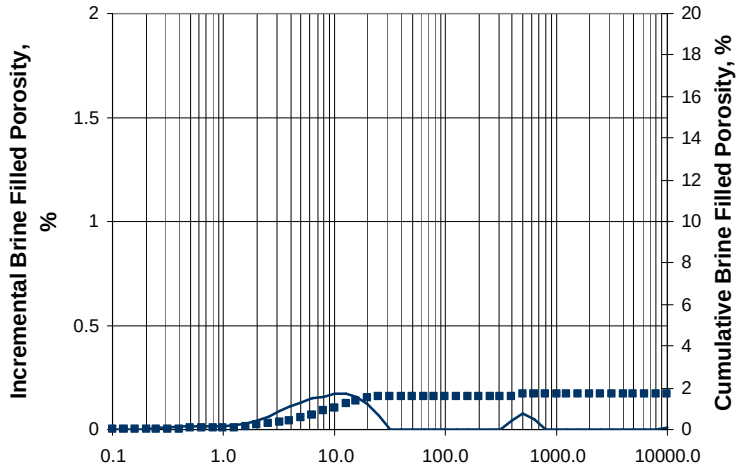

Sample 1487.7

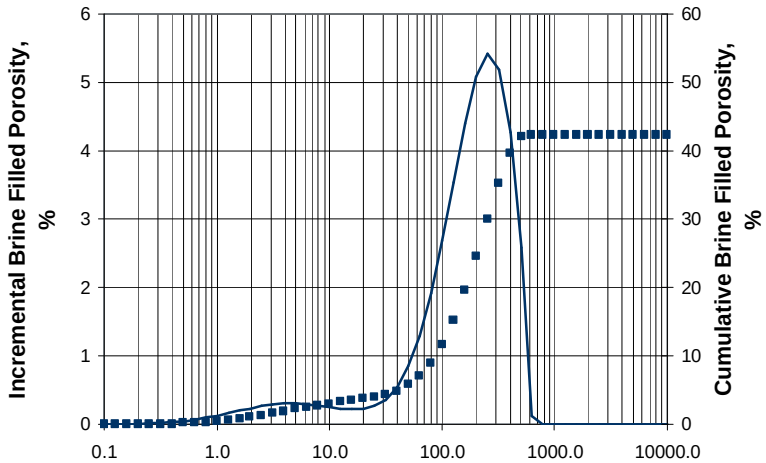

Sample 1489.4

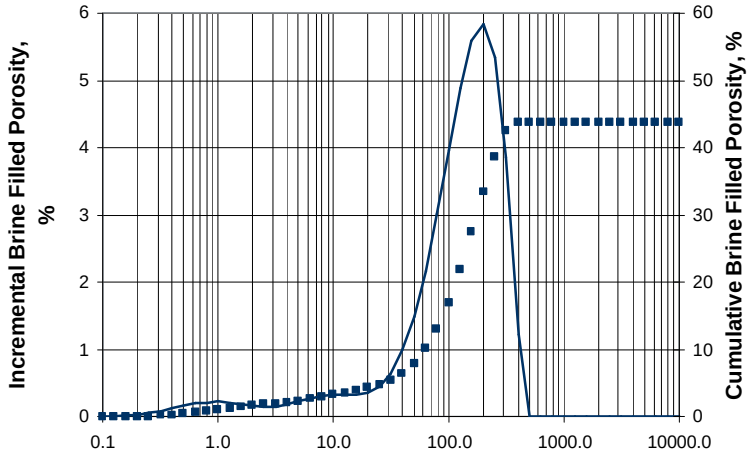

Sample 1489.4v

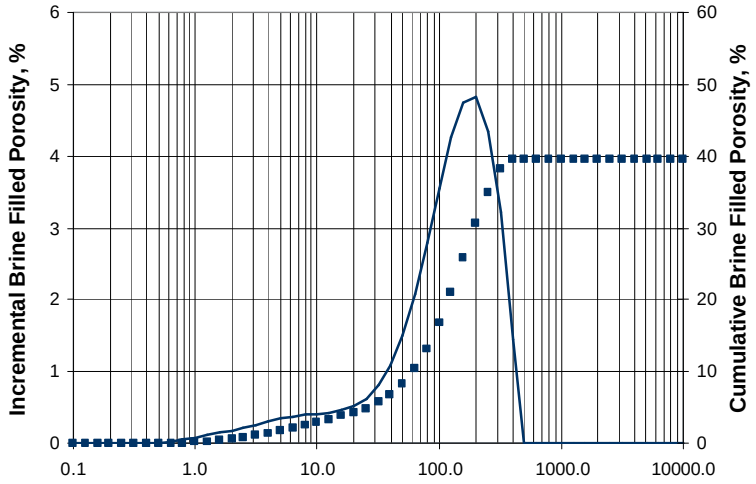

Sample 1493.6

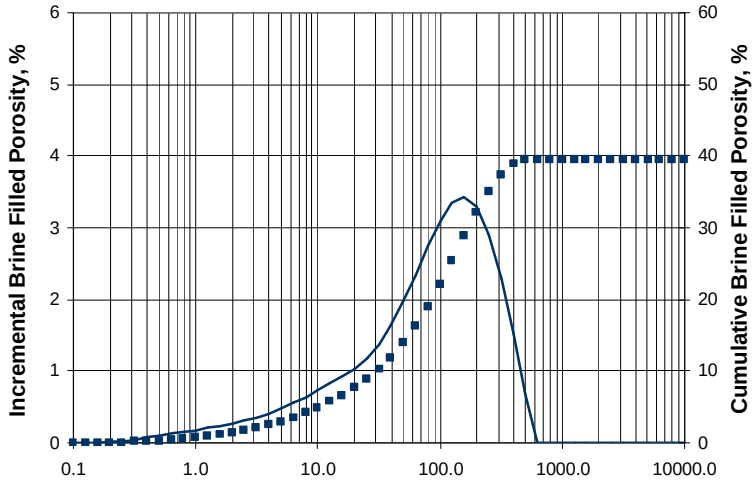

Sample 1498.4

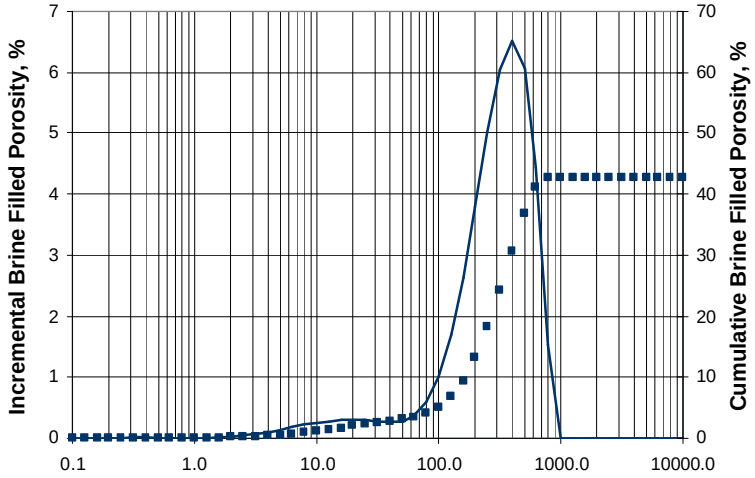

Sample 1502.4

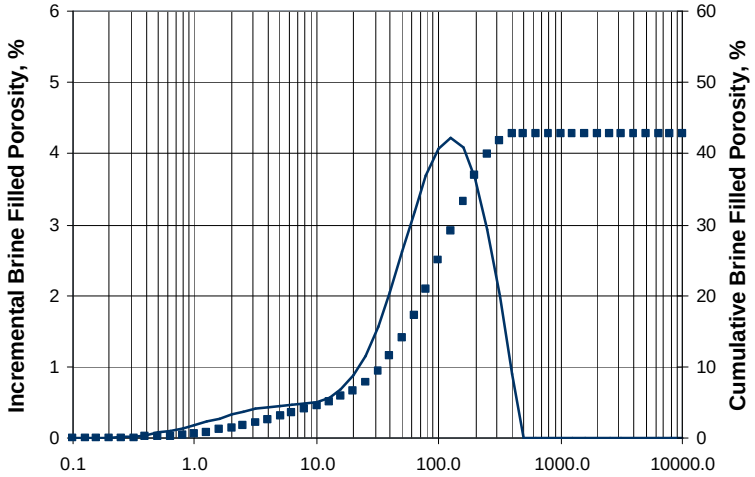

Sample 1506.1

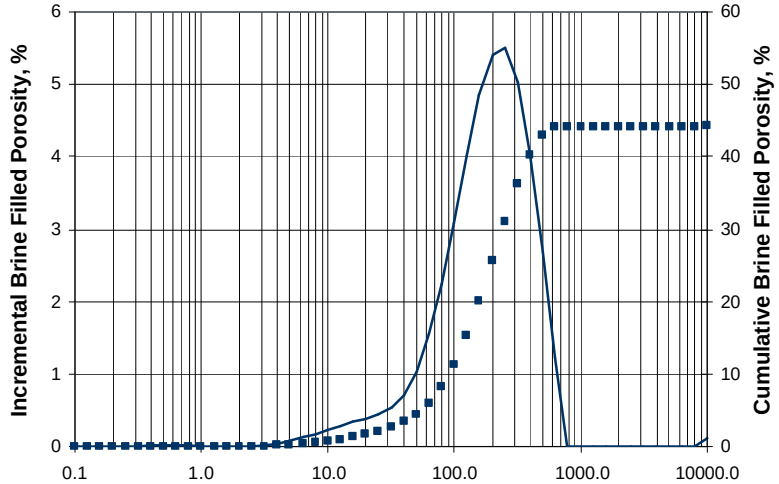

Sample 1517.3

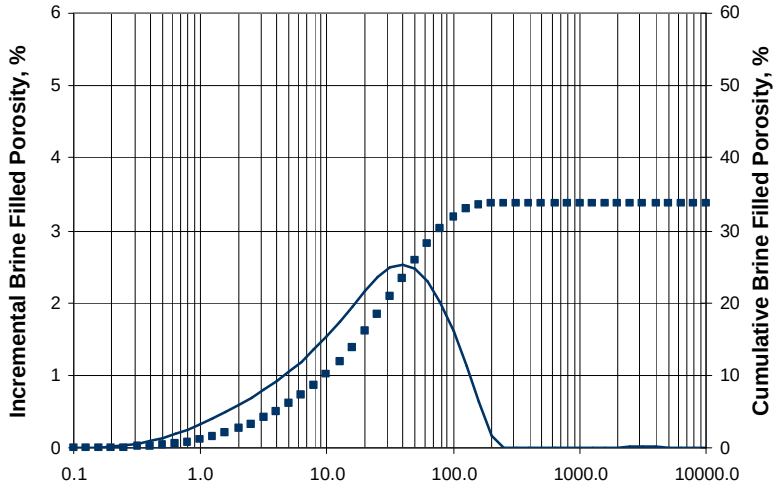

Sample 1520.3

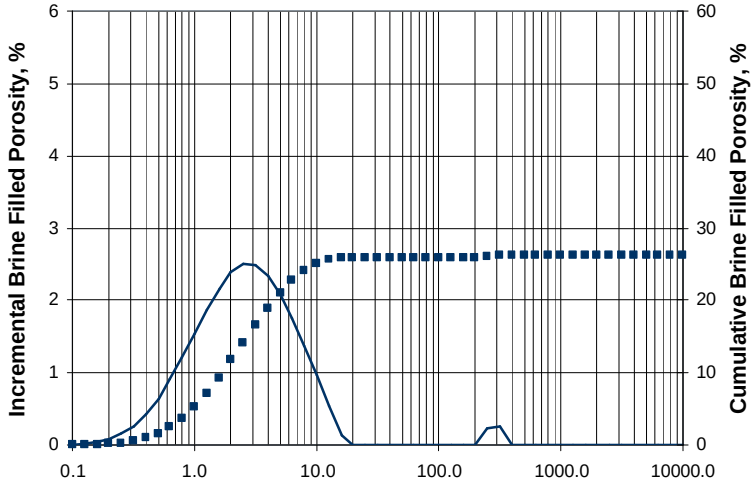

Sample 1525.3

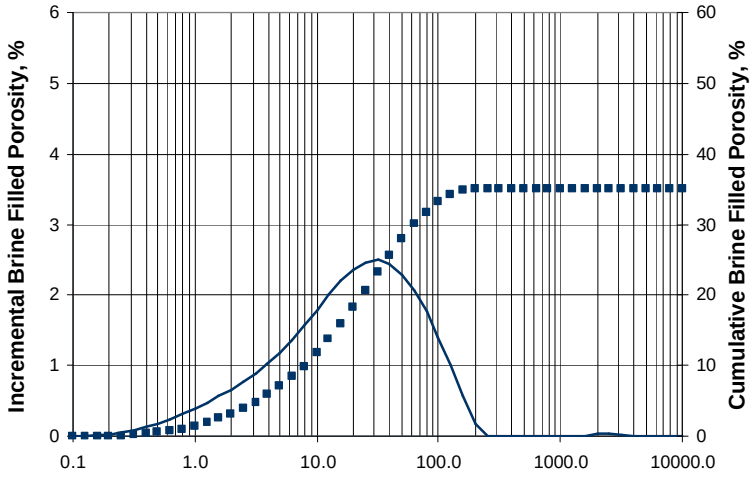

Sample 1530.7

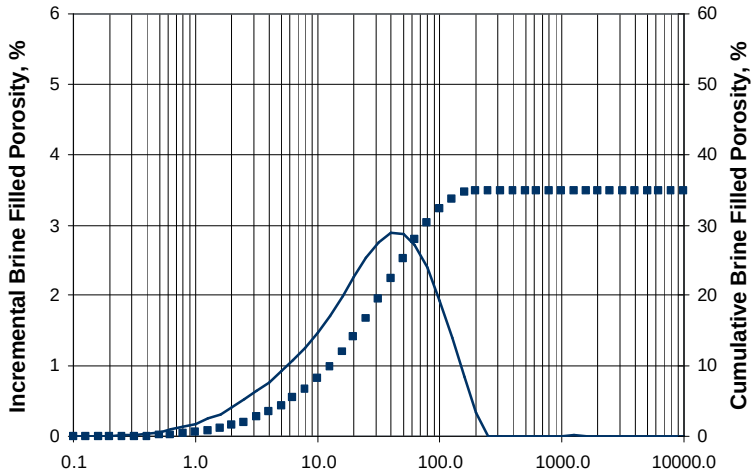

Sample 1535.4

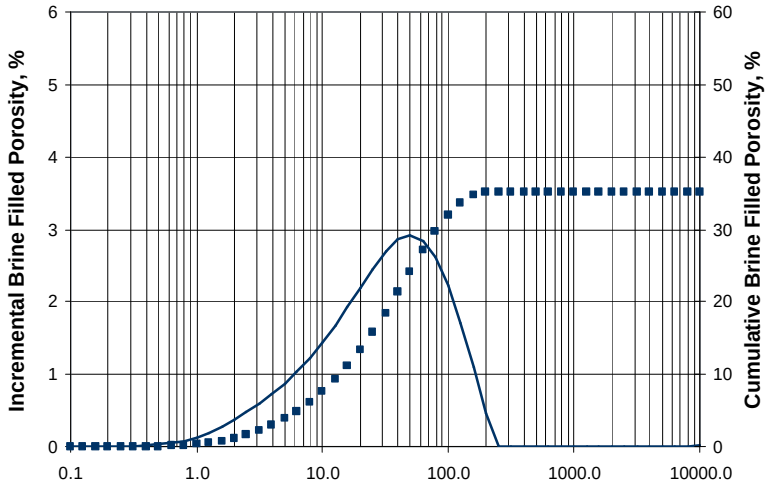

Sample 1697.2

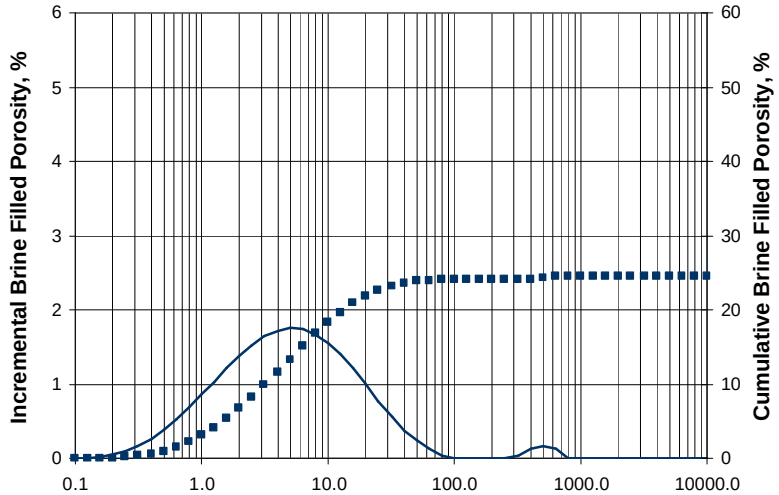

Sample 1701.9

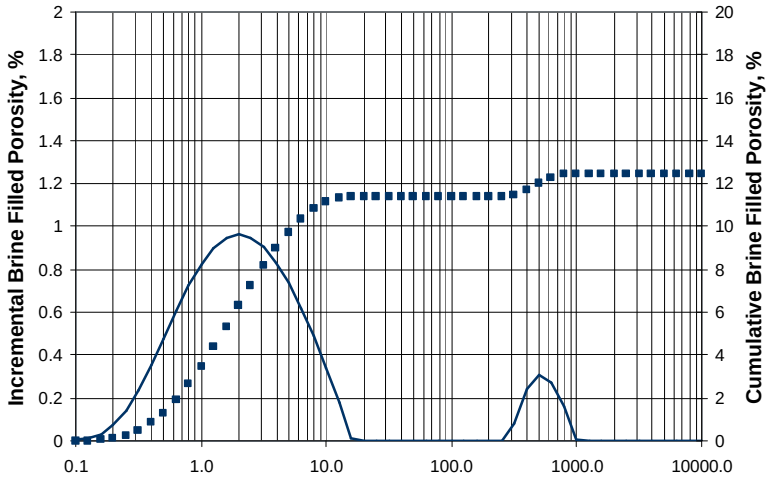

Sample 1702.1

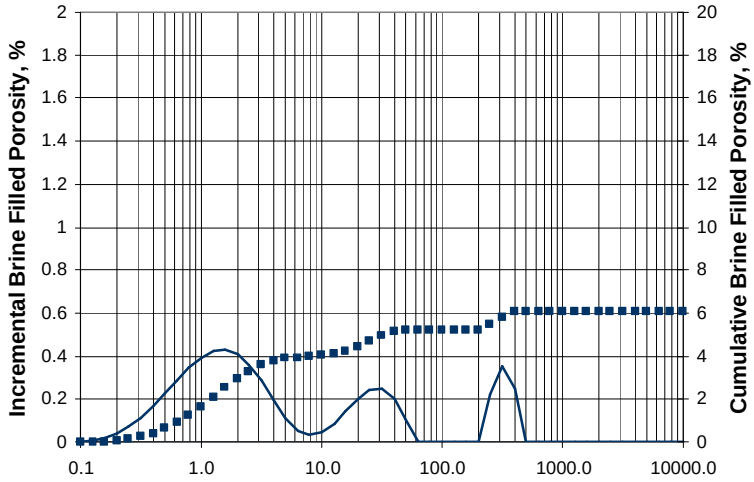

Sample 1730.2

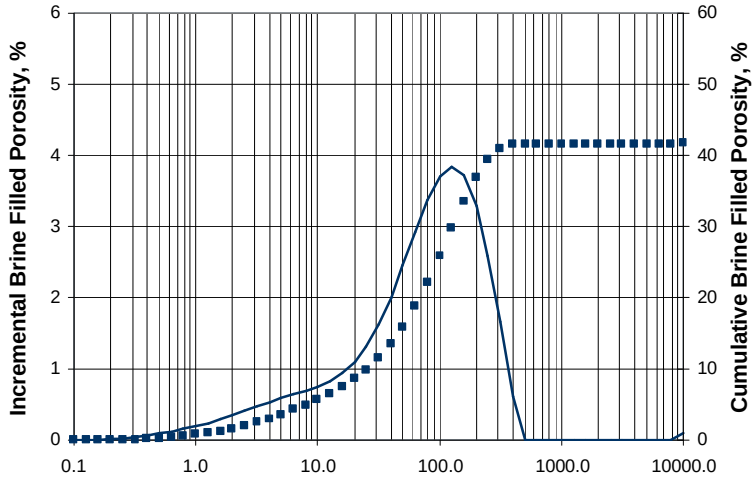

Sample 1734.9

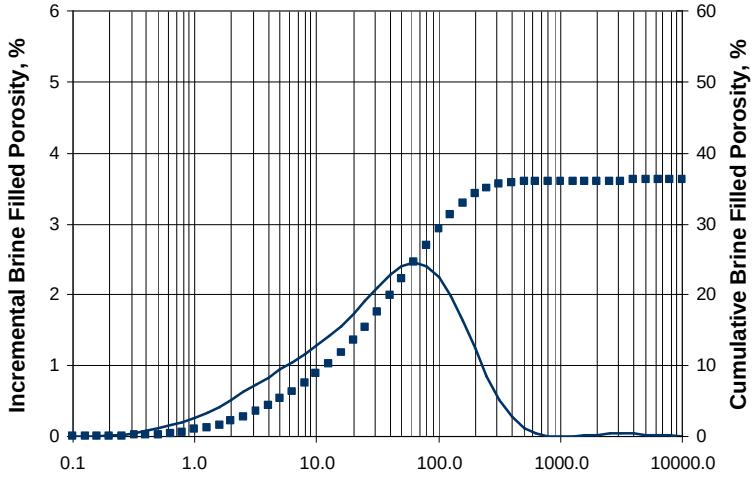

Sample 1740.2

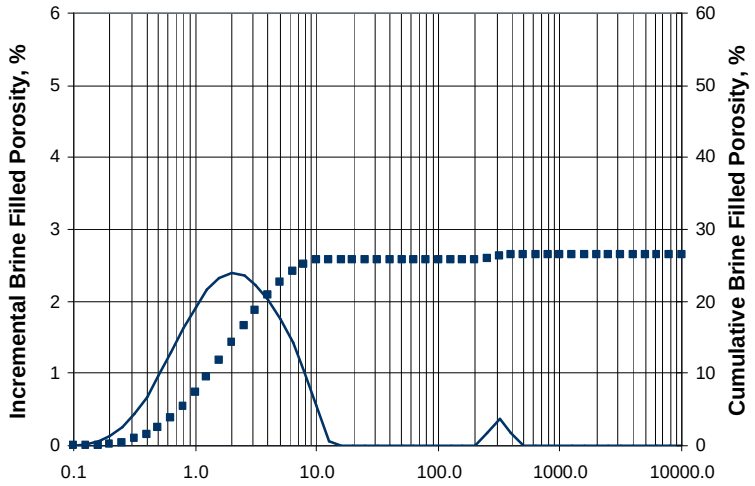

Sample 1745.1

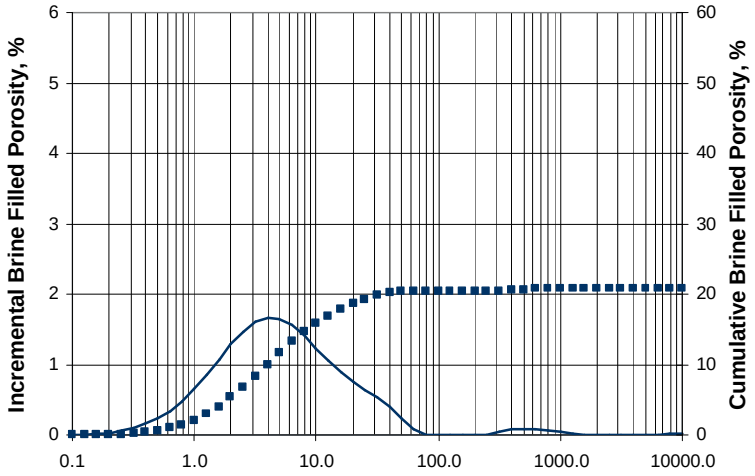

Sample 1754.8

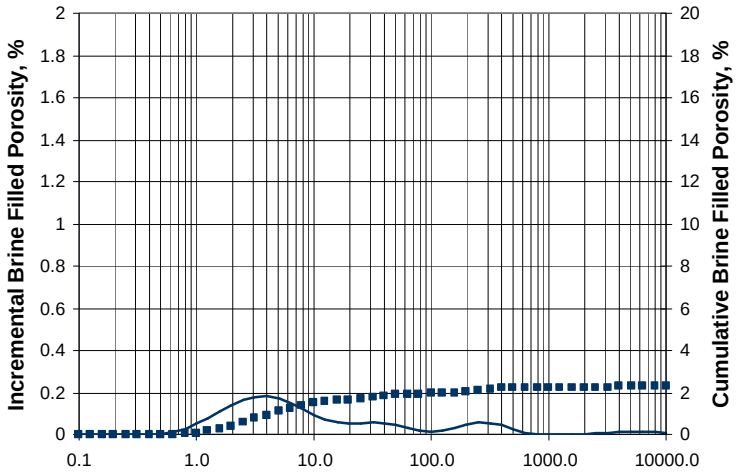

Sample 1758.5

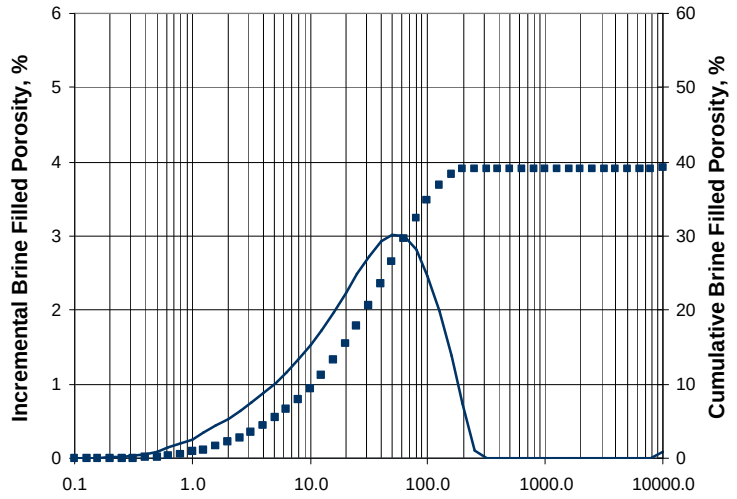

Sample 1784.7

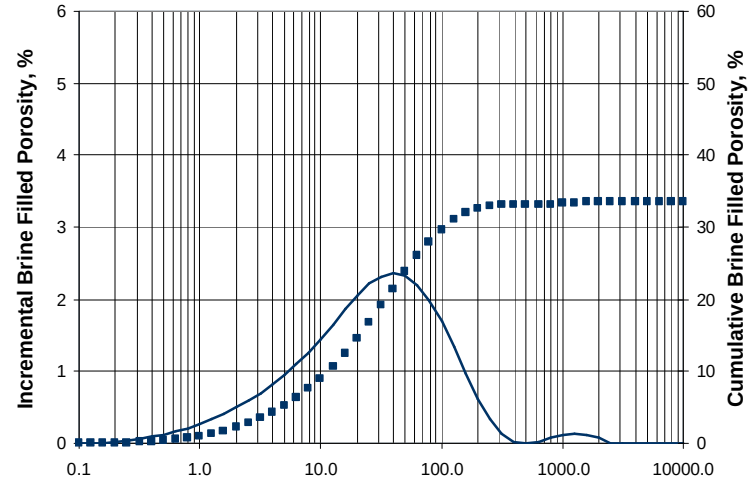

Sample 1828.0V

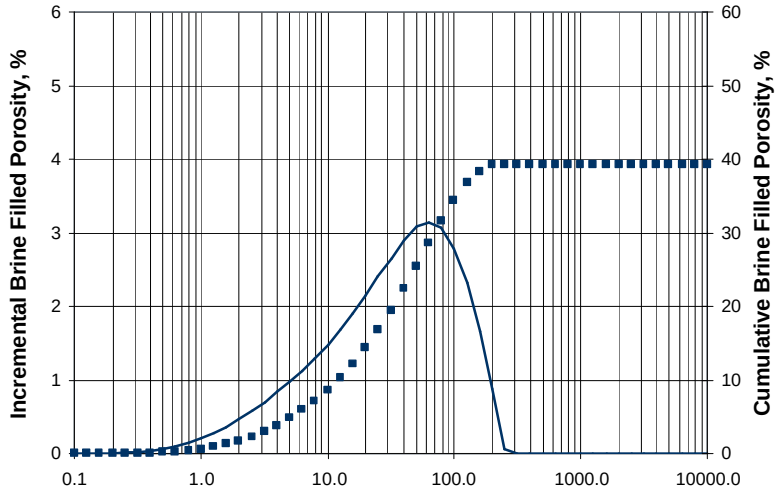

Sample 1833.4v

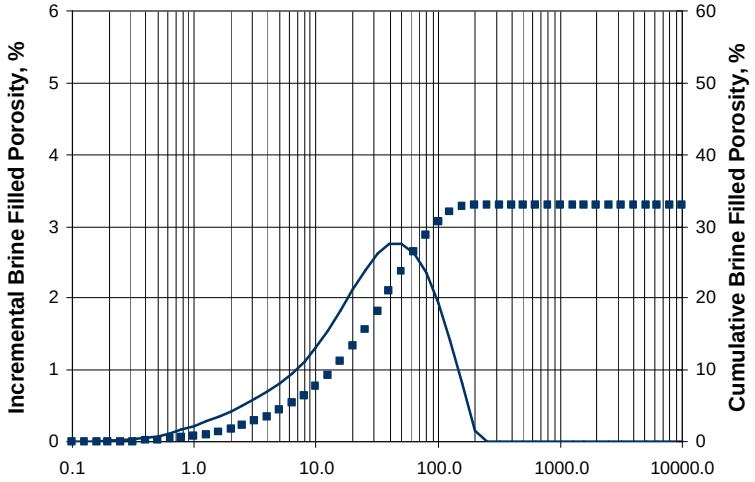

Sample 1873.9

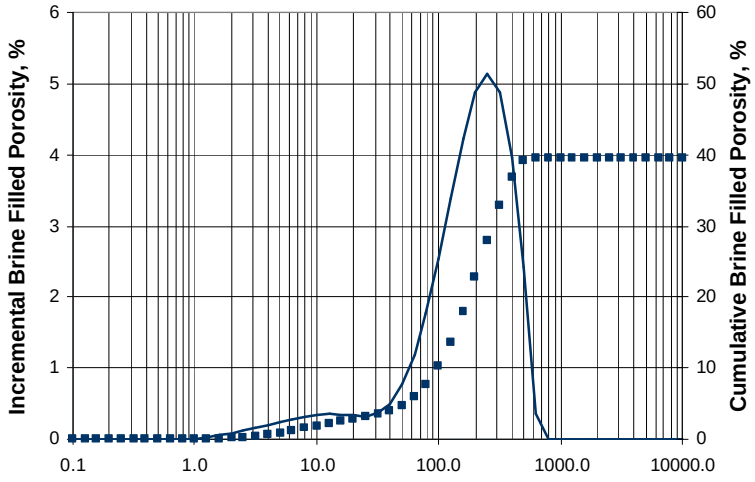

Sample 1877.8

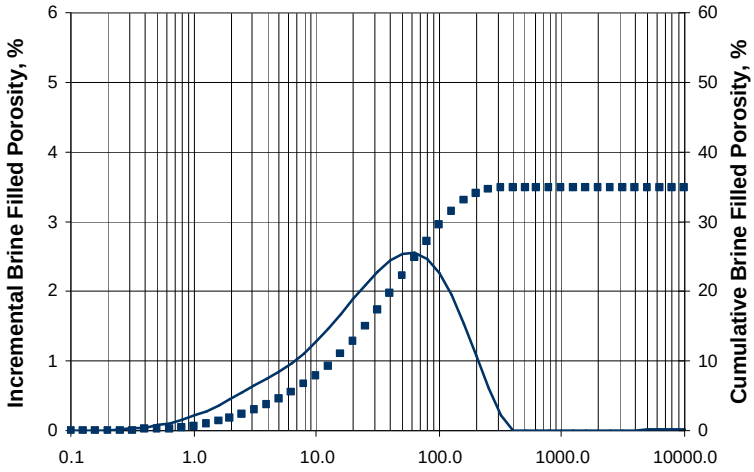

Sample 1911.8

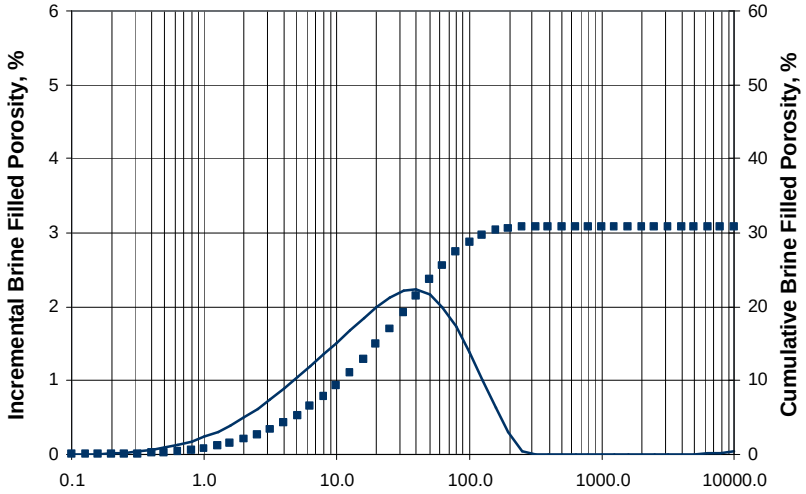

Sample 1918.4

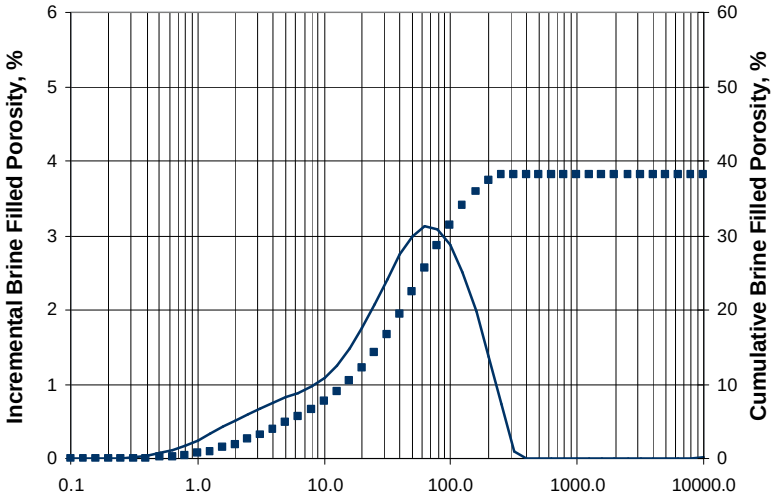

Sample 1924.2

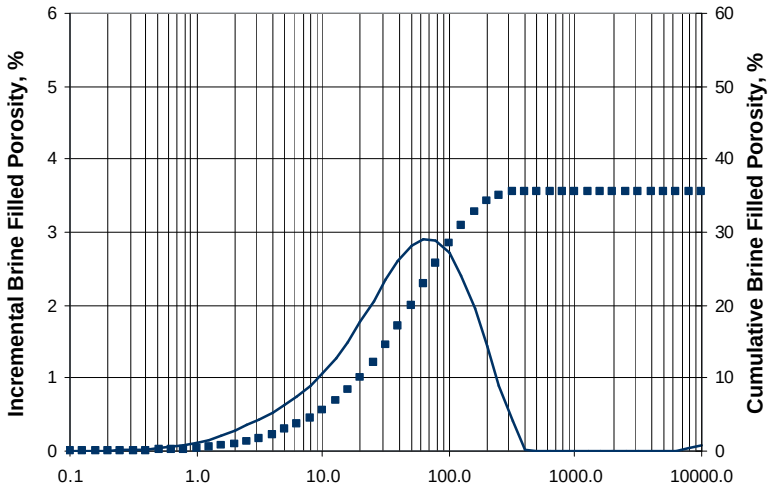

Sample 1930.1v

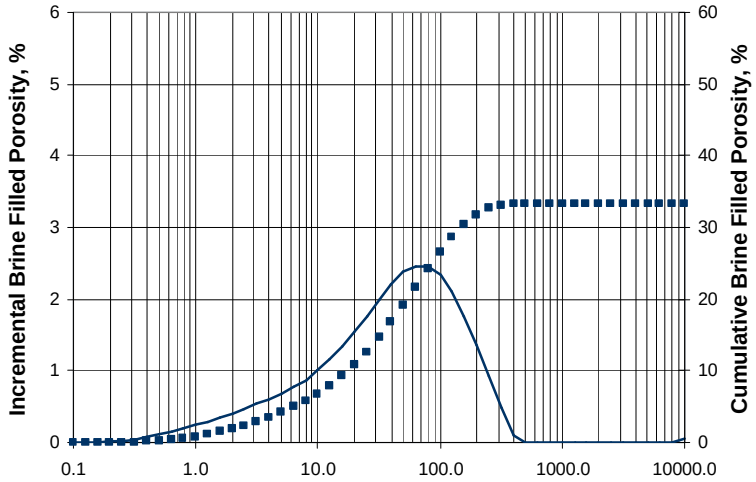

Sample 1933.0

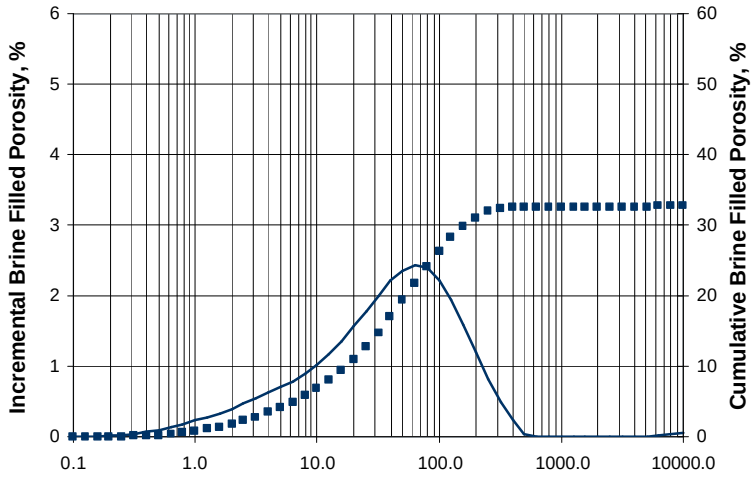

Sample 1941.1

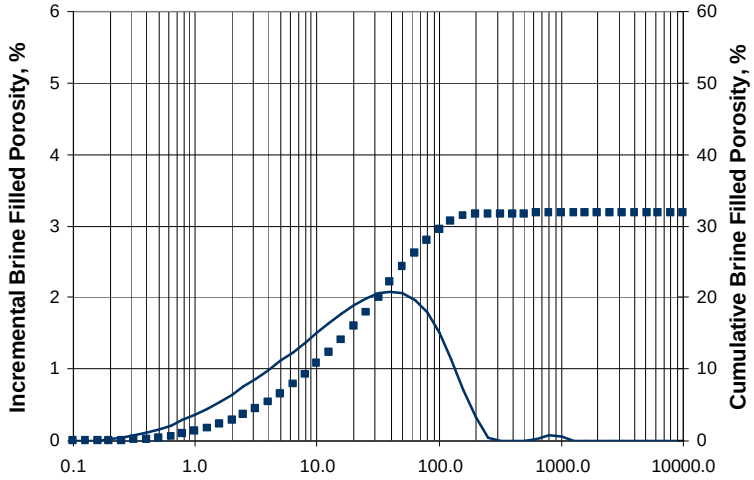

Sample 1959.0

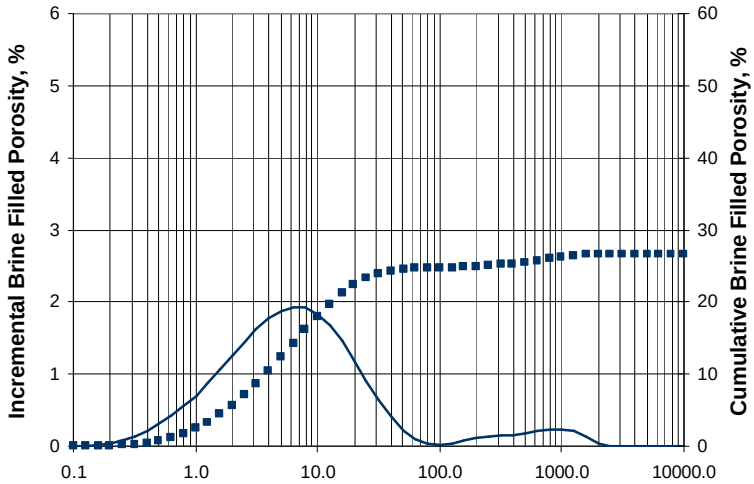

Sample 2019.0

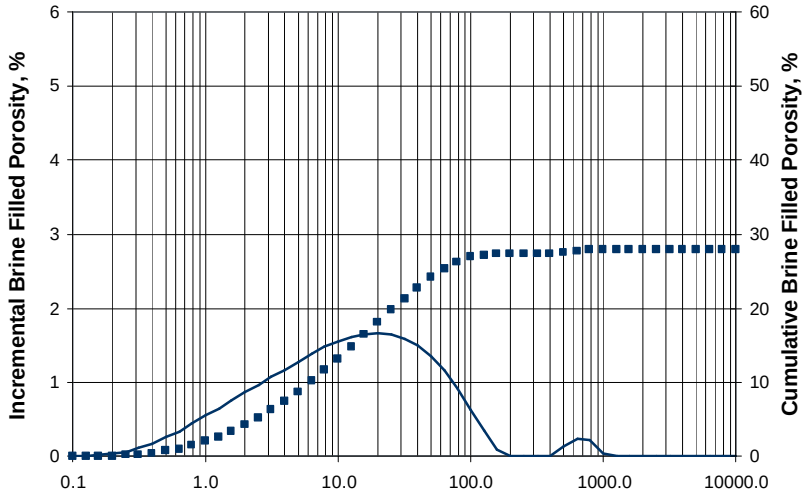

Sample 2204.6

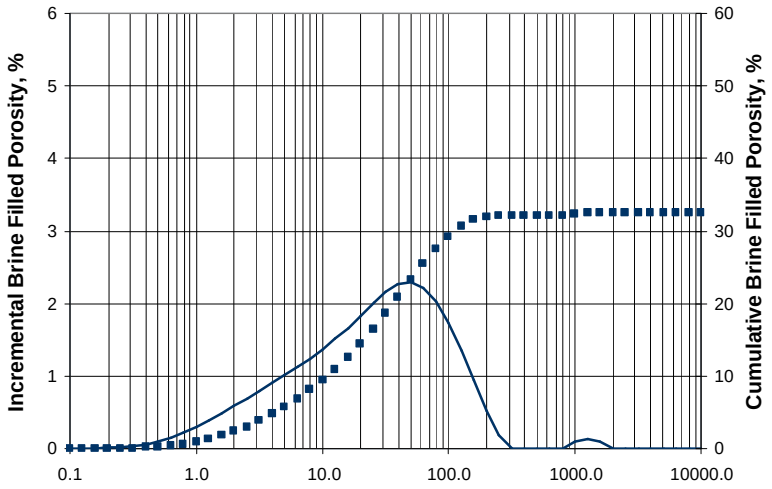

Sample 2207.3

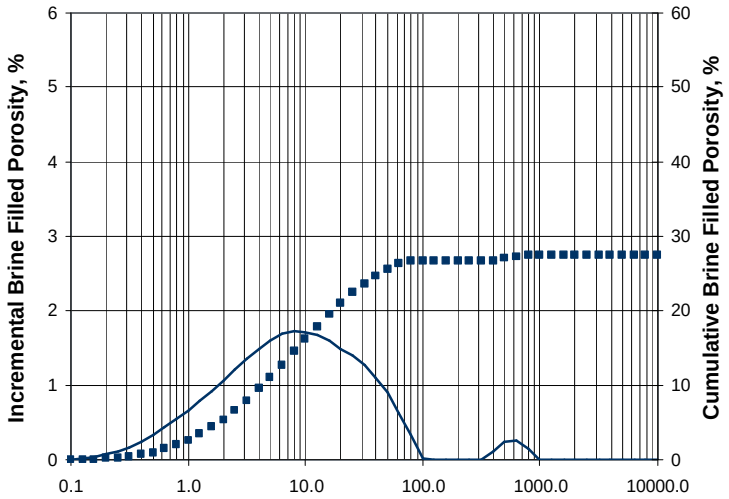

Sample 2313.1

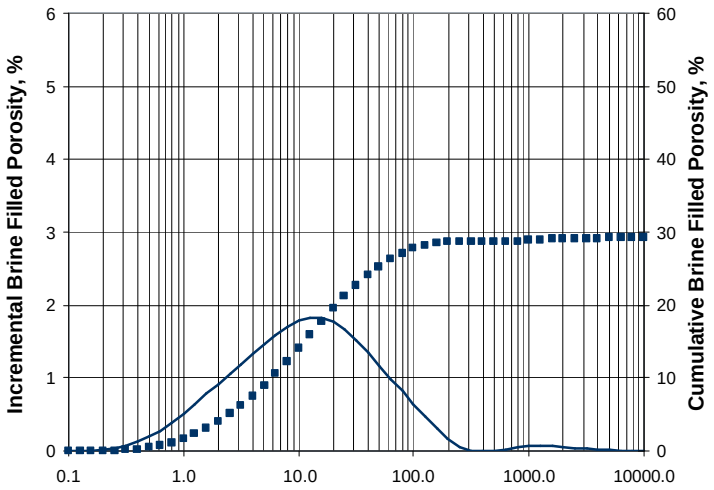

Appendix D:
NMR Measurements of Permafrost: Unfrozen Water Assay, Growth Habit of Ice, and Hydraulic Permeability of Sediments

R.L. Kleinberg and D.D. Griffin
Schlumberger-Doll Research, Old Quarry Road, Ridgefield, Connecticut 06877

R.F. Sigal
Anadarko Petroleum Corp., The Woodlands, Texas 77380

January 2004

Abstract

Nuclear magnetic resonance (NMR) measurements have been made on permafrost recovered from a well on the North Slope of Alaska. These measurements show that unfrozen water is correlated with the clay content of the sediments, and inversely correlated to ash content of the coals. NMR is sensitive to the pore-scale distribution of liquid water, so the growth habit of ice within the pore space of the sediment can be determined. Hydraulic permeability can be rapidly estimated, and has been found to depend strongly on the unfrozen water content. The ratio of the permeability of ice-affected sediment to the permeability of the same sediment saturated with liquid water appears to be surprisingly independent of lithology. Comparison between core measurements and wireline logs demonstrates that the unfrozen water content of permafrost can be predicted from borehole NMR measurements of thawed formations.

Table of Contents

1. Introduction

Anadarko Petroleum Corporation, Maurer Technology Inc., and Noble Drilling Corporation collaborated to drill the Hot Ice No. 1 well on the North Slope of Alaska. During the 2002-2003 drilling season an innovative drilling rig was constructed and a well drilled to the base of permafrost. A mobile arctic core laboratory was installed on the drilling rig to process core cut continuously from surface to total depth. Schlumberger-Doll Research provided personnel and a nuclear magnetic resonance (NMR) instrument to this laboratory *gratis*. After completion of drilling, Schlumberger Oilfield Services logged the well; magnetic resonance was included among the borehole measurements.

The objective of the project was to assess the potential gas hydrate reservoir and initiate production tests. No gas hydrate was detected in the permafrost zone, and time constraints prohibited drilling to hydrate deposits expected at greater depths. Therefore all scientific results from the first drilling season at Hot Ice No. 1 pertain to permafrost. The permafrost results are of interest in themselves. Moreover, although permafrost and gas hydrate deposits differ in many respects, similarities between ice and gas hydrate suggest that insight into one may be gained by study of the other.

Permafrost has been studied for many years, but fresh perspectives can be derived from the use of magnetic resonance well logging tools that have been developed over the last decade [*Kleinberg*, 1996]. One of these instruments [*Kleinberg et al.*, 1992] has the unusual capability of making measurements on compact samples external to the antenna and magnets of the apparatus. Because this instrument is designed to withstand the rigors of oilfield deployment, it can be used on an arctic drilling rig under conditions that would challenge the survivability of conventional laboratory equipment.

Nuclear magnetic resonance is commonly thought of as either a spectroscopic probe for organic chemistry or a medical imaging modality. The petrophysical applications of NMR are quite different from either of these [*Kleinberg and Flaum,* 1998; *Kleinberg*, 1999]. As used to characterize sedimentary rock, NMR quantitatively determines oil and water content, oil viscosity, and the pore size distribution of water-saturated rock. Knowledge of pore size distribution is used to estimate hydraulic permeability.

Recently these capabilities have been applied to the study of methane hydrate synthetically produced in rock and sediment under conditions thought to mimic earth processes [*Kleinberg et al.*, 2003a, 2003b], and to the well log evaluation of natural gas hydrate deposits [*Kleinberg et al.*, 2004]. These techniques are directly applicable to the study of permafrost, both in recovered core and *in situ* in the earth.

2. Location, Apparatus, and Methods

Measurements were made on the Anadarko Hot Ice No. 1 drilling rig, located approximately 35 km (22 miles) south of the Arctic coast of Alaska, 67 km (42 miles) east of Deadhorse AK, latitude N 70°06.535', longitude W 150°12.508' (NAD 83). Ground level elevation was 57

meters (188 feet) above mean sea level, and the kelly bushing of the drilling rig was 65 meters (214 feet) above mean seal level. Unless otherwise stated, all reported depths are relative to the kelly bushing. Continuous 7.6-cm (3.0-inch) diameter core was taken from surface to 428 meters (1403 feet) during March and April 2003. Lithologies in the drilled interval are unconsolidated fine sands ("sandstone"), clays ("mudstone"), ice lenses typically thinner than 1 cm, and coals.

Average temperature a few meters below the surface is -9°C [*Shiklomanov and Nelson*, 1999]. Observed base of permafrost is at a depth of 384 meters (1260 feet) (376 meters (1234 feet) below ground level). The base of permafrost does not, in general, correspond to the 0°C isotherm, which can be considerably deeper [*Lachenbruch et al.*, 1982; *Collett et al.*, 1993]. The cored interval overlaps several hundred meters of the gas hydrate stability zone [*Collett et al.*, 1993], but no evidence of free gas or gas hydrate was found.

Special core handling techniques were used to preserve the integrity of the permafrost core. After drilling a 3-m interval, a wireline-retrieved core barrel was recovered from the well, the core extracted, and then cut into 1-m lengths. The core was immediately delivered to a core analysis trailer adjacent to the rig floor for petrographic description and NMR measurement. The wellbore was maintained near -3°C, the rig floor and cutting shack were typically -14°C, and temperature of the core-analysis trailer was maintained between -5°C and -2°C. Generally speaking, approximately 60 minutes elapsed from the time core was recovered at the wellhead to the start of NMR measurements, which took approximately 5 minutes per sample.

The nuclear magnetic resonance instrument used in this investigation was the Schlumberger Combinable Magnetic Resonance Tool (CMR). The CMR is an oilfield wireline logging tool rated to survive and operate in arctic, tropical, desert, and marine environments. Deployment of this tool to drilling rigs on the North Slope of Alaska is routine. For the purpose of measuring whole core as it was retrieved from the well, the CMR was installed in the chilled core analysis trailer adjacent to the rig floor.

The CMR volume of investigation is approximately 15 cm long and 2x2 cm in cross-section, centered about 2.5 cm inside the sample. The primary calibration was a water-filled Plexiglas tube whose dimensions were identical to the recovered core. The calibration sample had the same concentration of potassium chloride as the drilling fluid, [KCl] = 1.4 moles/liter, and was doped with iron sulfate for measurement convenience. The calibration sample was remeasured about once a day to detect instrument drift; none was detected.

Typically, each 1-m long piece of core was measured at one location; hence coverage was 15 cm per meter of core length. Some attempt was made to minimize selection bias. Grossly washed-out sections and conglomerates were both undersampled, on the basis that measurements of these intervals would be meaningless in any event. Visible ice lenses, which comprised a very small fraction of the recovered core, were generally excluded from the measured volumes, as the goal of the investigation was to understand how permafrost interacts with pore space of the sediment.

The CMR is sensitive to electromagnetic interference at 2.2 MHz, and to broadband noise sources in general. To minimize measurement noise in the core analysis trailer, a 38-cm

diameter x 85-cm long open-ended wood-frame copper screen shield was installed around the tool antenna and core sample. It was found that when core protruded from the end of the shield it could conduct significant interference to the antenna. Thus, cores were broken when necessary so that the measured piece would fit entirely within the shield enclosure. Similarly, noise could be conducted to the antenna by salty debris on the conveyer belt used to position the cores at the CMR antenna. Occasional cleaning of the belt was required.

3. NMR Fundamentals

3.1 NMR Relaxation of Water in Sediments

Measurements of transverse nuclear magnetic relaxation times, T_2, have proven to be useful in porous media studies. The Carr-Purcell-Meiboom-Gill (CPMG) [*Carr and Purcell*, 1954; *Meiboom and Gill*, 1958] pulse sequence is used. When irradiated with this sequence, a nuclear spin system will radiate back a series of equally spaced magnetic field pulses, called spin echoes. Echo spacing, T_E, is typically on the order of 10^{-4} s. Measuring the decay of echo amplitudes during the sequence monitors the transverse magnetization relaxation. Zero-time amplitude of the proton NMR signal is proportional to the hydrogen content of the sample.

For most liquids in bulk, including water, transverse magnetization decay is exponential, so the amplitude of the n^{th} spin echo, occurring at time $t = n \cdot T_E$, is

$$M(t) = M_o \exp\left[-\frac{t}{T_{2B}}\right] \tag{1}$$

Amplitude M_o is proportional to the number of hydrogen nuclei in fluids in the volume of investigation. Characteristic decay time of the echo amplitudes, T_{2B}, is called the bulk transverse relaxation time. Bulk relaxation times, which are independent of the concentration of salt at ocean salinities, are $T_{1B} = T_{2B} = 1.762$ s at 0°C [*Simpson and Carr,* 1958].

NMR relaxation rate of fluids in porous media is largely controlled by relaxation at the pore/grain interface [*Bloch,* 1951]. Molecules in a fluid diffuse, eventually reaching a grain surface where their nuclear spins can be relaxed. For water in sediments and sandstones, the rate limiting step is the relaxation process at the surface, not the transport of unrelaxed spins to the surface [*Kleinberg et al.*, 1994]. Magnetization decay, M(t), in an individual pore is exponential:

$$M(t) = M_o \, exp\left[-\frac{t}{T_{2S}}\right]. \tag{2}$$

Decay rate does not depend on pore shape but only on the surface-to-volume ratio, S/V, of the pore:

$$\frac{1}{T_{2S}} = \rho_2 \left(\frac{S}{V}\right)_{pore}. \tag{3}$$

Thus, water in small pores relaxes rapidly, while water in large pores relaxes more slowly. The surface relaxivity coefficient ρ_2 is a characteristic of magnetic interactions at the fluid/solid interface [*Kleinberg et al.*, 1994; *Foley et al.*, 1996]. In sandstones and analogous materials it is dominated by paramagnetic ions residing at grain surfaces. It is independent of temperature [*Latour et al.*, 1992] and hydrostatic pressure [*Chen et al.,* 1994] over broad ranges. Its value is typically ρ_2 = 5 μm/s for sandstones [*Kleinberg*, 1999], which is expected to hold, at least approximately, for sediments encountered here.

Bulk and surface relaxation processes operate in parallel, so the observed magnetization decay is written as

$$M(t) = M_o \exp\left[-\frac{t}{T_2}\right] \tag{4}$$

where

$$\frac{1}{T_2} = \frac{1}{T_{2B}} + \frac{1}{T_{2S}} \tag{5}$$

Rocks and sediments generally have very broad distributions of pore sizes, and therefore magnetization decays can be expressed as a sum of exponential decays [*Gallegos and Smith,* 1988]:

$$M(t) = \sum_i m_i \exp\left[-\frac{t}{T_{2i}}\right] \tag{6}$$

where m_i is proportional to the volume of fluid relaxing at the rate $1/T_{2i}$. The sum of the volumes is proportional to the fraction of the material occupied by liquid, the porosity ϕ_{NMR}:

$$M_o = \sum_i m_i \sim \phi_{NMR} \tag{7}$$

Thus there is a direct mapping from the distribution of pore sizes, or more precisely the distribution of surface-to-volume ratios, to the distribution of relaxation times.

To analyze measurements reported here, monotonic but non-exponential magnetization decays were fit to Eqn (6), where M(t) typically represented the amplitudes of 5000 spin echoes with T_E = 200 μs, and the T_{2i} were typically 50 preselected time constants, equally spaced on a logarithmic scale between 0.3 ms and 5000 ms. The number of terms in the summation is somewhat arbitrary since the exponentially decaying basis functions are not linearly independent. In fact, there are far less than 50 independent pieces of information in a typically noisy decay. Therefore, the set of 50 $m(T_{2i})$ was found using a regularized nonlinear least-squares technique that renders the results smooth and stable in the presence of random noise [*Butler et al.*, 1981]. The function $m(T_2)$, conventionally called a T_2 distribution, maps linearly to a volumetrically weighted distribution of pore sizes [*Gallegos and Smith,* 1988; *Kleinberg*, 1999].

3.2 The Effect of Ice

Ice contains abundant hydrogen, but this hydrogen is invisible because the CMR is not sensitive to nuclei in solids. Therefore the presence of ice, like methane hydrate, reduces apparent NMR porosity [*Kleinberg et al.*, 2003a]. It also diminishes the integrated amplitude and changes the shape of the apparent (i.e. water-filled) pore size distribution. These changes depend on where the ice resides within the pore space, and on the magnetic coupling between pore water and ice.

If ice coats grain surfaces, its relaxivity to liquid water, ρ_2(water-ice), replaces ρ_2(water-rock) in Eqn (3). In principle, pore size information will be retained, but the transformation between T_2 and pore diameter is changed. On the other hand, if ice grows in the interior of pores, its surfaces add to the silica grain surfaces, and Eqn (3) must be generalized to account for the simultaneous influence of two different surfaces.

Relaxivity of the ice/water surface is unknown, but the following end-member scenarios can be identified:

1. Ice coats grain surfaces and ρ_2 (water-ice) << ρ_2(water-rock): In all but the smallest pores, the bulk relaxation process will dominate, and the relaxation time distribution $m(T_2)$ will tend to pile up at T_{2B} ~ 1.7 s.

2. Ice coats grain surfaces and ρ_2(water-ice) >> ρ_2(water-rock): Shapes of the relaxation time distributions are approximately preserved, but are reduced in amplitude and displaced toward shorter relaxation times relative to the same sediment fully saturated with liquid water.

3. Ice fills the largest pore spaces and ρ_2(water-ice) << ρ_2(water-rock): Water relaxes at grain surfaces while being excluded from large pore bodies. Signal disappears first at the longest values of T_2. Paradoxically, there will be a concomitant increase of signal at short values of T_2, which occurs due to rapid relaxation of remnant liquid water coating mineral grains in large pores mostly filled with ice.

4. Ice fills the largest pore spaces and ρ_2(water-ice) >> ρ_2(water-rock): Water relaxes at both grain and ice surfaces, so the relaxation time distribution is concentrated at short values of T_2.

In reality, the NMR response might be composed of a combination of these effects, for example if the grains are partially coated with ice. In general, as the pore space fills with ice, the amplitude will decrease, with likely distortion of the T_2 distribution.

4. Recovered Core Results

4.1 Unfrozen Water Assay

As expected, apparent permafrost NMR porosity (liquid-water-filled pore space as a fraction of total sediment volume) was generally less than 0.1, considerably lower than would be expected for shallow unfrozen liquid-water-saturated sediments. In contrast, coals were characterized by unfrozen water contents of about 0.20-0.25 of total volume. At the base of permafrost, which occurred within a reasonably massive sand body, NMR determined porosity increased rapidly over an interval of 4 m. A sudden systematic increase in NMR-determined unfrozen water content was an earlier indication of the base of permafrost than petrographic examination. These results are discussed further in connection with borehole log data in Section 5.

4.2 Growth Habit of Ice: Observations While Thawing

Two typical 30-cm lengths of core, one sand (from depth 211 m (692 feet)) and one mud (from depth 202 m (662 ft)), were removed from storage at -14°C and allowed to thaw in an 18°C room. NMR measurements were made on the cores approximately once an hour for nine hours. The unfrozen water porosities are plotted as a function of time in Figure 1. The sand started with significantly lower unfrozen water porosity than the mud. The mud completely thawed in 4.5 hours, and the sand in 6 hours. The data reflect conditions in a volume centered 2.5 cm from the surface of the 7.6-cm diameter cores, as described in Section 2.

In both cases, the unfrozen water at -14°C was significantly lower than the unfrozen water found when the core was first removed from the well, at a temperature of approximately -3°C. Wellhead values of apparent NMR porosity are denoted by horizontal lines in **Figure 1**.

Relaxation time distributions are shown in **Figure 2** for the mud and **Figure 3** for the sand. A pore space model is required to convert relaxation time to pore diameter. A convenient model is a network of interconnected cylindrical tubes; this is the model used (often implicitly) to analyze mercury porosimetry data for natural earth materials. In this model, surface-to-volume ratio of a pore is S/V = 4/D, where D is pore diameter. Then NMR-determined pore diameter is related to relaxation time T_2 by

$$D = 4\rho_2 T_2 = (20\ \mu m/s) \cdot T_2 \qquad (8)$$

For both sand and mud, the frozen cores are characterized by low amplitude distributions centered on short relaxation times. As the cores thawed, amplitude increased, especially at the longest relaxation times. In both **Figures 2** and **3** the topmost curves represent thawed fully liquid-water-saturated pore size distributions.

In **Figure 3**, growth of the porosity component around 2 ms (0.04 μm pore diameter) is not monotonic. This effect is widely observed in NMR well logs of natural gas reservoirs, and is easily explained. When a nonwetting phase occupies large pores, water generally continues to coat pore walls. Surface-to-volume ratio (S/V) of this pore-lining water is much greater than S/V

of water when it completely filled the same pore. Thus the remnant water relaxes at a faster rate, thereby appearing to add to the smaller-pore population [*Kleinberg and Boyd*, 1997].

Comparing these results to the four possibilities listed in Section 3.2, the mudstone results are consistent with (2), (3) or (4). Sandstone results are consistent only with (3).

4.3 Growth Habit of Ice: Transition Zone Sands

Fortuitously, the base of permafrost (at a depth of 384.0 m (1260 ft)) lay within a reasonably massive and homogeneous sand body. This sand body thus constituted a natural laboratory for exploring the development of frozen sediment. The transition from fully liquid water-saturated sediment to permafrost occurs over a depth interval of 4 m.

Relaxation time distributions through the transition zone are shown in **Figure 4**. Distributions at 384.7 m (1262 ft) and 386.8 m (1269 ft) appear to be trimodal while the others are bimodal. The trimodal curves are unlikely to represent three distinct populations in the liquid-water-filled pore size distribution, but instead represent a limitation of the nonlinear signal processing. A reasonable interpretation of the 384.7 m and 386.8 m curves is that they are essentially flat-topped.

Above the base of permafrost, the water signal is small and concentrated at short relaxation times. Following the same reasoning used in the discussion of the thawed samples, these observations indicate that unfrozen water is localized in small pore spaces, where it is in contact with grain surfaces that are not coated with ice. As depth increases, unfrozen water occupies more of the pore space. In the transition zone, water occupies small, mid-sized and large pore spaces of this sand, as reflected by the low NMR signal amplitude. At a depth of 387.7 m (1272 feet), water is completely unfrozen and the relaxation time distribution reflects the pore size distribution of the sediment.

As for the samples discussed earlier, excess signal at short relaxation time in the frozen samples reflects the presence of water coating the grain surfaces of large pores, the interiors of which are filled with ice. Results are consistent only with possibility (3) listed in Section 3.2: ice preferentially fills the largest pore spaces, and it is not an effective relaxing surface for liquid water.

4.4 Hydraulic Permeability

Hydraulic permeability of a porous medium depends generally on the square of the cross-sectional dimension of the flow channels [*Scheidegger*, 1960]. Sensitivity of NMR measurements to pore size makes it a good permeability indicator for sandstones [*Straley et al.*, 1994]. The NMR estimate of permeability has been tested on thousands of sandstones over the years; order-of-magnitude agreement with laboratory measured values is expected. However, the technique has not been systematically tested in unconsolidated sediments, nor in sediments consolidated by ice. Therefore we must proceed with some caution.

The empirical correlation that connects hydraulic permeability k_0 to porosity and a one-parameter measure of relaxation time, T_{2LM}, is

$$k_0 = C \cdot \phi_{NMR}^4 \cdot T_{2LM}^2 \tag{9}$$

where T_{2LM} is the logarithmic mean value of the T_2 distribution.

$$T_{2LM} = 10^{\left[(1/\phi)\sum_i m(T_{2i})\cdot \log_{10}(T_{2i})\right]} \tag{10}$$

C is a coefficient which depends on mineralogy and on the magnetic impurity content of the grain material. A large number of measurements on water-saturated clean and clay-rich sandstones showed that typically C = 4000 D/s^2 [*Straley et al.*, 1994] (1 Darcy $\approx$ 0.987x10^{-12} m^2).

4.5 Relative Permeability

Relative permeability is the permeability of sediment to a single fluid when two or more constituents occupy the pore space. In a rock or sediment containing oil, water, and/or or gas, each of these fluids will have different relative permeability, which depends on the saturations. Here we use the term to describe hydraulic permeability when part of the pore space is partially filled with ice:

$$k_{rw} = \frac{k(S_w)}{k_0} \tag{11}$$

where k_0 is permeability of the fully liquid-water-saturated sediment, and $k(S_W)$ is permeability at water saturation S_W, with the remaining pore space filled with ice at saturation $S_i = 1 - S_W$.

Relative permeability may be found when permeability measurements of both fully water-saturated sediment and the same sediment partially saturated with ice are available. This is the case in the thawing studies, where NMR properties of a sample are followed over a range of water saturations. It is also the case at the base of permafrost, to the extent that sediment properties are uniform over the transition zone. Water saturation is found from

$$S_w = \frac{\phi_{NMR}(S_w)}{\phi_{NMR}(S_w = 1)} \tag{12}$$

where $\phi_{NMR}(S_W)$ and $\phi_{NMR}(S_W=1)$ are apparent NMR porosities in the partially and fully water saturated sediment, respectively. Using this and Eqn (9), NMR estimated relative permeability is

$$k_{rw} = \frac{k(S_w)}{k_0} = S_w{}^4 \cdot \left(\frac{T_{2LM}(S_w)}{T_{2LM}(1.0)}\right)^2 \tag{13}$$

The mineralogy-dependent coefficient C does not appear in this ratio.

As noted above, this approach has some important limitations: the permeability estimate is based on an empirical correlation, not a flow measurement, and it assumes that the correlation is as valid for ice-affected sediment as it is for water-filled rock. A subsidiary assumption is that NMR relaxation of liquid water at an ice surface is no stronger than at a mineral grain surface, i.e., ρ_2(water-ice) << ρ_2(water-rock), as concluded in Sections 4.2 and 4.3. It also assumes that differences of the microgeometrical distribution of water in unfrozen and partially frozen rock do not invalidate the correlation.

Relative permeability estimates for the thawed samples, and for sands at the base of permafrost are shown in **Figure 5**. All data follow a common trend as a function of liquid water saturation. This is surprising since k_0 differs widely among these three samples, as noted above. However, the proportionate impact of the presence of ice appears to be the same.

The data can be compared to simple models for relative permeability derived elsewhere [*Kleinberg et al.*, 2003b]. Results for various models are:

ice coating the walls of capillary tubes:

$$k_{rw} = S_w^{\,2} \tag{14}$$

ice growing in the centers of capillary tubes:

$$k_{rw} = 1-(1-S_w)^2 + \frac{2S_w^{\,2}}{\log(1-S_w)} \tag{15}$$

ice coating the surfaces of a grain pack:

$$k_{rw} = S_w^{\,n+1} \tag{16}$$

For this model, the saturation exponent n equals 1.5 for $0<S_i<0.8$ ($1>S_w>0.2$) [*Spangenberg*, 2001]. For $S_i>0.8$ ($S_w<0.2$), the saturation exponent diverges, but in this regime relative permeability to water is already small, and the increase of the saturation exponent has only a minor effect.

ice growing in the centers of a grain pack pore space:

$$k_{rw} = \frac{S_w^{\,n+2}}{\left(1+(1-S_w)^{0.5}\right)^2} \tag{17}$$

Neglecting the effects of capillary pressure, the saturation exponent increases from n = 0.4 at S_i = 0.1 (S_w = 0.9) to unity at S_i = 1 (S_w = 0), [*Spangenberg*, 2001].

NMR estimates of relative permeability agree better with the models that assume ice fills the centers of pores than with those that assume ice coats pore walls. The same conclusion is independently drawn from the relaxation time distributions discussed above.

5. Core/Log Comparison

In addition to measurements made on recovered core, magnetic resonance well log measurements were made in the borehole after the completion of coring. The NMR instrument used for well logging was a nearly identical copy of the instrument used in the core lab to measure retrieved core samples. The pulse sequence was the same as that used for the core measurements. Pulse sequence parameters were somewhat different, but the differences are not expected to affect the results.

During the 15 days of coring operations the 428 m (1403 feet) deep wellbore was substantially thawed by the 1.4M KCl drilling fluid. Unconsolidated sediment sloughed into the wellbore with the result that it was enlarged beyond the 216-mm (8½-inch) diameter of the drill bit (**Figure 6**). The wireline tool was pressed against the borehole wall with a bow spring, but in the irregular borehole the sensor can intermittently lose contact with the surface. The wireline magnetic resonance measurement, like the NMR measurement on core, is made in a volume centered 25 mm from the face of the apparatus. If there is borehole fluid in this volume, the NMR amplitude will be erroneously high.

As **Figure 7** reveals, well log porosities frequently exceeded the maximum porosity expected in shallow terrestrial sediments, about 0.4. Except for a few minor intervals at the top of the well, there is no agreement between core measurements of unfrozen water porosity and well log porosity measurements, even where the borehole was not enlarged beyond bit size. This suggests that not only was the wellbore enlarged but also thawed, at least to the radial depth of the NMR measurement volume, prior to well logging. Even if near-wellbore sediments were below the freezing point of fresh water, KCl migration from the borehole into the pore space lowered the freezing point of the pore fluid.

In conventional interpretation of petrophysical measurements, the NMR signal is partitioned into bound water (small pore) and free water (large pore) porosity [*Kleinberg*, 1999]. In sandstone formations, this partition is conventionally made at T_{cutoff} = 33 ms. Water in pore spaces relaxing faster than 33 ms, corresponding to a pore diameter of about 0.7 μm, is not movable at a pressure difference of less than 0.7 MPa (100 psi). Taking into account the details of how water is trapped in porous media by capillary forces, a tapered function is applied to the fully-water-saturated pore size distribution to determine the amount of porosity included in the small-pore fraction [*Kleinberg and Boyd*, 1997]. For T_2 components below $T_{2cutoff}/4$ all measured porosity is included in the small-pore estimate. For $T_2 > T_{2cutoff}/4$

$$m(T_2)_{taper} = m(T_2)\left[\frac{T_{cutoff}}{2T_2} - \left(\frac{T_{cutoff}}{4T_2}\right)^2\right] \tag{18}$$

The small pore analysis is illustrated at 365.8 m (1200 ft) in **Figure 8**. The topmost curve is the well log relaxation time distribution of the thawed formation; the corresponding porosity is 0.317. Within it is plotted the small pore relaxation curve computed using Eqn (18), with a porosity of 0.047. The lowest curve (inverted for clarity) is the relaxation time distribution measured on the core taken from the same depth, with a porosity of 0.039. The small-pore-porosity from the well log and the unfrozen-water-porosity from the core agree to within the ±0.01 error bars of the measurement.

This analysis was repeated for the entire borehole, a representative section of which is shown in **Figure 9**. Below the base of permafrost (horizontal line at 384 m (1260 feet)), core unfrozen water includes both small-pore-porosity and large-pore-porosity, and therefore the core points fall above the log-derived small-pore-porosity. Above the base of permafrost the data are in excellent agreement.

Agreement persists even where the borehole is grossly washed out and NMR values spike to values well above 0.4, indicating that substantial amounts of borehole fluid must be included in the well log measurement, see e.g. 250–300 m. Log small-pore-porosity agrees with core unfrozen-water-porosity in washed out intervals because the borehole water contributes only to the free fluid (large pore) signal with $T_2 > 33$ ms. Although conventional oilfield drilling muds usually have T_{2B} around 20 ms, the drilling fluid used here had a relaxation time of 50 ms.

Since permafrost unfrozen water correlates with small-pore-porosity, it should be in greatest abundance in fine-grained sediments. During data taking it was noted that higher values of unfrozen water porosity were found in mudstone than in sandstone (see e.g. **Figure 1**). **Figure 10** shows a cross plot between log small-pore-porosity and log gamma ray amplitude. The latter is predominantly a clay indicator [*Hearst et al.*, 2000]. A correlation between high clay content and high small-pore-porosity is common in sandstones and sediments. The anomalous jet extending to the upper left is isolated in **Figure 11**. All the points in the jet originate in coals, identified petrographically in the recovered core. Natural gamma radioactivity correlates with ash content [*Reeves*, 1971]. **Figure 11** suggests that small pore porosity in coal is inversely correlated with ash content, and that therefore it is primarily associated with the organic component.

6. Conclusions

Nuclear magnetic resonance methods used in evaluation of oil- and gas-bearing formations are also useful in understanding pore-scale interactions between sediments and ice in permafrost. The quantitative assay of unfrozen water content is model independent and does not depend on any adjustable parameters.

NMR-derived pore size distribution is subject to interpretation. However, the preponderance of experimental results shows that the silt and clay sediments investigated here remain liquid-water-wet in the presence of ice, which tends to accumulate in the largest pore spaces.

Permafrost retrieved from the wellbore was well-consolidated and robust. The cohesiveness came from ice which, when melted, left loose silt and clay. Data presented in this work suggest

that ice does not preferentially cement grain contacts, but perhaps it stiffens the sediment by bridging large pores. This hypothesis is supported by the NMR and sonic well logs of the Mallik 5L-38 gas hydrate test well. There the dependence of sound speed on NMR-derived hydrate saturation was found to be consistent with hydrate partially supporting the granular matrix without coating the grains or cementing the grain contacts [*Kleinberg et al.*, 2004].

Although permeabilities of the various sediments, as estimated by NMR, vary widely, their relative permeabilities to water as a function of ice saturation are remarkably uniform. However, use of NMR to estimate permeability in permafrost is unproven. It would be very desirable to make laboratory permeability measurements of samples that are also characterized by NMR.

Although the borehole was thawed and washed out during the drilling process, and therefore no permafrost remained in the NMR volume of investigation during well logging, there is a strong correlation between well log NMR small-pore-porosity and core measurements of unfrozen water in intact permafrost.

Coals in permafrost formations have large unfrozen water contents that correlate inversely with ash content.

Acknowledgements

Profs. C.H. Sondergeld and C.S. Rai designed and constructed the mobile arctic core laboratory. Messrs. N. Emery, J. Eubanks, G. McCardle, W.G. McLeod, J. Van Eerde, and W.D. Zogg provided core handling and description services, and generously shared resources on the Hot Ice rig. Mr. S. Bartz aided in planning and coordination. Dr. T. Collett generously shared his knowledge of permafrost. This work could not have been carried out without the logistical support of Schlumberger Oilfield Services, Prudhoe Bay, AK, Anadarko Petroleum Corp., and Noble Drilling Corp. The project ("Methane Hydrate Production from Alaskan Permafrost") is funded by the US Department of Energy National Energy Technology Laboratory through a cooperative agreement with Maurer Technology (DE-FC26-01NT41331) in conjunction with Anadarko Petroleum Corporation.

Appendix: Notation

C: coefficient of NMR permeability correlation

k_{rw}: relative permeability to water of ice-affected sediment

k_0: permeability to water of water-saturated sediment

m_i: i^{th} coefficient of relaxation time distribution

$m(T_2)$: relaxation time distribution

$m(T_{2i})$: i^{th} coefficient of relaxation time distribution

M_0: initial amplitude of magnetization decay

M(t): magnetization decay as function of time

S_i: fraction of pore volume filled with ice

S_W: fraction of pore volume filled with water

S/V: surface to volume ratio of pore space

T_{cutoff}: T_2 value separating small-pore and large-pore water

T_E: spin echo spacing in CPMG sequence

T_{1B}: longitudinal relaxation time of bulk liquid

T_2: NMR transverse relaxation time

T_{2B}: transverse relaxation time of bulk liquid

T_{2i}: transverse relaxation time of i^{th} component

T_{2LM}: logarithmic mean of the relaxation time distribution

T_{2S}: relaxation time due to surface relaxivity

ϕ_{NMR}: apparent porosity measured by NMR

ρ_2: relaxivity of a solid surface to water protons

References

Bloch, F., 1951. Nuclear relaxation in gases by surface catalysis. *Phys. Rev*., 83: 1062-1063.

Butler, J.P., Reeds, J.A. and Dawson, S.V., 1981. Estimating solutions of first kind integral equations with nonnegative constraints and optimal smoothing. SIAM *J. Numer. Anal*., 18: 381-397.

Carr, H.Y. and Purcell, E.M., 1954. Effects of diffusion on free precession in nuclear magnetic resonance experiments. *Phys. Rev*., 94: 630-638.

Chen, R., Stallworth, P.E., Greenbaum, S.G. and Kleinberg, R.L., 1994. Effects of hydrostatic pressure on proton and deuteron magnetic resonance of water in natural rock and artificial porous media. *J. Magn. Reson*., A110: 77-81.

Collett, T.S., Bird, K.J. and Magoon, L.B., 1993. Subsurface temperatures and geothermal gradients on the North Slope of Alaska. *Cold Regions Sci. Tech*., 21: 275-293.

Foley, I., Farooqui, S.A. and Kleinberg, R.L., 1996. Effect of paramagnetic ions on NMR relaxation of fluids at solid surfaces. *J. Magn. Reson*., A123: 95-104.

Gallegos, D.P. and Smith, D.M., 1988. A NMR technique for the analysis of pore structure: Determination of continuous pore size distributions. *J. Colloid Interface Sci*., 122: 143-153.

Hearst, J.R., Nelson, P.H. and Paillet, F.L., 2000. *Well Logging for Physical Properties*. Wiley, Chichester.

Kleinberg, R.L., 1996. Well logging. In: D.M. Grant and R.K. Harris (Editors), *Encyclopedia of Nuclear Magnetic Resonance*, Vol. 8. Wiley, Chichester, pp. 4960-4969.

Kleinberg, R.L., 1999. Nuclear magnetic resonance. In: P.-Z. Wong (Editor), Experimental Methods in the Physical Sciences, Vol. 35: Methods in the Physics of Porous Media. Academic, San Diego, Calif., Chap. 9.

Kleinberg, R.L. and Boyd, A., 1997. Tapered cutoffs for magnetic resonance bound water volume, Society of Petroleum Engineers Paper 38737.

Kleinberg, R.L. and Flaum, C., 1998. Review: NMR detection and characterization of hydrocarbons in subsurface earth formations. In: B. Blumich, P. Blumler, R. Botto, E. Fukushima (Editors), Spatially Resolved Magnetic Resonance. Wiley-VCH, Weinheim, Chap. 54.

Kleinberg, R.L., Sezginer, A., Griffin, D.D. and Fukuhara, M., 1992. Novel NMR apparatus for investigating an external sample. *J. Magn. Reson*., 97: 466-485.

Kleinberg, R.L., Kenyon, W.E. and Mitra, P.P., 1994. Mechanism of NMR relaxation of fluids in rock. *J. Magn. Reson*., A108: 206-214.

Kleinberg, R.L., Flaum, C., Straley, C., Brewer, P.G., Malby, G.E., Peltzer, E.T., Friederich, G. and Yesinowski, J.P., 2003a. Seafloor nuclear magnetic resonance assay of methane hydrate in sediment and rock, *J. Geophys. Res*. 108(B3): 2137. doi:10.1029/2001JB000919

Kleinberg, R.L., Flaum, C., Griffin, D.D., Brewer, P.G., Malby, G.E., Peltzer, E.T. and Yesinowski, J.P., 2003b. Deep sea NMR: Methane hydrate growth habit in porous media and its relationship to hydraulic permeability, deposit accumulation, and submarine slope stability, *J. Geophys. Res*. 108(B10): 2508. doi:10.1029/2003JB002389

Kleinberg, R.L., Flaum, C. and Collett, T.S., 2004. Magnetic resonance log of Mallik 5L-38: Hydrate saturation, growth habit, relative permeability and control of accumulation. In: S.R. Dallimore and T.S. Collett (Editors), Scientific Results from the Mallik 2002 Gas Hydrate Production Research Well, Mackenzie Delta, Northwest Territories, Canada, Bulletin 585. Geological Survey of Canada, Ottawa.

Lachenbruch, A.H., Sass, J.H., Marshall, B.V. and Moses Jr., T.H., 1982. Permafrost, heat flow, and the geothermal regime at Prudhoe Bay, Alaska. *J. Geophys. Res*. B87: 9301-9316.

Latour, L.L., Kleinberg, R.L. and Sezginer, A., 1992. Nuclear magnetic resonance properties of rocks at elevated temperatures. *J. Colloid Interface Sci*., 150: 535-548.

Meiboom, S. and Gill, D., 1958. Modified spin echo method for measuring nuclear relaxation times. *Rev*. *Sci. Instrum*., 29: 688-691.

Reeves, D.R., 1986. In situ analysis of coal by borehole logging techniques. In: D.J. Buchanan and L.J. Jackson (Editors), Geophysics Reprint Series, No. 6: Coal Geophysics. Society of Exploration Geophysicists, Tulsa.

Scheidegger, A.E., 1960. *The Physics of Flow Through Porous Media*. Macmillan, New York.

Shiklomanov, N.I. and Nelson, F.E., 1999. Analytic representation of the active layer thickness field, Kuparuk River Basin, Alaska. *Ecological Modeling* 123: 105-125.

Simpson, J.H. and Carr, H.Y., 1958. Diffusion and nuclear spin relaxation in water. *Phys. Rev*., 111: 1201-1202.

Spangenberg, E., 2001. Modeling of the influence of gas hydrate content on the electrical properties of porous sediments, *J. Geophys. Res*. B106: 6535-6548.

Straley, C., Rossini, D., Vinegar, H., Tutunjian, P. and Morriss, C., 1994. Core analysis by low field NMR. Society of Core Analysts Paper SCA-9404. Proceedings of the 1994 International Symposium of the Society of Core Analysts, Stavanger, Norway.

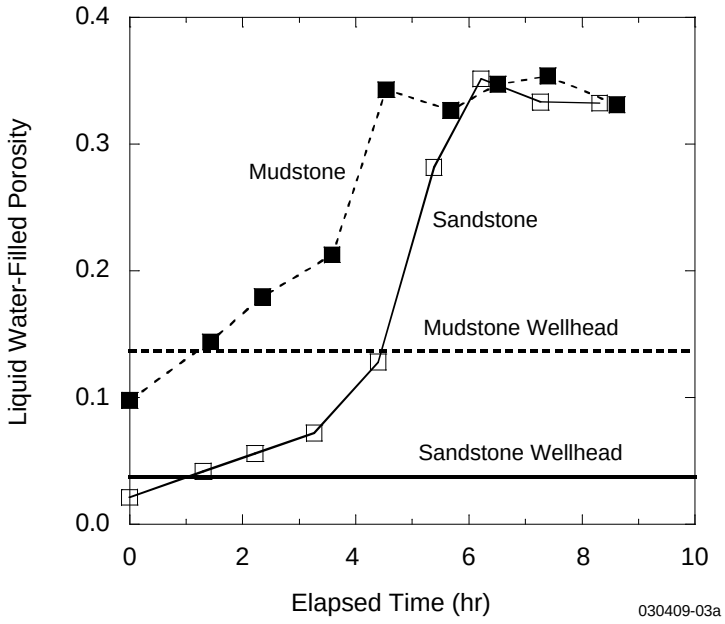

Figure 1. Thawing of mudstone and sandstone cores monitored by NMR porosity measurements. Cores were precooled to -14°C, then warmed in an 18°C room. The horizontal lines indicate porosity measurements immediately after retrieval of the core from the borehole, which was approximately -3°C.

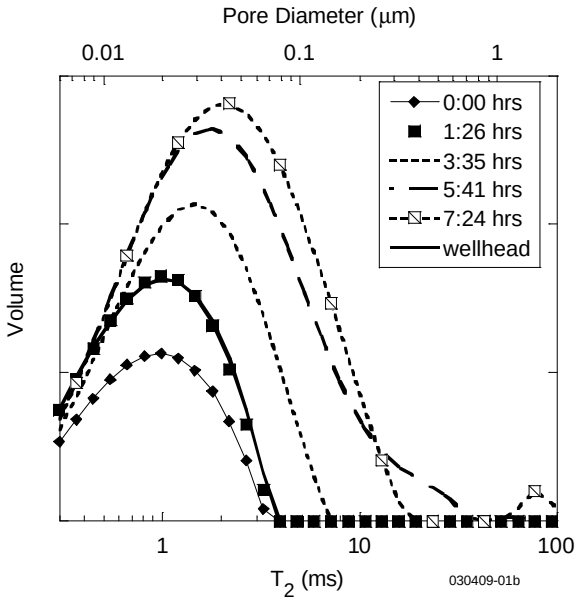

Figure 2. Relaxation time distributions of mudstone during thawing from -14°C to 18°C. Frozen samples are characterized by low NMR amplitudes and short relaxation times. After 1.5 hours of warming, core returned to the state in which it was removed from the wellbore (solid squares, heavy solid line). During melting process, the amount of NMR-visible (liquid) water increased, and successively larger pore spaces thawed. By 7.5 hours (outermost line) the permafrost had completely melted, revealing the pore size distribution of the water-saturated sediment.

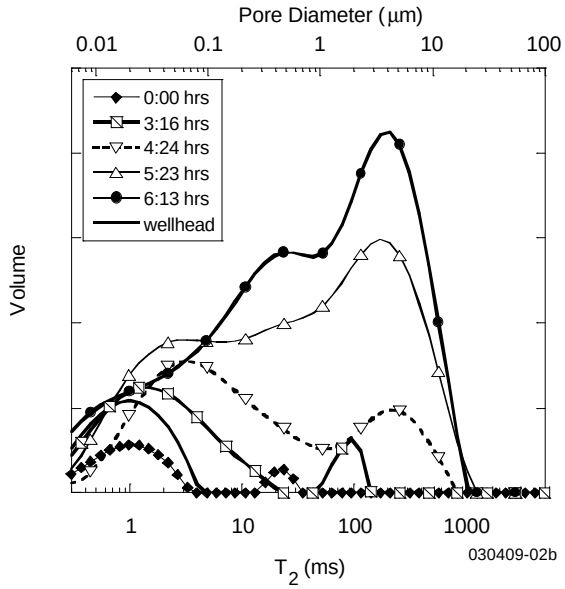

Figure 3. Relaxation time distributions of sandstone during thawing from -14°C to 18°C. Frozen samples are characterized by low NMR amplitudes and short relaxation times. During the melting process the amount of NMR-visible (liquid) water increased, and successively larger pore spaces thawed. By 6.25 hours (outermost line) the permafrost had completely melted, revealing the pore size distribution of the water-saturated sediment.

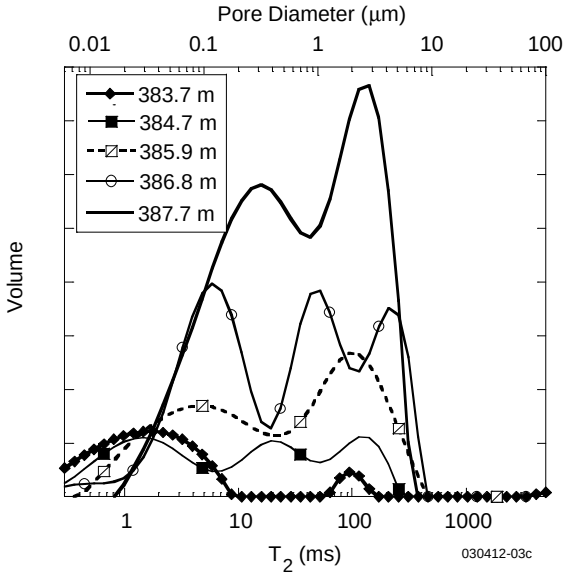

Figure 4. NMR relaxation time distributions near the base of permafrost (384 m, 1260 ft). Above the base of permafrost, cores are characterized by low NMR amplitudes and short relaxation times (solid diamond curve). As depth increased, successively more of the pore space was occupied by liquid water. The rock was fully liquid-water saturated 4 m below the base of permafrost, revealing the pore size distribution of the liquid-water-saturated sediment (topmost curve). The apparently trimodal curves are discussed in the text.

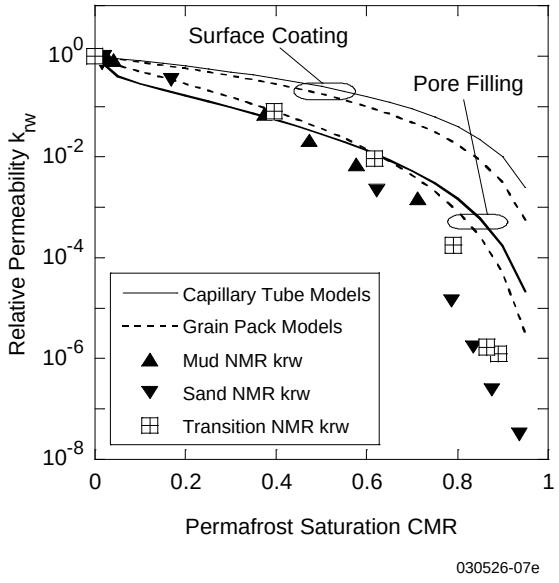

Figure 5. Relative permeability to water computed using Eqn (13) for three groups of samples: thawing mudstone (▲), thawing sandstone (▼), and cores from the base of permafrost (crossed squares). Curves are predictions of grain coating and pore filling models, as described in the text.

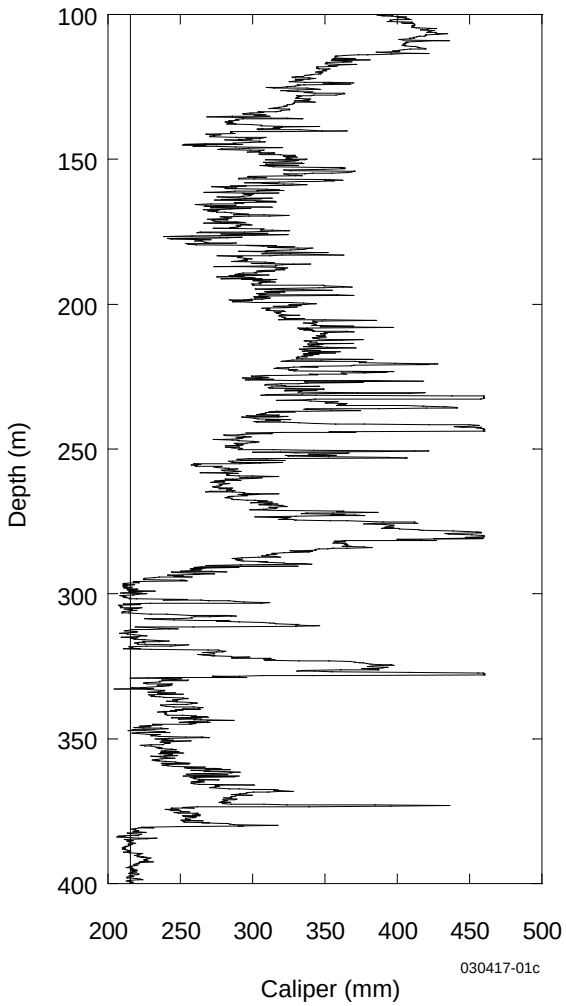

Figure 6. Wireline caliper log of borehole diameter. Vertical line is the 216-mm (8½-inch) bit size. The borehole was significantly washed out during coring operations.

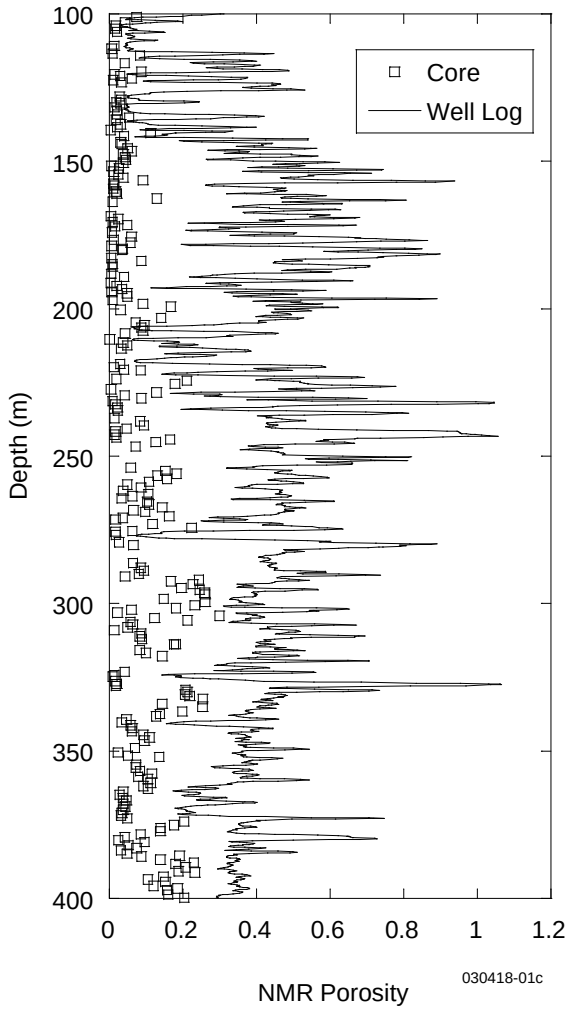

Figure 7. Wireline NMR log total porosity (solid curve) and laboratory NMR core unfrozen water porosity (squares). Anomalously high values of log porosity (>0.4) occurred at edges of washouts (see previous figure), where the sensitive volume of the logging tool included borehole water.

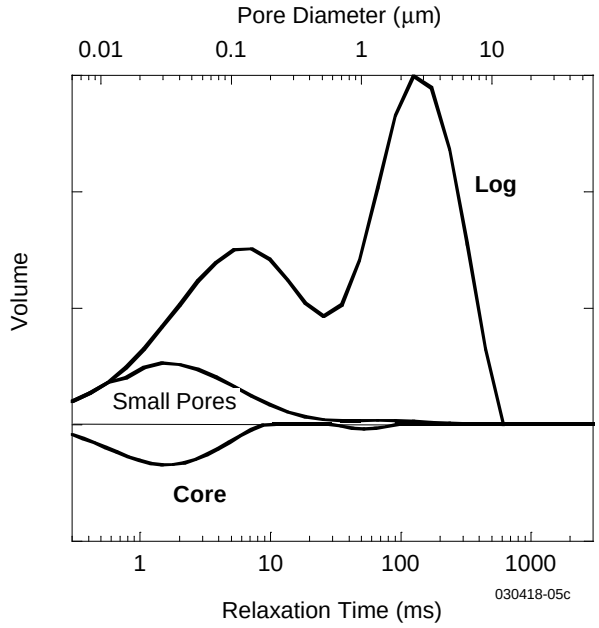

Figure 8. *Above horizontal line:* Relaxation time distribution from log at 365.8 m (1200 ft) (upper curve) and its small pore porosity computed from Eqn. (18) (lower curve). *Below horizontal line:* Relaxation time distribution of unfrozen water from permafrost core sample at the same depth (inverted for display purposes). Note similarities in the T_2 distributions of log small pore water and core unfrozen water.

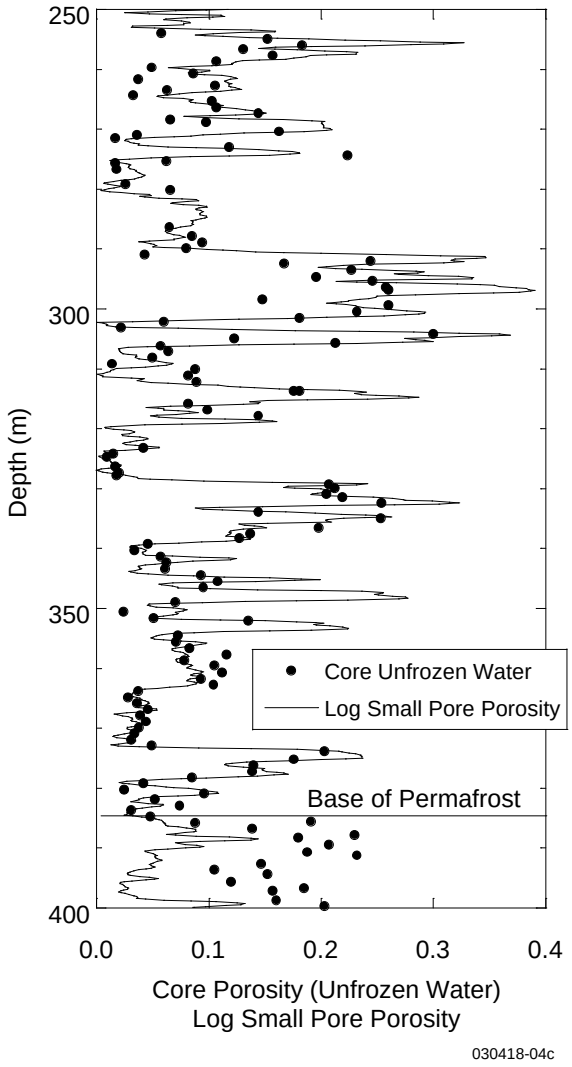

Figure 9. Log small-pore-porosity (solid curve) and core porosity (unfrozen water content) (symbols). Above the base of permafrost (horizontal line at 384 m, 1260 ft) the data are in excellent agreement. Below the base of permafrost, core unfrozen water includes both small pore porosity and large pore porosity, and therefore the core points fall above the log small-pore-porosity.

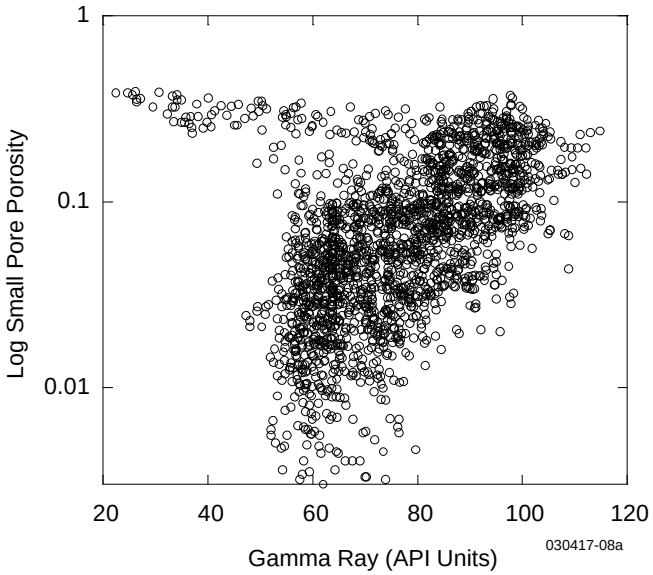

Figure 10. Cross plot of log small-pore-porosity and natural gamma-ray log. The latter is predominantly a clay indicator. A correlation between high clay content and high small-pore-porosity is common in sandstones and sand sediments. The anomalous jet extending to the upper left is explained in the text and the next figure.

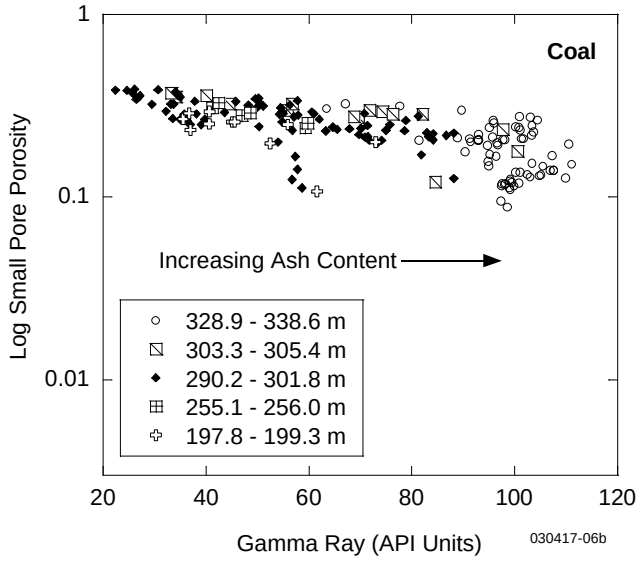

Figure 11. Points comprising the anomalous jet of Figure 10 are all from coals. The depth intervals indicated in the plot legend were identified as coal-bearing by visual examination of the cores. In coal, natural gamma radioactivity is associated with ash [Reeves, 1971]. Therefore, small-pore-porosity is proportional to organic matter content.

Appendix E:
An Application Used for Correcting Thermal Gradients Below Permafrost Using an Empirical Diffusion Model: Anadarko's Hot Ice No. 1 Gas Hydrates Case Study

Kent E. Newsham and Richard Sigal (Anadarko Petroleum Corporation)

Jonathan T. Kwan (University of Oklahoma)

Key Words: Gas Hydrates Stability Zone, Base of Permafrost, Thermal Diffusion, Geothermal Gradient

Abstract

Gas hydrates represent a very large global hydrocarbon resource that is attracting strategic research activities to recover and evaluate potential accumulations. Anadarko's Hot Ice No. 1 project is a collaborative effort of private business and the U.S. Department of Energy to evaluate subsurface hydrate occurrences in the North Slope of Alaska. The gas hydrate stability zone (HSZ) was assessed to aid in drilling site selection for the Hot Ice well. The subsurface HSZ was determined using Collett's pressure/temperature hydrate stability model (Collett et al. (1988) and Collett (1993)). The hydrate phase envelope is compared to a segmented geothermal gradient estimated in the permafrost and sub-permafrost intervals. Top and base of the HSZ is determined by the intersection of the geothermal gradient and phase envelope on a pressure/temperature plot. The critical path in this analysis of the HSZ position is determining position and temperature of the base of permafrost and the sub-permafrost geothermal gradient. The sub-permafrost geothermal gradient can be erroneous if thermal effects of drilling fluids on bottom-hole temperature measurements are not corrected. This paper is focused on the use of a thermal diffusion model to correct local geothermal gradients to improve estimation of the location of the HSZ in the Hot Ice well.

Table of Contents

Background

Anadarko Petroleum, Maurer Technology, and the U.S Department of Energy began a dedicated gas-hydrate drilling operation in March 2003 on the North Slope of Alaska. Cost of this project was partly supported by DOE as part of their long-term program to evaluate the resource potential of North Slope hydrate accumulations. Multiple objectives were served in drilling this well, including evaluation of subsurface hydrate occurrence, demonstration of a new and environmentally safe drilling technology, and characterization of potential hydrate reservoirs using in-situ measurements and continuous ice core studies provided on site by use of Anadarko's Mobile Core Laboratory.

Hot Ice No. 1 is located 20 miles south of the Kuparuk River Oil Field. The surface location is: latitude: 70°, 6 min, 31.39 sec; longitude: 150°, 12 min, 43.23 sec. The nearest offset wells are the Cirque 2, West Sak 20, and the Ruby State 1. The proposed total depth of the well was 2700 ft.

During the first stage of drilling (Phase I), Hot Ice No. 1 was drilled to the base of permafrost and then cased. Due to warming temperatures, operations were suspended on April 21, 2003. Depth of the well at that time was 1403 ft. Base of permafrost was found at 1046 ft TVDss, and a 7-inch casing was set in shale between the Ugnu and West Sak formations. Operations were scheduled to restart in the winter of 2004. No hydrate containing sediments were identified in Phase I.

This shallow section of the Hot Ice No. 1 was logged and continuously cored. The wire-line logging program included measurements of natural gamma-ray spectrometry, compensated neutron and density, array induction resistivity, dipole acoustic, and magnetic resonance. Dipole sonic data acquired included a mono-pole compressional slowness, cross-dipole shear slowness, and stoneley waves. Magnetic resonance was acquired from down-hole wireline operations and surface measurements of the core. Cores were acquired using a wireline coring system that recovered continuous cores 3.3 inches in diameter. A chilled mud system was used to aid in preservation and recovery of the cores. Fluid temperature was maintained at 23°F.

Cores were evaluated using Anadarko's on-site Mobile Core Laboratory. Both whole core and plug measurements were completed. Whole-core measurements included gamma ray, white light photography, infra-red temperature, acoustic velocity, CT scans, and continuous magnetic resonance provided by Schlumberger. In addition, a complete geologic description was obtained. Plug measurements included porosity, permeability, grain density, compression and shear velocities, gas spectrometry, thermal conductivity, resistivity, and magnetic resonance.

Objectives

A study encompassing three wells was undertaken to understand the shallow hazards associated with the permafrost, gas hydrates, and gas hydrate plumes of the Hot Ice area. The three wells studied were Cirque 2, West Sak 20, and Ruby State 1. Results were to be used as an aid in the pre-spud well planning of Hot Ice No. 1.

The purpose of this study was to:

1. Identify the base of the hydrate stability zone (BHSZ) using the Katz (1971) and Collett (1988 and 1993) thermal models, so that the complete potential hydrate zone is cored

2. Aid in design of proper casing programs to protect fresh water aquifers by defining the lower boundary of the permafrost
3. Understand the influence of formation salinity on position of the base of permafrost
4. Assess the presence of methane plumes within or below the HSZ

This paper focuses on use of a thermal diffusion model to correct local geothermal gradients and the model's impact on better estimation of the BHSZ.

Gas Hydrate Stability Zone

The hydrate stability zone (HSZ) is determined by subsurface temperature, pore pressure, pore water salinity, pore geometry of the sediment in which the hydrate forms, and gas composition. Calculations used in this study make the same assumptions and follow the same general approach as Collett's 1988 regional study of the HSZ on the North Slope. **Figure 1** shows Collett's pressure/temperature hydrate stability model. The blue line represents Collett's thermal model; the green line the geothermal gradient; the green square the base of permafrost. The HSZ is the interior region defined by the intersection of Collett's thermal model and the geothermal gradient, and is represented by diagonal lines. Top of the HSZ often occurs at shallow depths within the permafrost region.

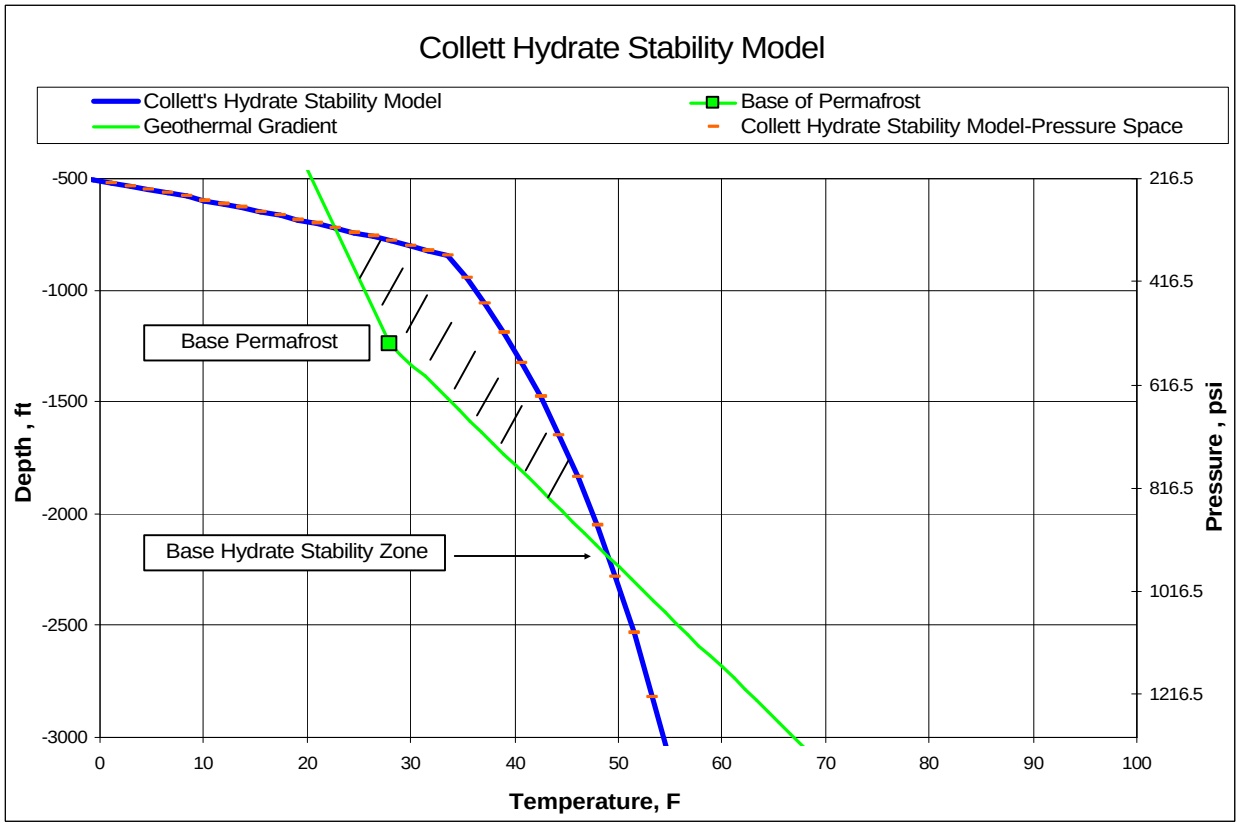

Figure 1. Collett thermal model used for defining hydrate stability envelope

The critical path in the analysis of the base of the HSZ is determining the position of the base of permafrost and the sub-permafrost geothermal gradient. We examine factors that influence the position of the base of permafrost and the geothermal gradient.

- ***Pore geometry influences on base of permafrost.*** Based on examination of resistivity and sonic logs within the permafrost, it appears that fine-grained sediments freeze less readily than coarse-grained sediments. Smaller pores tend to suppress the freezing point of water. A similar effect has been documented for hydrates. For sediments that form good reservoirs, this effect should be small. For this study, pore geometry has been ignored in calculating the local BHSZ.
- ***Salinity influences on base of permafrost (BOPF).*** Salinity variations in connate waters of the shallow permafrost sediment can alter the freezing point of water which will change the depth of the BOPF. An increase or decrease in depth of the BOPF will either expand or contract the HSZ, respectively. However, direct and indirect evidence shows that pore water salinity in permafrost is much less than sea water. For example, regional temperatures at the base of ice bearing permafrost reported by Collett (1988) require salinities less than 30 ppt. Based on the hydrate stability calculator in Slone (1998), this salinity will only suppress the stability temperature by about 1°C.
- ***Pressure influences on BOPF.*** Pore pressure can be influenced by salinity of connate water in the permafrost and by compaction disequilibrium effects. Since the connate waters are considered nearly fresh water and compaction is stalled by the permafrost, there is no evidence for abnormally pressured compartments at depths at which hydrates are expected to form. The pore pressure is considered to be hydrostatic.
- ***Geothermal gradient influences*.** Regional temperature gradient depends on effective average surface temperature, regional heat flux and thermal conductivity of the sediments. Local gradient is also affected by topography and adjacent bodies of water. Because replacing water by ice in a rock raises its thermal conductivity, it is expected that thermal gradients in the permafrost should be less than that in the sub-permafrost section. Hence, it is customary to use two thermal gradients, one above the BOPF, and one below. Maximum reading or bottom-hole thermometers used to determine the sub-permafrost geothermal gradient are influenced by cooling and/or heating effects of the drilling mud system. Non-chilled drilling fluids will cause a heating in the shallow, near-permafrost intervals and a cooling effect at depth. Thermal warming that occurs in the near permafrost area can shift the interpretation of the HSZ by as much as 30°F, creating a false indication that the HSZ is small to non-existent (see Figure 1). In this study, local bottom-hole temperature data recorded in the three adjacent wells were corrected using the thermal diffusion model documented by Lachenbruch et al. (1982). Corrected gradients were used to imply the local subsurface temperature gradient in the Hot Ice No. 1 well.

Study Methods

Determination of Geothermal Gradients

The geothermal gradient was determined as a two-segment gradient divided at the BOPF. The regional permafrost thermal gradient was determined from effective average surface temperature and temperature at the base of ice-bearing permafrost using regional maps in Collett (1993) and Collett et al. (1993). The permafrost thermal gradient for the three wells in this study was determined using average surface temperature and freezing temperature at the base of permafrost. Freezing temperature at the BOPF was estimated as a function of shale salinity in the zone between the base of permafrost and the base of the HSZ (see section on salinity determination).

The sub-permafrost geothermal gradient is determined from a composite of the maximum reading temperatures reported on the log headers for each log run corrected to an undisturbed bottom-hole temperature equivalent. Bottom-hole temperature data were corrected using the diffusion model documented by Lachenbruch et al. (1982). This part of the calculation contains the main deviation from the method employed by Collett (1988). **Figure 2** presents Lachenbruch's measured temperature diffusion between a temperature profile measured soon after circulation is stopped (red circles) and the undisturbed temperature profile projected to infinite dimensionless time after circulation was terminated. The incremental diffusion correction is represented by blue diamonds and is mathematically expressed by the line-slope equation.

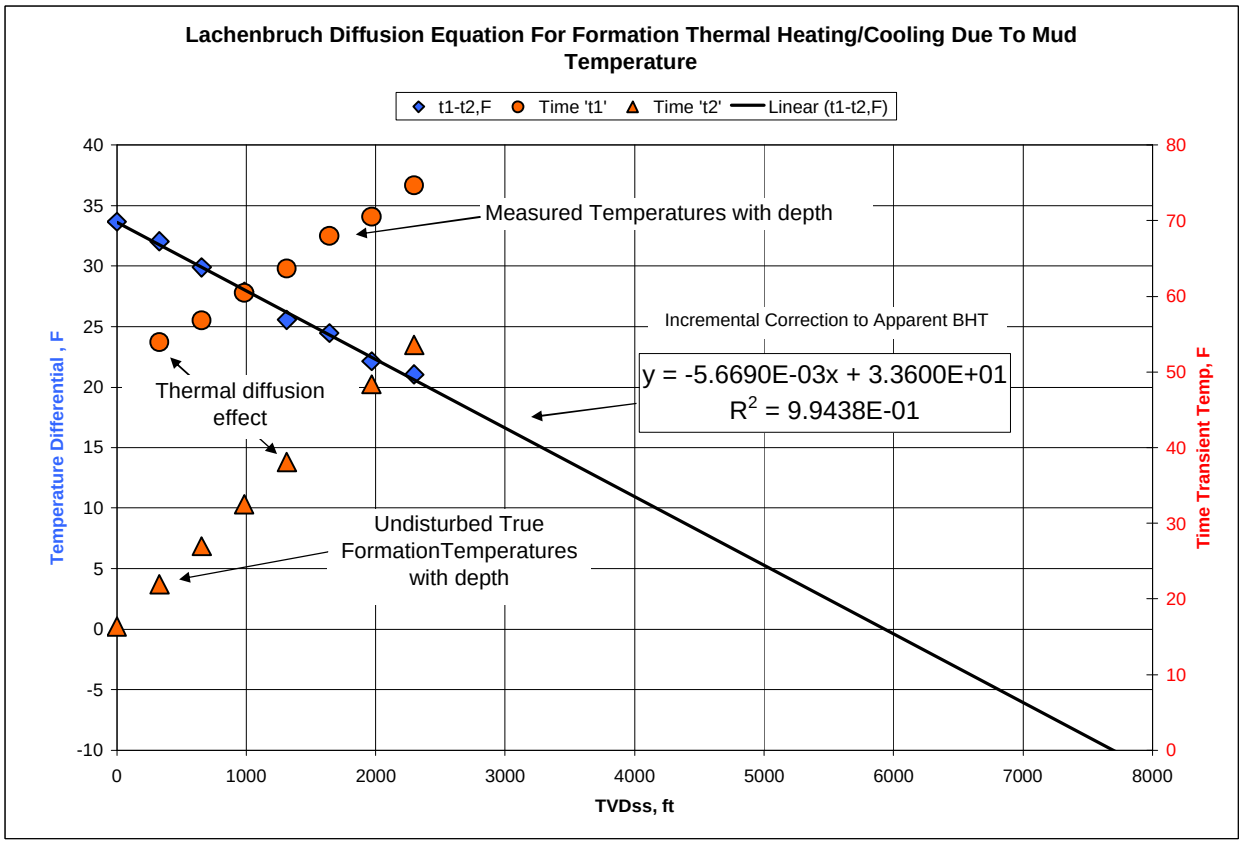

Figure 2. Lachenbruch thermal diffusion model used for correcting bottom-hole temperature data

Salinity-Based Estimate of BOPF Temperature

Salinity was estimated for the three wells in this study using the "Apparent Formation Water Resistivity" method (Rwa) and picked from the shale in the interval between the BOPF and the BHSZ. **Figure 3** shows the Rwa minimum value in the shales used to estimate the equivalent salinity. Once salinity is determined, freezing point temperature was estimated using algorithms documented by Fofonoff and Millard (1983) and available on-line at: http://gaea.es.flinders.edu.au/~mattom/Utilities/freeze.html.

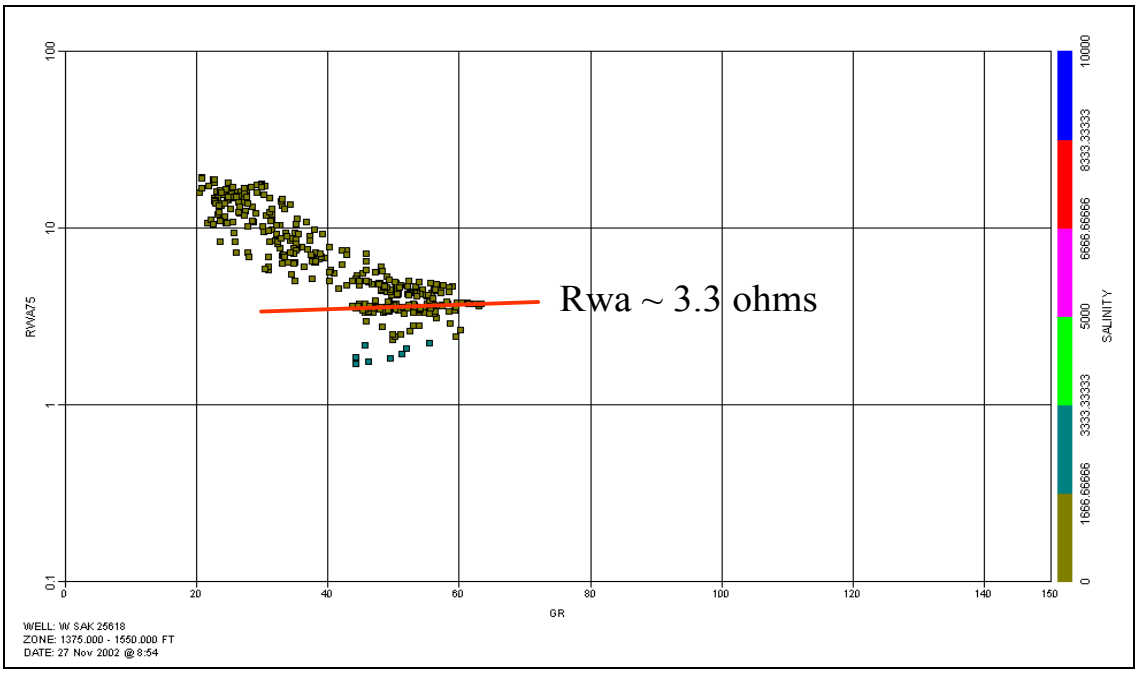

Figure 3. Rwa plot of West Sak 20; BOPF to BHSZ

Location of BOPF

Wire-line well logs were used to examine the response to permafrost (ice and rock mixture). Gamma ray, resistivity, compression sonic, density, and neutron logs are used to pick the BOPF based on physical properties complied by Prensky (1995) and Davidson (1983). **Table 1** was referenced for determining appropriate log response to permafrost and gas hydrates. Ice-bearing formations have less fluid porosity and tend to be more consolidated than comparable unfrozen sediments. This causes them to be more resistive and to have a higher sonic velocity. These effects are most pronounced in sandstones and less obvious in shale facies.

Table 1. Summary of Published Values for Properties of Ice and Pure Gas Hydrates
(modified from Davidson (1983))

Property	Ice	Hydrate
Dielectric Constant (at 273°K)	94	58
NMR rigid lattice second moment of H_2O Protons (G^2)	32	33±2
Water molecule reorientation time at 273°K (µsec)	21	10
Diffusional jump time of water molecules at 273°K (µsec)	2.7	>200
Isothermal Young's modulus at 268°K (10^9 Pa)	9.5	8.4
Velocity of longitudinal sound at 273°K (km/sec)	3.8	3.3
Transit time of longitudinal sound at 273°K (µsec/ft)	80	92
Velocity ratio Vp/Vs at 273°K	1.88	1.95
Poisson's ratio	0.33	0.33
Bulk modulus at 272°K	8.8	5.6
Shear modulus at 272°K	3.9	2.4
Bulk density (gm/cm^3)	0.916	0.912
Adiabatic shear compressibility at 273°K (10^{-11} Pa)	12	14
Thermal conductivity at 263°K (W/m-°K)	2.23	0.49±0.02

Determining Top/Base of HSZ

The base of the hydrate stability zone (BHSZ) was estimated from the phase envelope described by Katz (1971), Collett et al. (1988) and Collett (1993). A comparison of the gas hydrate model for pressure and temperature phase behavior is made to the local geothermal gradient of each well after correcting for the thermal diffusion effects (Lachenbruch (1982)). The conditions for hydrate formation are considered favorable when the geothermal gradient is less than the hydrate stability envelope. Depth (equivalent pressure) position of top and base of the HSZ is determined where the geothermal gradient intersects the hydrate stability envelope. Depth of the permafrost and the geothermal gradient are the most important parameters controlling thickness of the HSZ.

Discussion of Results

Salinity-Based Estimate of Base of Permafrost Temperature. **Table 2** lists results of the salinity estimates for wells in this study. Salinity is found to range from 1543 to 2760 ppm. The effect on salinity of lowering the freezing point of water is less than -0.6°C.

Table 2. Freezing Point Estimates for Salinities Determined using Rwa Method

	depth	tvdss	Pressure, psi	Pressure, Mpa	Freezing Point Calculator		
					Freezing Point of Water, C	Rwa@75F	Salinity, ppm
Ruby State 1	**KB=**	**386**					
top perma frost	0	386	14.7	0.101352928			
base perma frost	1480	-1094	473.702	3.26606018	-0.498	2.3	2256.882
base hydrate stability	2386	-2000	866	5.970859562			
run1 td	1868	-1482	641.706	4.424406935			
run2 td	3284	-2898	1254.834	8.651775505			
Cirque 2	**KB=**	**170**					
top perma frost	0	170	14.7	0.101352928			
base perma frost	1100	-930	402.69	2.776449696	-0.347	1.9	2759.992
base hydrate stability	1850	-1680	727.44	5.015522032			
run1 td	2254	-2084	902.372	6.221635664			
run2 td	7634	-7464	3231.912	22.28324789			
West Sak 20	**KB=**	**133**					
top perma frost	0	133	14.7	0.101352928			
base perma frost	1370	-1237	535.621	3.692976639	-0.565	3.3	1543.813
base hydrate stability	2333	-2200	952.6	6.567945518			
run1 td	2133	-2000	866	5.970859562			
run2 td	7133	-7000	3031	20.89800847			

Base of Permafrost (BOPF). The depth to BOPF was determined in the pre-drilling analysis from well logs and using log responses from Table 1 and reported in Table 2. An example of one of the study wells is shown in **Figure 4**. In this log display for the Ruby State 1, BOPF is evident from the sharp resistivity and acoustic log response breaks at 1480 ft MD. Based on the correlation from these three wells, the expected pre-spud BOPF at Hot Ice No. 1 was projected to be at 1100 ft TVDss and 1315 feet MD.

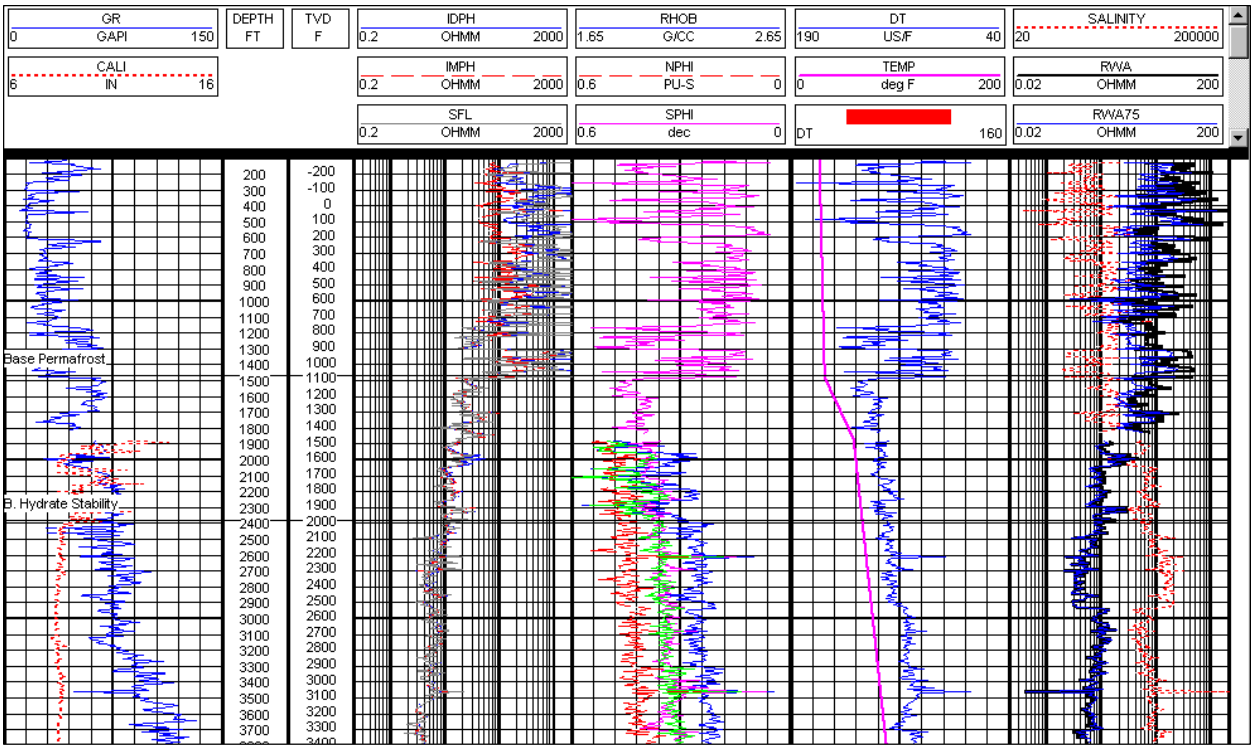

Figure 4. In Ruby State 1, resistivity (track 3) and acoustic slowness (track 3) provide the best indication for the position of BOPF found at 1480 ft MD.

In the Hot Ice No. 1, both core and log data show the well entering into unfrozen material at 1046 ft TVDss. Both observations agree to within a few feet. The base of frozen material occurs in a thick sand interval at this depth and is considered the lowest know permafrost. **Figure 5** is a log display for Hot Ice No. 1. Resistivity (track 2), acoustic slowness (track 4), and magnetic resonance logs (CMR in track 5) provide the best indication for the BOPF. CMR measurements were made directly on the cores at the surface.

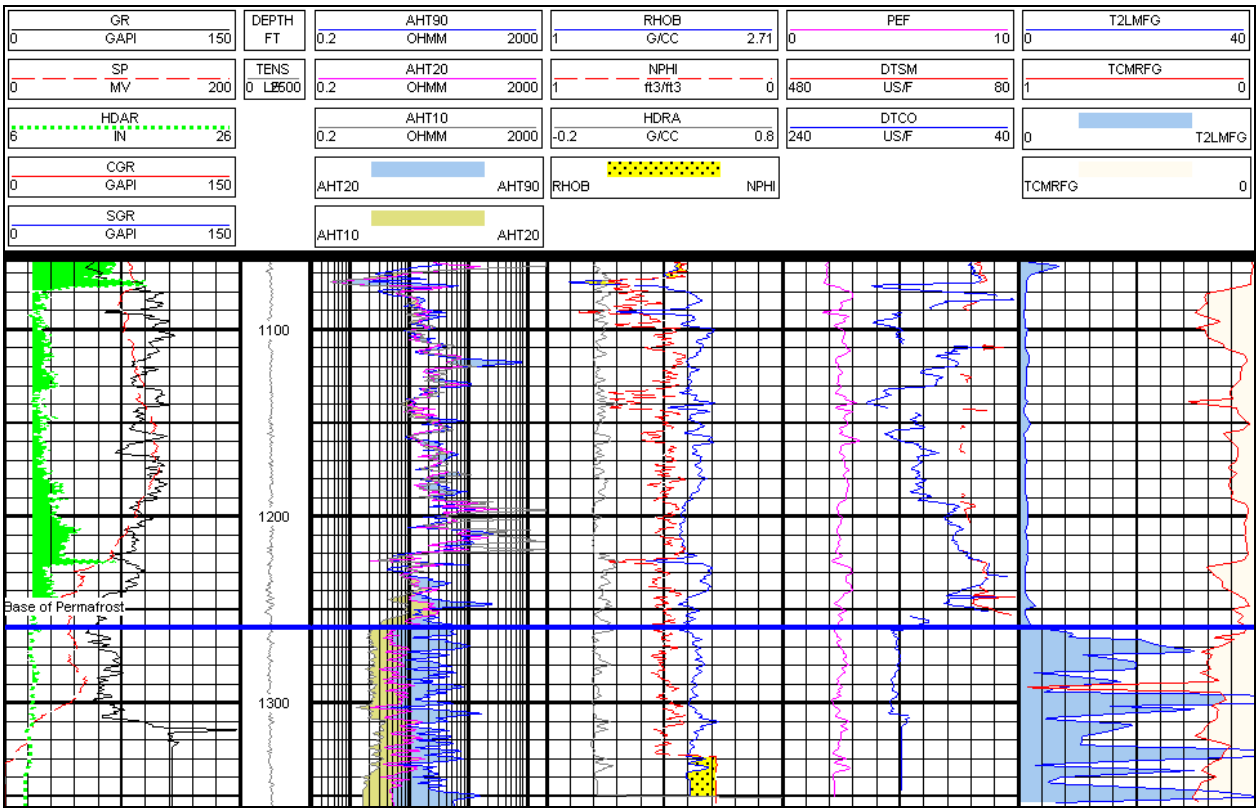

Figure 5. Resistivity (track 3), acoustic slowness (track 3) and magnetic resonance log (track 5) provide the best indication for position of the base of permafrost.

The core-based estimate of BOPF is slightly subjective since the drilling mud was maintained at -5°C, and the core passed through decreasing temperature zones as it was brought to the surface. Consequently, limited refreezing occurred. Observation of the transition from "frozen" to "unfrozen" section was made both from visual examination, and from CMR measurements made on the whole core by Kleinberg (2003) using a Schlumberger CMR tool located in the well site core analysis lab. The core-based estimate of BOPF was developed before wire-line logs were run. In Hot Ice No. 1 the transition from frozen to unfrozen sediments occurred in good sand so both the log and core signature were clear.

Geothermal Gradients. **Figure 6** presents the original and corrected geothermal gradients derived from the composite bottom-hole temperatures of the three wells in this study. Note that as the permafrost is approached (blue shading); diffusion-corrected temperatures are almost 30°F lower than uncorrected bottom-hole temperatures. Drilling fluids cause heating in the shallow intervals versus a cooling effect at depth. Depth at which the diffusion-corrected gradient and the uncorrected gradient are equal is defined as the temperature centroid. The temperature centroid occurs at approximately 6000 ft for these data. In the Hot Ice No. 1, a chilled drilling and coring fluid was used to prevent melting of the permafrost or destabilizing hydrates when encountered. This had the additional benefit of minimizing any thermal warming effects that the mud system would have on BHT in this well.

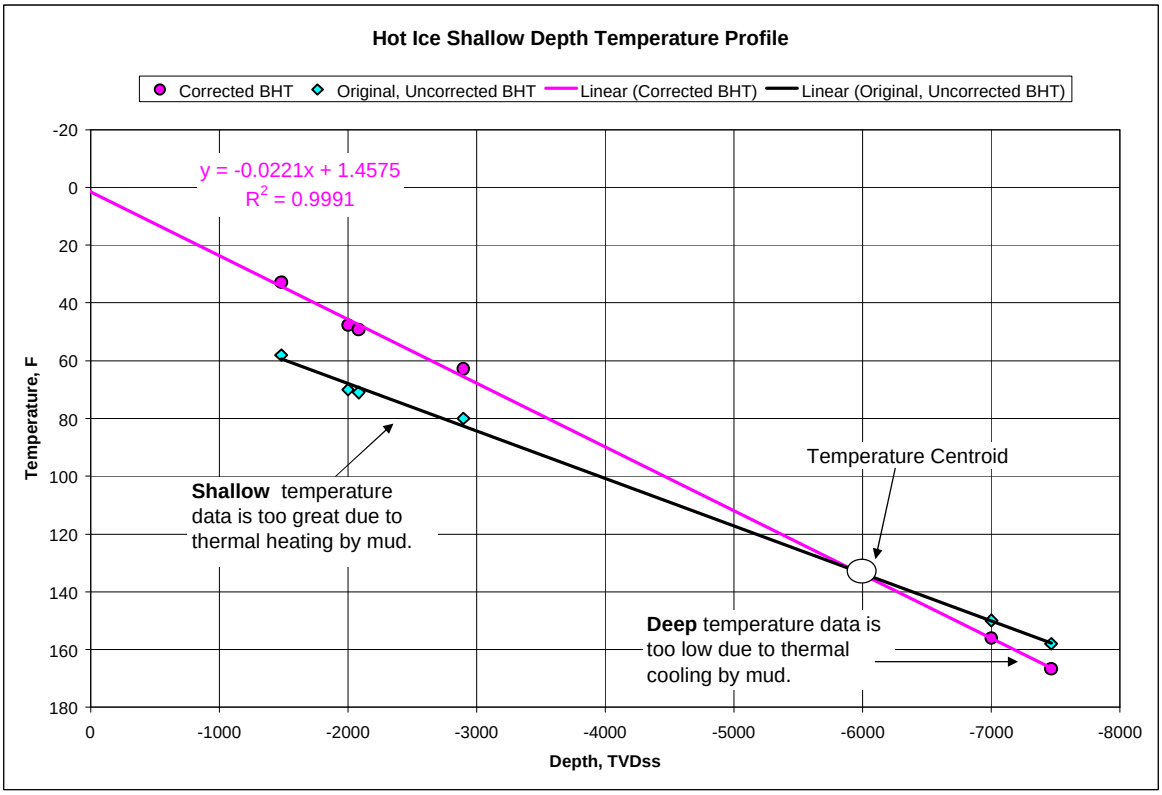

Figure 6. Results of applying Lachenbruch thermal diffusion model to bottom-hole temperatures from three wells in study

Calculated gradient in the Hot Ice No. 1 is one-third larger than regional gradient at the Hot Ice No. 1 location (**Figure 7**). Collett et al. (1988) based their thermal gradients primarily on 46 wells in which long-term thermal monitoring has been conducted. At the well sites these data certainly provide the best information on thermal gradients. The data set, however, is sparse. To improve coverage, Collett et al. (1988) and Collett (1993) used well logs in which they could identify the base of ice bearing permafrost, a regional average temperature at this depth, and the effective regional average surface temperature to compute a gradient in the frozen zone. The gradient below the frozen zone was calculated as the permafrost gradient multiplied by a regional value for ratio of the temperature gradient in unfrozen sediments divided by the gradient in the unfrozen zone. This provides an enhanced grid. The final grid is still sparse and includes data points with more potential for error.

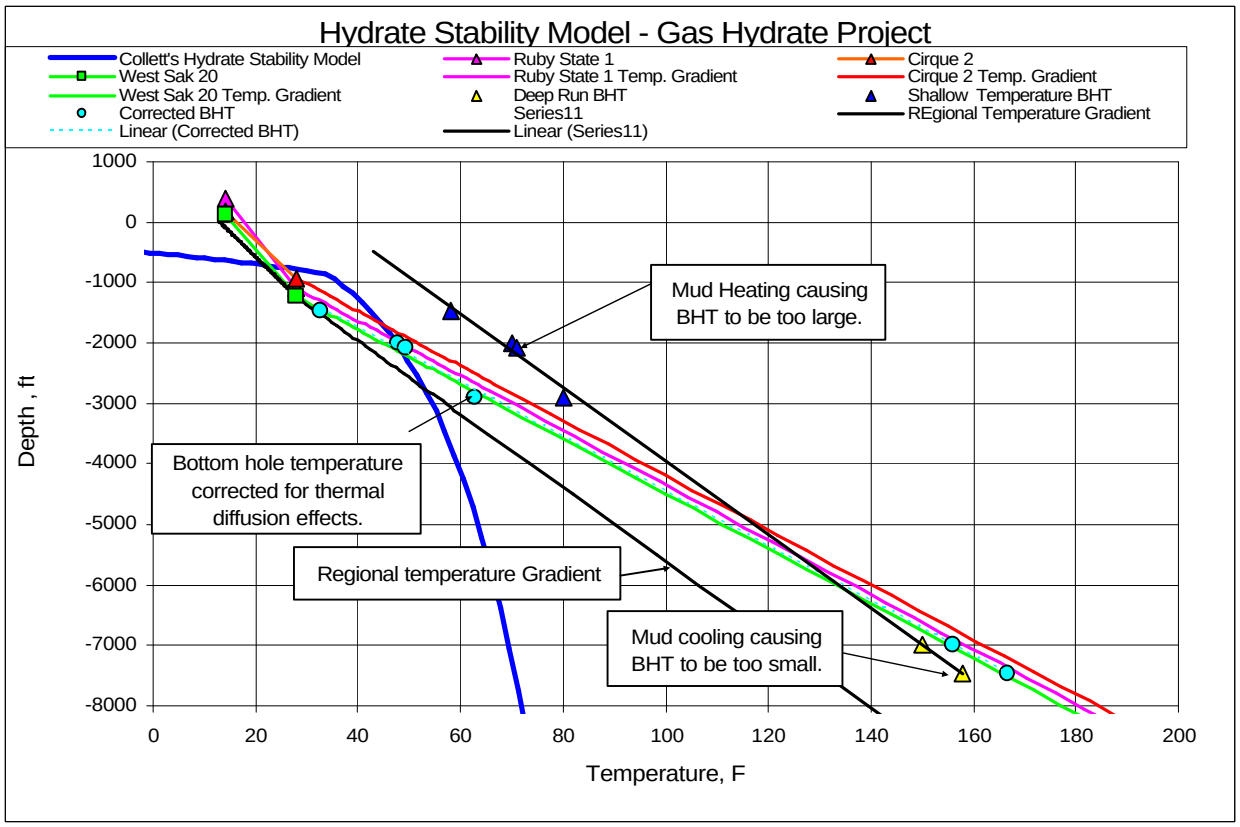

Figure 7. Offset well geothermal gradients after applying Lachenbruch et al.'s (1982) thermal diffusion model. Note local well gradients are greater than regional gradient estimated by Collett et al. (1988).

The local uncorrected geothermal gradient estimated from the three wells in the study is found to have the same gradient as Collett's regional gradient but is 30°F greater at the BOPF position (see Figure 7). Using this uncorrected gradient would result in an interpretation that no gas hydrates would be present in the Hot Ice No. 1 location, as the temperature gradient is outside the hydrate stability window. However, by correcting the scalar temperature values for the effect of thermal diffusion, a gas hydrates envelope is evident (**Figure 8**).

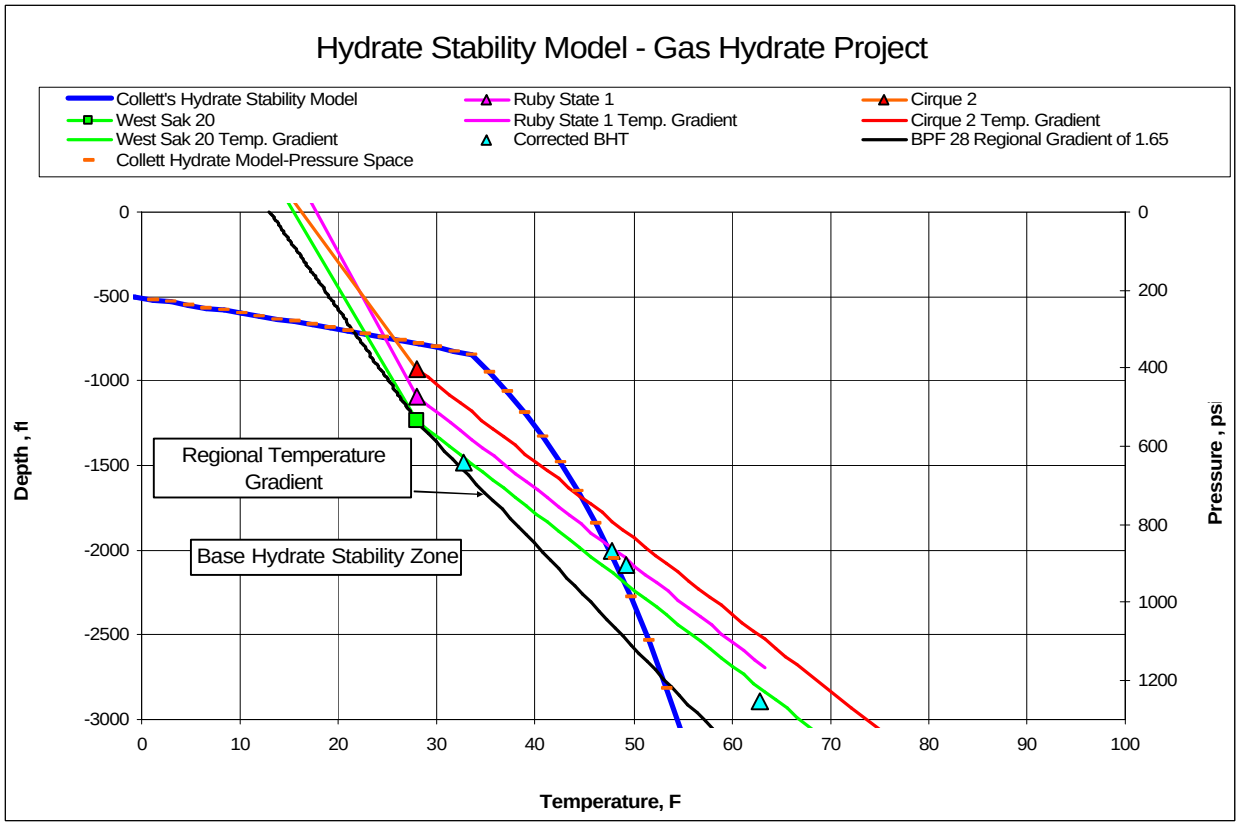

Figure 8. Offset well geothermal gradients after applying Lachenbruch (1982) thermal diffusion model. Note local well gradients are greater than regional gradient estimated by Collett et al. (1988)

Determining BHSZ. The BHSZ was estimated from the phase envelope described by Katz (1971), Collett et al. (1988) and Collett (1993). The estimated BHSZ for the three wells used is summarized in Table 2 and ranges from 1680 to 2200 ft TVDss. By correlation, the pre-spud BHSZ was estimated to be at 2000 ft TVDss in the Hot Ice No. 1 location. This is significantly shallower than the BHSZ estimates if the regional geothermal gradient were used, which would result in the BHSZ being as deep as 2572 ft TVDss. The difference in the intersection of the sub-permafrost geothermal gradient and Collett's hydrate stability envelope is the application of Lachenbruch et al.'s (1982) thermal diffusion model to the local BHT temperature measurements.

Once BOPF was determined in Hot Ice No. 1, the depth of BOPF was used to estimate the depth to BHSZ, using the local thermal gradient. This requires temperature at BOPF. Based on salinity calculated in the three study wells this temperature should be 31°F. The regional temperature map in Collett et al. gives a temperature of 28° F at BOPF. **Figure 9** presents calculations for both temperatures using the local thermal gradient, along with depth using the regional values. Using the local thermal gradient and the local estimate of BOPF temperature of 31°F, the BHSZ is estimated at -1812 ft TVDss. Based on the regional BOPF temperature of 28°F and the local thermal gradient, BHSZ is -2022 ft TVDss. Use of Collett et al.'s regional values result in a BHSZ depth of -2572 ft TVDss.

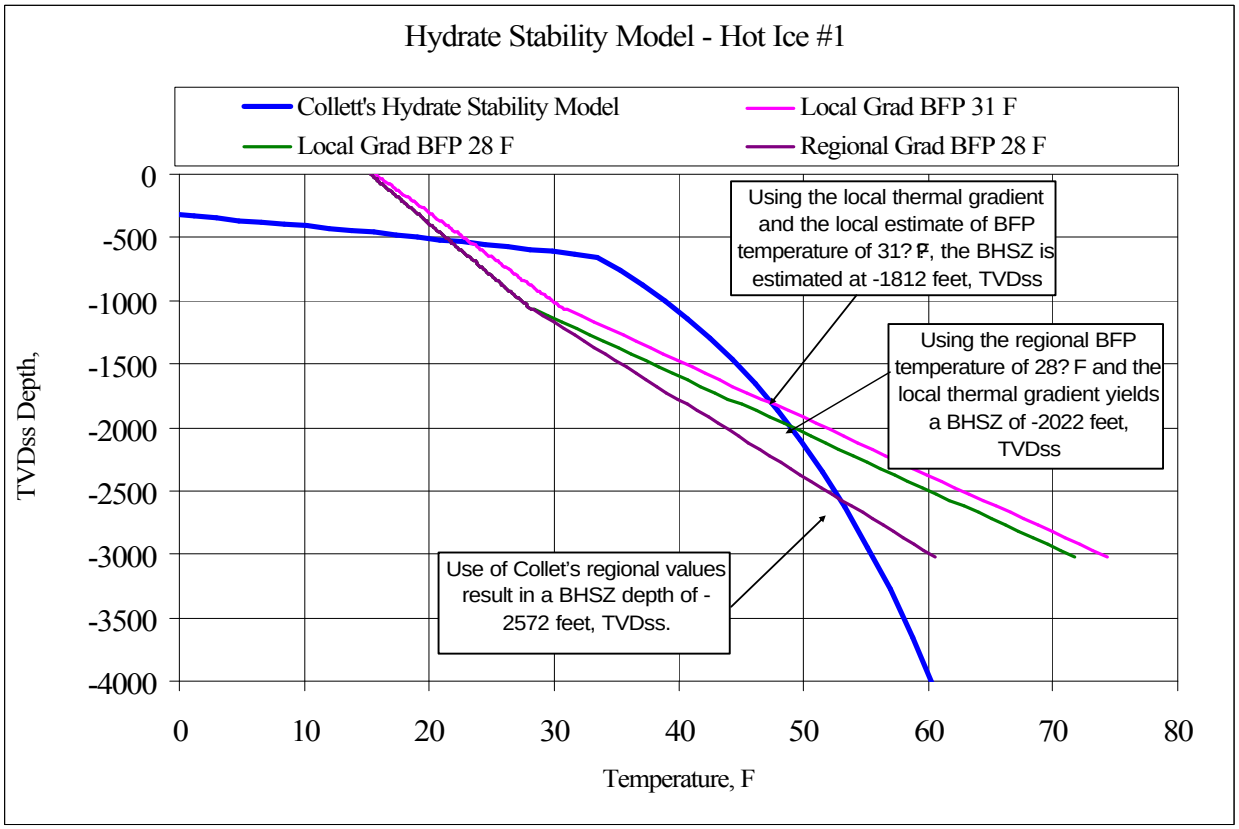

Figure 9. Estimates of BHSZ using various combinations of temperature gradients and BOPF temperatures derived from either regional or local correlations

Conclusions

The BHSZ (base of hydrate stability zone) was recalculated at the Hot Ice No. 1 using data from local wells to estimate pore fluid salinity and thermal gradients in and below the permafrost. Salinity calculated using the Rwa method raises the local temperature at the base of the frozen zone from that given on regional maps. Bottom-hole temperature calculated from measured bottom-hole temperature corrected for thermal diffusion gives a larger local thermal gradient than shown on the regional study. These results were combined into a new estimate for BHSZ that is 760 ft shallower than what would be predicted from regional studies.

Acknowledgments

The authors thank Anadarko Petroleum Corporation and the Department of Energy for providing the opportunity to work and publish this information on the Hot Ice No. 1. Robert Kleinberg of Schlumberger deserves recognition for his efforts in the acquisition and interpretation of the CMR log data on the Hot Ice No. 1 ice core.

References

Collett, T.S., 1993, "Natural Gas Hydrates of the Prudhoe Bay and Kuparuk River Area, North Slope, Alaska," *AAPG Bull., v. 77, no. 5*, p.793-812.

Collett, T.S., Bird, K.J., and Magoon, L.B., 1993, "Subsurface Temperatures and Geothermal Gradients on the North Slope of Alaska," *Cold Regions Science and Technology, 21, Elsevier Science Publishers B. V. Amstersdam,* pages 275-293.

Collett, T.S., Bird, K.J., Kvenvolden, K.A., and Magoon, L.B., 1988, "Geologic Interrelations Relative to Gas Hydrates Within the North Slope of Alaska," *USGS Open-file Report 88-389*, 150 p.

Davidson, D., 1983, "Gas Hydrates as Clathrate Ices," *in Cox, J., ed., Natural gas hydrates—properties, occurrence and recovery*: Butterworth, Woburn, MA, p. 1-16.

Fofonoff, P. and R.C. Millard Jr., 1983, "Algorithms for computation of fundamental properties of seawater," *Unesco Technical Papers in Marine Science 44*, 53 pages.

Katz, D.L., 1971, "Depths to Which Frozen Gas Fields (Gas Hydrates) May Be Expected," *Journal of Petroleum Technology, v.23*, p.419-423.

Kleinberg, R., 2003, (personal communication).

Lachenbruch, A.H., Sass, J.H, Lawver, L.A., Brewer, M.C., Marshall, B.V., Munroe, R.J., Kennelly, J.P., Galanis, S.P., and Moses, T.H., 1982, "Temperature and Depth of Permafrost on the Arctic Slope Of Alaska," *USGS Professional Paper 1399,* pages 645-657.

Prensky, S.E., 1995, "A review of gas hydrates and formation evaluation of hydrate-bearing reservoirs," (paper GGG), *Presented at 1995 meeting of the Society of Professional Well Log Analysts, Paris, France*, June 26-29.

Slone, E.D. Jr., 1998, *Clathrate Hydrates of Natural Gases*, Marcel Dekker, Inc., New York.

Appendix F:
Coalbed Methane Studies at Hot Ice No. 1 Gas Hydrate Well
First Report

Charles E. Barker
US Geological Survey
Denver, CO 80225

April 2003

Coal Gas Content Measurements

Six coal seams were sampled from the Hot Ice No. 1 well (160, 255, 650, 840, 960 and 1090 ft TVD) in the initial drilling phase (2003) to the casing point at 1400 ft. Canister desorption measurements indicate that coal samples from 160 to 960 ft TVD, taken from seams deeply embedded within the permafrost, did not contain significant sorbed coalbed gas. Somewhat dramatically, the last coal seam cored before the casing point at 1400 ft did have a measurable gas content. This coal seam (1090 ft TVD) yielded about 15 standard cubic feet of gas/ton of coal (SCF/ton).

Based on a streak test, the lack of complete gelification and the presence of still distinct tree limbs and so forth, these coals appear to be lignite to perhaps subbituminous C rank. In comparison, the somewhat higher rank subbituminous B to A coals of the prolific coalbed methane producing Powder River Basin of Wyoming contain about 25 SCF/ton. Gas content usually increases with depth and rank, so deeper coals expected immediately below the 1400 ft TVD casing point will have higher gas contents.

Ice Veins in Coal

Coal studies also show that coarsely crystalline ice in veins (**Figure 1**), whose cross-cutting relationship to coal bedding indicates they result from water injection and freezing in place. The injection and freezing process may occur in multiple episodes as indicated by layered vein structures (**Figure 2**). Injection of water (now seen as ice) is indicated by the ice cross-cutting the coal seam bedding (**Figures 3 and 4**) in all seams encountered up to about 960 ft TVD and, in at least one case, has been injected in a manner as to cause brecciation of coalbed (**Figure 5**). This injection and fracturing process is thought to be generated during initial stages of permafrost formation when cooling causes formation water to expand, pressuring the strata and inducing water movement. This pressurized water preferentially invades the structurally weaker coal seams within more competent clay-rich siliciclastic sedimentary strata.

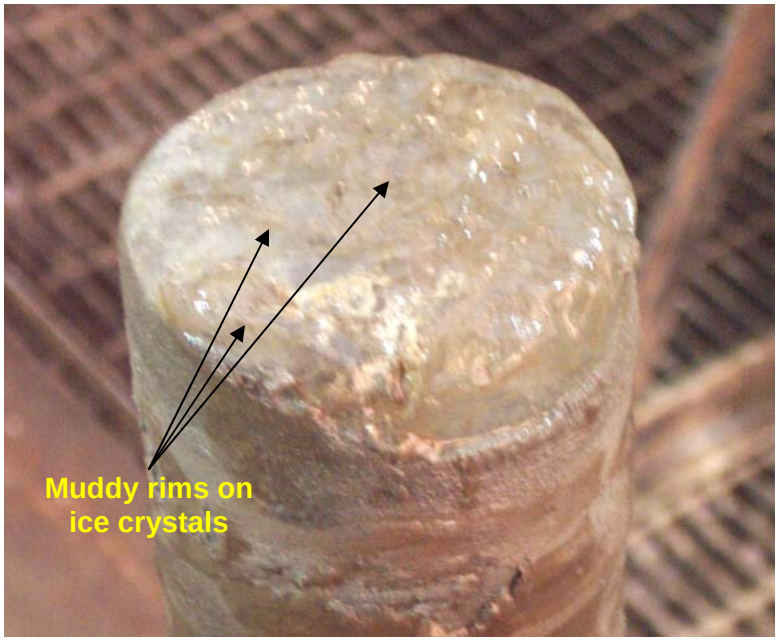

Figure 1. Broken core surface composed of coarsely crystalline ice crystals whose boundaries are delineated by muddy rims. Ice vein is cutting a matrix-supported conglomerate. Depth is about 520 ft TVD. (When in gauge, core diameter is about 3.4 inches.)

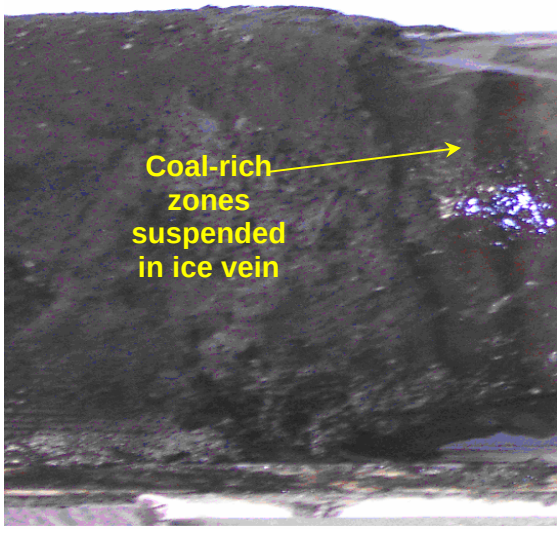

Figure 2. Layered ice vein, Anadarko Hot Ice No. 1 Well, 252.3 ft TVD

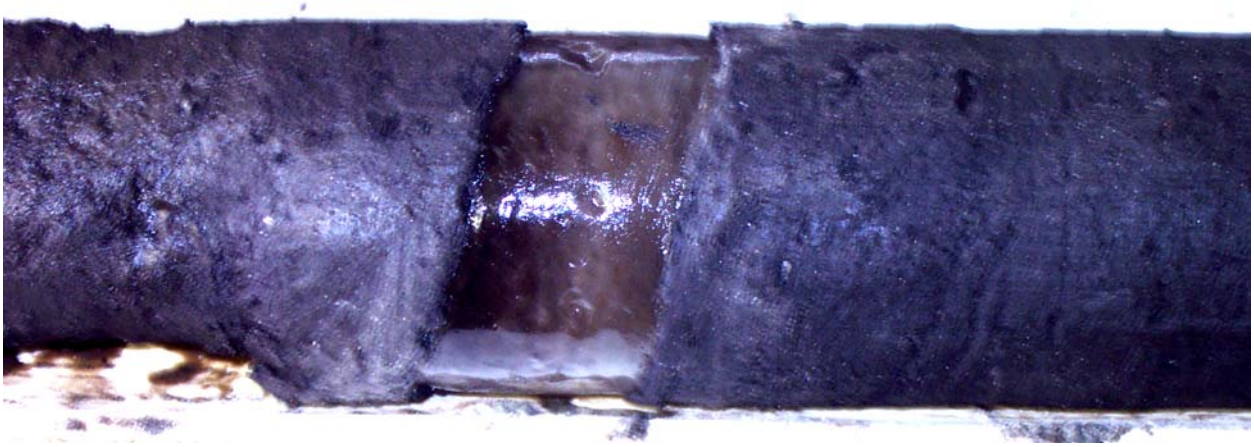

Figure 3. Ice vein, Anadarko Hot Ice No. 1 Well, 252.3 ft TVD

Figure 4. Ice vein cross-cutting coal, Anadarko Hot Ice No. 1 Well, 650-654 ft TVD

Figure 5. Another view of core shown in Figure 4 showing brecciation of the coal by the injection and freezing process that forms ice veins in Hot Ice Well, 650-654 ft TVD. Note brownish-black coloration of the coal typical of low rank coal.

Discussions with Tim Collett (USGS, Denver) and a preliminary literature search indicate these ice-vein features observed in the Hot Ice well occur at a much greater depth than previously reported. The photographs of these features clearly show ice veins 5 to 10 cm thick crosscutting the coalseam bedding. This phenomenon was observed in all of the gas-barren coalbeds down to 960 ft TVD. The 15-inch thick gassy coal bed at 1090 ft TVD did not display ice veining.

The relationship between the gas-barren coal seams and ice veining disrupting the coal seams in particular and the rock seals in general throughout the sedimentary column that may a genetic relationship. The ice veins may act to disrupt the gas-tight seals needed to retain gas in shallowly buried coal seams. Further, the relationship suggests a mechanism for the nearly complete gas loss in permafrost bound coals by gas seal disruption followed by simple buoyant gas seepage. This process may be enhanced by forced gas migration from the coals by solution or, as entrained bubbles, in the initially mobile water phase still present within the forming permafrost and eventual loss to the atmosphere through the now disrupted gas seals.

Probably most intriguing to science in general is that if this ice formed during permafrost formation about 1.5 Ma, ice in the coal seams at the Hot Ice well is on the order of a million years old. Samples taken for composition and isotopic analysis of the ice may yield data that have interesting paleoclimate implications as well as contain information on permafrost formation processes.

Implications of Gas-Barren Coals within the Permafrost

The lack of gas in shallower coal seams deeply embedded in the permafrost was forecast from gas log studies in wells across the North slope basin (Collett and others, 1989) and coal desorption data measured by the USGS at the Tarn field in 2000 – but had not been confirmed by coal core sampling. Thus, in the Hot Ice well, for the first time, we obtained coal core data

confirming our hypothesis about the loss of gas from shallowly buried coals embedded within the permafrost.

A question then arises: Why are these coals still barren of gas after their apparent depletion about 1.5 Ma when the permafrost formed? Chemically low rank coals are highly gas prone and capable of continued generation of copious amounts of microbial gas over the 1.5 Ma available since depletion. The coals are also prone to sorbing gas sourced from upward migration of deep basin gas. These gases can refill breached and depleted coalbed reservoir – if the gas seals are reconstituted when the permafrost forms and cements the sedimentary column. We conjecture that this process does not occur at the Hot Ice well for several reasons. One, biogenesis is likely markedly slowed at below-freezing temperatures. Second, upwardly seeping deep basin generated gases are likely bound up in the hydrate zone below the permafrost. Finally, perhaps the gas seals have not reconstituted above the coals and gas continues to escape to atmosphere.

Potential for Coal Seams after 1400-ft TVD Casing Point

The potential for coals when drilling recommences below 1400 ft is high. Log analysis for nearby wells indicates good chances for intersecting additional coal seams and carbonaceous shale (below the 1400 ft casing point) over a depth range of 1400 to 1550 ft TVD. Of particular interest to the coalbed methane study is a 5-ft thick coal bed indicated from log studies at 1525 to 1530 ft.

It cannot be stressed enough that collecting coal core from below the base of the permafrost is crucial to confirming the hypothesis for the mechanism for gas-barren coalbeds in permafrost.

Appendix G:

Dissociation Rates of Methane Hydrate at Elevated Pressures and of a Quartz Sand-Methane Hydrate Mixture at 0.1 MPa

Report of the Menlo Park USGS Research in Support of

the Maurer/Anadarko/DOE Methane Hydrate Project

Under the National Methane Hydrate Research and Development Program

National Energy and Technology Program, Department of Energy

March 5, 2003

Stephen H. Kirby, Susan Circone, and Laura A. Stern
U.S. Geological Survey
345 Middlefield Rd. MS 977
Menlo Park, CA 94025

Report prepared by Susan Circone

Results Summary:

- The dissociation rate of porous, synthetic methane hydrate decreases with increasing pressure, and the pressure effect on the dissociation rate is reversible when the pressure is changed. The slowest dissociation rates at elevated pressures were observed at 268 K. Below 273 K the rates exhibit a complex temperature-dependence similar to that observed at 0.1 MPa. Our results suggest that optimum preservation of sI methane-rich hydrate will occur in drill cores maintained near 268 K during retrieval.

- The dissociation behavior of porous, synthetic methane hydrate is not significantly affected by the rate of depressurization, based on a slow depressurization experiment designed to emulate the depressurization pathway during retrieval of a drill core sample. Methane pressure was reduced over 13 minutes from 2.34 MPa to 0.1 MPa, and dissociation was monitored for 3 days at 268 K, 0.1 MPa. The measured dissociation rate is identical to those measured on samples that were depressurized within 15 seconds to 0.1 MPa.

- A porous hydrate-quartz sand mixture (1:3 by volume) dissociated at 268 K by rapid pressure release to 0.1 MPa released gas at a higher rate than 1:1 mixed or layered samples. This indicates that reducing hydrate-hydrate grain contacts by introducing sediment increases the rate of dissociation, and this factor will strongly impact the success of hydrate preservation in drill core materials with high sediment to hydrate ratios.

- Two hydrate-bearing samples were fabricated for testing of trial materials in the Mobile laboratory prior to its mobilization to Alaska. The first was a large volume, porous methane hydrate + quartz sand sample (30%:70% by volume) that was shipped directly to Tulsa in a chilled, pressurized vessel. The second was a pure, porous, methane hydrate sample that was sent to LBNL for computed tomography (CT) x-ray imaging tests in an instrument package built by LBNL for use in the Mobile Laboratory.

Introduction

Previously, a comprehensive set of experiments performed at 0.1 MPa CH_4 gas pressure and temperatures between 204 and 289 K (Stern et al., 2001) showed that methane hydrate dissociation rates are significantly depressed between 242 and 271 K. The optimum temperature for sample preservation is 268 K. Above 271 K, rates increase rapidly and systematically with increasing temperature (Circone et al., 2000). The introduction of 100 μm quartz sand into the methane hydrate sample in layers and in a homogeneous mixture (1:1 ratios by volume) resulted in higher, but still depressed, rates. Structure II methane-ethane hydrate (80% CH_4: 20% C_2H_6) did not exhibit anomalously depressed dissociation rates at 268 K.

At the request of the Maurer/Anadarko project, rapid depressurization experiments were performed at 1.0 and 2.0 MPa and temperatures between 250 and 283 K for the present report to determine: (1) if the optimum preservation temperature at 1 and 2 MPa is also at 268 K, and (2) if the complex temperature dependence of the dissociation rate at 0.1 MPa is also observed at elevated pressures. This information will provide recommendations for optimizing hydrate preservation by control of mud temperature during drill core recovery. An additional sample of porous methane hydrate was dissociated, following a slow depressurization pathway that was

designed to emulate the depressurization pathway during retrieval of a drill core sample, to determine (3) if the depressurization rate affects the hydrate dissociation rate. (4) Finally, the dissociation rate of a 1:3 hydrate-quartz sand mixture at 268 K, 0.1 MPa was measured to determine what to expect in a similar experiment on a sample synthesized in our facility, which will be performed to test equipment and sample-handling protocol in the Mobile Laboratory prior to moving the laboratory to Alaska.

Experimental Method for Measuring Dissociation Rates

Experiments were performed on methane hydrate synthesized from 180-250 μm seed ice (packed to 40% porosity) and pressurized CH_4 gas by heating from 250 K to ~290 K, holding at 290 K for several hours at methane pressures above 22 MPa, then cooling to near 250 K (Stern et al., 1996; see Fig. 1). The resulting material is pure, sI methane hydrate with ~30% intergranular porosity and a measured stoichiometry of $n = 5.89 \pm 0.01$ (Circone et al., 2001).

Following synthesis, samples were thermally equilibrated at a fixed temperature between 250 and 283 K. Bath temperature T_{ext} was measured in the D-limonene bath surrounding the synthesis vessels, and internal sample temperatures were measured by thermocouples centered at the sample top, middle, and bottom and at the sample side (Setup #1, Fig. 1) or only at the sample middle (Setup #2). The pressure first was lowered to ~2 MPa above the equilibrium boundary. To start the dissociation experiment, the pressure was rapidly (~12 sec) decreased to the set point pressure, then opened to the back pressure regulator (Tescom ER 3000), which maintained the pressure within ±0.02 MPa of the set point.

Samples were held at constant temperature ($T_{iso} = T_{ext}$) for some time interval. As the hydrate sample dissociated, the back pressure regulator released methane to the flowmeter. The released gas was collected in our custom-built flowmeter at 0.1 MPa (gas flow rate is determined by monitoring the change in weight of an inverted, H_2O-filled cylinder as CH_4 gas displaces the H_2O; flow rate measurement capability ranges from 3000 to less than 0.1 cc/min; Circone et al., 2001). If $T_{ext} < 273$ K, the experiment was concluded by heating to 282 K to release any remaining methane gas and hence establish the gas content of the hydrate.

In addition, a methane hydrate sample, equilibrated at 268 K, was slowly depressurized from 2.34 MPa to 0.1 MPa at a rate of 0.17 MPa/minute while dissociation was monitored during and after the pressure release step (for 3 days at 0.1 MPa). The rate of pressure release was chosen to emulate the expected depressurization pathway during drill core retrieval at the "Hot Ice" site. The amount and rate of gas released from the hydrate was corrected for the amount of gas released from the free space in the vessel during the pressure release step.

Two porous hydrate-quartz sand mixtures (1:3 and 3:7 by volume, with ~35% porosity) were synthesized using the same technique but starting with a mixture of seed ice and 100 μm quartz sand to produce a 1-inch diameter by 14-inch long sample. For the dissociation experiment, the pressure was rapidly dropped to 0.1 MPa and then gas was released to the flowmeter, bypassing the back pressure regulator. The second sample was shipped to the Mobile Laboratory for testing.

Results

We measured the release of methane from methane hydrate samples held isothermally at 268, 273, 278, and 283 K and at 0.1, 1.0 and 2.0 MPa over time (Fig. 2 and Table 1). Three

effects are clearly evident: (1) dissociation rates at 268 K are significantly slower than those at higher temperatures, (2) the samples completely dissociate within hours at $T_{iso} \geq 273$ K, and (3) rates of dissociation decrease with increasing pressure (at constant isothermal temperature). What is not evident from Fig. 2 is that, in the experiments at $T \geq 273$ K, the internal sample temperatures plummet below 273 K following the depressurization step and are buffered for most of the dissociation event at 272 -273 K in the sample interior, as found by Circone et al. (2000) in experiments at 0 1 MPa. Additional experiments were performed at 250 to 263 K and 1.0 MPa to determine the effect of pressure over a wider temperature range for comparison with the previous results at 0.1 MPa.

Experimental results have been summarized in Fig. 3, in which the average rate of dissociation has been plotted as a function of isothermal hold temperature. This also shows that elevated methane pressure has depressed the dissociation rates both in the anomalous preservation regime and at the warmer temperatures. Furthermore, the rates remain significantly depressed at 268 K and elevated pressure. Note that in all experiments performed to date at 0.1 to 2.0 MPa, the dissociation rates decrease continually over time, never reaching a steady-state rate.

Also at the request of Anadarko, a methane hydrate/quartz sand sample (1:3 ratio, homogeneous mixture) was synthesized and shipped to their Mobile Laboratory then under development in Tulsa, Oklahoma. Synthesis took place in a newly acquired (with funding from this project) large, volume (1.5-inch diameter by 15-inch length) pressure vessel rated to 48 MPa (Fig. 4). The sample was to be rapidly depressurized to 0.1 MPa in a laboratory maintained at 268 K while undergoing testing of their equipment. In order to provide a reference time line for the sample composition while undergoing testing, an identical sample was dissociated in our laboratory by dropping the pressure from 4 to 0.1 MPa in 15 seconds while maintaining a constant external temperature of 268 K (Fig. 5). Our previous work shows that the hydrate dissociation rates increase with increasing volume fractions of sand, especially in homogeneous mixtures as opposed to layered hydrate/sand mixtures.

Finally, because the dissociation experiments that we have performed all followed a more rapid depressurization pathway than is anticipated during actual drill core recovery, we measured the dissociation rate on a sample that underwent the slower, expected depressurization rate (13 minutes vs. ~15 s). The results (Fig. 5) suggest that the rate of pressure release will not significantly affect the dissociation behavior if the drill core temperature is maintained near 268 K.

Summary

Based on the experimental results described in this report, the following observations can be made with respect to maximizing the preservation of a sI methane-rich hydrate during drill core retrieval:

1) Maintaining drill core mud near an optimum temperature of 268 K should greatly enhance the preservation of hydrate within the cores, as cores follow a P, T pathway of decreasing pressure (from $P > P_{equilibrium}$ to 0.1 MPa) and constant temperature.

2) Hydrate preservation will depend to large degree on the relative proportions and distributions of hydrate and sediment in the retrieved material. Hydrate preservation should be greater in hydrate-rich layers relative to sediment -rich layers.

References

Circone, S.; Kirby, S.H.; Pinkston, J.C.; Stern, L.A. *Rev. of Sci. Instrum.* **2001**, *72*, 2709.

Circone, S.; Stern, L.A.; Kirby, S.H.; Pinkston, J.C.; Durham, W.B. In *Gas Hydrates: Challenges for the Future*; Holder, G., Bishnoi, P., Eds.; **2000**; pp 544-555.

Stern, L.A.; Circone, S.; Kirby, S.H.; Durham, W.B. *J. Phys. Chem. B* **2001**, 105, 1756.

Stern, L.A.; Circone, S.; Kirby, S.H.; Durham, W.B. *Can. J. Phys.* **2003**, *in press*.

Stern, L.A.; Kirby, S.H.; Durham, W.B. *Science* **1996**, 273, 1843.

Table 1. Summary of rapid depressurization experiments performed at elevated pressures

Sample ID	Sample weight (g)	T_{iso} (K)	P initial (MPa)	P final (MPa)	Time to drop P (s)	# of t.c.'s	Time at T_{iso} (h)	Gas Released At T_{iso} (%)	Gas Released Total (%)
040502B[a]	29.9	268.2	4.0	2.0		4	19.3	71.7	103.3
040502A[b]	34.5	268.2	4.0	2.0	98	none	188.9	30.2	98.4
042602A	29.9	273.2	5.0	2.0	34	1	22.5	98.0	98.1
042602B	29.9	277.8	7.0	2.0	17	4	2.6	92.9	92.9
120202B	29.9	283.2	9.6	2.0	13	4	2.0	96.6	96.6
053002B	29.9	249.5	3.0	1.0	14	4	18.9	57.9	100.2
072402A	29.9	253.2	3.0	1.0	15	1	886.1	41.2	98.4
091702A	29.9	257.8	3.5	1.0	12	1	460.0	52.5	99.2
012103B	29.9	262.8	4.0	1.0	15	4	382.7	51.1	100.1
010603A[c]	29.9	263.2	2.6	1.0	9	1	44.1	59.8	101.7
101502A	29.9	268.2	4.0	1.0	17	1	861.9	26.6	96.6
091702B	29.9	272.9	5.0	1.0	24	4	7.0	97.5	97.5
072402B	29.9	277.4	7.1	1.0	15	4	1.8	91.8	91.8
010603B	29.9	283.0	9.5	1.0	16	4	1.2	85.2	85.2
012103A[d]	29.9	268.3	2.3	0.1	753	1	72.5	26.3	101.3
112102[e]	37.4	268.3	4.0	0.1	15	none	21.0	49.3	93.3

Note: Total gas released includes that released upon heating from T_{iso} through 273 K and is based on a starting composition of $CH_4 \cdot 5.89\ H_2O$.

[a] During depressurization, P accidentally dropped to 1.2 MPa, then abruptly to 0.1 MPa, where sample dissociated at rates consistent with anomalous preservation. Then sample was pressurized to 2.0 MPa (up to this point, 13.0 mol% released), and the dissociation rate increased dramatically. Sample lost 58.7 % over next 19.1 h. This suggests that repressurizing samples to a CH_4 pressure below the equilibrium boundary may not decrease but instead enhance the dissociation rate.

[b] After 167 h at 2.0 MPa, P was dropped to 1.0 MPa for 8.1 h (lost 2.3 %), then increased to 2.0 MPa for 14.1 h (2.1%), before heating the sample to 282 K.

[c] Depressurization step complicated, as valve to gas booster was left open. This may have affected the dissociation rate, and the experiment will have to be duplicated.

[d] Sample slowly depressurized from 2.34 MPa to 0.1 MPa at a rate of 0.17 MPa/minute.

[e] Hydrate mixed with quartz sand, 33%:67% by volume.

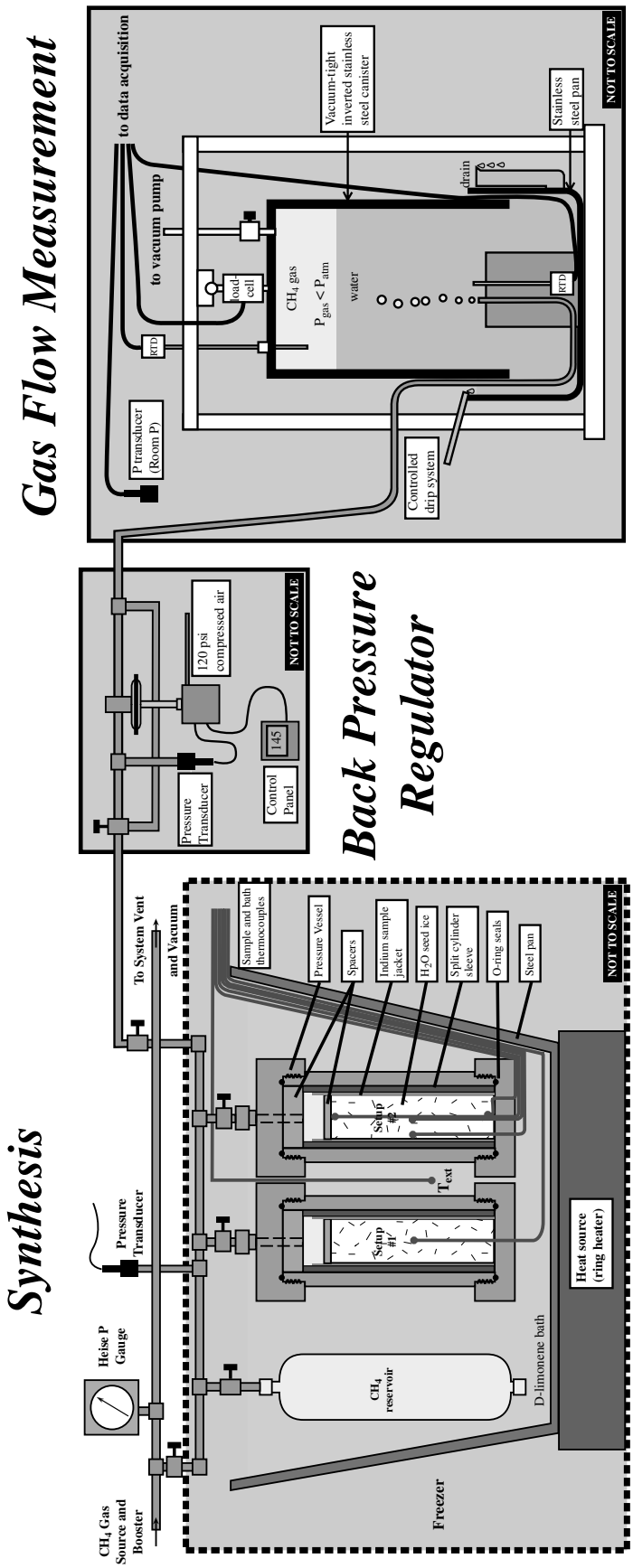

Figure 1. Schematic diagram of methane hydrate synthesis apparatus, back pressure regulator, and flowmeter apparatus

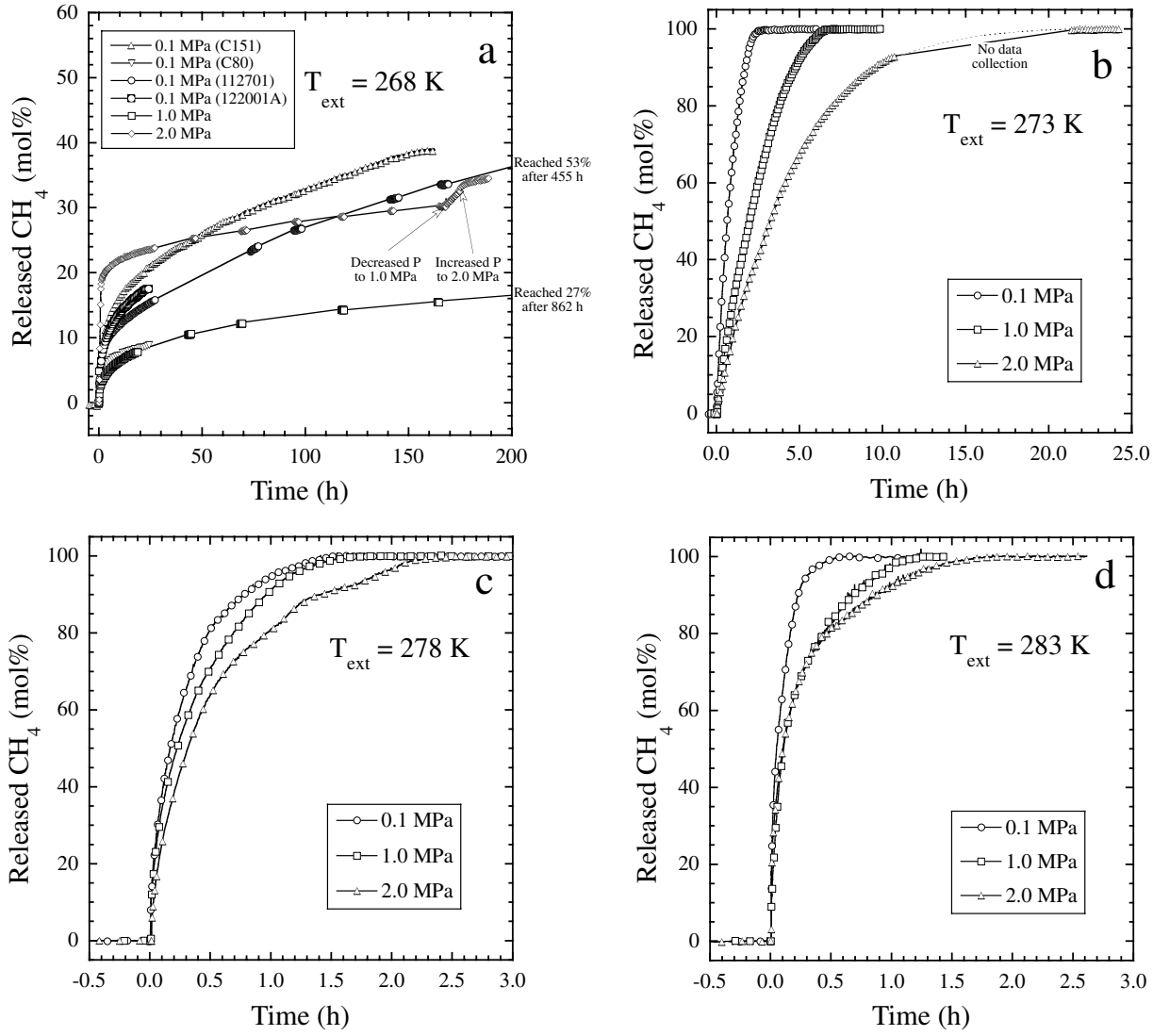

Figure 2. Evolution of methane gas from methane hydrate samples following rapid depressurization from elevated pressure to 0.1, 1.0, or 2.0 MPa at time t = 0 hours. Experiments were performed at isothermal bath temperatures of **(a)** 268 K, **(b)** 273 K, **(c)** 278 K, and **(d)** 283 K. Figure 1a includes curves of four dissociation experiments at 0.1 MPa. Note that the amount of dissociation in the first few hours is variable and does not appear to correlate with pressure. This variability significantly affects the amount of time to 50% dissociation but has little effect on the rate after the first few hours of dissociation, where the rates show a systematic decrease with increasing pressure. These experiments were concluded by heating to 282 K to release the remaining methane gas. In the 2.0 MPa experiment, we demonstrated that the pressure effect on the dissociation rate is reversible. Decreasing the pressure from 2.0 MPa to 1.0 MPa slightly increased the dissociation rate; returning to 2.0 MPa decreased the rate to near the prior value. At 0.1 MPa, similarly reversible rate changes were obtained by varying the temperature from 268 to as low as 251 K. In figures **(b)**, **(c)**, and **(d)**, the decrease in dissociation rate with increasing pressure is apparent, especially at 273 and 278 K.

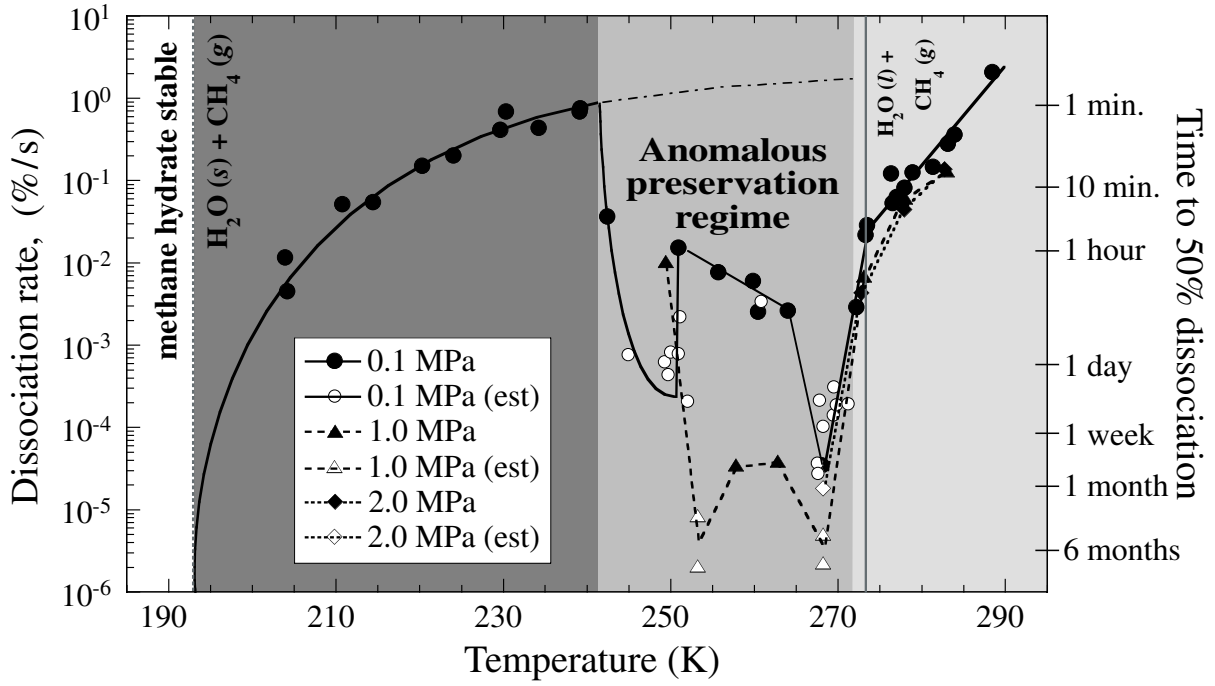

Figure 3. The average dissociation rate, as determined from the time (in seconds) required to release 50% of the gas content from the hydrate sample, as a function of the isothermal hold temperature. The right-hand axis shows the rates converted to relevant time scales. Solid symbols show results for experiments that reached 50% dissociation during the isothermal holds; open symbols show estimated times to 50% dissociation, based on extrapolations using the rates measured near the end of the isothermal hold (this extrapolation yields the minimum time to 50%; the two lowest rates at 253 and 268 K, 1.0 MPa were extrapolated assuming a continued decrease in the dissociation rate with time). Note that at 268 K, the average rate at 2.0 MPa appears higher than that at 1.0 MPa, due to the initially rapid release of methane at the start of the experiment (see Fig. 2a).

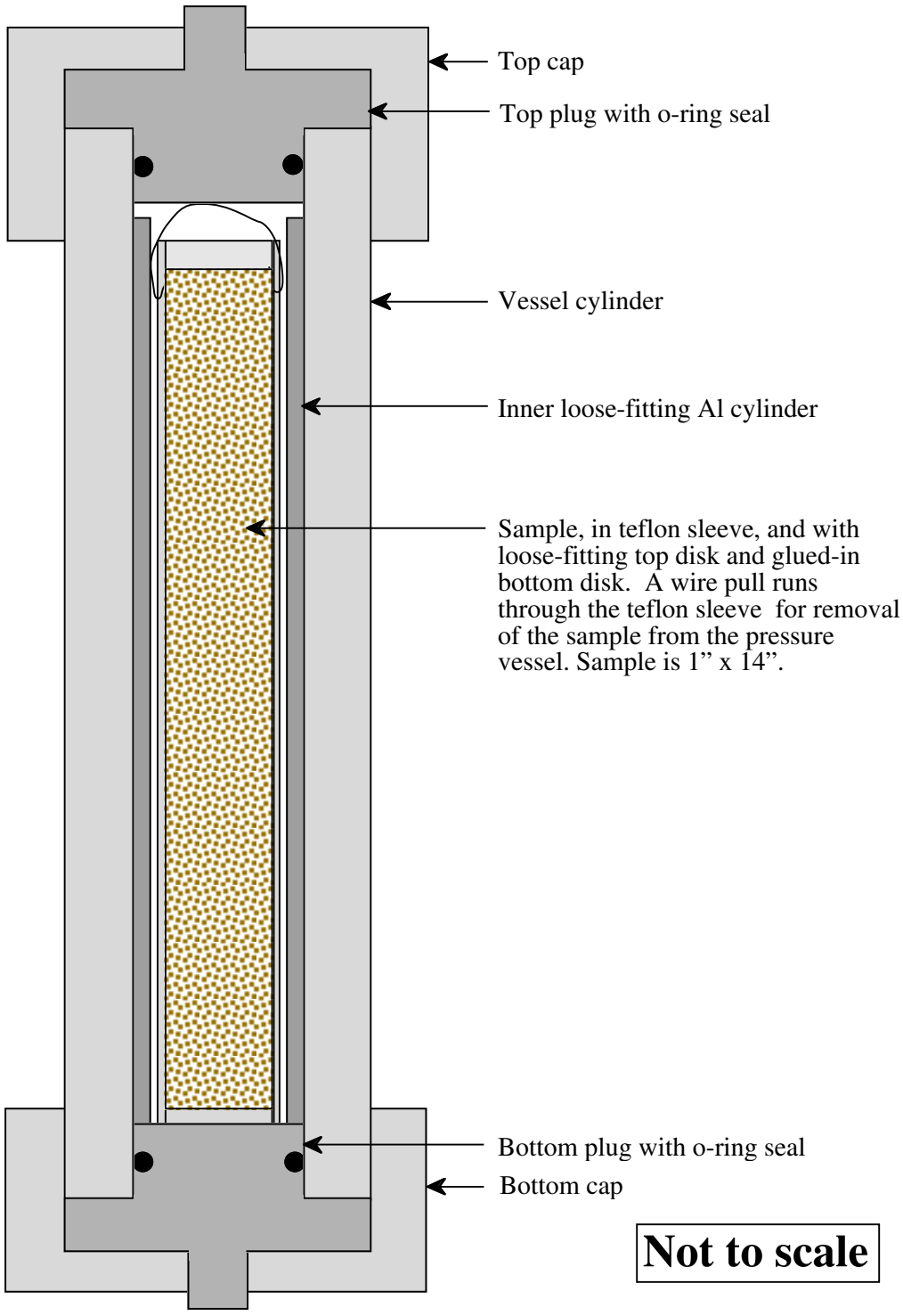

Figure 4. Schematic of vessel and sample of a porous hydrate-quartz sand mixture (30% hydrate: 70% sand by volume) synthesized at the U.S. Geological Survey and shipped for testing in the Mobile Laboratory at Anadarko in Tulsa, Oklahoma.

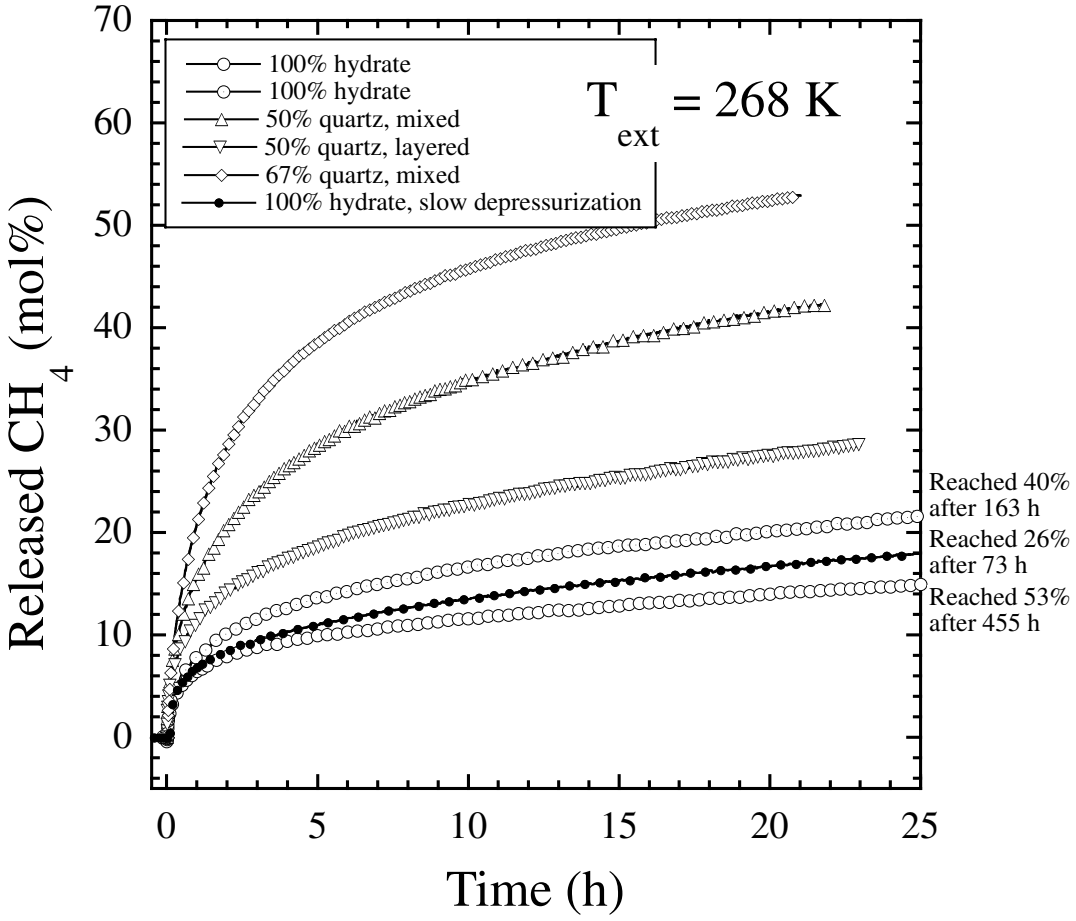

Figure 5. Release of methane from methane hydrate samples with varying amounts of quartz sand in layers (4 hydrate : 3 sand, 50% sand by volume) and in homogeneous mixtures (50% and 67% sand by volume). At 0 hours, the pressure was decreased in ~12 seconds to 0.1 MPa.